

TOXIC GAS ADSORPTION AND WATER STABILITY IN
METAL-ORGANIC FRAMEWORKS

Lauren Nicole McHugh

A Thesis Submitted for the Degree of PhD
at the
University of St Andrews



2019

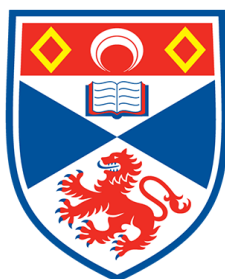
Full metadata for this item is available in
St Andrews Research Repository
at:
<http://research-repository.st-andrews.ac.uk/>

Identifiers to use to cite or link to this thesis:
DOI: <https://doi.org/10.17630/10023-18848>
<http://hdl.handle.net/10023/18848>

This item is protected by original copyright

Toxic Gas Adsorption and Water Stability in Metal-Organic Frameworks

Lauren Nicole McHugh



University of
St Andrews

This thesis is submitted in partial fulfilment for the degree of

Doctor of Philosophy (PhD)

at the University of St Andrews

August 2019

Candidate's declaration

I, Lauren Nicole McHugh, do hereby certify that this thesis, submitted for the degree of PhD, which is approximately 40,000 words in length, has been written by me, and that it is the record of work carried out by me, or principally by myself in collaboration with others as acknowledged, and that it has not been submitted in any previous application for any degree.

I was admitted as a research student at the University of St Andrews in September 2015.

I received funding from an organisation or institution and have acknowledged the funder(s) in the full text of my thesis.

Date

Signature of candidate

Supervisor's declaration

I hereby certify that the candidate has fulfilled the conditions of the Resolution and Regulations appropriate for the degree of PhD in the University of St Andrews and that the candidate is qualified to submit this thesis in application for that degree.

Date

Signature of supervisor

Permission for publication

In submitting this thesis to the University of St Andrews we understand that we are giving permission for it to be made available for use in accordance with the regulations of the University Library for the time being in force, subject to any copyright vested in the work not being affected thereby. We also understand, unless exempt by an award of an embargo as requested below, that the title and the abstract will be published, and that a copy of the work may be made and supplied to any bona fide library or research worker, that this thesis will be electronically accessible for personal or research use

and that the library has the right to migrate this thesis into new electronic forms as required to ensure continued access to the thesis.

I, Lauren Nicole McHugh, confirm that my thesis does not contain any third-party material that requires copyright clearance.

The following is an agreed request by candidate and supervisor regarding the publication of this thesis:

Printed copy

Embargo on all of print copy for a period of 2 years on the following ground(s):

- Publication would preclude future publication

Supporting statement for printed embargo request

Publications related to this work are currently in progress and further publications are expected.

Electronic copy

Embargo on all of electronic copy for a period of 2 years on the following ground(s):

- Publication would preclude future publication

Supporting statement for electronic embargo request

Publications related to this work are currently in progress and further publications are expected.

Title and Abstract

- I agree to the title and abstract being published.

Date

Signature of candidate

Date

Signature of supervisor

Underpinning Research Data or Digital Outputs

Candidate's declaration

I, Lauren Nicole McHugh, understand that by declaring that I have original research data or digital outputs, I should make every effort in meeting the University's and research funders' requirements on the deposit and sharing of research data or research digital outputs.

Date

Signature of candidate

Permission for publication of underpinning research data or digital outputs

We understand that for any original research data or digital outputs which are deposited, we are giving permission for them to be made available for use in accordance with the requirements of the University and research funders, for the time being in force.

We also understand that the title and the description will be published, and that the underpinning research data or digital outputs will be electronically accessible for use in accordance with the license specified at the point of deposit, unless exempt by award of an embargo as requested below.

The following is an agreed request by candidate and supervisor regarding the publication of underpinning research data or digital outputs:

Embargo on all of electronic files for a period of 2 years on the following ground(s):

- Publication would preclude future publication

Supporting statement for embargo request

Publications related to this work are currently in progress and further publications are expected.

Date

Signature of candidate

Date

Signature of supervisor

Acknowledgements

First of all, thank you Russell for the opportunity to work on this thoroughly enjoyable project and for your invaluable help and guidance over the last four years. It truly has been a pleasure working with you.

Thank you to the EPSRC (grant number EP/N50936X/1) and Dstl for funding this project and very special thanks to Martin and Corinne at Dstl for their continued assistance in the testing of materials and for always making me feel welcome during my regular trips down to Porton.

The work in this thesis would not be possible without our collaborators and many thanks to Prof. Sharon Ashbrook and Dr. Daniel Dawson at the University of St Andrews for performing solid-state NMR measurements and Dr. Gianpiero Buscarino, Angela Terracina and Michela Todaro at the University of Palermo for performing EPR measurements.

Thank you to Dr. Laura McCormick McPherson and Dr. Samuel Morris for collecting the synchrotron single crystal data discussed in this thesis and thanks to Dr. Paul Wheatley for his assistance with surface area analysis.

Many thanks to the technical staff at the University of St Andrews, in particular Dr. David Cordes for collecting single crystal measurements and Mrs. Sylvia Williamson for her assistance with TGA measurements.

Thank you also to Dr. Yuri Andreev (PXRD), Mr. Ross Blackley (SEM and EDX) and Dr. Tomas Lebl (NMR).

A huge thank you to the members of the Morris group past and present. I couldn't have hoped to work with a better bunch of people and I can honestly say it's been great fun! I've had the pleasure of making some friends for life and I'm sure we'll see each other again.

To my best friends Farah and Phoebe, you have both been incredibly supportive throughout my PhD and have always been there to give a good pep-talk. I'm so grateful to you guys!

To Jason, Rebecca and Catherine (aka my lunch buddies). We've been friends since our Undergraduate days and have all gone through the PhD experience together. Thank you for our daily gossip sessions at the lunch table and regular get-togethers.

Last but not least, I would like to give a heartfelt thank you to my parents John and Jessie. You have always given me a huge amount of love and support and have encouraged me to chase my dreams. I wouldn't have come this far without you!

Research data underpinning this thesis are available at <https://doi.org/10.17630/c7b0027d-b2d4-4f67-984f-a63834197d5c>

Abstract

This thesis largely focuses on the development of water stable metal-organic frameworks (MOFs) for the removal of toxic industrial chemicals (TICs) from airstreams. The aim of the research is to investigate the water stability and adsorptive properties of a series of copper MOFs for potential use inside a filter in future air purification systems.

Chapter 4 introduces a member of the STAM series of MOFs: STAM-17-OEt, which has formed the main focus of the project. STAM-17-OEt displays exceptional hydrolytic stability and ammonia adsorption properties that are in part explained by the new crumple zone mechanism shown by the material.

The other members of the STAM series of MOFs are presented in chapter 5, where the long-term water stability first seen in STAM-17-OEt is shown to be present for other members of the series. Ammonia adsorption testing provides promising results, with a clear linear adsorption trend visible across the series, and though the materials remove hydrogen cyanide from an airstream, testing does not show a clear trend.

Chapter 6 describes the synthesis of MOF-activated carbon composite materials, where selected STAM MOFs are grown inside BPL activated carbon at a series of loadings. The composites allow a typically powdered MOF sample to be manufactured into a form that may potentially be used inside a filter and by altering the loading of MOF within the composites, the materials may be tailored to remove a broader range of contaminants than the individual components alone.

Chapter 7 discusses the synthesis and characterisation of two new copper frameworks, where STAM-NMe₂ is a member of the STAM series with a nitrogen-containing side chain and copper-1,3-bis(4-carboxyphenyl)-5-ethoxybenzene forms as a 'layered coordination framework' and is not related to the STAM series.

Publications

Publications arising from this thesis

Chapter 4:

- L. N. McHugh, M. J. McPherson, L. J. McCormick, S. A. Morris, P. S. Wheatley, S. J. Teat, D. McKay, D. M. Dawson, C. E. F. Sansome, S. E. Ashbrook, C. A. Stone, M. W. Smith and R. E. Morris, *Nat. Chem.*, 2018, **10**, 1096-1102.

Chapters 4 and 5:

- A. Terracina, L. N. McHugh, M. Todaro, S. Agnello, P. S. Wheatley, F. M. Gelardi, and R. E. Morris and G. Buscarino, 2019, manuscript under review.

Chapter 5:

- D. M. Dawson, C. E. F. Sansome, L. N. McHugh, M. J. McPherson, L. J. McCormick McPherson, R. E. Morris and S. E. Ashbrook, *Solid State Nucl. Magn. Reson.*, 2019, **101**, 44-50.

Chapter 6:

- L. N. McHugh, A. Terracina, P. S. Wheatley, G. Buscarino, M. W. Smith and R. E. Morris, *Angew. Chem. Int. Ed.*, 2019, **58**, 11747-11751.

Chapter 7:

- L. N. McHugh, L. J. Olivera Perez, P. S. Wheatley, D. B. Cordes, A. M. Z. Slawin and R. E. Morris, *CrystEngComm*, 2019, **21**, 5387-5391.
- L. N. McHugh, D. B. Cordes, P. S. Wheatley, A. M. Z. Slawin and R. E. Morris, 2019, manuscript submitted.

Publications outside the scope of this thesis

- S. E. Henkelis, S. A. Morris, M. Mazur, P. S. Wheatley, L. N. McHugh, and R. E. Morris, *J. Mater. Chem. A*, 2018, **6**, 17011-17018.

Table of Contents

Acknowledgements	v
Abstract	vii
Publications	viii
Abbreviations used Throughout this Thesis	xv
Chapter 1: Introduction	1
1.1 Toxic Industrial Chemicals	1
1.1.1 Ammonia.....	2
1.1.2 Hydrogen Cyanide	5
1.2 Respirator Canisters	7
1.3 Porous Solids.....	8
1.4 Activated Carbons	8
1.5 Metal-organic Frameworks	9
1.5.1 Overview	9
1.5.4 Copper MOFs	16
1.5.5 General Applications of MOFs	20
1.5.5.1 Biomedical Applications.....	20
1.5.5.2 Gas Storage.....	21
1.5.5.3 Catalysis	22
1.5.6 Toxic Gas Adsorption in MOFs	23
1.5.7 Physical Form of MOFs	25
1.5 References.....	26
Chapter 2: Aims	37
Chapter 3: Experimental Techniques	38
3.1 Solvothermal Synthesis	38
3.1.1 Synthesis of MOFs and Composite Materials.....	39

3.2 Crystallography	39
3.3 X-ray Diffraction	43
3.3.1 Powder X-ray Diffraction.....	45
3.3.2 Single Crystal X-ray Diffraction	48
3.3.3 Synchrotron Radiation	51
3.4 Thermogravimetric Analysis	53
3.5 Activation of Materials	54
3.6 Gas Adsorption.....	56
3.6.1 Surface Area Determination.....	57
3.6.2 Micro-breakthrough	63
3.7 Water Stability and Cyclohexane Adsorption	69
3.8 Infrared Spectroscopy.....	70
3.9 Nuclear Magnetic Resonance Spectroscopy.....	71
3.9.1 Solution Phase NMR.....	72
3.9.2 Solid-State NMR.....	72
3.10 Electron Paramagnetic Resonance Spectroscopy.....	73
3.11 Electron Microscopy.....	75
3.11.1 Scanning Electron Microscopy.....	75
3.11.2 Energy Dispersive X-ray Analysis.....	76
3.12 References	77
Chapter 4: Water Stability and Ammonia Adsorption in the Hemilabile Metal-organic Framework: STAM-17-OEt	80
4.1 Aim	80
4.2 Introduction	80
4.3 Experimental Procedure.....	81
4.3.1 Synthesis of STAM-17-OEt linker.....	81
4.3.1 Synthesis of STAM-17-OEt.....	83

4.4 Results and Discussion	85
4.4.1 Formation of STAM-17-OEt	85
4.4.2 Crystallographic Characterisation Techniques	86
4.4.2.3 Crystal Structure Analysis of STAM-17-OEt.....	88
4.4.3 Bulk Activation of STAM-17-OEt	98
4.4.4 Solid-State NMR Spectroscopy	99
4.4.5 Porosity of STAM-17-OEt.....	102
4.4.6 Water stability of STAM-17-OEt.....	103
4.4.7 EPR spectroscopy.....	111
4.4.8 Ammonia Adsorption.....	115
4.4.9 “Crumple-zone” mechanism.....	119
4.4.10 Long-Term Humidity Study.....	122
4.5 Conclusion.....	127
4.6 References.....	127

Chapter 5: Toxic Gas Adsorption and Water Stability in the STAM Series of MOFs

.....	130
5.1 Aim	130
5.2 Introduction	130
5.3 Experimental Procedure.....	131
5.3.1 Ligand Syntheses.....	131
5.3.2 MOF Synthesis.....	139
5.4 Results and Discussion	141
5.4.1 Formation of the STAM Series	141
5.4.2. Crystal Structure Analysis.....	143
5.4.3 Porosity Measurements.....	145
5.4.4 Water Adsorption and Stability in the STAM Series.....	146
5.4.5 Ammonia Adsorption.....	157

5.4.6 Hydrogen Cyanide Adsorption.....	160
5.5 Conclusion.....	164
5.6 References.....	165
Chapter 6: Metal-organic Framework-Activated Carbon Composite Materials for the Removal of Ammonia from Contaminated Airstreams	166
6.1 Aim	166
6.2 Introduction	166
6.3 Experimental Procedures	168
6.3.1 Synthesis of STAM-17-OEt@BPL composites	168
6.3.2 Synthesis of STAM-17-OnPr@BPL Composites.....	169
6.3.3 Attempted Synthesis of STAM-17-OEt@Coconut Shell Carbon Composites	169
6.3.4 Attempted Synthesis of STAM-17-OEt@Carbon Foam Composites.....	170
6.4 Results and Discussion	170
6.4.1 Formation of STAM@BPL Composites.....	170
6.4.2 Powder X-ray Diffraction of STAM@BPL Composites	172
6.4.3 Scanning Electron Microscopy.....	174
6.4.3.1 Scanning Electron Microscopy Analysis of STAM-17-OEt@BPL Composites	175
6.4.3.2 Scanning Electron Microscopy Analysis of Other Selected Attempted Composites.....	177
6.4.4 Surface Area Analysis.....	179
6.4.4.1 Surface Area Analysis of STAM-17@BPL Composites.....	180
6.4.5 Adsorption Isotherms of STAM-17-OEt@BPL Materials.....	182
6.4.6 Ammonia Uptake.....	185
6.4.6.1 Micro-breakthrough	186
6.4.7 EPR Spectroscopy	191
6.4.7.1 EPR Spectroscopy of STAM-17-OEt@BPL Materials	192

6.5 Conclusion	194
6.6 References	195
Chapter 7: Synthetic and Crystallographic Investigation of Two Novel Copper Frameworks.....	197
7.1 Aim	197
7.2 Introduction	197
7.3 Experimental Procedure.....	198
7.3.1 Preparation of STAM-NMe ₂	198
7.3.2 Preparation of Copper-1,3-bis(4-carboxyphenyl)-5-ethoxybenzene	199
7.4 Results and Discussion	203
7.4.1 Formation of an Amine Member of the STAM Series.....	203
7.4.2 Crystal Structure Determination of STAM-NMe ₂	204
7.4.3 Characterisation of STAM-NMe ₂	209
7.4.4 Formation of Copper-1,3-bis(4-carboxyphenyl)-5-ethoxybenzene	213
7.4.5 Crystal Structure Determination of Copper-1,3-bis(4-carboxyphenyl)-5-ethoxybenzene	214
7.5 Conclusions	224
7.6 References.....	225
Chapter 8: Conclusions and Future Work.....	227
8.1 Conclusions.....	227
8.2 Future Work.....	230
Chapter 9: Appendix.....	232

Abbreviations used Throughout this Thesis

MOF	Metal-organic framework
TIC	Toxic industrial chemical
STAM	St Andrews MOF
NH₃	Ammonia
HCN	Hydrogen cyanide
HKUST-1	Hong Kong University of Science and Technology
RH	Relative humidity
PXRD	Powder X-ray diffraction
IR	Infrared
NMR	Nuclear magnetic resonance
BTC	Benzenetricarboxylate
CUS	Coordinatively unsaturated site
TGA	Thermogravimetric analysis
BET	Brunauer, Emmett and Teller
DVS	Dynamic vapour sorption
MAS	Magic angle spinning
EPR	Electron paramagnetic resonance
SEM	Scanning electron microscopy
EDX	Energy dispersive X-ray spectroscopy
DMF	Dimethylformamide

Chapter 1: Introduction

In the following introduction, toxic industrial chemicals are introduced and the chemistry of the contaminants used in this study is discussed, while the current technologies used to mitigate their effects within the field of air purification are described. Metal-organic frameworks are then presented, their underlying structural properties are examined and their general applications are investigated. Finally, the potential of metal-organic frameworks in the adsorption of toxic chemicals is discussed and ways to improve their physical form are introduced.

1.1 Toxic Industrial Chemicals

Toxic industrial chemicals (TICs) are industrial chemicals produced on a large scale that may be stored, transported and used worldwide. They can exist in the gaseous, liquid and solid-state and are highly hazardous. Though their manufacture is necessary for a wide-range of legitimate applications, TICs present a serious health risk to those who come in close contact with them and due to their toxic nature and the large quantities available, are an attractive improvised chemical weapon for militants.

TICs were used as the first chemical weapons of the modern era, where chlorine gas (Cl_2) was released in the First World War to devastating effect and other common TICs include chemicals such as ammonia (NH_3), hydrogen cyanide (HCN) and hydrogen sulfide (H_2S).¹ This section will discuss the chemistry of two TICs used in this project: NH_3 and HCN and their effects on the body.

1.1.1 Ammonia

Ammonia is a colourless gas which has a characteristically pungent odour. NH_3 is found in nature in trace amounts, though it is produced industrially in vast quantities, typically by the Haber-Bosch process.² NH_3 is widely used in nature and industrially, where it is a vital precursor to nitrogen compounds such as amino acids and urea and is used in the production of fertilisers and synthetic fibres.³ Despite its wide range of uses, NH_3 is a highly hazardous chemical and is considered toxic if inhaled. The sharp, pungent odour associated with NH_3 fumes is a significant irritant to the skin, eyes and nose and may cause serious damage to the respiratory tract. High concentrations may lead to permanent lung damage and even death.⁴

1.1.1.1 Structure, Physical and Chemical Properties of Ammonia

An ammonia molecule has a trigonal pyramidal shape and the molecule is formed by overlap of three sp^3 hybrid orbitals and orbitals from the three hydrogens, with a fourth sp^3 hybrid orbital occupied by a lone-pair (Figure 1.1). The H-N-H bond within the molecule is 107° , which is smaller than the tetrahedral angle of 109° due to repulsions between the lone pair and bond pair pushing the N-H bonds slightly inwards.⁵

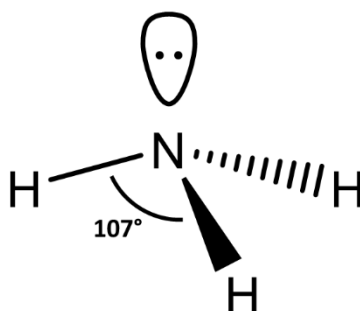


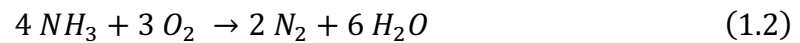
Figure 1.1. Structure of an ammonia molecule from VSEPR theory.

The shape of NH_3 gives the molecule polarity, which enables hydrogen bond formation and facilitates water solubility. The basic nature of the aqueous NH_3 solution is responsible for the neutralization of several acidic gases in the atmosphere, which leads to the formation of secondary particulate matter and the subsequent degradation of air quality and visibility.⁶

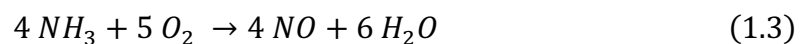
Due to the strong basicity of NH_3 , it readily combines with acids to form salts. One such example is the formation of ammonium chloride, which involves the reaction of humid NH_3 and hydrochloric acid (Equation 1.1).⁷



NH_3 is also highly combustible in air and reacts with oxygen in the atmosphere to form nitrogen and water, as seen in equation 1.2.



The thermodynamic product of combustion is dinitrogen, as all nitrogen oxides are unstable with respect to nitrogen and oxygen. Nitric oxide (NO) can be formed as a kinetic product in the presence of a platinum-rhodium catalyst (Equation 1.3).⁸



1.1.1.2 Effects of Ammonia on the Body

Inhalation of ammonia is perhaps the most common exposure route for those who may be exposed to the chemical, such as industrial workers or first responders. Upon acute NH_3 exposure, the clinical manifestations are usually observed immediately and its toxic effects are experienced through its irritant and corrosive properties. The pungent odour of ammonia is discernible at approximately 50 ppm.^{4,9} However after prolonged exposure, the nose becomes unable to distinguish the odour, making its presence difficult to detect.

More serious health effects become apparent at exposure levels higher than 700 ppm, with immediate irritation to the eyes and throat. Coughing and lung damage occur at levels greater than 1500 ppm and prolonged exposure may be fatal at levels above 2500 ppm.¹⁰

A summary of the toxic effects upon acute NH_3 inhalation may be observed in Table 1.1.

Table 1.1. Summary of toxic effects after acute NH_3 inhalation. Table taken from reference 10.

Exposure (ppm)	Signs and symptoms
50	Irritation to eyes, nose and throat (2 hours)
100	Eye and respiratory tract irritation (rapid onset)
250	Generally tolerable (30-60 mins)
700	Immediate irritation to eyes and throat
>1500	Pulmonary oedema, coughing and laryngospasm
2500-4500	Fatal (30 minutes)
5000-10000	Fatal due to airway obstruction, possible skin damage (rapid)

1.1.2 Hydrogen Cyanide

Hydrogen cyanide is a colourless, highly flammable and extremely toxic gas or liquid with a characteristic smell of bitter almonds. HCN is produced on an industrial scale and is a widely used commodity in applications ranging from chemical and polymer synthesis to mining operations.¹¹

HCN is produced by various processes, though perhaps the most important is the Andrussov oxidation, which involves the reaction of methane and ammonia in an oxygen environment at 1200 °C over a platinum catalyst (Equation 1.4).¹²



HCN is a well-known toxin and acts as a systematic chemical asphyxiant, which disrupts the uptake of oxygen within the body and can be rapidly fatal.¹³

1.1.2.1 Structure, Physical and Chemical Properties of Hydrogen Cyanide

A molecule of hydrogen cyanide has a linear shape, with a triple bond present between the carbon and nitrogen atoms (Figure 1.2).

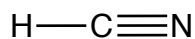
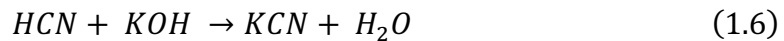
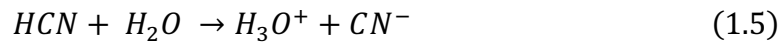


Figure 1.2. Structure of a molecule of hydrogen cyanide.

HCN is a weak acid, with a pK_a of 9.2 and partially ionises in water to provide the cyanide anion (CN^-) (Equation 1.5) and reacts with bases such as potassium hydroxide to form salts called cyanides (Equation 1.6).¹⁴



1.1.2.2 Effects Hydrogen Cyanide on the Body

Exposure routes to hydrogen cyanide can be through skin adsorption, ingestion through contaminated food or water or by inhalation. HCN can be absorbed via the gastrointestinal tract or skin and is rapidly absorbed via the respiratory tract. Once absorbed, cyanide is rapidly distributed throughout the body, though the highest levels are typically found in the liver, lungs, blood, and brain.¹⁵

HCN is a systemic poison, where toxicity is caused by inhibition of the enzyme cytochrome oxidase, which prevents cellular utilization of oxygen. The chemoreceptors of the carotid and aortic arteries are stimulated, which leads to a short period hyperpnea and cardiac irregularities can also occur and the terminal step of electron transport in cells of the brain is affected, which results in a loss of consciousness, respiratory arrest, and eventually, death.¹¹

Acute exposure guideline levels (AEGLs) describe the human health effects from once-in-a-lifetime or rare exposure to airborne chemicals, where AEGL 1 would represent only mild discomfort and AEGL 3 describes life-threatening effects. A person may be exposed to 1.0 ppm for up 8 hours without any serious health effects, though increasing the exposure level to 17 ppm for only 10 minutes can lead to long-lasting health effects and exposure to 27 ppm for 10 minutes can be life-threatening or even fatal.¹⁶

A summary of the toxic effects upon acute HCN inhalation may be observed in Table 1.2.

Table 1.2. Acute exposure guidelines for HCN. Table taken from reference 16.

	10 minutes	30 minutes	60 minutes	4 hours	8 hours
AEGL 1 (discomfort, non-disabling) – ppm	2.5	2.5	2.0	1.3	1.0
AEGL 2 (irreversible or other serious, long-lasting effects or impaired ability to escape) – ppm	17	10	7.1	3.5	2.5
AEGL 3 (life-threatening effects or death) – ppm	27	21	15	8.6	6.6

1.2 Respirator Canisters

Gas masks are an invaluable piece of personal protective equipment used by military personnel and first responders. Air contaminants can affect the ability to perform tasks and the judgement of the individual exposed and may result in serious injury or mortality. Respirators provide the wearer with a way to safely continue their work and time to remove themselves from the harmful environment altogether.

Respirator canisters typically consist of a two main parts: a particulate filter and a packed bed of impregnated activated carbon. The particulate filters out larger particles and the activated carbon bed allows the adsorption of harmful vapours from the surrounding environment.¹⁷

Current gas mask filters contain activated carbon impregnated with metals such as copper, zinc, silver, molybdenum, and the organic compound triethylenediamine.¹⁸ The current respirator canister used by the British Armed Forces is the General Service Respirator (GSR),¹⁹ which has been in use since 2010 and research is underway by Government bodies and industrial companies into developing improved adsorbents for potential use in future respirator canisters.

1.3 Porous Solids

Porous solids are a class of materials with channels or cavities incorporated within them.²⁰ They may be classified according to their pore size, where the three main classes are: microporous, mesoporous and macroporous. Microporous solids have internal pore sizes of less than 2 nm, mesoporous solids have internal pore sizes of between 2-50 nm and macroporous solids have internal pore sizes of greater than 50 nm.²¹

Porous solids may be inorganic, organic, or hybrid inorganic-organic. Inorganic zeolites are aluminosilicates²² and are the most widely studied porous solids.²³⁻²⁶ Their cage-like structure allows them to be used in a variety of processes, such as ion exchange²⁷ and catalysis.²⁸ Organic porous solids are also well known and include activated carbons, whose high surface areas allow them to be used as adsorbents and filter materials.²⁹

1.4 Activated Carbons

Activated carbon is one of the most well-known and extensively used adsorbent materials. Its uses range from decaffeination and water purification systems to the filtration of airstreams in respirator canisters.^{30,31} Activated carbon is easily purchased, is simple and inexpensive to synthesise and is a commercially low-cost material.

Activated carbons are derived from a variety of sources, including coal,³² coconut shells³³ and corn.³⁴ Processing of the source materials to form the activated carbon typically involves heating the source material under either an inert or oxidising atmosphere and produces materials with high levels of porosity and large surface areas.³⁵

Activated carbons are available in a variety of forms, including granular activated carbons, powdered activated carbons, beaded activated carbons and impregnated activated carbons.

Granular activated carbons have a relatively large particle size and are typically used for the adsorption of gases and vapours and water treatment due to the rapid diffusion within them.³⁶ BPL activated carbon is a granular carbon that is typically used in gas-phase applications. It is a bituminous coal-based product that is activated using high temperature in a controlled atmosphere.³⁷ BPL activated carbon has a reported surface area of 1200 m²/g and due to its surface area and strength characteristics, it can be reactivated and reused. BPL activated carbon has a high pore volume, and a strongly adsorbing pore structure that allows adsorption of a broad range of contaminants.³⁸

Impregnation with various types of inorganic cations such as Al⁺ and Li⁺ have been used in air pollution control and silver-loaded activated carbon has been used in the purification of drinking water. Activated carbons on their own adsorb organic vapours well, though require chemical impregnation with other substances such as metal salts in order to adsorb low molecular weight gases.³⁹

1.5 Metal-organic Frameworks

1.5.1 Overview

The deliberate design of a coordination polymer was first proposed by Hoskins and Robson in 1989⁴⁰ and the term metal-organic framework (MOF) was reported by Yaghi *et al.* in 1995.⁴¹

Interest within the field of porous materials has intensified within the last few decades, after the discovery of MOFs.⁴²⁻⁴⁴ MOFs are microporous, crystalline solids that incorporate both inorganic and organic constituents and are comprised of an open framework of metal ions, connected to organic linkers and extending in 1, 2 or 3-dimensions.⁴⁵ According the International Union of Pure and Applied Chemistry (IUPAC), the definition of a MOF is:

“Metal-Organic Framework, abbreviated to MOF, is a Coordination Polymer (or alternatively Coordination Network) with an open framework containing potential voids”.⁴⁶

The nature of the open framework may create voids or ‘pores’ within the material, which can result in high surface areas and pore volumes.⁴⁷⁻⁴⁹ Many MOFs show high surface areas, where the very well-known MOF-5 (Figure 1.3),⁵⁰ HKUST-1 (Hong Kong University of Science and Technology)⁵¹ and MIL-101 (Materials Institute Lavoisier)⁵² are prime examples.

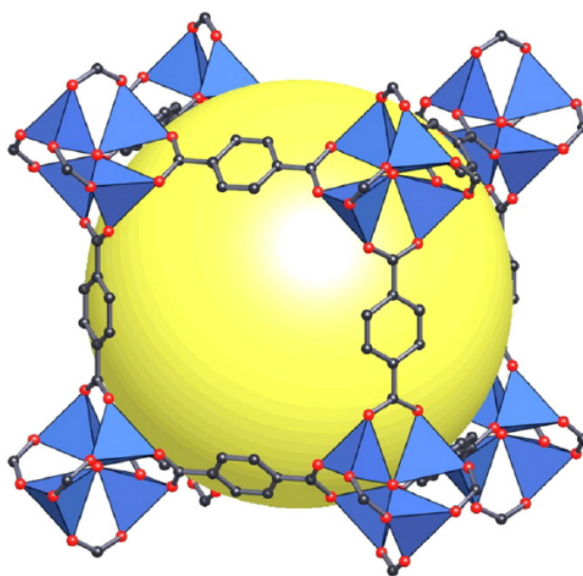


Figure 1.3. Structure of the zinc MOF: MOF-5. The large yellow sphere represents the void space within the framework that leads to the high porosity observed in the material. Figure adapted from reference 50.

1.5.2 Synthesis and General Features

Typical MOF synthesis occurs solvothermally or hydrothermally, though many may also be synthesised under reflux or at ambient temperature. Solvothermal or hydrothermal synthesis usually provides the highest quality samples,⁵³ though the technique is less suitable for larger

scale synthesis. Reflux or ambient temperature syntheses are much more appropriate for commercialisation due to their scalability and lower costs.

In addition to traditional syntheses, the framework may be further modified after the initial synthesis in a technique known as postsynthetic modification.⁵⁴ Typical MOF synthesis is a “one pot” process, where there is no opportunity to adjust the properties of the material during synthesis. Postsynthetic modification (PSM) (Figure 1.4) allows the chemical derivitisation of MOFs after their formation and may involve further reactions to the functional groups within the framework, or simply the removal of guest solvent molecules from within the pores or metal sites by heating under vacuum. New guest molecules may then subsequently be introduced and can bind to open metal sites. The ability to tailor the properties of MOFs for specific requirements makes them exciting materials for a variety of applications.

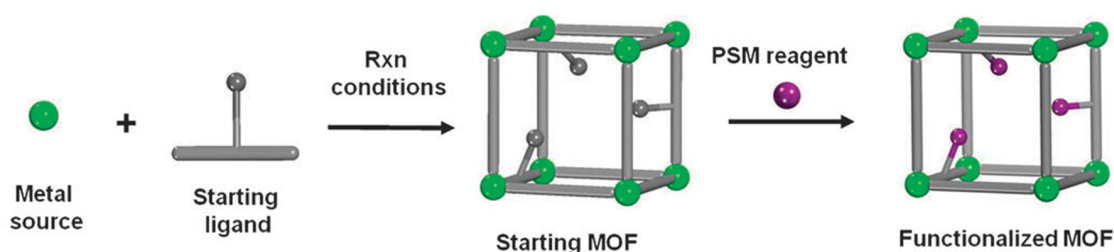


Figure 1.4. Generic postsynthetic modification scheme for MOFs. Figure adapted from reference

54.

Though there are a vast number of possibilities for metal and linker combinations, the most common linkers used in MOF synthesis contain nitrogen and oxygen donors, where dicarboxylates, imidazolates and pyridine complexes dominate. Some metals such as copper

and zinc form polyatomic units known as secondary building units (SBUs) during synthesis, which provide perhaps some of the most common structural entities in MOF chemistry, including the copper paddlewheel $[\text{Cu}_2(\text{CO}_2)_4]$ and $[\text{Zn}_4\text{O}]$ cluster.

The concept of SBUs as structural entities of MOFs comes from zeolite chemistry.⁵⁵ They are molecular complexes and cluster entities that are linked together by organic linkers to form extended porous networks and these precursors allow the synthesis of targeted topologies. Some common SBUs may be seen in Figure 1.5.

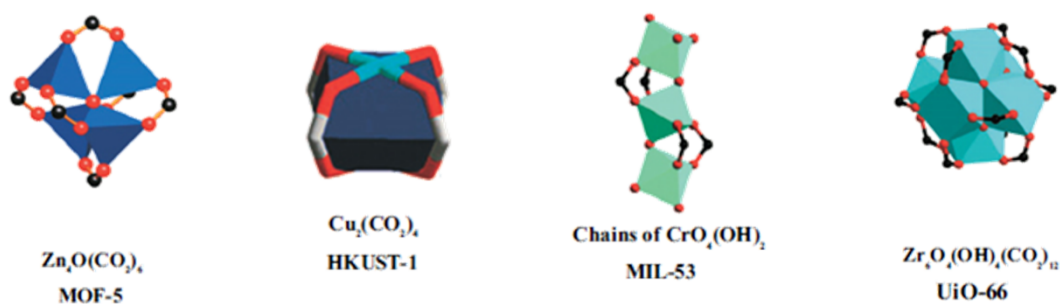


Figure 1.5. Common metal node secondary building units. Figure adapted from reference 56.

The synthetic challenge is to change the chemical composition, functionality and molecular dimensions of the material without altering the underlying topology and one such synthetic approach is reticular synthesis, where experiments are designed to produce materials of predetermined ordered structures.⁵⁷ This technique was developed to identify the factors that underpin framework assembly, and the factors are then used to develop new frameworks with similar topologies, but with varying functional groups and properties.⁵⁸ Yaghi *et al.* produced a series of isorecticular metal-organic frameworks (IRMOFs) differing in the polarity, reactivity, and bulk of the pendant groups on the aromatic linker (Figure 1.6).⁵⁹ This

series of IRMOFs demonstrates the design of porous structures in which pore size and functionality are varied systematically.

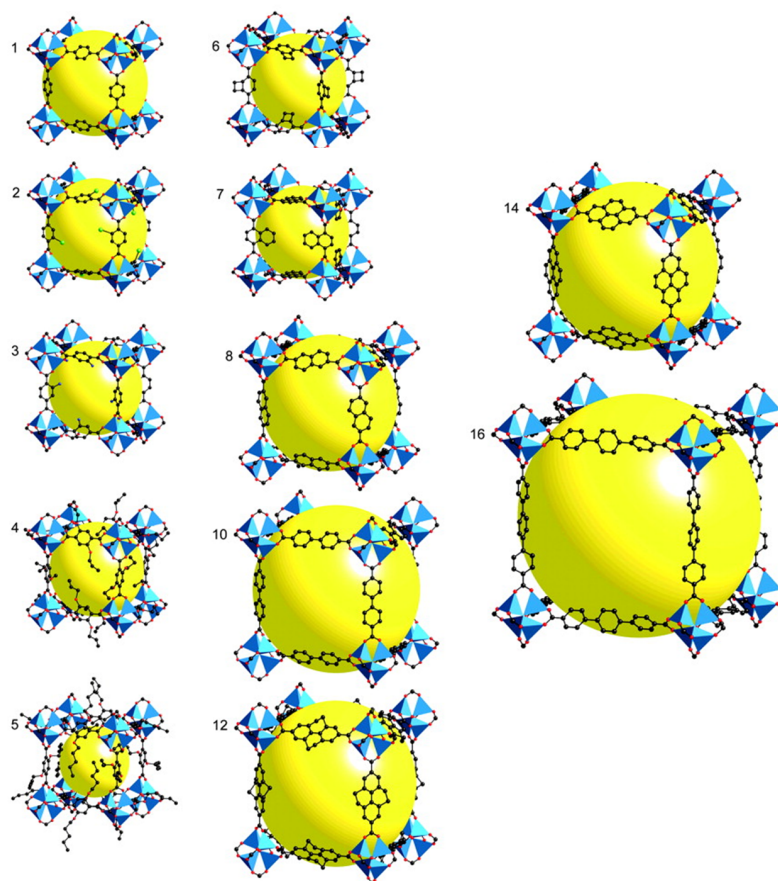


Figure 1.6. The series of isoreticular MOFs which are synthesised using the same Zn_4O cluster, though the length of the linker is varied incrementally to correspondingly increase the pore volume.

Figure adapted from reference 59.

1.5.3 Water Stability in MOFs

Water stability in MOFs is perhaps one of the most important aspects of their structural properties, especially so in terms of their applicability. As many applications involve exposure to atmospheric moisture, in order to be viable, materials must be stable to such humid

atmospheres.⁶⁰ Many MOFs suffer from instability to moisture and this is considered to be one of the greatest barriers in the field from an applications perspective. Most pollution control applications, such as the removal of contaminants from airstreams involve exposure to water vapour,^{61,62} and in other applications, such as in air separation units, the materials used will often be exposed to up to 40% relative humidity (RH).⁶³ Water stability is thus a crucial factor that must be taken into account when considering new materials for environmental applications.

The stability of MOFs to moisture is well-documented and some of the most studied materials with known stability issues are HKUST-1,⁶⁴⁻⁶⁷ and the CPO (Coordination Polymer of Oslo) series.⁶⁸⁻⁷¹ The water stability of a MOF is determined by a number of factors, including the metal-ligand bond strength⁶⁷ and the lability of the metal centre with water.⁷²

The strength of the interactions within the fundamental structural units upon exposure to moisture is critical and in cases of materials with low stability, the structural units typically degrade, leading to a collapse of the framework.⁷³

Water stability may be divided into two sub-categories; thermodynamic and kinetic stability, where thermodynamically stable MOFs can withstand exposure to liquid water, while kinetically stable materials can only tolerate exposure to water in the vapour phase. Certain MOFs maintain stability over long periods in humid air without any loss of crystallinity or surface area, though immediate structural breakdown upon exposure to liquid water may still be observed.⁷⁴

Thermodynamically stable MOFs include MIL-100(Cr),^{75,76} MIL-101(Cr),^{77,78} and ZIF-8 (Zeolitic Imidazolate Framework)^{79,80} and the key structural feature common to these MOFs is the presence of an inert metal cluster that makes an irreversible hydrolysis reaction unfavourable under high water loadings.

Kinetically stable MOFs include the zirconium-based frameworks UIO-66 (Universitetet i Oslo),⁸¹ NU-1000 (Northwestern University),⁸² and several of the DUT (Dresden University of Technology) series such as DUT-51(Zr)⁸³ and DUT-67(Zr).⁸⁴ The kinetic stability within these materials is due to the presence of somewhat inert metal centres, with high coordination numbers between the metal and ligand. Hydrolysis is therefore less favourable due to the increased steric hindrance within the materials.

One of the most common ways to determine whether a material is stable to moisture is to compare the powder X-ray diffraction (PXRD) pattern of the material prior to and post-moisture exposure and other techniques such as infrared (IR) spectroscopy and solid-state nuclear magnetic resonance (NMR) are commonly used to obtain insight into the structural changes upon water exposure.⁸⁵

For water stable porous materials, the shape of the recorded water adsorption isotherm can determine the degree of hydrophobicity or hydrophilicity in a material (Figure 1.7). A hydrophilic material has a high affinity for water and a hydrophobic material has low water affinity. Adsorption loadings at low pressure may be used to determine the relative hydrophobicity among adsorbent materials.

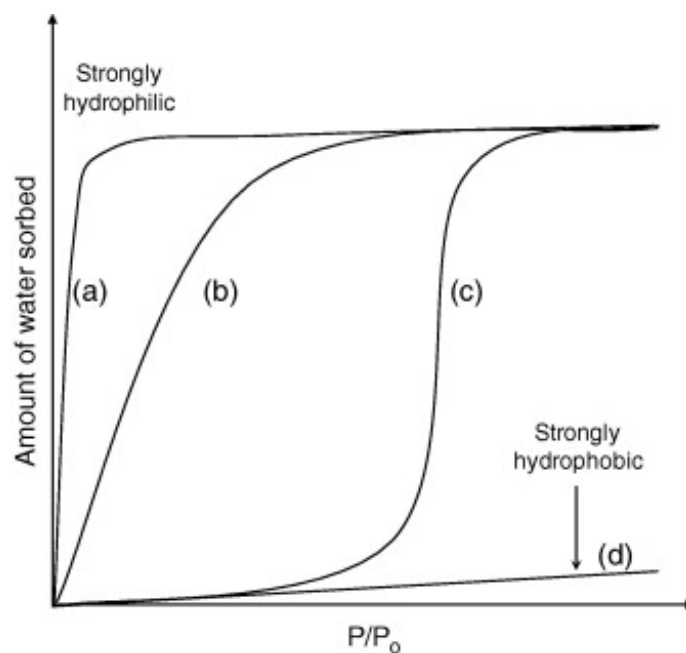


Figure 1.7. Water adsorption isotherms for adsorbents with different degrees of hydrophilicity at ambient temperature and over the 0–1 P/P_0 domain. Figure adapted from reference 85.

1.5.4 Copper MOFs

Two main literature copper MOFs were studied during this project: HKUST-1⁵¹ and STAM-1 (St Andrews MOF-1).⁸⁶

HKUST-1 (Figure 1.6) was first reported in 1999 by Chui *et al.* and has since become one of the most famous MOFs. The repeating unit within HKUST-1 is an octahedral cage, with copper paddlewheel units at the six vertices of the octahedra and a 1,3,5-benzenetricarboxylate (BTC) ligand occupying four of the eight faces. An infinite framework extending in three-dimensions is produced, where copper paddlewheel units connect adjacent octahedral cages so that each cage is connected to six others. The octahedral cages are arranged so that each cage occupies one corner of a cube, leading to a cubic lattice. The material is porous and contains an intersecting three-dimensional system of large square shaped pores of approximately $9 \times 9 \text{ \AA}$. Solvent may travel freely through the pores and

through the four faces of the octahedral cages that are not blocked by the BTC ligands. Such faces act as windows between the pores and the free space within the cages.

In HKUST-1, coordinated water molecules are bound to the copper atoms within the copper paddlewheel dimer units. Such molecules may be removed by the application of heat and by exposing the material to a reduced pressure environment. Upon removal of coordinated water molecules, the resulting coordinatively unsaturated metal sites are free for guest molecule binding.

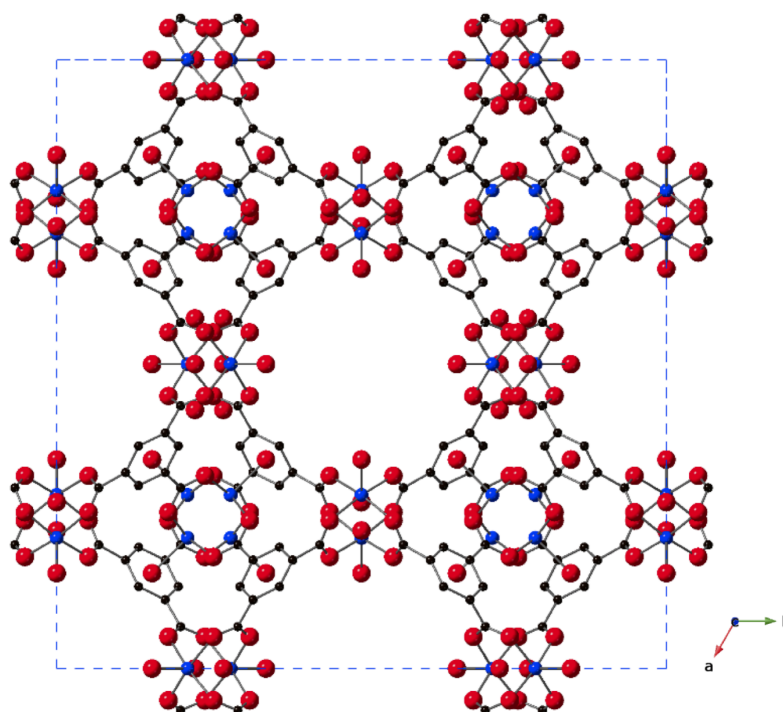


Figure 1.8. Crystal structure of the MOF: HKUST-1 viewed down the crystallographic c axis. Key:

blue: Cu; red: O; black: C. H atoms have been omitted for clarity.

As highlighted previously, HKUST-1 suffers from significant water stability issues, which have been well documented and explained mechanistically. The poor water stability of HKUST-1 under humid conditions is caused by hydrolysis of the copper paddlewheel units

within the structure, where critical metal-carboxylate bonds are broken and which leads to eventual decomposition of the framework.^{87,88}

Efforts have been undertaken to improve the stability of the framework upon contact with moisture, including treating the framework using plasma-enhanced chemical vapour deposition (PECVD) of perfluorohexane, creating a hydrophobic form of HKUST-1.⁸⁹

STAM-1 is the first in a series of new MOFs developed in St Andrews and was first reported by Mohideen *et al.* in 2011. The material is synthesised by the reaction of copper nitrate trihydrate and trimesic acid in a 50:50 aqueous methanol solution, under similar conditions to those used in the synthesis of HKUST-1. The use of an aqueous methanol solution during synthesis leads to selective mono-esterification of the trimesic acid linker and selective formation of the monomethyl MOF derivative (Figure 1.9).

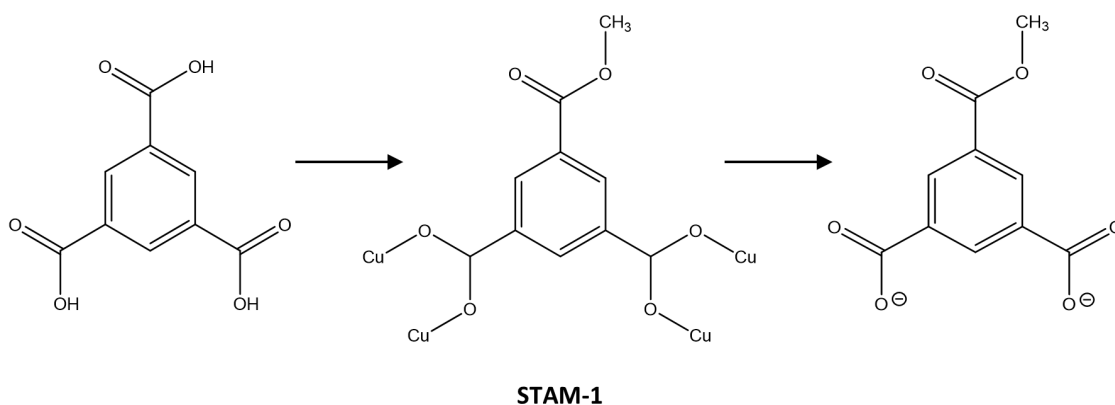


Figure 1.9. STAM-1 as a protecting group for the monomethyl esterification of benzene-1,3,5-tricarboxylic acid. Figure adapted from reference 86.

Unlike HKUST-1, STAM-1 is a 2-dimensional framework and forms a dual-pore structure, with both hydrophobic and hydrophilic channels. The hydrophobic channels result from the non-coordinating methyl ester groups protruding into the pore and the hydrophilic channels result from the protrusion of coordinated water molecules and disordered water molecules within the pores (Figure 1.10).

Despite the similarities in the synthesis and structures of HKUST-1 and STAM-1, the properties of the two materials are very different. While the structural integrity of HKUST-1 is lost upon prolonged contact with water, STAM-1 proves much more resilient and the material was therefore seen as a promising candidate for the adsorption of gases in humid environments.

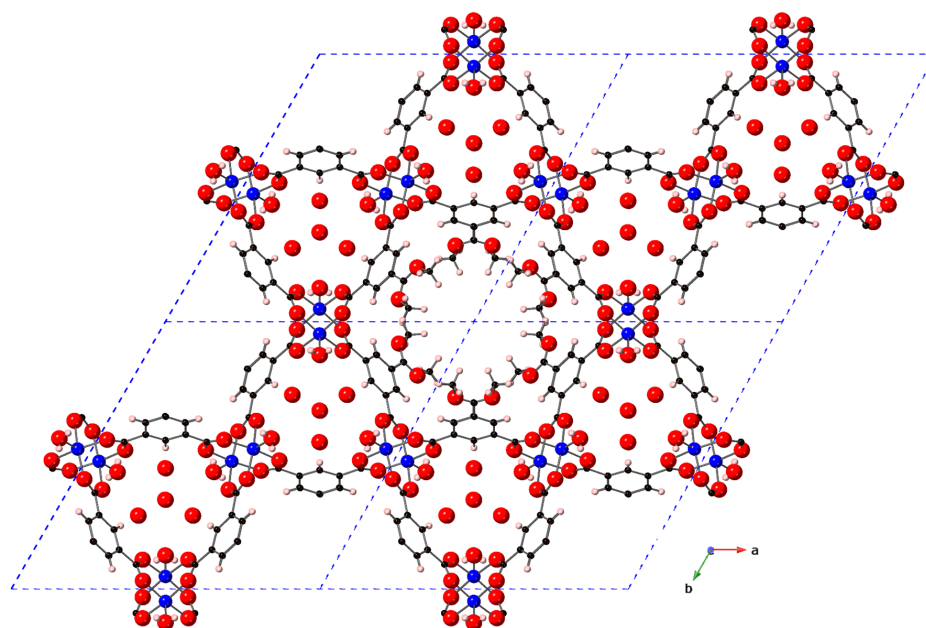


Figure 1.10. Crystal structure of STAM-1 viewed down the crystallographic c axis, displaying the hydrophobic channels lined by disordered methyl ester groups (central channel), and the hydrophilic channels containing ordered water molecules. Key: blue: Cu; red: O; black: C; pink:

H.

1.5.5 General Applications of MOFs

The high porosities observed in many MOFs give them potential for a large number of applications, such as biomedical applications,⁹⁰⁻⁹⁴ gas storage and release,⁹⁵⁻⁹⁷ catalysis⁹⁸ and sensing.⁹⁹

The ability to reversibly adsorb guest molecules that is generally observed in MOFs, either by the application of pressure or temperature, significantly enhances the viability of the materials. Coordinated solvent molecules may be removed from the frameworks and new guest molecules may be introduced without damaging the structural integrity of the materials. Such reversible coordination is particularly useful in applications such as gas adsorption.¹⁰⁰

1.5.5.1 Biomedical Applications

MOFs have recently been proposed for use in biological applications, such as the delivery of drug molecules or biologically active gases. The materials are generally biodegradable due to the lability within the frameworks and many contain non-toxic components. Such features make them comparatively safe to use within the human body.

Drug delivery in MOFs depends on the pore size within the framework, which must be large enough for the desired drug to fit within. Promising examples include MIL-53¹⁰¹ and MIL-101,^{101,102} which were shown to uptake the drug ibuprofen when activated.

Nitric oxide (NO) is well known as a toxic gas, though is also known for its therapeutic properties within the human body and is essential for many biological functions. Such functions include vascular regulation, neurotransmission, immune response and wound healing.¹⁰³⁻¹⁰⁸ Recent research in the Morris group has focused on using the MOF CPO-27 to store and release NO and thus promote vascular relaxation (Figure 1.11).¹⁰⁹

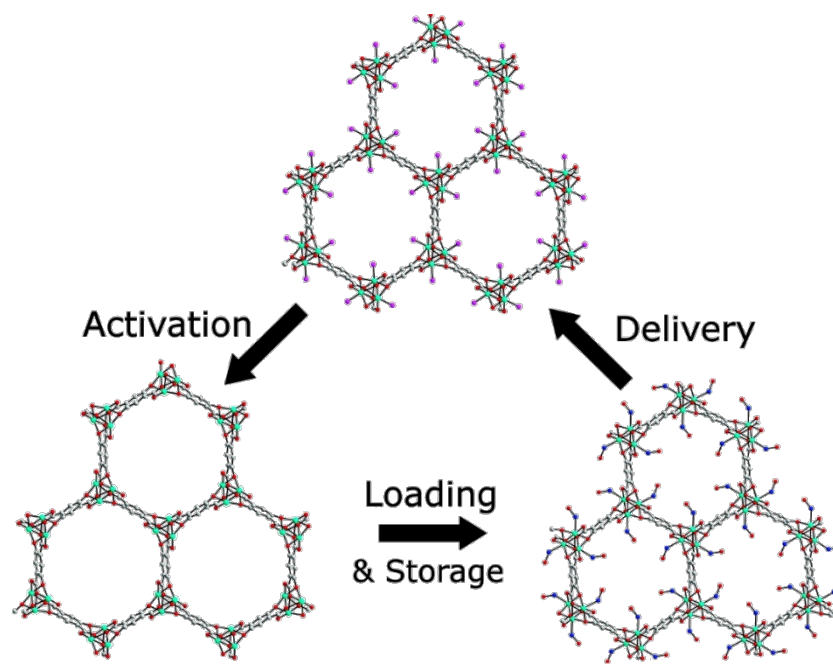


Figure 1.11. NO adsorption-storage-delivery cycle in CPO-27 showing the activation, loading and delivery of NO. The sample is first dehydrated to activate the material (bottom left) and is then loaded with NO (bottom right). NO is then delivered when required upon re-exposure to moisture (top). Figure adapted from reference 109.

1.5.5.2 Gas Storage

Due to concerns regarding the environmental impact caused by emissions from fossil fuels, significant research has focused on MOFs as materials in the storage of gases such as carbon dioxide (CO₂),^{110,111} methane (CH₄)^{112,113} and Hydrogen (H₂).^{114,115}

Potential applications may range from the storage of H₂ in a hydrogen fuelled car, to the capture of CO₂ from the environment to assist in the reduction of greenhouse gas levels.

Recent research in the Long group identified a nickel MOF with exceptional hydrogen storage capacity (Figure 1.12).¹¹⁶ They found that in Ni₂(*m*-dobdc), a single pore contained seven specific binding sites for hydrogen gas that enabled very dense packing of the fuel and

the material set a new record for hydrogen storage capacity of 11.9 g of fuel per litre of MOF crystal at ambient temperature and a tank pressure much lower than is currently used in hydrogen fuelled vehicles.

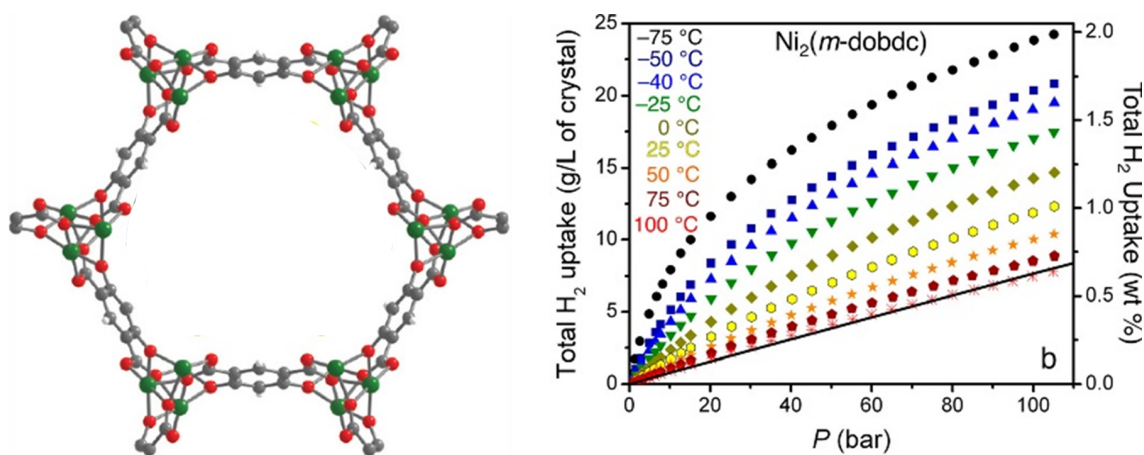


Figure 1.12. A single pore of $\text{Ni}_2(m\text{-dobdc})$ (left) and the associated hydrogen adsorption isotherms for the material (right). The black line in the plot represents the volumetric density of pure compressed H_2 at 25 °C. Figure adapted from reference 116.

1.5.5.3 Catalysis

MOFs have gained attention as potential catalysts due in part to the high concentrations of catalytically active sites present in highly porous solids, the opportunity to include complementary catalytic groups both during synthesis and by postsynthetic modification and the tailorable nature of their pore structures.¹¹⁷⁻¹¹⁹

Some of the MOFs perhaps most associated with catalysis are zirconium-based frameworks, which include UIO-66,^{120,121} NU-1000¹²² and MOF-808.¹²³

Recent research from Farha and Hupp demonstrated the high effectiveness of the zirconium MOF NU-1000 in the catalytic destruction of chemical warfare agents (Figure 1.13), where

the material broke down half of the chemical warfare agent simulant dimethyl 4-nitrophenyl phosphate (DMNP) in 15 minutes and 50% breakdown of the nerve agent *O*-pinacolyl methylphosphonofluoridate (GD) took only 3 minutes. The rapid breakdown was attributed to the high availability of the zirconium ion active sites within the structure.¹²⁴

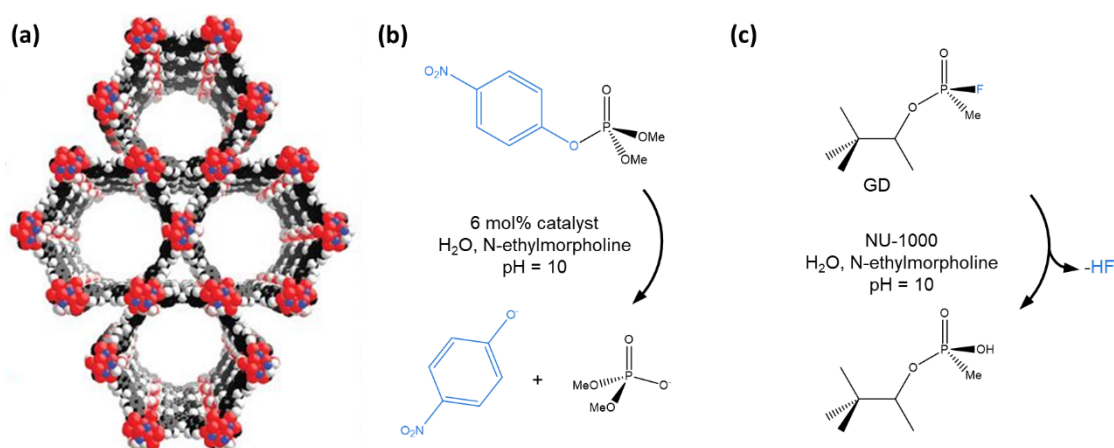


Figure 1.13. (a) Framework topology of NU-1000; (b) reaction conditions for the catalytic decomposition of DMNP using NU-1000 and (c) conditions for the catalytic decomposition of GD using NU-1000. Figure adapted from reference 124.

1.5.6 Toxic Gas Adsorption in MOFs

The threat of the atmospheric release of anthropogenic toxic pollutants is an issue of worldwide concern and MOFs have been highlighted as very promising materials in remediation applications,¹²⁵ and the tunability in MOFs means that they are much more tailorable than currently used activated carbons. Benefits of using MOFs for gas adsorption and storage include the option of post-synthetic modification and the use of functionalised

ligands, which allow the targeted development and tuneable functionality of a particular material's properties.

MOFs have been shown to adsorb a variety of harmful gases such as hydrogen sulfide,¹²⁶⁻¹²⁸ sulfur dioxide (SO₂)^{129,130} and ammonia¹³¹ and this is partially due to hydrogen-bonding donor-acceptor groups and open metal sites within the materials. The availability of open metal sites upon removal of guest solvent molecules allows binding of chemicals to the framework and thus removal from the surrounding environment.¹²⁵

Many MOFs have been studied for such applications and their differing chemistries allows them to be tailored for the uptake of specific chemicals. For example, members of the MIL series such as MIL-53 (Al, Cr) and MIL-47 (V) adsorb significant quantities of the harmful gas H₂S and exhibit reversible adsorption behaviour,¹³² while M-CPO-27 (M = Ni, Zn) has also shown that it can bind H₂S relatively strongly, allowing storage of the gas for several months. Though H₂S is a rather aggressive chemical, Ni-CPO-27 showed only a slight loss in crystallinity after storage and powder X-ray diffraction and X-ray pair distribution function analysis revealed that H₂S is clearly coordinated to coordinatively unsaturated metal sites.¹³³

Figure 1.14 shows an image of Ni-CPO-27 with H₂S coordinated to the metal centres.

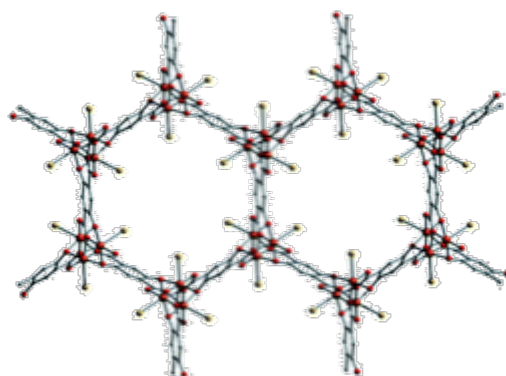


Figure 1.14. Ni-CPO-27 with H₂S bound to the metal centres. Figure adapted from reference 133.

MOFs have been widely studied in the adsorption of NH_3 and interactions between the chemical and the framework can occur through strong hydrogen bonding interactions between the linker and the chemical. Such interactions are due to the presence of particular functional groups such as $-\text{NH}_2$ and $-\text{OH}$ on the framework and additional chemisorption mechanisms through functional groups such as $-\text{COOM}$, where $\text{M} = \text{Cu}, \text{Ag}, \text{Na}$ or K can also occur.¹³⁴⁻¹³⁵ Copper MOFs have been highlighted as promising materials in ammonia uptake and this is partially due to the presence of coordinatively unsaturated sites (CUSs) upon activation. This activation provides vacant Cu^{2+} species for the gas to bind to and thus promotes NH_3 adsorption.¹³⁶ Copper MOFs such as HKUST-1,¹³⁷ Cu-CPO-27¹³⁸ and STAM-17-OEt¹³⁹ are promising examples in this area, as NH_3 can form strong covalent bonds to the CUSs. Figure 1.15 shows the structures of HKUST-1, Cu-CPO-27 and STAM-17-OEt.

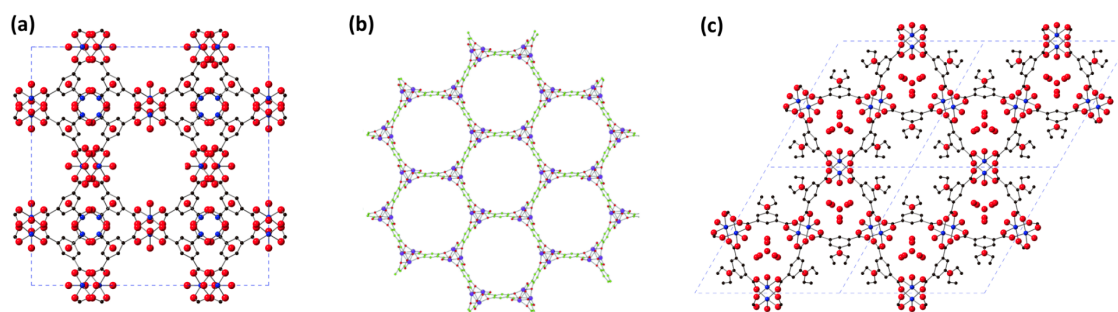


Figure 1.15. Copper MOFs that may be used in the uptake of ammonia: (a) HKUST-1; (b) Cu-CPO-27 and (c) STAM-17-OEt.

1.5.7 Physical Form of MOFs

MOFs are highly promising materials in the adsorption of harmful chemicals, though if they are to be used in future respiratory filtration systems, the physical form of the materials must

be addressed. MOFs are typically formed as powdered samples, but it is not possible to breathe through a fine powder. Recent work by companies such as Johnson Matthey has focused on improving the physical form of MOFs for gas adsorption applications and one such way is by the application of pressure to form a pelletized material.¹⁴⁰

Another possibility is to form a granular composite material by growing MOF crystals inside an activated carbon such as BPL activated carbon, which improves the physical form, while using an inexpensive and widely-available carbon support.¹⁴¹

1.5 References

- [1] *J R Army Med Corps*, 2002, **148**, 371-381.
- [2] F. Haber, Improvements in the Manufacturing of Ammonia, Patent No. 14,023, UK, 1910.
- [3] G. C. Miller, *J. Chem. Educ.*, 1981, **58**, 424-426.
- [4] Agency for Toxic Substances and Disease Registry. 2004. *Toxicological profile for Ammonia* [ATSDR Tox Profile]. Atlanta, GA: U.S. Department of Health and Human Services, Public Health Service.
- [5] W. M. Haynes, Ed., *CRC Handbook of Chemistry and Physics*, 94th Edn., CRC Press, Boca Raton, 2013.
- [6] B. H. Baek and V. P. Aneja, *J. Air and Waste Manage. Assoc.*, 2004, **54**, 623-633.
- [7] H. Bereton Baker, *J. Chem. Soc., Trans.*, 1894, **65**, 611-624.
- [8] D. Tudela, *J. Chem. Educ.*, 1999, **76**, 468.
- [9] International Programme on Chemical Safety (IPCS). 1986. *Ammonia. Environmental Health Criteria 54*, World Health Organization: Geneva.

- [10] Ammonia: health effects, incident management and toxicology. 2015. *Ammonia Toxicological Overview*, Public Health England.
- [11] National Research Council. 2002. *Acute Exposure Guideline Levels for Selected Airborne Chemicals: Volume 2*, Washington DC: The National Academies Press.
- [22] L. Andrussow, *Angew. Chem.*, 1935, **48**, 593-595.
- [13] Chemical Hazards and Poisons Report. 2010. *A Toxicological Review of the Products of Combustion*, Centre for Radiation, Chemical and Environmental Hazards, Health Protection Agency.
- [14] U.S. EPA. 2010. *IRIS Toxicological Review of Hydrogen Cyanide and Cyanide Salts* (Final Report). U.S. Environmental Protection Agency, Washington, DC, EPA/635/R-08/016F.
- [15] International Programme on Chemical Safety (IPCS). 2004. *Hydrogen Cyanide and Cyanides: Human Health Aspects*, Concise International Chemical Assessment Document 61, World Health Organization: Geneva.
- [16] Centers for Disease Control and Prevention, The National Institute for Occupational Safety and Health (NIOSH), *Emergency Response Safety and Health Database, Hydrogen Cyanide (AC): Systemic Agent*, page accessed July 2019.
https://www.cdc.gov/niosh/ershdb/emergencyresponsecard_29750038.html
- [17] E. S. Moyer, S. J. Smith and G. O. Wood, *Am. Ind. Hyg. Assoc. J.*, 2001, **62**, 494-507.
- [18] M. Jacoby, *Chem. Eng. News.*, 2014, **92**, 34-38.
- [19] J. Harvey, Ed., *CBRN Newsletter*, 2010, **3**, 1-20.
- [20] J. Rouquerol, F. Rouquerol, P. Llewellyn, G. Maurin and K. S. W. Sing, *Adsorption by Powders and Porous Solids*, 2nd Edn., Academic Press, Oxford, 2014.
- [21] J. Rouquerol, D. Avnir, C. W. Fairbridge, D. H. Everett, J. H. Haynes, N. Pernicone, J. D. F. Ramsay, K. S. W. Sing and K. K. Unger, *Pure Appl. Chem.*, 1994, **66**, 1739-1758.

- [22] E. Koohsaryan and M. Anbia, *Chin. J. Catal.*, 2016, **37**, 447-467.
- [23] M. Alcón, A. Corma, M. Iglesias and F. Sánchez, *J. Organomet. Chem.*, 2002, **655**, 134-145.
- [24] M. Dams, L. Drijkoningen, B. Pauwels, G. Van Tendeloo, D. E. De Vos and P. A. Jacobs, *J. Catal.*, 2002, **209**, 225-236.
- [25] B. Yilmaz and U. Müller, *Top. Catal.*, 2009, **52**, 888-895.
- [26] J. Cejka, R. E. Morris and P. Nachtigall, Eds., *Zeolites in Catalysis*, Royal Society of Chemistry, Cambridge, 2017.
- [27] H. S. Sherry and H. F. Walton, *J. Phys. Chem.*, 1967, **71**, 1457-1465.
- [28] J. Weitkamp, *Solid. State. Ion.*, 2000, **131**, 175-188.
- [29] J. Hu, A. Aarts, R. Shang, B. Heijman and L. Rietveld, *J. Env. Man.*, 2016, **177**, 45-52.
- [30] B. Caballero, L. Trugo and P. M. Finglas, Eds., *Encyclopedia of Food Science and Nutrition*, 2nd Edn., Academic Press, London, 2003.
- [31] M. Jahangiri, J. Adl, S. J. Shahtaheri, A. Rashidi, A. Ghorbanali, H. Kakooe, A. R. Forushani and M. R. Ganjali, *Iranian. J. Environ. Health. Sci. Eng.*, 2013, **10**, 10-15.
- [32] B. A. Akash and W. S. O'Brien, *Int. J. Energy Res*, 1996, **20**, 913-922.
- [33] M. K. B. Gratuító, T. Panyathanmaporn, R.-A. Chumnanklang, N. Sirinuntawittaya, and A. Dutta, *Bioresour. Technol*, 2008, **99**, 4887-4895.
- [34] W. Buah, J. MacCarthy and S. Ndur, *International Journal of Environmental Protection and Policy*, 2016, **4**, 98-103.
- [35] N. Indayaningsih, F. Destyorini, R. I. Purawiardi, D. R. Insiyanda and H. Widodo, *J. Phys. Conf. Ser.*, 2017, **817**, 012006-012011.
- [36] T. J. Bandosz, Ed., *Activated Carbon Surfaces in Environmental Remediation*, Vol. 7., Academic Pres, Oxford, 2006.

- [37] BPL 4x10 Data Sheet, CalgonCarbon, Moon Township, PA, page accessed July 2019.
<https://www.calgoncarbon.com/app/uploads/DS-BPL4x1015-EIN-E1-.pdf>
- [38] B. P. Russell and M. D. Levan, *Carbon*, 1994, **32**, 845-855.
- [39] L. C. Wu and Y. C. Chung, *J. Air. Waste. Manag. Assoc.*, 2009, **59**, 258-265.
- [40] B. F. Hoskins and R. J. Robson, *J. Am. Chem. Soc.*, 1989, **111**, 5962-5964.
- [41] O. M. Yaghi and H. Li, *J. Am. Chem. Soc.*, 1995, **117**, 10401-10402.
- [42] M. Eddaoudi, D. B. Moler, H. Li, B. Chen, T. M. Reineke, M. O'Keeffe and O. M. Yaghi, *Acc. Chem. Res.*, 2001, **34**, 319-330.
- [43] S. Kitagawa, R. Kitaura and S-i. Noro, *Angew. Chem. Int. Ed.*, 2004, **43**, 2334-2375.
- [44] G. Férey, *Chem. Soc. Rev.*, 2008, **37**, 191-214.
- [45] C. Janiak, *Dalton Trans.*, 2003, **13**, 2781-2804.
- [46] S. R. Batten, N. R. Champness, X.-M. Chen, J. Garcia-Martinez, S. Kitagawa, L. Öhrström, M. O'Keefe, M. Paik Suh and J. Reedijk, *Pure. Appl. Chem.*, 2013, **85**, 1715-1724.
- [47] N. Hosono and S. Kitagawa, *Acc. Chem. Res.*, 2018, **51**, 2437-2446.
- [48] M. Eddaoudi, J. Kim, N. Rosi, D. Vodak, J. Wachter, M. O'Keeffe and O. M. Yaghi, *Science*, 2002, **295**, 469-472.
- [49] S. Chavan, J. G. Vitillo, E. Groppo, F. Bonino, C. Lamberti, P. D. C. Dietzel and S. Bordiga, *J. Phys. Chem. C.*, 2009, **113**, 3292-3299.
- [50] H. Li, M. Eddaoudi, M. O'Keeffe and O. M. Yaghi, *Nature*, 1999, **402**, 276-279.
- [51] S. S.-Y. Chui, S. M.-F. Lo, J. P. H. Charmant, A. G. Orpen and I. D. Williams, *Science*, 1999, **283**, 1148-1150.
- [52] G. Férey, C. Mellot-Draznieks, C. Serre, F. Millange, J. Dutour, S. Surble and I. Margiolaki, *Science*, 2005, **309**, 2040-2042.
- [53] Y. Sun and H-C. Zhou, *Sci. Technol. Adv. Mater.*, 2015, **16**, 054202-054212.

- [54] K. K. Tanabe and S. M. Cohen, *Chem. Soc. Rev.*, 2011, **40**, 498-519.
- [55] C. Baerlocher, W. M. Meier and D. Olson, *Atlas of zeolite framework types*; 5th rev. Edn., Elsevier: Amsterdam, New York, 2001.
- [56] Z. Zhang, Y. Cui and G. Qian, *Curr. Org. Chem.*, 2018, **22**, 1792-1808.
- [57] O. M. Yaghi, M. O'Keeffe, N. W. Ockwig, H. K. Chae, M. Eddaoudi and J. Kim, *Nature*, 2003, **423**, 705-715.
- [58] M. Zaworotko, *J. Chem Commun.*, 2001, 1-9.
- [59] J. L. C. Rowsell and O. M. Yaghi, *Micropor. Mesopor. Mat*, 2004, **73**, 3-14.
- [60] N. C. Burtch, H. Jasuja and K. S. Walton, *Chem. Rev.*, 2014, **114**, 10575-10612.
- [61] W. H. Tao, T. C. K. Yang, Y. N. Chang, L. K. Chang and T. W. Chung, *J. Environ. Eng.*, 2004, **130**, 1210-1216.
- [62] J. Rodriguez-Mirasol, J. Bedia, T. Cordero and J. Rodriguez, *J. Sep. Sci. Technol.*, 2005, **40**, 3113-3135.
- [63] D. Ferreira, R. Magalhaes, P. Taveira and A. Mendes, *Ind. Eng. Chem. Res.*, 2011, **50**, 10201-10210.
- [64] P. Kusgens, M. Rose, I. Senkovska, H. Froede, A. Henschel, S. Siegle and S. Kaskel, *Microporous Mesoporous Mater.*, 2009, **120**, 325-330.
- [65] P. M. Schoenecker, Carson, C. J. Carson, H. Jasuja, C. J. J. Flemming and K. S. Walton, *Ind. Eng. Chem. Res.*, 2012, **51**, 6513-6519.
- [66] G. D. Pirngruber, L. Hamon, S. Bourrelly, P. L. Llewellyn, E. Lenoir, V. Guillermin, C. Serre and T. Devic, *ChemSusChem*, 2012, **5**, 762-776.
- [67] J. J. Low, A. I. Benin, P. Jakubczak, J. F. Abrahamian, S. A. Faheem and R. R. Willis, *J. Am. Chem. Soc.*, 2009, **131**, 15834-15842.

- [68] H. Furukawa, F. Gandara, Y.-B. Zhang, J. Jiang, W. L. Queen, M. R. Hudson and O. M. Yaghi, *J. Am. Chem. Soc.*, 2014, **136**, 4369-4381.
- [69] T. Remy, S. A. Peter, S. Van der Perre, P. Valvekens, D. E. De Vos, G. V. Baron and J. F. M. Denayer, *J. Phys. Chem. C*, 2013, **117**, 9301-9310.
- [70] A. C. Kizzie, A. G. Wong-Foy and A. J. Matzger, *Langmuir*, 2011, **27**, 6368-6373.
- [71] J. Liu, A. I. Benin, A. M. B. Furtado, P. Jakubczak, R. R. Willis and M. D. LeVan, *Langmuir*, 2011, **27**, 11451-11456.
- [72] I. J. Kang, N. A. Khan, E. Haque and S. H. Jung, *Chem. Eur. J.*, 2011, **17**, 6437-6442.
- [73] M. Todaro, G. Buscarino, L. Sciortino, A. Alessi, F. Messina, M. Taddei, M. Ranocchiaro, M. Cannas and F. M. Gelardi, *J. Phys. Chem. C*, 2016, **120**, 12879-12889.
- [74] H. Jasuja, N. C. Burtch, Y.-G. Huang, Y. Cai and K. S. Walton, *Langmuir*, 2013, **29**, 633-642.
- [75] G. Akiyama, R. Matsuda and S. Kitagawa, *Chem. Lett.*, 2010, **39**, 360-361.
- [76] K. A. Cychosz and A. J. Matzger, *Langmuir*, 2010, **26**, 17198-17202.
- [77] Y.-K. Seo, J. W. Yoon, J. S. Lee, Y. K. Hwang, C.-H. Jun, J.-S. Chang, S. Wuttke, P. Bazin, A. Vimont, M. Daturi, S. Bourrelly, P. L. Llewellyn, P. Horcajada, C. Serre and G. Ferey, *Adv. Mater.*, 2012, **24**, 806-810.
- [78] J. Ehrenmann, S. K. Henninger and C. Janiak, *Eur. J. Inorg. Chem.*, 2011, 471-474.
- [79] K. S. Park, Z. Ni, A. P. Cote, J. Y. Choi, R. Huang, F. J. Uribe-Romo, H. K. Chae, M. O'Keeffe and O. M. Yaghi, *Proc. Natl. Acad. Sci. U.S.A.*, 2006, **103**, 10186-10191.
- [80] S. Han, Y. Huang, T. Watanabe, Y. Dai, K. S. Walton, S. Nair, D. S. Sholl and J. C. Meredith, *ACS Comb. Sci.*, 2012, **14**, 263-267.
- [81] E. Soubeyrand-Lenoir, C. Vagner, J. W. Yoon, P. Bazin, F. Ragon, Y. K. Hwang, C. Serre, J.-S. Chang and P. L. Llewellyn, *J. Am. Chem. Soc.*, 2012, **134**, 10174-10181.

- [82] J. E. Mondloch, M. J. Katz, N. Planas, D. Semrouni, L. Gagliardi, J. T. Hupp and O. K. Farha, *Chem. Commun.*, 2014, **50**, 8944-8946.
- [83] V. Bon, V. Senkovskyy, I. Senkovska and S. Kaskel, *Chem. Commun.*, 2012, **48**, 8407-8409.
- [84] V. Bon, I. Senkovska, I. A. Baburin and S. Kaskel, *Cryst. Growth Des.*, 2013, **13**, 1231-1237.
- [85] E.-P. Ng, and S. Mintova, *Microporous Mesoporous Mater.*, 2008, **114**, 1-26.
- [86] M. I. H. Mohideen, B. Xiao, P. S. Wheatley, A. C. McKinlay, Y. Li, A. M. Z. Slawin, D. W. Aldous, N. F. Cessford, T. Düren, X. Zhao, R. Gill, K. M. Thomas, J. M. Griffin, S. E. Ashbrook and R. E. Morris, *Nat. Chem.*, 2011, **3**, 304-310.
- [87] M. Todaro, L. Sciortino, F. M. Gelardi and G. Buscarino, *J. Phys. Chem. C.*, 2017, **121**, 24853-24860.
- [88] M. Todaro, G. Buscarino, L. Sciortino, A. Alessi, F. Messina, M. Taddei, M. Ranocchiari, M. Canas and F. M. Gelardi, *J. Phys. Chem. C.*, 2016, **120**, 12879-12889.
- [89] J. B. Decoste, G. W. Peterson, M. W. Smith, C. A. Stone and C. R. Willis, *J. Am. Chem. Soc.*, 2012, **134**, 1486-1489.
- [90] S. Keskin and S. Kizilel, *Ind. Eng. Chem. Res.*, 2011, **50**, 1799-1812.
- [91] N. J. Hinks, A. C. McKinlay, B. Xiao, P. S. Wheatley and R. E. Morris, *Microporous Mesoporous Mater.*, 2010, **129**, 330-334.
- [92] A. C. McKinlay, P. K. Allan, C. L. Renouf, M. J. Duncan, P. S. Wheatley, S. J. Warrender, D. Dawson, S. E. Ashbrook, B. Gil, B. Marszalek, T. Düren, J. J. Williams, C. Charrier, D. K. Mercer, S. J. Teat and R. E. Morris, *APL Mater.*, 2014, **2**, 124108-124115.

- [93] S. R. Miller, E. Alvarez, L. Fradcourt, T. Devic, S. Wuttke, P. S. Wheatley, N. Steunou, C. Bonhomme, C. Gervais, D. Laurencin, R. E. Morris, A. Vimont, M. Daturi, P. Horcajada and C. Serre, *Chem. Commun.*, 2013, **49**, 7773-7775.
- [94] S. Rojas, P. S. Wheatley, E. Quartapelle-Procopio, B. Gil, B. Marszalek, R. E. Morris and E. Barea, *CrystEngComm*, 2013, **15**, 9364-9367.
- [95] D. Cattaneo, S. J. Warrender, M. J. Duncan, R. Castledine, N. Parkinson, I. Haley and R. E. Morris, *Dalton Trans.*, 2015, **45**, 618-629.
- [96] P. D. C. Dietzel, B. Panella, M. Hirscher, R. Blom and H. Fjellvåg, *Chem. Commun.*, 2006, 959-961.
- [97] A. C. McKinlay, J. F. Eubank, S. Wuttke, B. Xiao, P. S. Wheatley, P. Bazin, J.-C. Lavalley, M. Daturi, A. Vimont, G. De Weireld, P. Horcajada, C. Serre and R. E. Morris, *Chem. Mater.*, 2013, **25**, 1592-1599.
- [98] D. Ruano, M. Díaz-García, A. Alfayate and M. Sánchez-Sánchez, *ChemCatChem*, 2015, **7**, 674-681.
- [99] P. Kumar, A. Deep and K.-H. Kim, *Trends Anal. Chem.*, 2015, **73**, 39-53.
- [100] S. Chavan, F. Bonino, J. G. Vitillo, E. Groppo, C. Lamberti, P. D. C. Dietzel, A. Zecchina and S. Bordiga, *Phys. Chem. Chem. Phys.*, 2009, **11**, 9811-9822.
- [101] K. Matsuyama, N. Hayashi, M. Yokomizo, T. Kato, K. Ohara and T. Okuyama, *J. Mater. Chem. B*, 2014, **2**, 7551-7558.
- [102] P. Horcajada, C. Serre, M. Vallet-Regí, M. Sebban, F. Taulelle and G. Férey, *Angew. Chem. Int. Ed. Engl.*, 2006, **45**, 5974-5978.
- [103] A. W. Carpenter, J. A. Johnson and M. H. Schoenfish, *Colloid Surf. A-Physicochem. Eng. Asp.*, 2014, **454**, 144-151.
- [104] M. T. Gladwin, J. H. Crawford and R. P. Patel, *Free Radic. Biol. Med.*, 2004, **36**, 707-17.

- [105] K. D. Bloch, F. Ichinose, J. D. Roberts Jr. and W. M. Zapol, *Cardiovascular Research*, 2007, **75**, 339-348.
- [106] K. Peikert, L. J. McCormick, D. Cattaneo, M. J. Duncan, F. Hoffmann, A. H. Khan, M. Bertmer, R. E. Morris and M. Fröba, *Microporous Mesoporous Mater.*, 2015, **216**, 118-126.
- [107] D. Cattaneo, S. J. Warrender, M. J. Duncan, C. J. Kelsall, M. M. Doherty, P. D. Whitfield, I. L. Megson and R. E. Morris, *RSC Adv.*, 2016, **6**, 14059-14067.
- [108] P. Pacher, J. S. Beckman and L. Liaudet, *Physiol. Rev.*, 2007, **87**, 315-424.
- [109] A. C. McKinlay, B. Xiao, D. S. Wragg, P. S. Wheatley, I. L. Megson and R. E. Morris, *J. Am. Chem. Soc.*, 2008, **130**, 10440-10444.
- [110] K. Sumida, D. L. Rogow, J. A. Mason, T. M. McDonald, E. D. Bloch, Z. R. Herm, T.-H. Bae and J. R. Long, *Chem. Rev.*, 2012, **2**, 724-781.
- [111] X. Lian, L. Xu, M. Chen, C.-e. Wu, W. Li, B. Huang and Y. Cui, *J. Sci. Technol*, 2019, **19**, 3059-3078.
- [112] Y. He, W. Zhou, G. Qian and B. Chen, *Chem. Soc. Rev.*, 2014, **43**, 5657-5678.
- [113] T. Tian, Z. Zeng, Z. D. Vulpe, M. E. Casco, G. Divitini, P. Midgley, J. Silvestre-Albero, J.-C. Tan, P. Z. Moghadam and D. Fairen-Jimenez, *Nat. Mat*, 2018, **17**, 174-179.
- [114] M. P. Suh, H. J. Park, T. K. Prasad and D.-W. Lim, *Chem. Rev.*, 2011, **112**, 782-835.
- [115] P. García-Holley, B. Schweitzer, T. Islamoglu, Y. Liu, L. Lin, S. Rodriguez, M. H. Weston, J. T. Hupp, D. A. Gómez-Gualdrón, T. Yildirim and O. K. Farha, *ACS Energy Lett.*, 2018, **3**, 748-754.
- [116] M. T. Kapelewski, T. Runčevski, J. D. Tarver, H. Z. H. Jiang, K. E. Hurst, P. A. Parilla, A. Ayala, T. Gennett, S. A. FitzGerald, C. M. Brown and J. R. Long, *Chem. Mater.*, 2018, **30**, 8179-8189.
- [117] A. Corma, H. Garcia and F. X. Llabrés i Xamena, *Chem. Rev.*, 2010, **110**, 4606-4655.

- [118] J. Lee, O. K. Farha, J. Roberts, K. A. Scheidt, S. T. Nguyen and J. T. Hupp, *Chem. Soc. Rev.*, 2009, **38**, 1450-1459.
- [119] D. Farrusseng, S. Aguado and C. Pinel, *Angew. Chem., Int. Ed.*, 2009, **48**, 7502-7513.
- [120] J. Y. Ye and J. K. Johnson, *ACS Catal.*, 2015, **5**, 6219-6229.
- [121] M. Kalaj, J. M. Palomba, K. C. Bentz and S. M. Cohen, *Chem. Commun.*, 2019, **55**, 5367-5370.
- [122] S. Ahn, S. L. Nauert, C. T. Buru, M. Rimoldi, H. Choi, N. M. Schweitzer, J. T. Hupp, O. K. Farha and J. M. Notestein, *J. Am. Chem. Soc.*, 2018, **140**, 8535-8543.
- [123] H.-H. Mautschke, F. Drache, I. Senkovska, S. Kaskel and F. X. Llabrés i Xamena, *Catal. Sci. Technol.*, 2018, **8**, 3610-3616.
- [124] J. E. Mondloch, M. J. Katz, W. C. Isley III, P. Ghosh, P. Liao, W. Bury, G. W. Wagner, M. G. Hall, J. B. DeCoste, G. W. Peterson, R. Q. Snurr, C. J. Cramer, J. T. Hupp and O. K. Farha, *Nat. Mat.*, 2015, **14**, 512-516.
- [125] E. Barea, C. Montoro and J. A. R. Navarro, *Chem. Soc. Rev.*, 2014, **43**, 5419-5430.
- [126] C. Petit, B. Mendoza and T. J. Bandosz, *ChemPhysChem*, 2010, **11**, 3678-3684.
- [127] J. N. Joshi, G. Zhu, J. J. Lee, E. A. Carter, C. W. Jones, R. P. Lively and K. S. Walton, *Langmuir*, 2018, **34**, 8443-8450.
- [128] J. J. Gutiérrez-Sevillano, A. Martín-Calvo, D. Dubbeldam, S. Caleroa and S. Hamad, *RSC Adv.*, 2013, **3**, 14737-14749.
- [129] J. H. Carter, X. Han, F. Y. Moreau, I. da Silva, A. Nevin, H. G. W. Godfrey, C. C. Tang, S. Yang and M. Schröder, *J. Am. Chem. Soc.*, 2018, **140**, 15564-15567.
- [130] L. M. Rodríguez-Albelo, E. López-Maya, S. Hamad, A. R. Ruiz-Salvador, S. Calero and J. A. R. Navarro, *Nat. Commun.*, 2017, **8**, 14457-14466.

- [131] D. Britt, D. Tranchemontagne and O. M. Yaghi, *Proc. Natl. Acad. Sci. U. S. A.*, 2008, **105**, 11623-11627.
- [132] L. Hamon, C. Serre, T. Devic, T. Loiseau, F. Millange, G. Férey and G. De Weireld, *J. Am. Chem. Soc.*, 2009, **131**, 8775-8777.
- [133] P. K. Allan, P. S. Wheatley, D. Aldous, M. I. Mohideen, C. Tang, J. A. Hriljac, I. L. Megson, K. W. Chapman, G. De Weireld, S. Vaesen and R. E. Morris, *Dalton Trans.*, 2012, **41**, 4060-4066.
- [134] K. C. Kim, D. Yu and R. Q. Snurr, *Langmuir*, 2013, **29**, 1446-1456.
- [135] D. Yu, P. Ghosh and R. Q. Snurr, *Dalton Trans.*, 2012, **41**, 3962-3973.
- [136] K. Vikrant, V. Kumar, K-H. Kim and D. Kukkar, *J. Mater. Chem. A*, 2017, **5**, 22877-22896.
- [137] G. W. Peterson, G. W. Wagner, A. Balboa, J. Mahle, T. Sewell and C. J. Karwacki, *J. Phys. Chem. C.*, 2009, **113**, 13906-13917.
- [138] M. J. Katz, A. J. Howarth, P. Z. Moghadam, J. B. DeCoste, R. Q. Snurr, J. T. Hupp and O. K. Farha, *Dalton Trans.*, 2016, **45**, 4150-4153.
- [139] L. N. McHugh, M. J. McPherson, L. J. McCormick, S. A. Morris, P. S. Wheatley, S. J. Teat, D. McKay, D. M. Dawson, C. E. F. Sansome, S. E. Ashbrook, C. A. Stone, M. W. Smith and R. E. Morris, *Nat. Chem.*, 2018, **10**, 1096-1102.
- [140] S. Hindocha and S. Poulston, *Faraday Discuss.*, 2017, **201**, 113-125.
- [141] L. N. McHugh, A. Terracina, P. S. Wheatley, G. Buscarino, M. W. Smith and R. E. Morris, *Angew. Chem. Int. Ed.*, 2019, **58**, 11747-11751.

Chapter 2: Aims

The main aim of this thesis was to assess the potential of MOFs for use in the adsorption of toxic industrial chemicals from contaminated airstreams. The main application considered throughout was a respirator canister, where MOFs may one day replace or be incorporated into the currently used impregnated activated carbons within respirator canisters

The recently developed STAM series of MOFs were identified as potential candidates and their ability to withstand exposure to moisture, along with their ability to remove both ammonia and hydrogen cyanide from contaminated airstreams was investigated.

STAM-17-OEt was chosen as the main member of the series and a detailed structural analysis of the material was undertaken, highlighting the underlying structural features that contribute to hydrolytic stability. STAM-17-OEt was also tested against a humid stream of ammonia in order to assess its viability in conditions closer to those experienced in the field.

Further steps towards the proposed application were taken, where selected members of the STAM series were incorporated into an activated carbon similar to those currently used in respirator canisters, to provide composite materials where the physical form of the materials is more suited for use in breathing apparatus.

Finally, two novel copper frameworks were synthesised and their crystallographic and structural properties were investigated.

Chapter 3: Experimental Techniques

3.1 Solvothermal Synthesis

Many of the MOFs reported in the literature involve solvothermal synthesis, which is a synthetic method used to prepare typically crystalline solids under autogenous pressure.¹ The elevated pressure is introduced by heating the solvents used to above one bar of pressure, promoting solvent diffusion. The synthesis takes place by dissolving or suspending pre-weighed quantities of reagents in one or more solvent inside a Teflon-lined stainless-steel autoclave (Figure 3.1) at pressures greater than 1 bar and temperatures typically greater than 100 °C.



Figure 3.1. Teflon-lined stainless-steel autoclaves used in solvothermal synthesis. Stainless steel autoclave with lid (left); opened steel autoclave (middle) and Teflon liner (right).

3.1.1 Synthesis of MOFs and Composite Materials

Many MOFs are synthesised under solvothermal synthesis, utilising the high pressures and temperatures involved, to produce highly crystalline materials.² The MOFs used in this project were synthesised either solvothermally, under reflux or at room temperature. Reflux and room temperature syntheses are advantageous in the larger scale synthesis of materials, due to the larger reaction vessels available, the lower pressures involved and the lower energy required. The MOF-activated carbon composite materials produced were synthesised under reflux conditions, to ensure thorough mixing of the components during the reaction.

3.2 Crystallography³⁻⁶

A crystal structure is a specific arrangement of atoms, repeated periodically on a lattice in three dimensions. The smallest repeating unit displaying the overall symmetry of the crystal structure is the unit cell, which is repeated throughout a crystal to form a lattice. Each unit cell is defined in terms of the lattice points present (Figure 3.2).

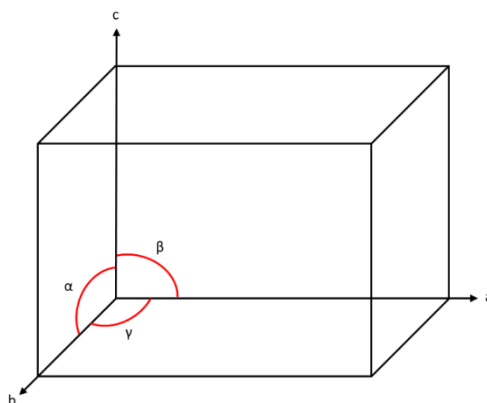


Figure 3.2. A schematic of a unit cell.

The unit cells may be divided into 4 classes: Primitive (P), body centred (I), face centred (F) or base centred (A, B or C) (Figure 3.3).

In a P cell, the lattice points are at the corners of the unit cell, in the I cell, the lattice points occupy the corners of the cell along with one in the centre and in the F cell, the points occupy the corners and the faces of the unit cell. In a base centred cell, there are two additional lattice points centred on a pair of cell faces in a primitive cell.

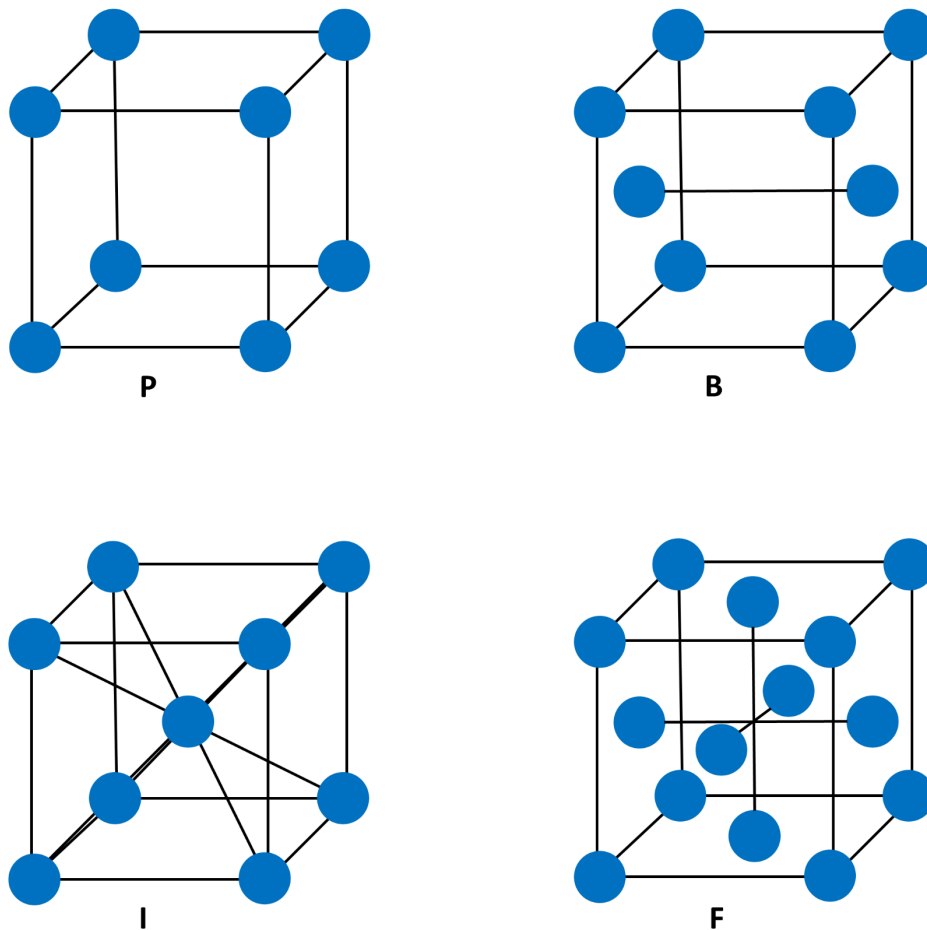


Figure 3.3. Possible lattice positions within unit cells, where B shows the lattice points centred on the B plane of a primitive cell.

Crystal structures may be classified based on the symmetry of their unit cells. There are seven crystal systems (Table 3.1) and they are categorised regarding the relationships between the lengths of the unit cell edges (a , b , and c) and the angles of the unit cell (α , β and γ). The seven different crystal systems arise from the seven possible length and angle combinations.

Table 3.1. The seven crystal systems, their essential symmetry, the associated angles and axes and the fourteen Bravis lattices for each system.

Crystal System:	Essential Symmetry:	Axes:	Angles:	Bravis Lattice Type:
Cubic	Four three-fold rotation axes	$a=b=c$	$\alpha=\beta=\gamma=90^\circ$	P, F, I
Hexagonal	One six-fold rotation	$a=b\neq c$	$\alpha=\beta=90^\circ$, $\gamma=120^\circ$	P
Trigonal	One three-fold rotation	$a=b=c$	$\alpha=\beta=\gamma\neq 90^\circ$	P
Tetragonal	One four-fold rotation	$a=b\neq c$	$\alpha=\beta=\gamma=90^\circ$	P, I
Orthorhombic	Three two-fold rotations and/or mirror planes	$a\neq b\neq c$	$\alpha=\beta=\gamma=90^\circ$	P, B, I, F
Monoclinic	One two-fold rotation and/or mirror plane	$a\neq b\neq c$	$\alpha=\gamma=90^\circ$, $\beta\neq 90^\circ$	P, C
Triclinic	None	$a\neq b\neq c$	$\alpha\neq\beta\neq\gamma\neq 90^\circ$	P

Additional symmetry elements may be contained within a unit cell, which can be divided further into point symmetry or space symmetry. Point symmetry occurs through a point, such as reflection or rotation and space symmetry involves additional translation, such as screw axes and glide planes. Point symmetry may also be divided into both proper and improper rotations, where proper rotations are performed by rotating a molecule 360° around an axis, while retaining the original configuration. Improper rotations involve rotating a molecule 360° around an axis, followed by reflection through a plane perpendicular to the rotation axis, while maintaining the original configuration.

In point symmetry, the elements may occur alone or in combination with others to provide the 32 possible crystallographic point groups, generated using the seven crystal systems. There are 230 possible arrangements for symmetry elements, which are called space groups. Space groups describe all the symmetry elements within a crystal and can provide atomic positions for every atom within a unit cell when combined with the atomic positions of the asymmetric unit.

The asymmetric unit is the smallest part of the unit cell which may be used to generate the complete unit cell by application of symmetry operations.⁷

3.3 X-ray Diffraction^{4,8}

A crystal may be thought of as parallel lattice planes and these planes may be described by Miller indices, represented by three integers (hkl) . Miller plane examples may be seen in Figure 3.4.

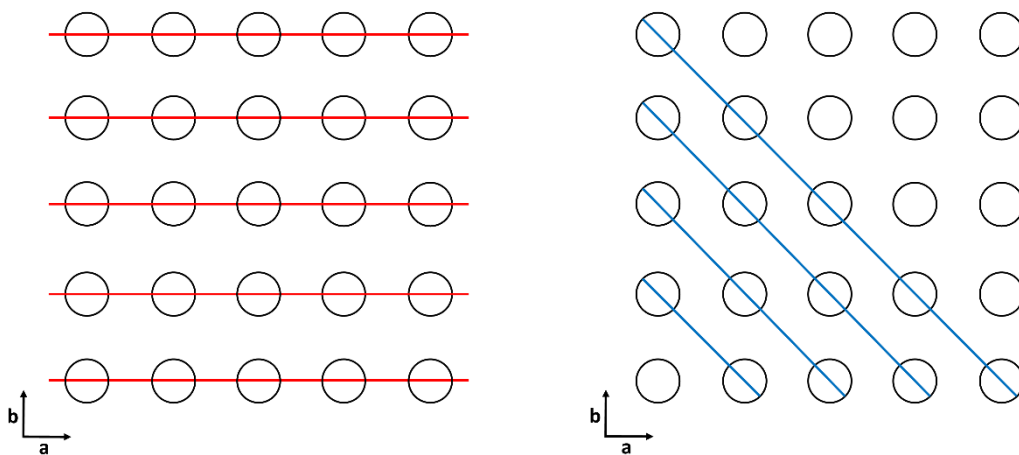


Figure 3.4. Schematic representations of Miller planes. The red lines are representations of the (010) planes, where only the b axis is intercepted and the blue lines represent the (110) planes, where both the a and b axes are intersected.

Peaks result when an X-ray beam with a wavelength (λ) comparable to the constant separation distance between the planes (d) is focused onto a crystal and the resulting reflections interfere constructively. This may be explained by Bragg diffraction, which was first proposed by W. H. and W. L. Bragg in 1913. A simple diagram (Figure 3.5) may be used to aid the derivation of the equation underpinning this theory, known as the Bragg equation (Equation 3.1).

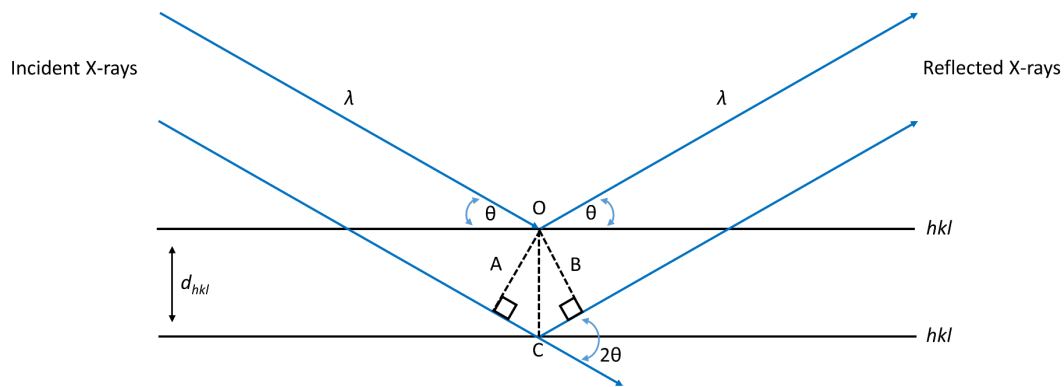


Figure 3.5. Simplistic schematic illustration of Bragg diffraction, showing the interaction of X-rays with lattice planes in a crystal. Trigonometry may be used in the derivation of the Bragg equation.

In the theory, n is an integer, λ is the wavelength of the incident X-ray beam, d is the distance between the lattice planes within the crystal and θ is the glancing angle.

The first step in the derivation of the Bragg equation is to observe that the two incident X-rays travel on a parallel trajectory and are in phase with one-another until the first X-ray is scattered by atom O and the second X-ray travels to the next lattice plane where it is scattered by atom C. In order to continue their parallel trajectory after scattering, the second beam must travel an additional distance either side of the point C after scattering ($AC + CB$). In order for both beams to remain in phase, the additional distance travelled is required to be a multiple of λ , providing the ' n ' λ term in the Bragg equation.

As a consequence:

$$n \lambda = AC + CB$$

$$\text{since } AC = CB; n \lambda = 2AC$$

Using trigonometry, where ' d ' is the hypotenuse of the right-angled triangle A C O.

Therefore:

$$\sin \theta = AC/d; AC = d \sin \theta$$

$$n \lambda = 2AC$$

By substitution of equations, the Bragg equation may be expressed as:

$$n\lambda = 2d\sin\theta \quad (3.1)$$

3.3.1 Powder X-ray Diffraction^{9,10}

Powder X-ray diffraction (PXRD) is an experimental technique used as a way to quickly examine the crystallinity of a bulk sample. The technique is especially useful in cases where a single crystal of a material cannot be obtained, such when polycrystalline or granular materials are obtained. Samples typically consist of multiple, randomly orientated small crystals and in these polycrystalline samples, multiple crystallites may satisfy Bragg's law. To minimise preferential orientation, MOF samples are typically ground using a pestle and mortar. In a typical powder diffraction experiment, a detector and X-ray tube rotate around the stationary sample, and the detector position, 2θ (2θ), represents the angle measured between the detector and X-ray tube. The intensity arises from the number of X-rays

measured by the detector at each 2θ angle. A diffraction ring may be observed, arising from the many crystallite orientations within a bulk sample (Figure 3.6).

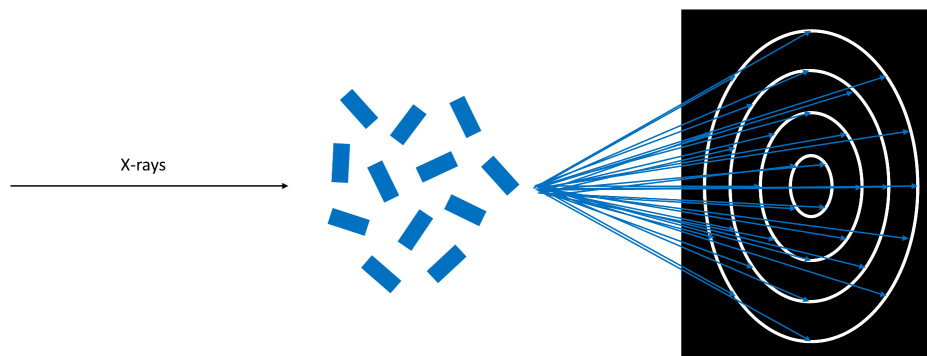


Figure 3.6. Schematic illustration of powder X-ray diffraction.

In order to compress the three-dimensional diffraction pattern into a one-dimensional pattern, the intensity of a cross section of the rings is plotted as a function of scattering angle (2θ), where 2θ increases outwards from the centre of the ring. A typical powder X-ray diffraction pattern may be observed in Figure 3.7.

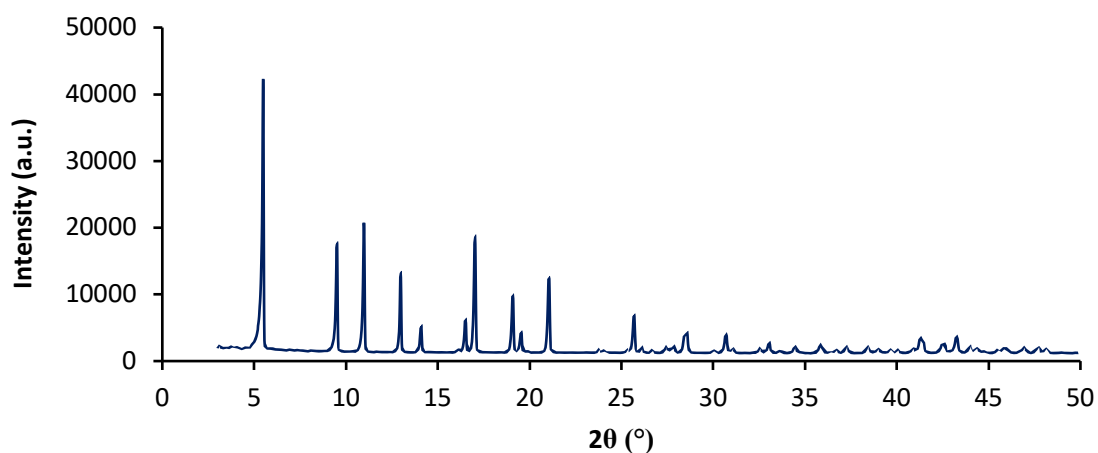


Figure 3.7. Typical experimental powder X-ray diffraction pattern (STAM-17-OEt shown), where intensity is plotted as a function of scattering angle (2θ).

3.3.1.1 Data Collection

In this thesis, data were collected either “in-house” or at the Diamond Light Source.

“In-house” powder X-ray diffraction data was collected using either flat plate discs or glass capillaries.

For disc measurements, samples (ca. 150 mg) were typically ground and packed into aluminium discs. It was ensured that the surface of the sample was flush with the surface of the disc, in order to obtain accurate 2θ values. In some cases, a Teflon insert was used to decrease the quantity of sample required. Measurements were performed using a PANalytical Empyrean Cu X-ray tube primary beam monochromator diffractometer, using Cu $K\alpha_1$ radiation. Disc measurements typically provide patterns with higher intensities, though do require larger quantities of sample.

For capillary measurements, samples (ca. 20 mg) were ground and packed into glass capillaries with 0.5 mm internal diameter. The capillary is mounted on the goniometer, then centred in the beam and the capillary is rotated in position while exposed to the X-rays. The programme WINXPOW is used to control the step size, 2θ range and overall run time. Samples were collected on a STOE STADIP Cu X-ray tube primary beam monochromator diffractometer, operated in capillary Debye-Scherrer mode and using Cu $K\alpha_1$ radiation. Capillary diffraction was used when smaller quantities of sample were produced and in the case of activated samples, where capillaries were flame sealed.

In the case of variable temperature powder X-ray diffraction, samples (ca. 500 mg) were ground and packed into an alumina disc. It was again ensured that the surface of the sample was flush with the surface of the disc, in order to obtain accurate 2θ values. Variable temperature powder X-ray diffraction allows control of both the atmosphere and

temperature that a sample experiences while exposed to X-rays and in this work, measurements were conducted under vacuum to investigate the change in phase after removal of solvent molecules at elevated temperature. Measurements were performed using a PANalytical Empyrean diffractometer Mo X-ray tube β -filter (Mo $K\alpha_{1,2}$ radiation) X'celerator with RTMS detector.

3.3.2 Single Crystal X-ray Diffraction^{5,11,12}

Single crystal X-ray diffraction is a non-destructive experimental technique that provides detailed information about the crystallinity of a particular crystal. The information collected includes crystal structure, space group and unit cell dimensions. This information may be used to determine the overall crystal structure of a material.

The method provides greater detail than powder X-ray diffraction, though to be used, crystals must be of sufficient size (typically larger than $5 \times 5 \times 5 \mu\text{m}$) and quality. Single crystal X-ray diffraction leads to a pattern of spots with varying intensity that are dependent on the crystal structure (Figure 3.8)

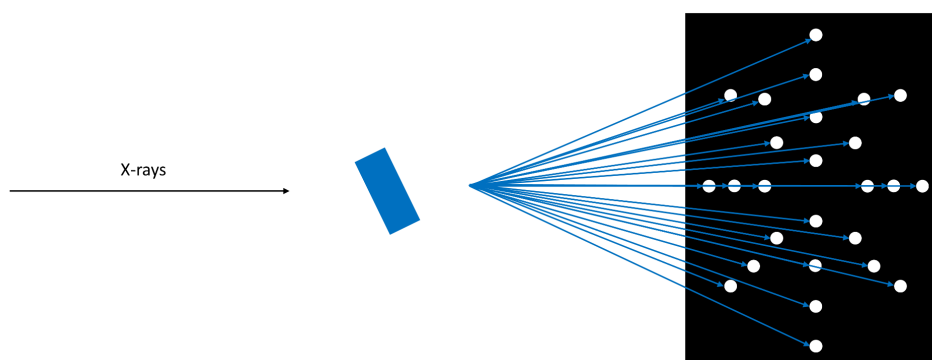


Figure 3.8. Schematic illustration of single crystal X-ray diffraction.

Upon completion of single crystal measurements, the measured intensities and corresponding standard deviations are mathematically reduced to structure factors (F) and their associated standard deviations (σF).

The structure factor (F_{hkl}) is a mathematical expression describing a diffracted wave's amplitude, where h , k , l are the Miller indices that correspond to a lattice plane within a crystal. Scattering factors (f_j) and coordinates ($x_j a, y_j b, z_j c$) from atoms within a crystal's unit cell lead to the overall equation for the calculation of a structure factor. The structure factor may be expressed in Equation 3.2.

$$F_{hkl} = \sum_j f_j \exp^{i\phi_{hkl}} \quad (3.2)$$

Where:

$$\phi_{hkl}(j) = 2\pi(hx_j + ky_j + lz_j)$$

The crystal structure refinement is assigned an associated residual factor (R-factor), which is a measure of the agreement between structure factors from the original crystallographic data (F_o) and those calculated from the refined crystallographic model (F_c). The R-factor is calculated using a least-squares refinement and determines the quality of the crystallographic model. As a result, a low R-factor value is desirable.

The R-factor, R , associated with a refined crystallographic model refers to the conventional R-factor and may be expressed mathematically in Equation 3.3.

$$R_1 = \frac{\sum |F_o| - |F_c|}{\sum |F_o|} \quad (3.3)$$

The weighted R factor, wR , (Equation 3.4) attempts to take into consideration the errors of how well measured the intensities are ($\sigma(F)$) during the refinement process, where w is the weighting of each reflection.

$$wR = \left[\frac{\sum w(F_o^2 - F_c^2)^2}{\sum w(F_o^2)^2} \right]^{\frac{1}{2}} \quad (3.4)$$

The goodness of fit, S , (Equation 3.5) should be as close to 1 as possible to indicate a correctly weighted refinement. N_R refers to the number of reflections in the refinement and N_P refers to the number of refined parameters.

$$S = \left[\frac{\sum w(F_o^2 - F_c^2)^2}{(N_R - N_P)} \right]^{\frac{1}{2}} \quad (3.5)$$

3.3.2.1 Data Collection

In this thesis, data were collected either “in-house” or at the Advanced Light Source.

Single crystals of sufficient size for “in-house” diffraction were collected at 173 K on either a Rigaku FR-X Ultra-high brilliance diffractometer with Mo K α radiation source ($\lambda = 0.71073$ Å) and a RigakuXtaLAB P200 detector or on a Rigaku MM-007HF diffractometer with Cu K α radiation source ($\lambda = 1.54184$ Å) and a RigakuXtaLAB P100K detector. Measurements at 125 K were collected on a Rigaku MM-007HF diffractometer with Cu K α radiation source ($\lambda = 1.54184$ Å) and a RigakuXtaLAB P200K detector. Absorption corrections were applied using multi-scan methods in CrysAlisPro 1.171.38.46.¹³ Structure solutions were obtained using SHELXT¹⁴ and refined by full matrix on F^2 using SHELXL¹⁵ within the Olex2¹⁶ suite. All full occupancy non-hydrogen atoms were refined with anisotropic thermal displacement parameters. Aromatic hydrogen atoms and hydrogen atoms belonging to coordinated water molecules were included at their geometrically estimated positions.

3.3.3 Synchrotron Radiation

“In-house” X-ray sources are useful in the analysis of materials and provide details on the crystallinity and purity of samples and may be used to determine whether a material is indeed the desired product from a reaction. In order to conduct more complicated experiments, such as the determination of dehydrated or gas-loaded structures or to conduct further analytical techniques such as Rietveld refinement, synchrotron X-ray diffraction data is often required to provide data of a high enough standard.

In a synchrotron, a high energy beam of electrons is accelerated around a fixed closed-loop path. A magnetic field is used to bend the beam into its closed path and produces high intensity synchrotron light (X-rays) (Figure 3.9). Synchrotron facilities have advantages over in-house diffractometers including the higher quality data produced, shorter collection periods and in the case of single crystal diffraction, they allow the measurement of significantly smaller crystals than may be measured in-house.

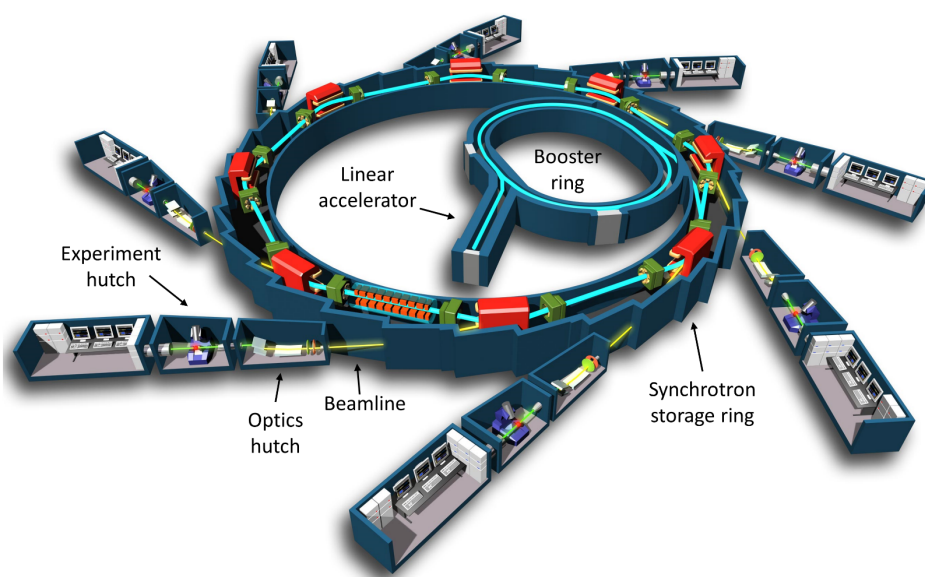


Figure 3.9. Schematic illustration of a synchrotron facility reproduced from reference 17.

Powder synchrotron data was obtained using synchrotron X-rays ($\lambda = 0.8260 \text{ \AA}$) from beamline I11 at the Diamond Light Source in the UK. Single crystal synchrotron data was obtained using a Bruker D8 diffractometer equipped with a PHOTON100 detector on station 11.3.1 at the Advanced Light Source ($\lambda = 0.7749(1) \text{ \AA}$) in the USA. Single crystals

were mounted on MiTeGen MicroGrippers and were sealed inside an in-house built gas cell. Data were collected at 300(2) K and ambient pressure, before evacuating the cell for 15 min to 17 mtorr and collecting a second data set under dynamic vacuum (down to 7 mtorr) to provide a dehydrated crystal structure. Dehydration completion was assessed by solution of the crystal structure, which showed an absence of coordinated and non-coordinated water molecules.

3.4 Thermogravimetric Analysis¹⁸

Thermogravimetric analysis (TGA) determines the mass loss with increasing temperature in microporous materials. A small sample of material was placed into a pre-weighed alumina crucible and the weight was noted. The crucible was then gradually heated under a gaseous atmosphere and the loss of mass was recorded. This provides details on the structural stability of the material and shows at which temperature solvent molecules, such as water, are lost. The samples were analysed using a Stanton Redcroft STA-780 series thermal analyser under an air atmosphere. A typical TGA curve may be observed in Figure 3.10.

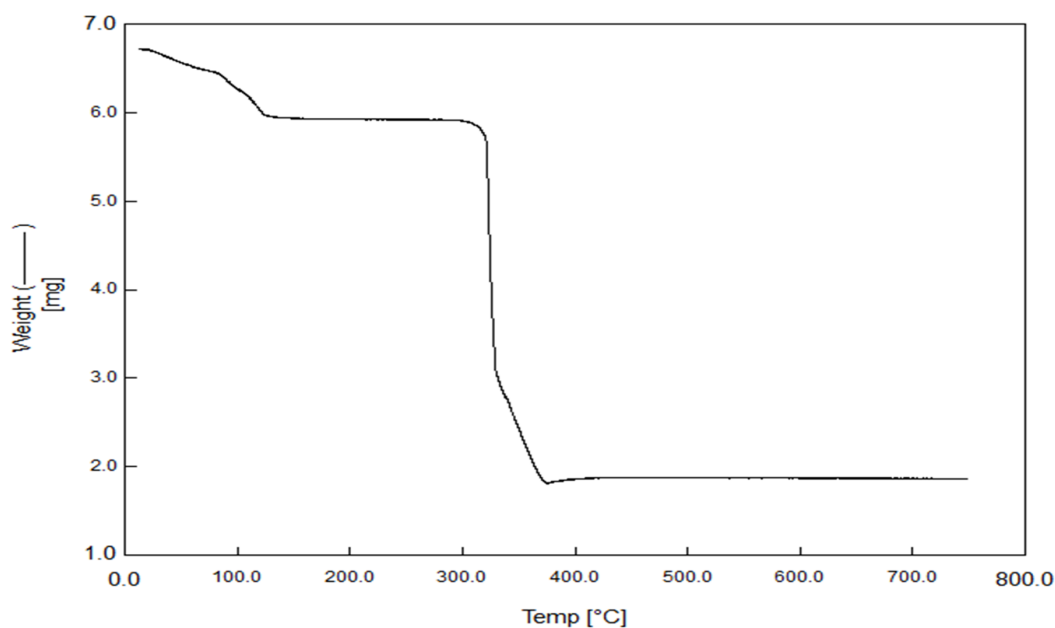


Figure 3.10. Experimental TGA curve for the metal-organic framework STAM-17-OEt showing two distinct mass losses. The first is at 40-120 °C, which indicates the loss of solvent from within the pores (in this case, water) and the second at approximately 320 °C is when the framework begins to collapse due to decomposition of the organic linker. From this data, a safe activation temperature is 150-200 °C, in the middle of the plateau.

3.5 Activation of Materials

In order to remove residual solvent molecules and to expose open metal sites for the adsorption of chemicals, samples were activated under vacuum on a dehydration rig (Figure 3.11) and sealed under an argon atmosphere to prevent re-exposure to atmospheric moisture. Pre-weighed samples were transferred into glass ampoules or glass capillaries and a small piece of glass wool was used to lightly “plug” the opening of the vessel to minimise sample loss upon exposure to vacuum. The samples were placed inside a Schlenk tube, which was

sealed with a Subaseal and samples were slowly exposed to rotary vacuum (ca. $\times 10^{-1}$ – $\times 10^{-2}$ Torr), before the samples were heated to the desired temperature for activation in a Büchi glass oven (typically 150 °C). Once the samples reached temperature, they were exposed to dynamic vacuum, provided by a diffusion pump (ca. $\times 10^{-3}$ – $\times 10^{-4}$ Torr). The samples were left overnight at temperature and under dynamic vacuum, before being cooled to ambient temperature and flame sealed under argon. An ampoule pre- and post-dehydration may be observed in Figure 3.12.

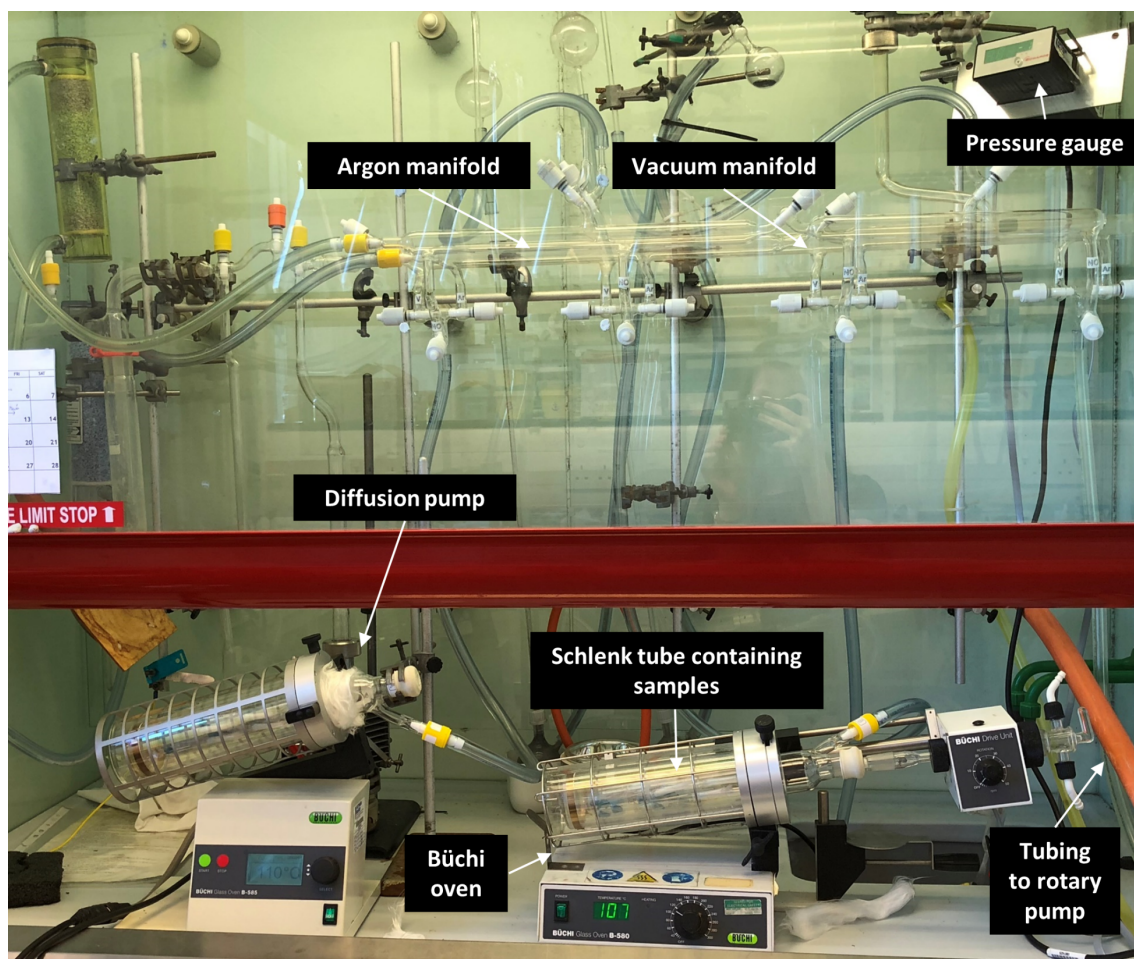


Figure 3.11. Labelled image of the dehydration rig used to activate samples.



Figure 3.12. Glass ampoule containing powdered MOF sample pre- (left) and post-activation (right).

3.6 Gas Adsorption¹⁹

Gas adsorption of adsorbates onto a surface may occur in one of two ways: via physisorption or chemisorption. Physisorption occurs via a Van der Waals interaction between the adsorbate and the surface. The interactions are weak but long-ranging and lead to small enthalpy changes in the region of 20 kJ mol^{-1} that are insufficiently high enough to lead to bond-breaking, thus the structural integrity of an adsorbent molecule is retained.

Chemisorption results in the formation of, usually covalent, chemical bonds between the adsorbate molecules and the surface. This generally leads to shorter distances between the adsorbate and the surface and provides much greater enthalpy changes when compared to physisorption in the region of 200 kJ mol^{-1} .

3.6.1 Surface Area Determination²⁰

Surface area measurements allow the determination of how much gas a material will store and for microporous materials, the two most commonly used data analysis tools are the Langmuir equation and the BET equation.

Adsorption isotherms are recorded using an adsorption gas such as nitrogen or argon, conducted at a constant temperature and is plotted as the amount of gas adsorbed per gram of adsorbent as a function of the equilibrium pressure (P/P_0).

Gas adsorption isotherms may be measured using volumetric or gravimetric analysis. In volumetric analysis, a known pressure of gas is introduced into a known volume of sample, and the amount of gas adsorbed by the sample may be calculated from the equilibrium pressure attained. This method is used in all nitrogen adsorption isotherms. In gravimetric analysis, the mass of the sample is constantly monitored and may be used to determine the mass of the adsorbed gas. There are six types of adsorption isotherms known for porous materials (Figure 3.13) as defined by Brunauer²¹ and Sing²² and their shapes may be used to determine their mechanism of gas adsorption.

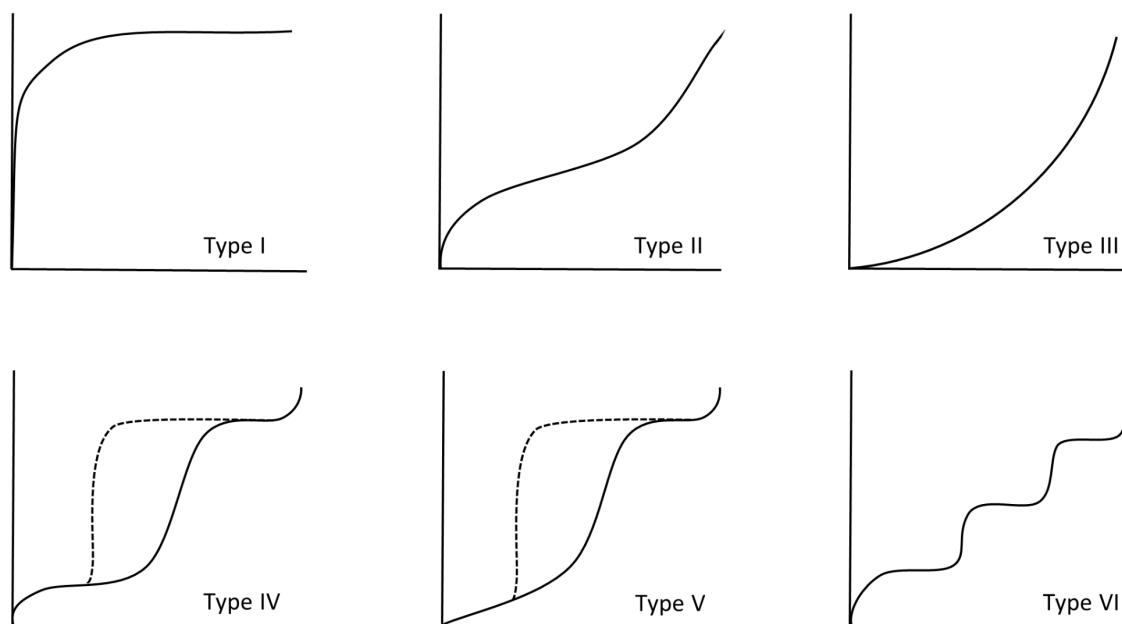


Figure 3.13. The six basic types of adsorption isotherm according to the Brunauer classification.²¹

The dashed lines represent the desorption branches of the isotherms.

Type I isotherms (also known as Langmuir isotherms) are typically observed with microporous solids and are noted for the rapid rise in the volume adsorbed at low pressure. This initial rise typically indicates monolayer deposition of molecules in the pores. The extended plateau section is determined by the total pore volume and may be interpreted as gradual filling of the micropores. Occasionally there is a rise at high partial pressure, which may be attributed to multilayer coverage on the surface of the pores. A nitrogen adsorption isotherm displaying multilayer coverage may be observed in Figure 3.14.

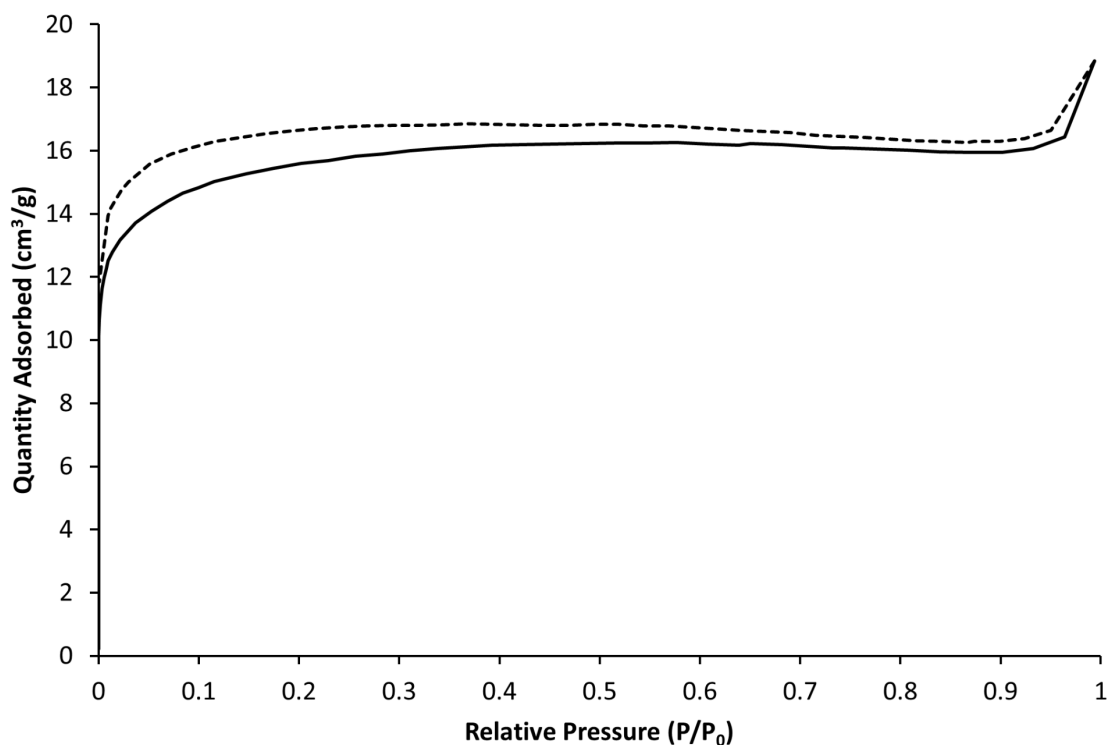


Figure 3.14. Experimental nitrogen adsorption isotherm obtained at 77 K for STAM-17-OEt, showing a type I isotherm with a small second rise from multilayer coverage on the external surface. The solid line represents the adsorption branch and the dashed line represents the desorption branch.

Type II and IV isotherms indicate non-porous materials or mesoporous materials. Type III and V isotherms are characteristic of adsorbents with a higher affinity for each other than for the material. Type VI isotherms are rare and signify a nonporous material with a very uniform surface.²³

3.6.1.1 Langmuir Theory²⁴⁻²⁶

The Langmuir isotherm is one of the simplest possible adsorption isotherms and is based on three fundamental assumptions: where adsorption cannot continue once a monolayer has been formed, all adsorption sites are equal on an even surface and no interactions exist between adsorbate molecules. For these reasons, Langmuir theory is more applicable to chemisorption, rather than physisorption.

At equilibrium, there is no change between the rates of adsorption and desorption, therefore the rates are equal. This leads to the derivation of the Langmuir isotherm equation (Equation 3.6), where θ is the fractional coverage, V_a is the volume of gas adsorbed, V_m is the volume of the monolayer, K is the empirical constant and P is the pressure.

$$\theta = \frac{V_a}{V_m} = \frac{KP}{1 + KP} \quad (3.6)$$

The equation may also be expressed in terms of pressure:

$$\frac{P}{V} = \frac{P}{V_m} + \frac{1}{KV_m} \quad (3.7)$$

3.6.1.2 BET Theory²⁷⁻²⁹

Brunauer, Emmett and Teller (BET) theory assumes that further physical adsorption may occur on top of the initial adsorbed layer, leading to multilayer formation. While on a Langmuir plot, the isotherm is expected to level off at high pressure; the BET isotherm will rise infinitely. In the BET adsorption equation (Equation 3.8), P is the partial vapour pressure of the adsorbate gas at 77 K, P_0 is the saturated pressure of the adsorbate gas, V_a is the volume of gas adsorbed, V_m is the volume of the monolayer and C is the dimensionless BET constant.

$$\frac{1}{\left[V_a \left(\frac{P_0}{P} - 1\right)\right]} = \frac{C - 1}{V_m C} \times \frac{P}{P_0} + \frac{1}{V_m C} \quad (3.8)$$

Plotting the BET value of $1/[V_a ((P_0/P) - 1)]$ against P/P_0 leads to a straight-line plot (Figure 3.15). The slope and the intercept may be determined and are equal to $C-1/V_m C$ and $1/V_m C$ respectively. V_m is equal to $1/(\text{slope} + \text{intercept})$ and C is calculated as $(\text{slope} + \text{intercept}) + 1$.

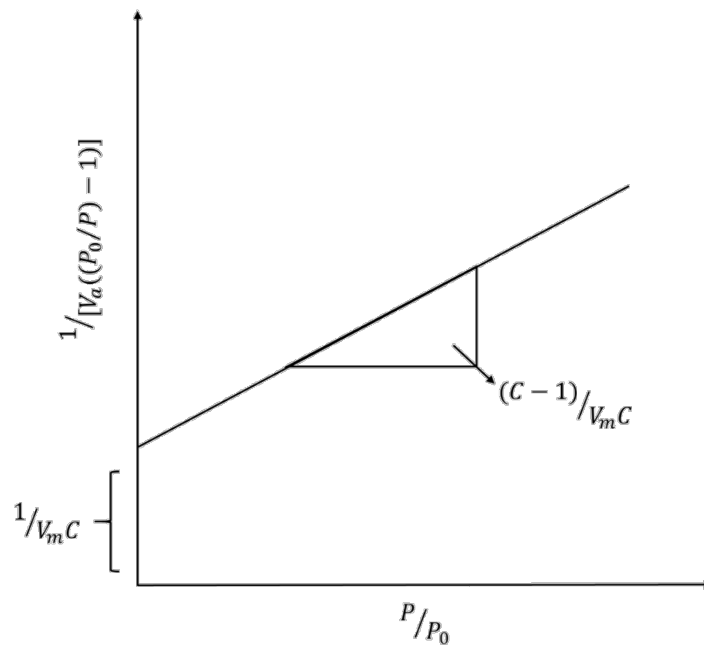


Figure 3.15. Schematic depiction of a BET isotherm.

V_m may be used to calculate the total (S_{total}) and specific (S_{BET}) BET surface areas using Equations 3.9 and 3.10 respectively. N is Avogadro's number, s is the cross-sectional area of an adsorbate molecule, V is the molar volume of the adsorbate gas and a is the mass of the adsorbent.

$$S_{total} = \frac{(V_m N_s)}{V} \quad (3.9)$$

$$S_{BET} = \frac{S_{total}}{a} \quad (3.10)$$

3.6.1.3 Equipment Used for Gas Adsorption Measurements

Porosity measurements were performed on a Micromeritics ASAP 2020 surface area and porosity analyser. Samples (100-150 mg) were placed in a glass bulb, which was sealed with a rubber frit to prevent atmospheric exposure. The material was activated by heating under vacuum at 150 °C for approximately 16 hours in order to remove residual solvent molecules from the pores, before the sample was moved to the analysis port where the desired gas was dosed incrementally onto the sample. The volume of gas adsorbed by the sample was recorded as a function of partial gas pressure. Nitrogen measurements were carried out at 77 K, using a bath of liquid nitrogen around the sample and argon measurements were performed at 87 K. BET surface areas were calculated by the ASAP 2020 software.

3.6.2 Micro-breakthrough

Gas breakthrough studies determine the time taken for a particular gas to 'break through' a material and provide an indication of the time that a material will offer protection against that particular gas. Micro-breakthrough studies allow such studies to be performed on a small scale and are useful for providing an initial indication of a particular material's capability. The small scale of such measurements is particularly advantageous in testing harmful gases.

3.6.2.1 Micro-breakthrough Experimental Procedure

Ammonia and hydrogen cyanide micro-breakthrough studies were performed on a micro-breakthrough rig at Dstl Porton Down using the general experimental set up shown in Figure 3.16.

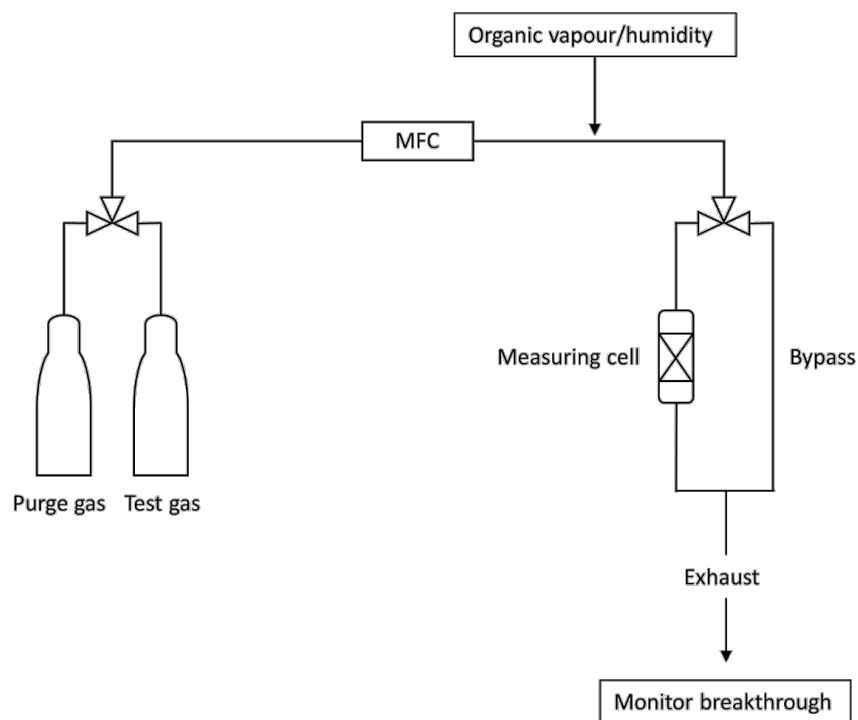


Figure 3.16. Schematic representation of a general micro-breakthrough apparatus set-up.

Experiments were performed by either packing a sample between two glass wool plugs in a glass tube or by placing the sample on a metal frit and flowing the challenge gas through the sample at a known concentration and flow rate. The challenge gas output concentration was monitored using a photoionization detector (Phocheck Tiger).

The experimental set-up and testing technique were derived from a method developed by Peterson *et al.*³⁰⁻³²

The first micro-breakthrough experimental set-up involved packing a pre-weighed sample (10-20 mg) between two pieces of glass wool inside a glass tube with an internal diameter of 4 mm (Figure 3.17). A known concentration of challenge gas contained within a pre-filled gas bag was passed through the micro-breakthrough rig and through the bottom of the sample plug. The flow rate was set using a mass flow controller and the time taken for the

photoionization detector to register a rise in the concentration of the harmful gas is considered to be the breakthrough time. The challenge gas was also passed through an empty tube to determine the “dead time”. The area above the curve of the graph if continued until $C_{out} = C_{in}$ represents the total capacity of the material. An example micro-breakthrough curve may be seen in Figure 3.18.



Figure 3.17. Image of a MOF sample packed between two glass wool plugs. The lighter blue at the bottom of the plug is sample that has been exposed to ammonia and the darker blue on top is sample that has not had ammonia pass through it.

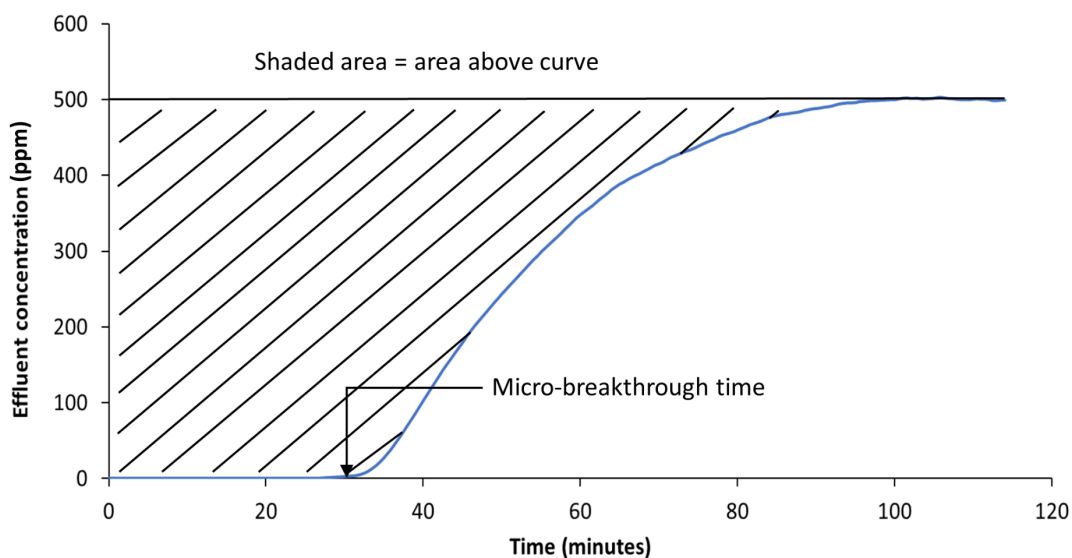


Figure 3.18. Example of a micro-breakthrough curve. The point where the plot begins to curve upwards is taken as the time for the gas to ‘break through’ a material and is known as the breakthrough time. The capacity may be measured by calculating the area above the curve.

The second type of testing involved an adjustment for the weight of sample, where pre-weighed samples (20-30 mg) were placed on a metal frit in an 8 mm diameter sample holder, ensuring enough sample was used to cover the surface of the frit (Figure 3.19).

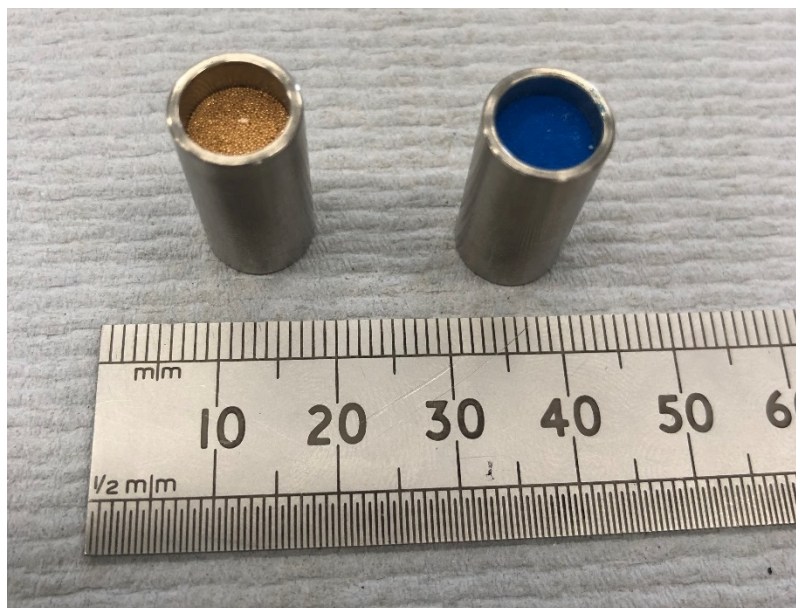


Figure 3.19. Image of an empty metal sample holder containing a frit (left) on which a thin bed of sample may be placed on the surface (right).

The metal frit was placed within an InfraSORP instrument and a known concentration of challenge gas from a gas bottle was passed through the instrument and thus through the sample. The flow rate was set using a mass flow controller and a photoionization detector was again used to register a rise in the concentration of the challenge gas. Due to the very thin sample bed on the metal frit, breakthrough is reached almost immediately in all samples and thus breakthrough time is not an accurate measurement of uptake (Figure 3.20). Consequently, the ammonia uptake is expressed as the number of milligrams of ammonia adsorbed per gram of sample.

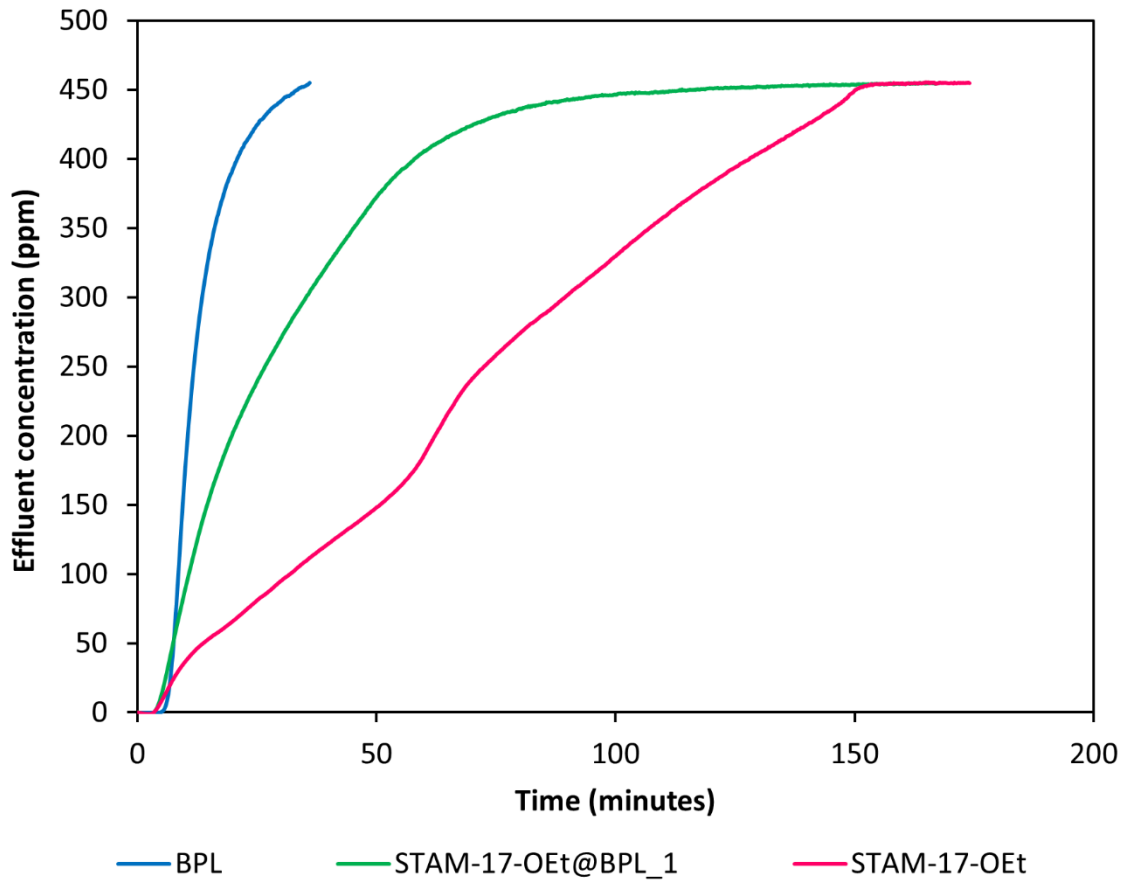


Figure 3.20. Example of micro-breakthrough curves measured using a thin sample bed. The gas breaks through almost immediately for all samples, so the area above the curve is calculated to provide the ammonia capacity of the material.

3.7 Water Stability and Cyclohexane Adsorption³³

Dynamic vapour sorption (DVS) analysis may be used to characterise the response of a material to changes in humidity. A sample of material is placed on the microbalance and the sample enclosure may then be evacuated under controlled temperature to ensure desolvation of any residual solvent within the sample. The humidity within the sample enclosure may then be increased to the desired level and the associated weight change in the sample may be monitored.

Water and cyclohexane adsorption were both measured using a DVS Advantage (Surface Measurement Systems Ltd.) apparatus at Porton Down (Figure 3.21). A sample of material (ca. 20 mg) was placed in a stainless-steel pan and was heated to 423 K for 3 hours in dry air to remove residual moisture. For isotherm measurements, the relative pressure within the instrument was gradually increased in a series of steps to 95%, and the mass of the sample was monitored throughout. The temperature remained constant at 298 K during the experiments.

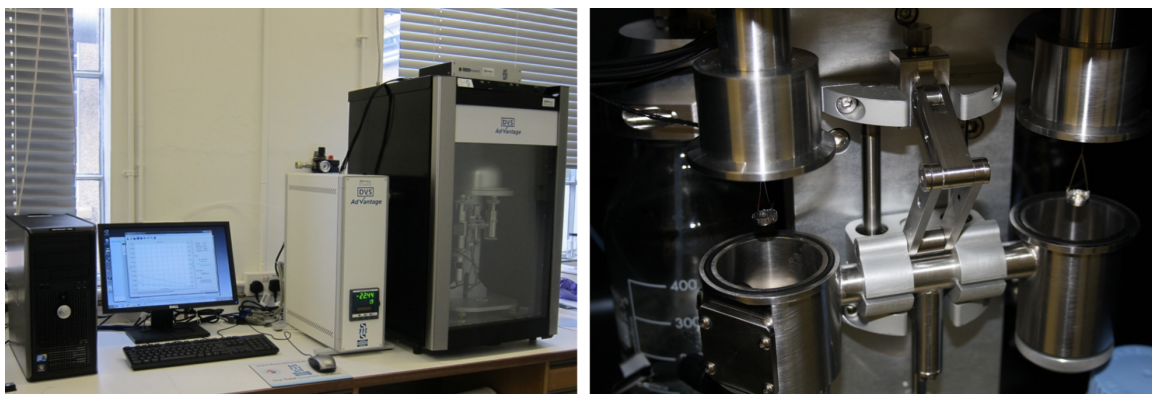


Figure 3.21. Experimental set-up of a DVS apparatus (left) and a view of the internal components of the instrument (right), where the sample pans may be observed.

Water stability was also monitored using a DVS apparatus, where a sample of material (ca. 20 mg) was placed in a stainless-steel pan. The relative humidity within the instrument was increased to 90% and sustained over the course of 5 days (298 K), and the mass of the sample was monitored. Humidity cycling experiments were completed in a DVS system by changing the relative humidity from 0 to 90% every 8 h. The temperature was held constant at 298 K and the mass of the samples was monitored. The experiments lasted 120 h (eight full cycles).

3.8 Infrared Spectroscopy³⁴

Fourier transform infrared (IR) spectroscopy is a very common spectroscopic technique used in the characterisation of chemical compounds. Infrared radiation passes through a sample and the energy of the transmitted radiation is measured at each wavelength. By studying the transmitted energy at certain wavelengths, it is possible to discern details regarding the molecular structure and to determine the particular functional groups contained within a material. The technique is used in this case to determine the functional groups contained within particular MOFs and to investigate how the groups are affected by factors such as exposure to humidity and particular chemicals.

IR spectroscopy utilises the fact that molecules absorb frequencies characteristic to their structure and such frequencies are known as resonant frequencies. In order to be IR active, a change in dipole moment must be involved and a molecule may vibrate in a number of different ways, known as vibrational modes. A molecule may undergo a stretching vibration where the atoms move back and forth, which may be symmetric or asymmetric. It may also undergo a bending vibration, where the angle is changed between the bonds.

IR spectra were collected on powdered samples using a Shimadzu IRAffinity-1S spectrometer fitted with an ATR accessory. The measurements provided information on the functional groups on the organic linker molecules within the MOF framework structure and how they were impacted by exposure to humidity and gases.

3.9 Nuclear Magnetic Resonance Spectroscopy³⁴

Nuclear magnetic resonance (NMR) spectroscopy is an important technique that is widely used within chemistry to obtain both chemical and structural information from compounds. The technique may be used in both the solution and solid-states.

In NMR spectroscopy, the energy of radio waves is absorbed by nuclei within a molecule, when it is placed in a strong magnetic field (B_0) and the interaction of the nuclei with the magnetic field results in a transition between nuclear spin states. Only nuclei which have a nuclear spin are NMR active and will therefore provide an NMR spectrum. Some nuclei have integral spins (e.g. $I = 1, 2, 3$), while some have fractional spins (e.g. $I = 1/2, 3/2, 5/2$), and some such as ^{12}C have no spin ($I = 0$). The nuclear spin of an isotope can be described in terms of its spin quantum number (I) and will have $2I + 1$ orientations (e.g. a nucleus with spin $1/2$ will have 2 possible orientations). The orientations are of equal energy when no external magnetic field is applied, whereas in the presence of a magnetic field, the energy levels split and each level is given a magnetic quantum number, m .

The frequency of radiation (ν) that is required to give rise to spin flipping or nuclear magnetic resonance may be given by Equation 3.11.

$$\nu = \left(\frac{1}{2\pi}\right) \gamma B_0 \quad (3.11)$$

Where: γ = the gyromagnetic ratio of the nucleus.

3.9.1 Solution Phase NMR

Solution phase NMR was performed using Bruker Avance II 400 spectrometers, which operated at 400 MHz and Mestrelab Mnova software was used in data analysis. The technique was used to identify and assess the purity of MOF linkers.

3.9.2 Solid-State NMR³⁵

Solid-state NMR is usually utilised in the characterisation of MOFs and other porous materials due to their insolubility in typical NMR solvents. Solid-state NMR usually provides broader peaks than solution state NMR due to anisotropic effects and orientation-dependent interactions. Peak broadening may be reduced by rapidly rotating the sample at an angle of 54.74° with respect to the applied magnetic field. This angle is known as the magic angle and the technique as “magic angle spinning” (MAS) (Figure 3.22).³⁶ Solid-state NMR was performed using Bruker Avance III solid-state spectrometers equipped with wide-bore 9.4 or 14.1 T superconducting magnets. Samples were packed into 1.9 mm zirconia rotors and rotated at the magic angle at rates between 37.5 and 60 kHz.

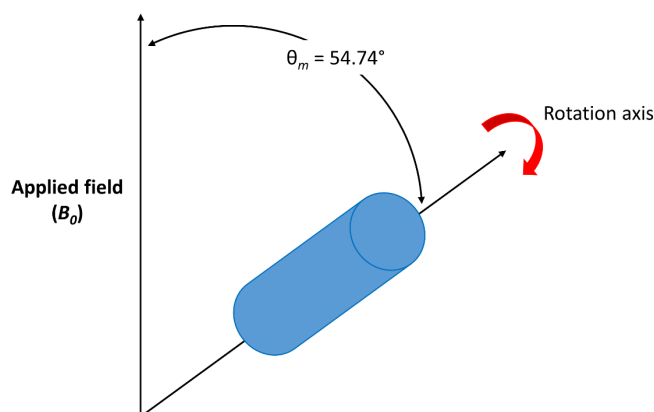


Figure 3.22. Schematic illustration of magic angle spinning, where the sample is rotated at an angle of 54.74° relative the applied magnetic field.

3.10 Electron Paramagnetic Resonance Spectroscopy³⁷

Electron paramagnetic resonance (EPR) spectroscopy is used to study materials with unpaired electrons and the technique excites electron spins. The concepts are analogous to those of NMR spectroscopy, though it is the electron spins that are excited, rather than those of the atomic nuclei. The technique may be used to investigate the properties of metals, such as copper, within MOFs.

EPR signals originate from the magnetic moment and spin quantum number, $S = 1/2$, with magnetic components $m_s = + 1/2$ and $m_s = - 1/2$. The magnetic moment of the electron aligns itself either parallel ($m_s = - 1/2$) or antiparallel ($m_s = + 1/2$) with the external magnetic field, B_0 , and each alignment has a specific energy (E) due to the Zeeman effect (Equation 3.12).

$$E = m_s g_e \mu_B B_0 \quad (3.12)$$

Where: g_e is the g-factor of the electron and μ_B is the Bohr Magnetron.

The splitting of the energy levels is a function of the magnetic field, B_0 (Figure 3.23).

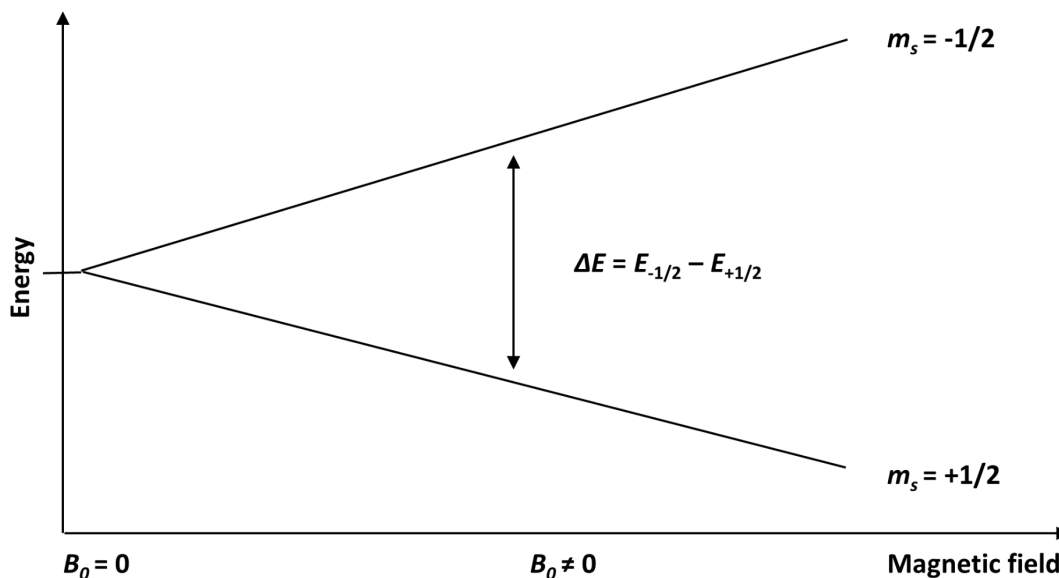


Figure 3.23. Effect on the energy levels within an atom upon the application of a strong magnetic field.

EPR measurements were performed using a Bruker EMX micro spectrometer, working at a frequency of approximately 9.5 GHz (X-band), with a magnetic-field modulation frequency set at 100 kHz. Samples were placed into a Clear Fused-Quartz EPR tube, which was closed with a stopper and a layer of Parafilm. The spectra were acquired by inserting the EPR tube containing the sample inside a Dewar flask. For measurements conducted at 77 K, the Dewar flask was filled with liquid nitrogen.

3.11 Electron Microscopy³⁸

3.11.1 Scanning Electron Microscopy

Scanning Electron Microscopy (SEM) is an imaging technique used when conventional optical microscopy no longer provides images of a suitable resolution and magnification. SEM provides the user with information on the morphology, the surface topography and the chemical composition of a material and can therefore be used in the characterisation of MOFs.

SEM operates by firing a single beam of electrons from an electron gun, where the electron beam is focused through multiple lenses to form a spot on the sample surface. The beam is scanned over the surface of a sample and the resulting reflections are collected via a detector. Two types of reflection result - secondary and back scattering. Secondary scattering is when an electron is emitted from an atom upon excitation from an electron beam. Back scattering occurs when the atom's atomic number is proportional to the intensity of the reflected signal and the initial electron is reflected by the sample. A complete image of the sample surface is generated by deflecting the beam over the whole sample using the scan coils (Figure 3.24).

SEM studies were performed using a Jeol JSM-5600 Scanning Electron Microscope with a tungsten filament electron gun and operating voltage of 5-25 kV and gold coating of samples was performed using a Quorum Q150R ES, to help prevent a build-up of charge on the sample's surface.

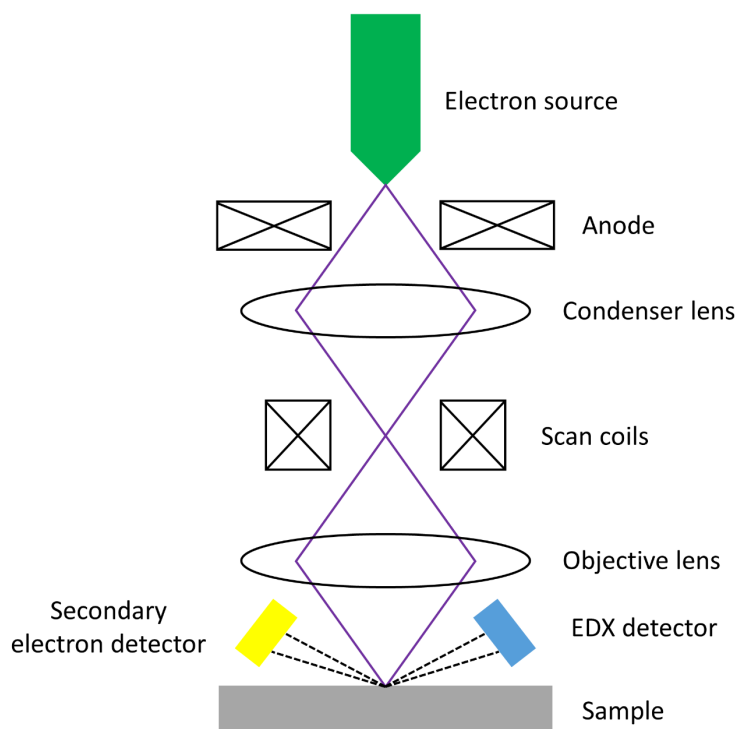


Figure 3.24. Schematic illustration of a typical scanning electron microscope.

3.11.2 Energy Dispersive X-ray Analysis³⁹

Energy dispersive X-ray spectroscopy (EDX) operates by ejecting electrons from the inner shells of atoms within an element, using a high-powered electron beam, resulting in the production of X-rays characteristic to a particular element.

The EDX set up involves an X-ray detector, where the X-rays are converted into electrical signals. A pulse processor is then used to measure the amount of energy within each X-ray and these characteristic values may be observed with the recorded counts as an EDX spectrum. The spectrum provides information on the elements present within a sample and their respective ratios. The technique may be used for elemental mapping, where the spatial

distribution of a particular element may be visualised. EDX analysis was also recorded on a Jeol JSM-5600 Scanning Electron Microscope at 25 kV, using an Oxford Inca Energy system.

3.12 References

- [1] G. Demazeau, *J. Mater. Sci.*, 2008, **43**, 2104-2114.
- [2] N. Stock and S. Biswas, *Chem. Rev.*, 2012, **112**, 933-969.
- [3] J. P. Glusker and K. N. Trueblood, *Crystal Structure Analysis: A Primer*, Oxford University Press, New York, 2010.
- [4] C. Giacovazzo, *Fundamentals of crystallography*, International Union of Crystallography, Oxford University Press, Oxford, 1992.
- [5] W. Clegg, *Crystal structure determination*, Oxford University Press, New York, 1998.
- [6] A. J. Blake and W. Clegg, *Crystal structure analysis: principles and practice*, 2nd Edn., Oxford University Press, New York, 2009.
- [7] T. Hahn, U. Shmueli, A. J. C. Wilson and International Union of Crystallography., *International tables for crystallography*, D. Reidel Pub. Co, sold and distributed in the U.S.A. and Canada by Kluwer Academic Publishers Group, Dordrecht, Holland, Boston, MA, 1984.
- [8] A. Khondker and S. Lakhani, *Int. J. Interdiscip. Res. Innov.*, 2015, **3**, 60-64.
- [9] V. K. Pecharsky and P. Y. Zavalij, *Fundamentals of powder diffraction and structural characterization of materials*, Springer, New York, 2009.
- [10] R. E. Dinnebier and S. J. L. Billinge, *Powder diffraction: theory and practice*, Royal Society of Chemistry, Cambridge, 2008.
- [11] P. Atkins and J. de Paula, *Physical Chemistry*, 8th Edn., Oxford University Press, New York, 2006.

- [12] P. G. Jones, *Chem. Soc. Rev.*, 1984, **13**, 157-172.
- [13] CrysAlisPro 1.171.38.46, Oxford Diffraction/Agilent Technologies UK Ltd, Yarnton, England.
- [14] G.M. Sheldrick, *Acta Crystallogr. Sect. A*, 2015, **71**, 3-8.
- [15] G.M. Sheldrick, *Acta Crystallogr. Sect. A*, 2015, **71**, 3-8.
- [16] O. V. Dolomanov, L. J. Bourhis, R. J. Gildea, J. A. K. Howard and H. Puschmann, *J. Appl. Cryst.*, 2009, **42**, 339-341.
- [17] Synchrotron Soleil, p Schéma de Principe Copyright © Chaix & Morel et Associés.
- [18] A. W. Coats and J. P. Redfern, *Analyst*, 1963, **88**, 906-924.
- [19] J. U. Keller and R. Staudt, *Gas adsorption equilibria: experimental methods and adsorptive isotherms*, Springer, New York, 2005.
- [20] P. A. Wright, *Microporous framework solids*, RSC Publishing, London, 2008.
- [21] S. Brunauer, *The adsorption of gases and vapors*, Oxford University Press, London, 1943.
- [22] K. S. W. Sing, D. H. Everett, R. A. W. Haul, L. Moscou, R. A. Pierotti, J. Rouquerol and T. Siemieniewska, *Pure. Appl. Chem.*, 1985, **57**, 603-619.
- [23] W. Krätschmer, J. Rathouský and A. Zukal, *Carbon*, 1999, **37**, 301-305.
- [24] I. Langmuir, *J. Am. Chem. Soc.*, 1916, **38**, 2221-2295.
- [25] I. Langmuir, *Physical Review.*, 1916, **8**, 149-176.
- [26] I. Langmuir, *J. Am. Chem. Soc.*, 1918, **40**, 1361-1403.
- [27] K. S. W. Sing, *Adv. Colloid. Interface. Sci.*, 1998, **76-77**, 3-11.
- [28] S. Lowell, J. E. Shields, M. A. Thomas, and M. Thommes, *Characterization of Porous Solids and Powders: Surface Area, Pore Size and Density*, Springer Netherlands, New York, 2004.
- [29] F. Jiménez, F. Mondragón and D. López, *J. Therm. Anal. Calorim.*, 2015, **120**, 1723-1730.

- [30] T. G. Glover, G. W. Peterson, B. J. Schindler, D. Britt and O. Yagi, *Chem. Eng. Sci.*, 2011, **66**, 163-170.
- [31] G. W. Peterson, J. Mahle, A. Balboa, G. Wagner, T. Sewell, and C. J. Karwacki, "Evaluation of MOF-74, MOF-177, and ZIF-8 for the removal of toxic industrial chemicals", ECBC-TR-659, United States Army Research, Development and Engineering Command: Edgewood Chemical Biological, 2008, 1-26.
- [32] J. B. Decoste and G. Peterson, *J Vis Exp.*, 2013, **80**, 51175-51181.
- [33] H. Furukawa, F Gándara, Y-B. Zhang, J. Jiang, W. L. Queen, M. R. Hudson and O. M. Yaghi, *J. Am. Chem. Soc.*, 2014, **136**, 4369-4381.
- [34] A. K. Brisdon, *Inorganic spectroscopic methods*, Oxford University Press, New York, 1998.
- [35] J. J. Fitzgerald and S. M. Depaul, *Solid-State NMR Spectroscopy of Inorganic Materials*, ACS Symposium Series; American Chemical Society, Washington DC, 1999.
- [36] T. Polenova, R. Gupta and A. Goldbourt, *Anal. Chem.*, 2015, **87**, 5458-5469.
- [37] V. Chechik, E. Carter and D. Murphy, *Electron Paramagnetic Resonance*, Oxford Chemistry Primers, Oxford University Press, Oxford, 2016.
- [38] J. Goldstein, D. E. Newbury, J. R. Michael, N. W. M. Ritchie, J. H. J. Scott and D. C. Joy, *Scanning electron microscopy and x-ray microanalysis*, 4th Edn., Springer, New York, 2018.
- [39] N. Taylor, *Energy Dispersive Spectroscopy*, 2nd Edn., John Wiley & Sons Ltd., Chichester, 2015.

Chapter 4: Water Stability and Ammonia Adsorption in the Hemilabile Metal-organic Framework: STAM-17-OEt

4.1 Aim

The aim of this chapter is to investigate the hydrolytic stability of a member of the STAM series of MOFs: STAM-17-OEt, which has been the main focus of this project. The chapter discusses in detail the structural features that enable the excellent hydrolytic stability and gas adsorption properties observed in the material and explains the techniques used to investigate them.

4.2 Introduction

MOFs are a class of porous solids that have undergone exciting developments over the past few decades and show promise for a wide range of applications.¹ Despite their promise, many studies have highlighted the significant stability issues observed in MOFs and this is especially apparent with respect to their interactions with water,² which severely limits the practical potential of many materials. Numerous applications require pre-activation of MOFs in order to expose the CUSs required for adsorption,³⁻⁵ and the behaviour of such materials upon desolvation is crucial in their suitability for application.⁶⁻⁷

In this chapter, the concept of hemilability will be introduced,⁸ where the presence of 'sacrificial' bonds within the coordination environment of metal centres provides a dehydrated copper MOF, known as STAM-17-OEt,⁹ with excellent hydrolytic stability.

When activated STAM-17-OEt is exposed to water, rather than the typical indiscriminate breaking of coordination bonds that usually results in structure degradation, it is non-critical, weak interactions between the paddlewheel clusters in the MOF that are broken. This allows

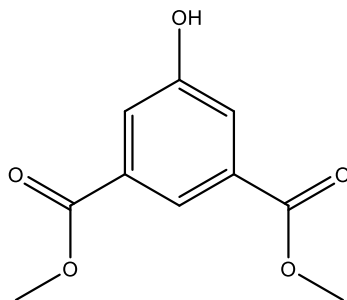
the framework to revert back to its original, as synthesised and hydrated structure without losing its overall structural integrity. This is in contrast to the compositionally similar MOF HKUST-1,¹⁰ which lacks the sacrificial bonds in STAM-17-OEt and therefore degrades in humid conditions.¹¹ HKUST-1 shall be used in this chapter for the comparison of properties with STAM-17-OEt.

4.3 Experimental Procedure

All commercially sourced reagents were used without further purification unless specified. HKUST-1 was purchased from Sigma Aldrich.

4.3.1 Synthesis of STAM-17-OEt linker

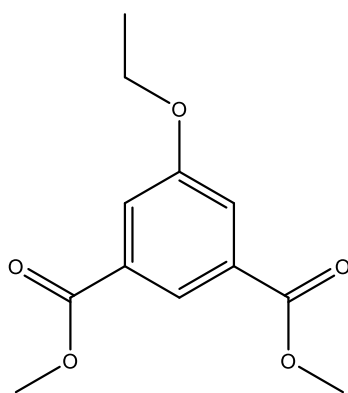
Synthesis of 1,3-dimethyl 5-hydroxybenzene-1,3-dicarboxylate:¹²



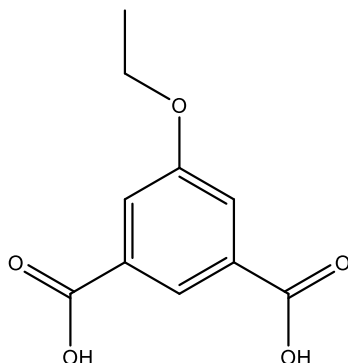
Concentrated sulfuric acid (19.5 mL) was added to a suspension of 5-hydroxybenzene-1,3-dicarboxylic acid (53.40 g, 293.2 mmol) in methanol (625 mL) and the mixture was heated to reflux for approximately 8 hours. The cooled solution was neutralised with saturated aqueous sodium bicarbonate (625 mL) and the solvent was removed under reduced pressure. The residue was suspended in water (100 mL) and was extracted with dichloromethane (total volume - 4 L). The combined organic layers were dried over anhydrous magnesium sulfate

and the solvent was removed under reduced pressure to afford 1,3-dimethyl 5-hydroxybenzene-1,3-dicarboxylate as a colourless solid (48.72 g, 231.8 mmol, 79% yield). ^1H (400 MHz, d_4 -MeOD) δ_{H} 8.11 (t, 1H, aromatic, $J = 2.80$ Hz), 7.63 (d, 2H, aromatic, $J = 1.60$ Hz), 3.93 (s, 6H, $-\text{CH}_3$) ppm.

Synthesis of 1,3-dimethyl 5-ethoxybenzene-1,3-dicarboxylate:¹³



1,3-dimethyl 5-hydroxybenzene-1,3-dicarboxylate (11.44 g, 54.43 mmol) and potassium carbonate (13.69 g, 99.06 mmol) were dissolved in acetone (260 mL). Iodoethane (5.00 mL, 62.5 mmol) was added to the solution and the reaction was boiled for 16 hours. Upon cooling, the solvent was removed under reduced pressure and the residue taken up in DCM (300 mL) and distilled water (300 mL). The mixture was extracted with DCM (3 x 200 mL), before the divided organic layers were washed with brine (100 mL) and dried over anhydrous magnesium sulfate. The solvent was removed under reduced pressure to afford 1,3-dimethyl 5-ethoxybenzene-1,3-dicarboxylate as a white solid (12.44 g, 52.22 mmol, 96% yield). ^1H (400 MHz, d_4 -MeOD) δ_{H} 8.18 (t, 1H, aromatic, $J = 3.20$ Hz), 7.71 (d, 2H, aromatic, $J = 1.60$ Hz), 4.14 (q, 2H, $-\text{CH}_2-$, $J = 20.8$ Hz), 3.94 (s, 6H, $-\text{CH}_3$), 1.44 (t, 3H, $-\text{CH}_3$, $J = 14.0$ Hz) ppm.

Synthesis of 5-ethoxybenzene-1,3-dicarboxylic acid:¹⁴

Potassium hydroxide (11.99 g, 213.7 mmol) and 1,3-dimethyl 5-ethoxybenzene-1,3-dicarboxylate (10.05 g, 42.18 mmol) were dissolved in methanol (250 mL). The mixture was heated to reflux for 18 hours, before cooling to room temperature. 2M hydrochloric acid (250 mL) was added to the cooled solution and the resulting precipitated solid was collected by vacuum filtration. The white solid was washed copiously with water until the washings reached pH 6 and 5-ethoxybenzene-1,3-dicarboxylic acid was then dried in air for several days (8.55 g, 40.7 mmol, 96% yield). ¹H (400 MHz, *d*₄-MeOD) δ_H 8.24 (t, 1H, aromatic, *J* = 2.80 Hz), 7.74 (d, 2H, aromatic, *J* = 1.20 Hz), 4.15 (q, 2H, -CH₂-, *J* = 20.8 Hz), 1.45 (t, 3H, -CH₃, *J* = 14.0 Hz) ppm.

4.3.1 Synthesis of STAM-17-OEt

STAM-17-OEt was typically synthesised hydrothermally, though reflux and room temperature syntheses were also performed.

Hydrothermal synthesis of STAM-17-OEt:⁹

STAM-17-OEt was synthesised by heating copper acetate monohydrate (0.20 g, 1.00 mmol), 5-ethoxybenzene-1,3-dicarboxylic acid (0.21 g, 1.00 mmol) and distilled water (15 mL) in a stainless-steel autoclave at 110 °C for up to 3 days. The autoclave contents were filtered upon cooling and the solid was washed with distilled water and ethanol, before drying in air. A typical yield was 0.24 g, 0.80 mmol, 80%.

Reflux synthesis of STAM-17-OEt:

STAM-17-OEt was synthesised by heating copper acetate monohydrate (31.94 g, 160.0 mmol), 5-ethoxybenzene-1,3-dicarboxylic acid (33.63 g, 160.0 mmol) and distilled water (800 mL) under reflux for up to 3 days. The resulting solid was filtered upon cooling and was washed with distilled water and ethanol, before drying in air. A typical yield was 46.40 g, 153.8 mmol, 96%.

Room temperature synthesis of STAM-17-OEt:

STAM-17-OEt was synthesised by stirring copper acetate monohydrate (0.20 g, 1.00 mmol), 5-ethoxybenzene-1,3-dicarboxylic acid (0.21 g, 1.00 mmol) and distilled water (5 mL) at room temperature for 3 days. The resulting solid was filtered and washed with distilled water and ethanol, before drying in air. A typical yield was 0.26 g, 0.86 mmol, 86%.

4.4 Results and Discussion

4.4.1 Formation of STAM-17-OEt

STAM-17-OEt was synthesised in a quantitative yield using the 5-ethoxybenzene-1,3-dicarboxylic acid linker and copper acetate monohydrate, using water as a solvent (Figure 4.1). The material is a member of the STAM-17-n series of MOFs and is related to the literature compound STAM-1. While STAM-1 requires solvothermal synthesis to form, STAM-17-OEt may be produced hydrothermally, under reflux or at room temperature without the formation of an HKUST-1 impurity or any other side products.

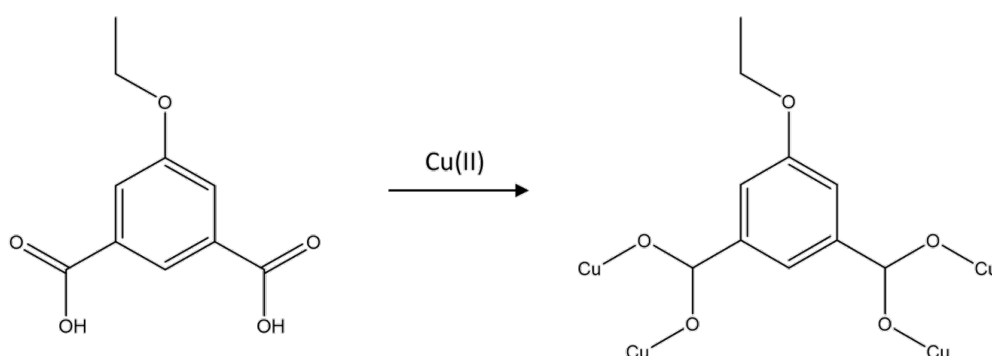


Figure 4.1. 5-ethoxybenzene-1,3-dicarboxylic acid linker used in the synthesis of the copper MOF: STAM-17-OEt.

The synthesised material is highly crystalline and crystals of sufficient size for single crystal analysis may be attained from a bulk batch achieved through hydrothermal synthesis. A calculated powder X-ray diffraction pattern obtained from the crystallographic information file of STAM-17-OEt may be compared to an experimentally acquired bulk powder sample to indicate the purity of the bulk material (Figure 4.2).

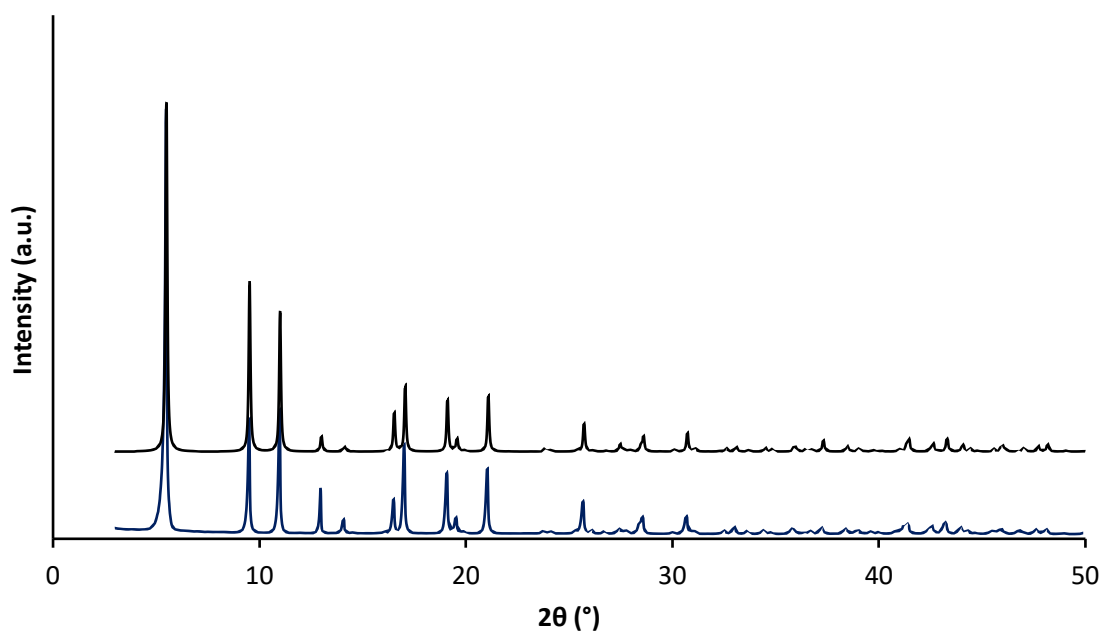


Figure 4.2. Comparison of experimental (blue trace) and simulated (black trace) powder X-ray diffraction patterns of STAM-17-OEt. The simulated pattern is calculated from the experimentally refined structural model that was found.

4.4.2 Crystallographic Characterisation Techniques

This section focuses on the underlying crystallography in STAM-17-OEt, where single crystal X-ray diffraction experiments were undertaken using synchrotron radiation at the Advanced Light Source and powder X-ray diffraction experiments were performed “in house” or at the Diamond Synchrotron.

4.4.2.1 Crystal Structure Determination

A single crystal of STAM-17-OEt was mounted on a MiTeGen MicroGripper and was sealed inside an in-house built gas cell. Data were collected on a Bruker D8 diffractometer equipped with a PHOTON100 detector, on station 11.3.1 of the Advanced Light Source ($\lambda = 0.7749(1) \text{ \AA}$). An initial data set were collected at 300(2) K at ambient pressure, before

evacuating the cell for 15 min to 17 mTorr and collecting a second data set under dynamic vacuum (down to 7 mTorr). Multi-scan absorption corrections were applied to both data sets using SADABS.¹⁵ Structural solutions were obtained from SHELXT¹⁶ and refined on F^2 using SHELX-2014 within the ShelXle software.¹⁷ Appropriate scattering factors were applied using the XDISP program¹⁸ within the WinGX suite of programs.¹⁹ In the hydrated phase, all full-occupancy non-H atoms were refined with anisotropic thermal displacement parameters and aliphatic and aromatic H atoms were included at their geometrically estimated positions. The ethyl group was found to be disordered over two symmetry-related sites, and the carbon atoms were refined anisotropically with site occupancies of 50%. Residual peaks of electron density were assigned as the oxygen atoms of partial occupancy water molecules. For the dehydrated phase, the significant structural rearrangement was reflected in the quality of the diffraction pattern. All aliphatic and aromatic H atoms were included at their geometrically estimated positions, though only Cu1 and Cu2 were refined with anisotropic thermal displacement parameters due to a combination of poor data quality and the potential disorder described in the following. Large positive and negative peaks of electron density surrounding the Cu3-Cu4 paddlewheel suggest that this unit exists in two positions within the crystal, probably due to incomplete conversion of the crystal between the hydrated and dehydrated phases.

4.4.2.2 Powder X-ray Diffraction

Experiments were completed “in house” using Cu $K\alpha$ radiation or synchrotron X-rays ($\lambda = 0.8260 \text{ \AA}$) on beamline I11 at the Diamond Synchrotron Light Source. Pre-activated samples were sealed inside glass capillaries to prevent exposure to atmospheric moisture. All experiments were carried out at 298 K.

4.4.2.3 Crystal Structure Analysis of STAM-17-OEt

STAM-17-OEt was collected as hexagonal blue crystals and the material was found to crystallise in the trigonal space group $P\bar{3}m1$ with unit cell dimensions of $a = 18.576(12)$ Å and $c = 6.8056(6)$ Å. The framework has a Kagome lattice-type topology and the final crystallographic parameters may be observed in Table 4.1.

Table 4.1. Crystallographic data from the structure determination of STAM-17-OEt (associated bond lengths and angles may be found in appendix tables 9.1 and 9.2 respectively).

Identification code	STAM_17_OEt_hydrated_300K
Empirical formula	$C_{10}H_{11.33}CuO_{6.67}$
Formula weight	301.73 g mol ⁻¹
Temperature	300(2) K
Wavelength	Synchrotron (0.7749 Å)
Crystal system, space group	Trigonal, $P\bar{3}m1$
Unit cell dimensions	$a = 18.5676(12)$ Å
	$b = 18.5676(12)$ Å
	$c = 6.8056(6)$ Å
Volume	2031.9(3) Å ³
Z	6
Calculated density	1.479 g cm ⁻³
Absorption coefficient	2.060 mm ⁻¹
$F(000)$	922.0
GooF on F^2	1.061
Crystal size	0.070 x 0.030 x 0.020 mm ³
Theta range for data collection	4.784 to 66.368 °
Reflections collected/unique	26279/2174 [$R_{(int)} = 0.0673$]
Final R indices ($I > 2\sigma(I)$)	$R_1 = 0.0367$ $wR_2 = 0.0973$
Final R indices (all data)	$R_1 = 0.0478$ $wR_2 = 0.1033$

The framework is comprised of four-connecting copper carboxylate paddlewheel units, bridged by the dicarboxylate linkers, to create an infinite 2D framework. Coordinated water molecules occupy the apical coordination site on each of the copper centres and form hydrogen bonds ($\text{O}\cdots\text{O}$, 3.072(3) Å) to the coordinated carboxylate O atoms on the sheets above and below. All copper centres are crystallographically equivalent, as are all dicarboxylate anions. The ethyl group is disordered over two symmetry-related sites (Figure 4.3).

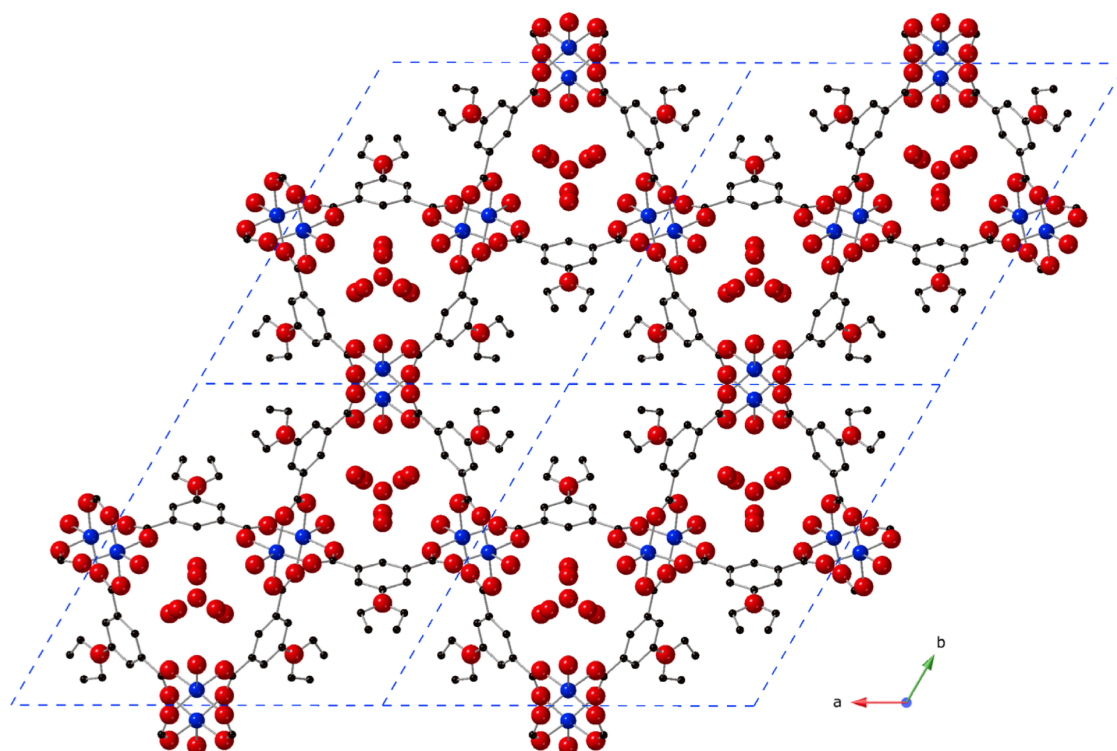


Figure 4.3. Structure of STAM-17-OEt viewed down the crystallographic c axis, showing copper paddlewheel dimers connected by bridging dicarboxylate linkers. The ethyl groups are disordered over two possible sites, each of which is 50% occupied. Key: blue: Cu; red: O; black: C. H atoms have been omitted for clarity.

The structure of STAM-17-OEt is related to those of other copper-based MOFs containing copper paddlewheel units and polycarboxylate bridging ligands. Examples of such MOFs include HKUST-1¹⁰ and STAM-1.²⁰ HKUST-1 may be used as a comparison for STAM-17-OEt in this study due to the similarities in their syntheses, chemistry and structures. Like STAM-17-OEt, HKUST-1 contains copper paddlewheel dimer units, though they are connected in three-dimensions rather than the two observed in STAM-17-OEt (Figure 4.4).

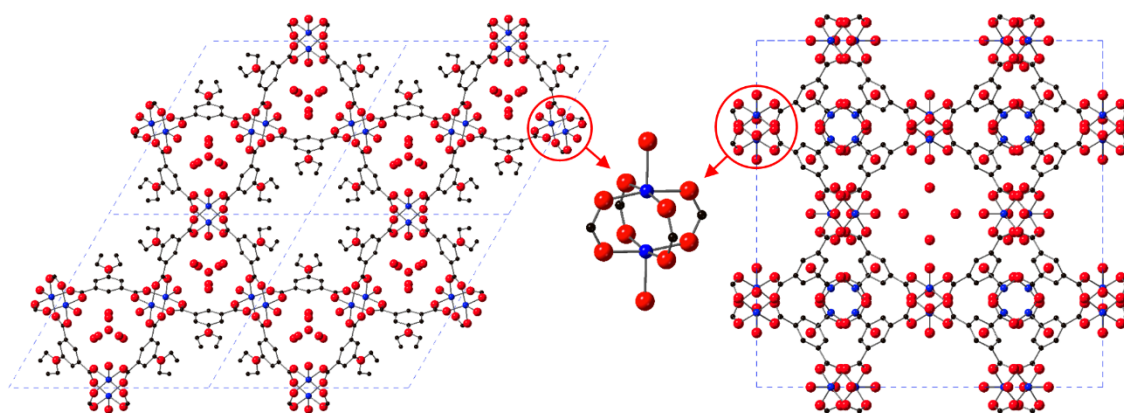


Figure 4.4. Structures of STAM-17-OEt (left) and HKUST-1 (right) viewed down their crystallographic c axes, highlighting the presence of the paddlewheel dimer in both structures.

Key: blue: Cu; red: O; black: C. H atoms have been omitted for clarity.

The Kagome lattice in STAM-17-OEt has two types of channel extending through the sheet, with either hexagonal or triangular cross-sections. Coordinated water molecules protrude into the triangular channels, which also contain disordered guest water molecules. The hexagonal channels contain the disordered ethyl groups, which contain no guest solvent molecules. Both types of channel extend perpendicular to the Kagome sheets through the

whole depth of the crystal and hydrogen bonds can form between coordinated water molecules and carboxylate oxygen atoms on adjacent copper paddlewheel units.

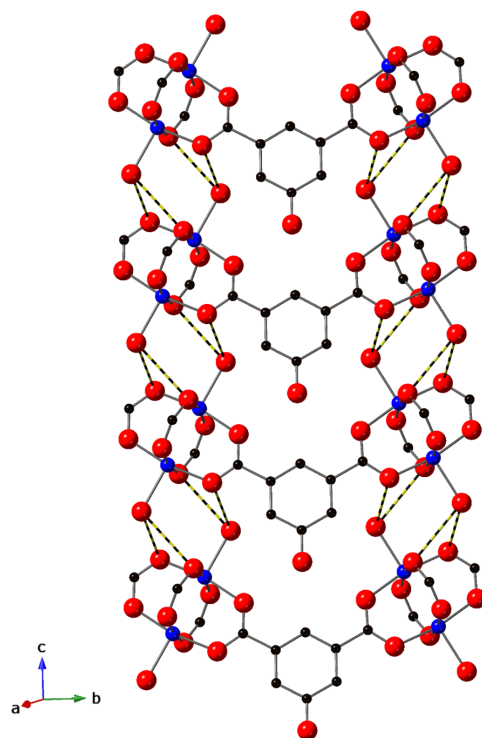


Figure 4.5. Arrangement of copper paddlewheel units in STAM-17-OEt. Key: blue: Cu; red: O; black: C. H atoms have been omitted for clarity. Hydrated hydrogen bonds are represented by black and yellow dashed bonds.

Crystallographic studies after desolvation of the same single crystal of STAM-17-OEt using a sealed gas cell showed that the crystal had undergone a single-crystal-to-single-crystal transition. The unit cell parameters change to $a = 33.028(3) \text{ \AA}$ and $c = 5.2047(6) \text{ \AA}$ and the dehydrated phase exists in space group $P31m$ (Figure 4.6). The final crystallographic parameters may be observed in Table 4.2.

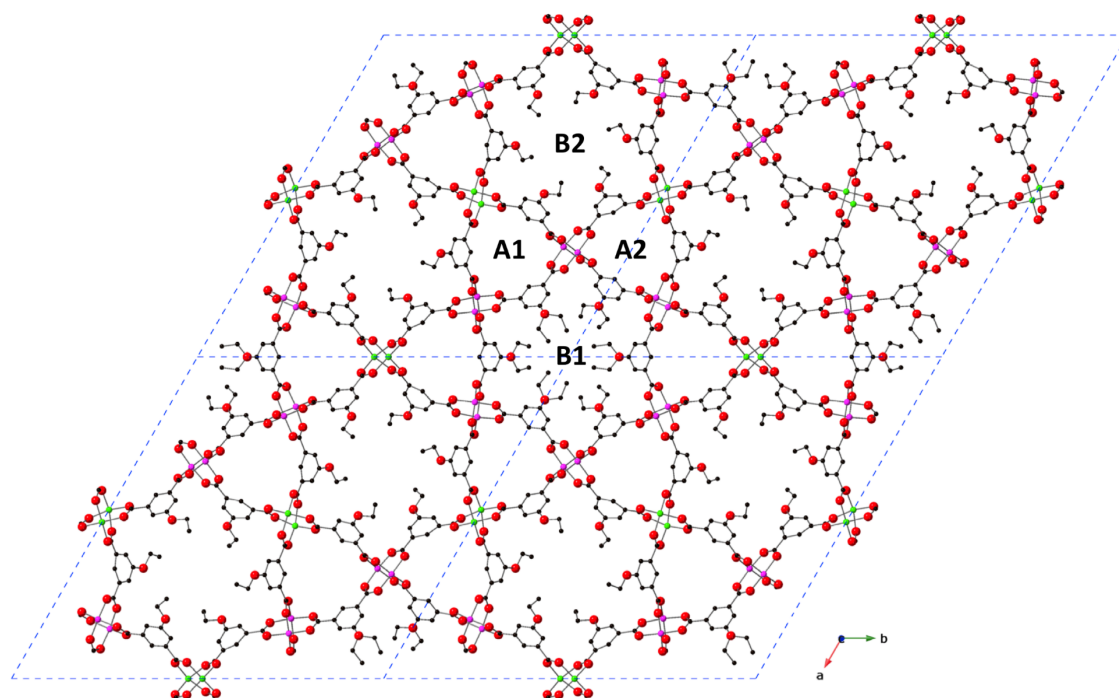


Figure 4.6. Dehydrated structure of STAM-17-OEt viewed down the crystallographic *c* axis, showing the four types of pore system present: two triangular hydrophilic (A) and two hexagonal hydrophobic (B) channels. Key: pink and green spheres represent Cu atoms in different local environments; red: O; black: C. H atoms have been omitted for clarity.

Table 4.2. Crystallographic data from the structure determination of dehydrated STAM-17-OEt (associated bond lengths and angles may be found in appendix tables 9.3 and 9.4 respectively).

Identification code	STAM_17_OEt_dehydrated_vac_300K
Empirical formula	C ₁₀ H ₈ CuO ₅
Formula weight	271.70 g mol ⁻¹
Temperature	300(2) K
Wavelength	Synchrotron (0.7749 Å)
Crystal system, space group	Trigonal, <i>P</i> 31 <i>m</i>
Unit cell dimensions	<i>a</i> = 33.028(3) Å
	<i>b</i> = 33.028(3) Å
	<i>c</i> = 5.2047(6) Å
Volume	4917.0(10) Å ³
Z	18
Calculated density	1.652 g cm ⁻³
Absorption coefficient	2.529 mm ⁻¹
<i>F</i>(000)	2466.0
GooF on <i>F</i>²	1.104
Crystal size	0.070 x 0.030 x 0.020 mm ³
Theta range for data collection	4.658 to 48.158 °
Reflections collected/unique	26548/4168 [R(int) = 0.0955]
Final R indices (<i>I</i> > 2σ(<i>I</i>))	R ₁ = 0.1515 wR ₂ = 0.3291
Final R indices (all data)	R ₁ = 0.1685 wR ₂ = 0.3410

Upon dehydration, both free and coordinated water molecules are removed from the structure. The framework is now composed of four crystallographically unique copper centres arranged into two distinct copper paddlewheels and four unique dicarboxylate ligands. In this dehydrated phase there are four crystallographically distinct types of channel

present: two triangular hydrophilic channels and two hexagonal hydrophobic channels, where one contains disordered ethyl groups and the other contains ordered ethyl groups (Figure 4.7).

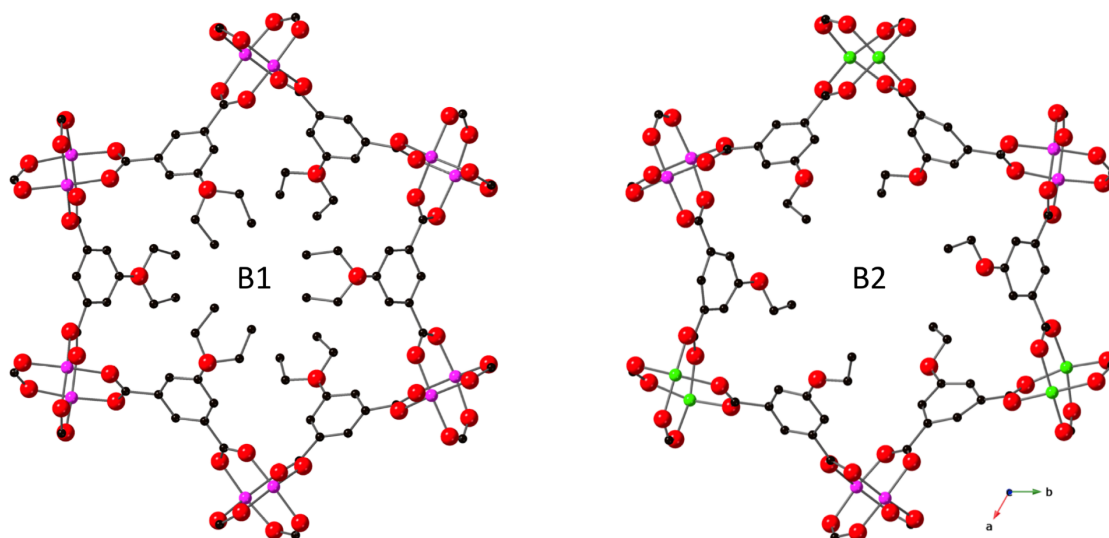


Figure 4.7. The two distinct hydrophobic pores in dehydrated STAM-17-OEt viewed down the crystallographic c axis, where the ethyl groups are disordered over two crystallographic sites (B1) and where they have been resolved on one crystallographic site (B2). Key: pink and green: Cu; red: O; black: C. H atoms have been omitted for clarity.

The Kagome sheets have deformed such that on half of the copper paddlewheels (pink spheres in Figure 4.8), the coordination sites that were previously occupied by coordinated water molecules (Cu-O distance = 2.150(2) Å) are now occupied by μ_2 -coordinated carboxylate O atoms (Cu-O, 2.24(2) Å or 2.19(3) Å) belonging to a paddlewheel unit in the sheet directly above or below. This change in coordination environment of the copper centres alters the dimensionality of the framework from 2D to 3D. The remaining half of

the paddlewheels (green spheres in Figure 4.8) are arranged such that the copper centres of one lie almost equidistant between the carboxylate O atoms on neighbouring paddlewheels with much longer Cu-O distances of 2.87(3) Å and 2.98(4) Å. This change in the coordination sphere of the copper centres, the hemilability, allows the weaker μ_2 -O-CO groups to bind at sites that were vacated by the water molecules, rather than leaving these sites vacant (Figure 4.8).

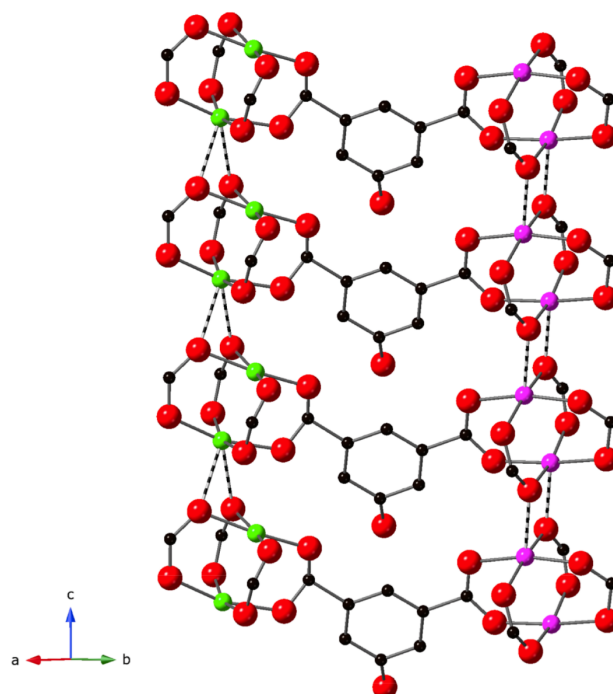


Figure 4.8. Arrangement of copper acetate units in dehydrated STAM-17-OEt. Key: pink and green: Cu; red: O; black: C. H atoms have been omitted for clarity.

Powder X-ray diffraction also indicates that the transition between the hydrated and dehydrated states occurs in the dehydration of bulk powders and not only in single crystals, where the crystallinity of the sample has been retained upon dehydration (Figure 4.9).

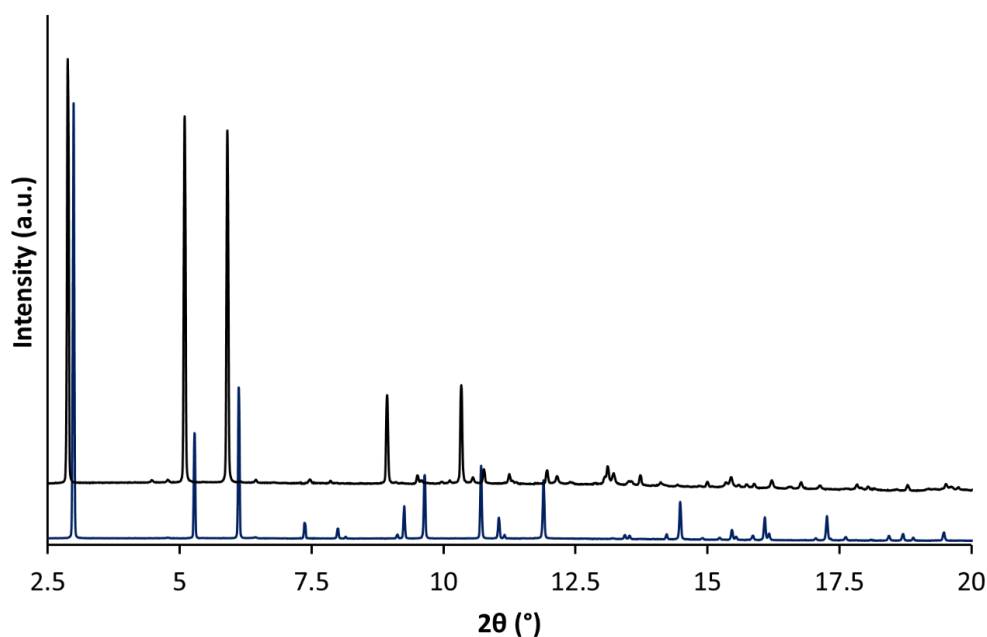


Figure 4.9. Comparison of high-resolution synchrotron powder X-ray ($\lambda = 0.826048 \text{ \AA}$) diffraction patterns of as-made STAM-17-OEt (blue line) and dehydrated STAM-17-OEt (black line), displayed from $2.5\text{-}20^\circ$ 2θ , indicating the change in the unit cell upon dehydration of the material.

On exposure to moisture the crystal of STAM-17-OEt reverts to the original as-made structure. In order to accomplish this, energy must be used to break the weak interactions and move the paddlewheels relative to each other. The energy released upon interaction of the adsorbed water molecules with the copper atoms in the framework is used to change the coordination and relative positions of the paddlewheel units and is not, therefore, available to break further bonds in the material (Figure 4.10).

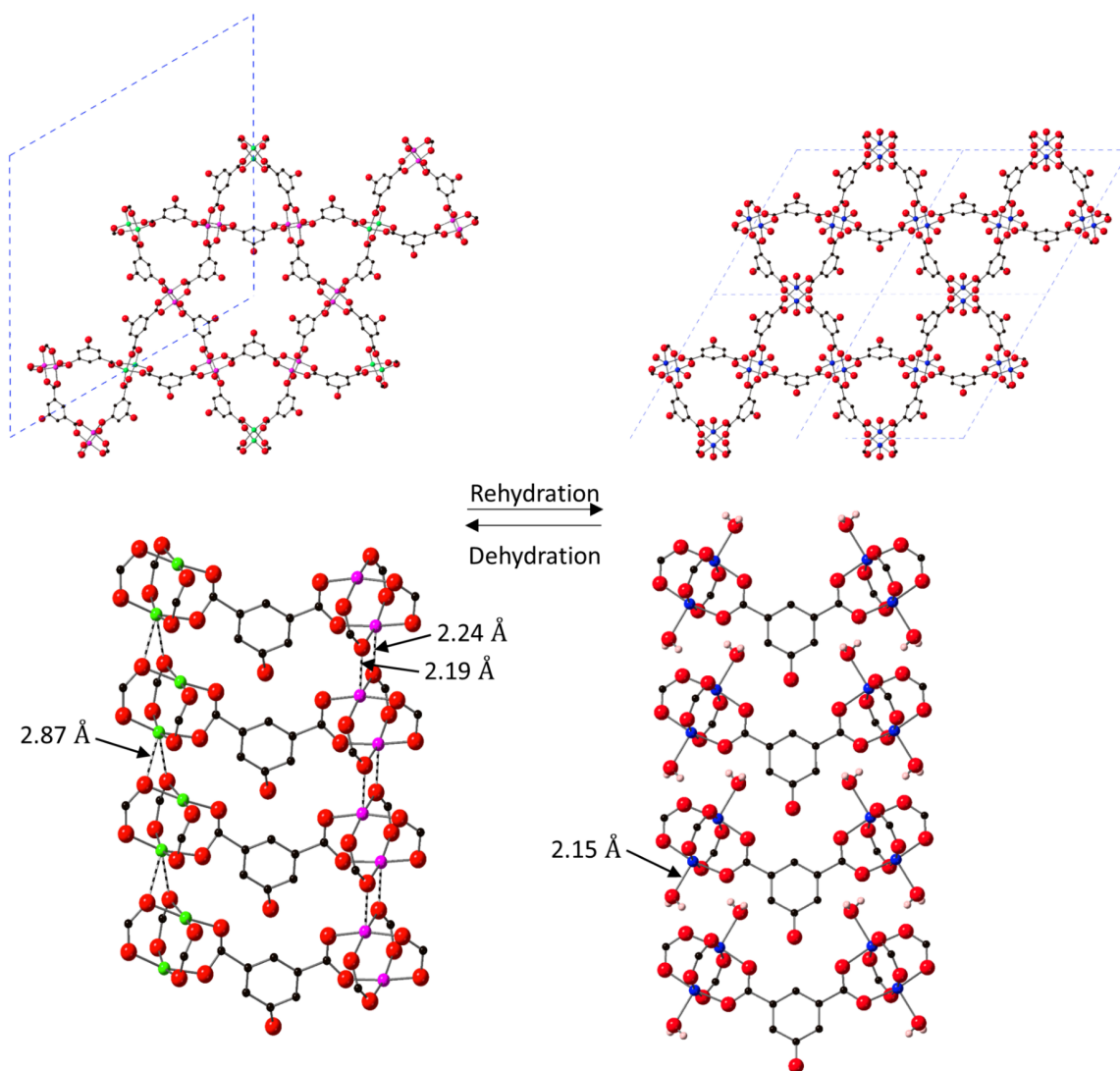


Figure 4.10. Structural change upon rehydration of dehydrated STAM-17-OEt. On the left-hand side of the diagram, the structure may be observed parallel and perpendicular to the crystallographic c axis in the top left and bottom left panels, respectively. The right-hand side of the figure shows the same views of the structures after rehydration, illustrating the change in the unit cell. The longer Cu...O interactions (indicated by dashed bonds) are broken and replaced by stronger Cu-OH₂ interactions. Key: blue, green or pink: Cu (in different local environments); red: O; black: C. H atoms of the aromatic and alkyl groups and C atoms of the alkyl chains have been omitted for clarity.

4.4.3 Bulk Activation of STAM-17-OEt

In order to conduct measurements using the dehydrated bulk powder of STAM-17-OEt, the material first required activation to remove residual solvent molecules. This was performed by heating samples inside glass ampoules to an experimentally determined temperature while under vacuum for 16 hours, before flame sealing the ampoules under an argon atmosphere. TGA was used to determine the temperature required for activation and the trace shows that residual water is lost from the structure at approximately 125 °C, with a plateau from approximately 125 °C to 325 °C (Figure 4.11). Bulk samples were therefore activated under vacuum at 150 °C.

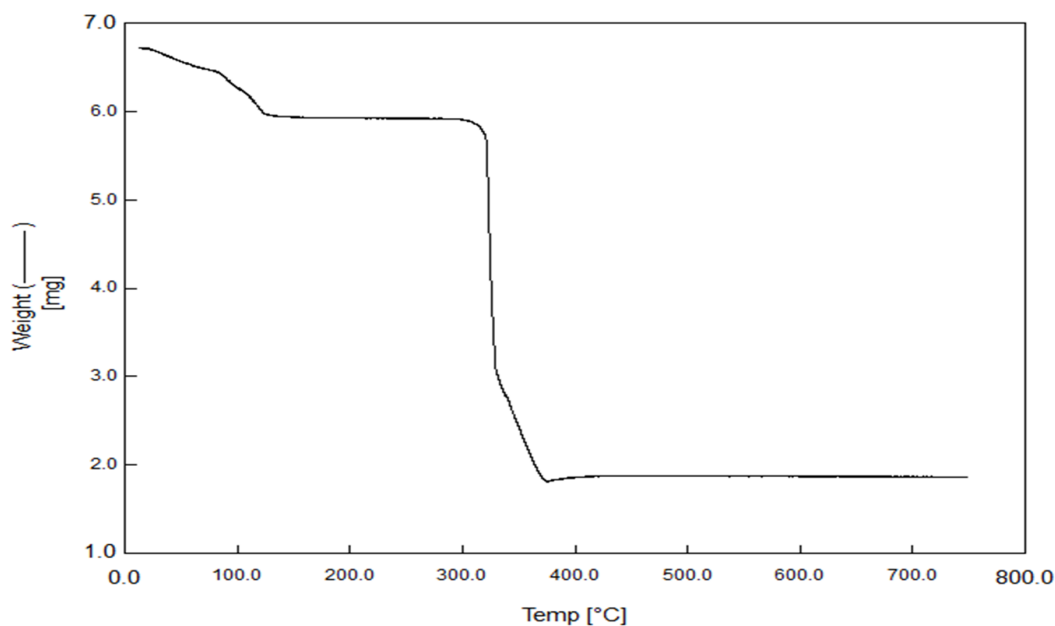


Figure 4.11. TGA trace of STAM-17-OEt, showing the loss of water from the structure at approximately 125 °C. The dehydrated structure is stable until approximately 325 °C.

4.4.4 Solid-State NMR Spectroscopy

Solid-state NMR was performed using Bruker Avance III solid-state spectrometers equipped with wide-bore 9.4 or 14.1 T superconducting magnets. Samples were packed into 1.9 mm zirconia rotors and rotated at the magic angle at rates of 37.5-60 kHz. Dehydrated samples were pre-activated at 423 K prior to measurement and all measurements were performed at 298 K.

4.4.4.1 Solid-State NMR of STAM-17-OEt

The change in the structure of STAM-17-OEt upon dehydration may be clearly observed in the ^{13}C solid-state NMR spectra. The paramagnetic nature of the copper ions in the material leads to a much wider shift range than typically observed for diamagnetic materials, but for the analogous copper paddlewheel MOFs: HKUST-1 and STAM-1, the shift range is well characterised and the resonances have been fully assigned.²¹ By analogy, and using a combination of magic angle spinning (MAS) and cross-polarization MAS experiments, the resonances for STAM-17-OEt may be assigned as shown in Figure 4.12. The resonances for C3 and C5 are overlapped at 298 K but can be separated at higher temperature (Figure 4.12 (c)) and the resonance for C1 (observed at ~ 830 ppm) is shown separately in Figure 4.13.

In the hydrated material, the signals from each of the carbon atoms of the linker are present as single resonances (including those for the disordered carbons of the ethyl group, C6 and C7, suggesting rapid exchange between the possible orientations rather than static disorder). However, upon dehydration there are significant changes to the local structure of STAM-17-OEt, and these are reflected in the ^{13}C NMR spectrum shown in Figure 4.12 (d). The single signal from this carbon atom in the hydrated material splits into four resolvable resonances for the dehydrated solid. These four resonances have an approximate intensity ratio of

1:1:1:3, which is entirely consistent with the six expected independent C2 carbons from the single-crystal X-ray diffraction structure. These changes in local structure are most pronounced for the carboxylate carbon, C2, as it is closest to the paddlewheel units. As one moves further away from the paddlewheel units the resonances are less and less affected by the structural changes. For example, the resonances for carbons C6 and C7 in the ethyl group are not visibly affected at all by the structural changes. The cross-polarization MAS spectra for STAM-17-OEt may be observed in Figure 4.14.

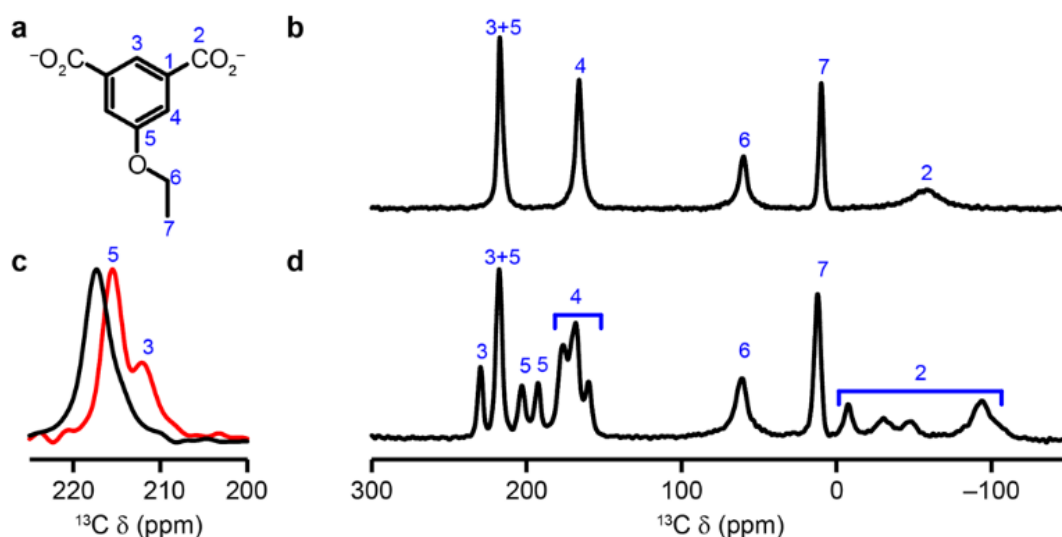


Figure 4.12. Solid-state ^{13}C NMR data for as-made and dehydrated STAM-17-OEt. (a) Numbering scheme for the chemically distinct C atoms in STAM-17-OEt. (b) ^{13}C (14.1 T, 37.5 kHz MAS, 298 K) NMR spectrum of as-made STAM-17-OEt. (c) Expansion of the C3+C5 resonance of as-made STAM-17-OEt at 298 K (black) and 338 K (red), where the two signals are resolved at the higher temperature. (d) ^{13}C (14.1 T, 40 kHz MAS, 298 K) NMR spectrum of dehydrated STAM-17-OEt.

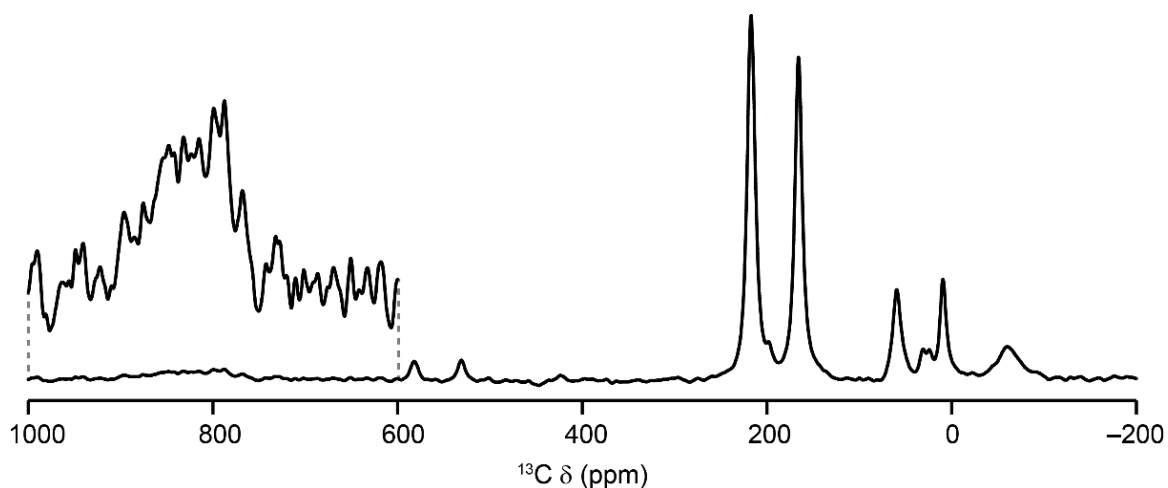


Figure 4.13. ^{13}C (14.1 T, 60 kHz MAS) NMR spectrum of STAM-17-OEt with the inset showing a vertical expansion of the region from 1000 to 600 ppm. The very broad resonance for C1 is observed at ~ 830 ppm.

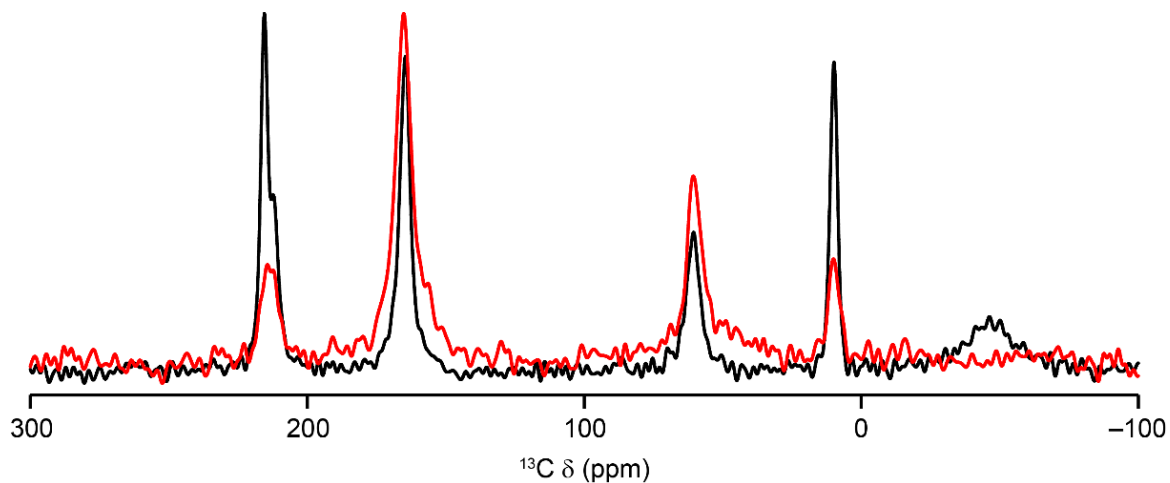


Figure 4.14. ^{13}C (9.4 T, 40 kHz MAS) NMR spectra of STAM-17-OEt recorded with direct excitation (black spectrum) and cross polarisation (CP) with a short spin lock duration of 0.1 ms (red spectrum) to show only ^{13}C with directly attached ^1H .

4.4.5 Porosity of STAM-17-OEt

Nitrogen BET analysis was performed on STAM-17-OEt samples at 77 K on a micromeritics ASAP 2020 Surface Area and Porosity Analyser and the BET surface areas were calculated using the Rouquerol method.²²

Samples were activated at either 298 K or 423 K overnight prior to measurement, to provide BET surface areas of $4.2 \pm 0.1 \text{ m}^2/\text{g}$ and $58.4 \pm 0.3 \text{ m}^2/\text{g}$ respectively. STAM-17-OEt displays Type I adsorption behaviour with a slight rise at high partial pressure, which is usually attributed to multilayer coverage on the surface of the pores. The combined Langmuir adsorption isotherms may be seen in Figure 4.15.

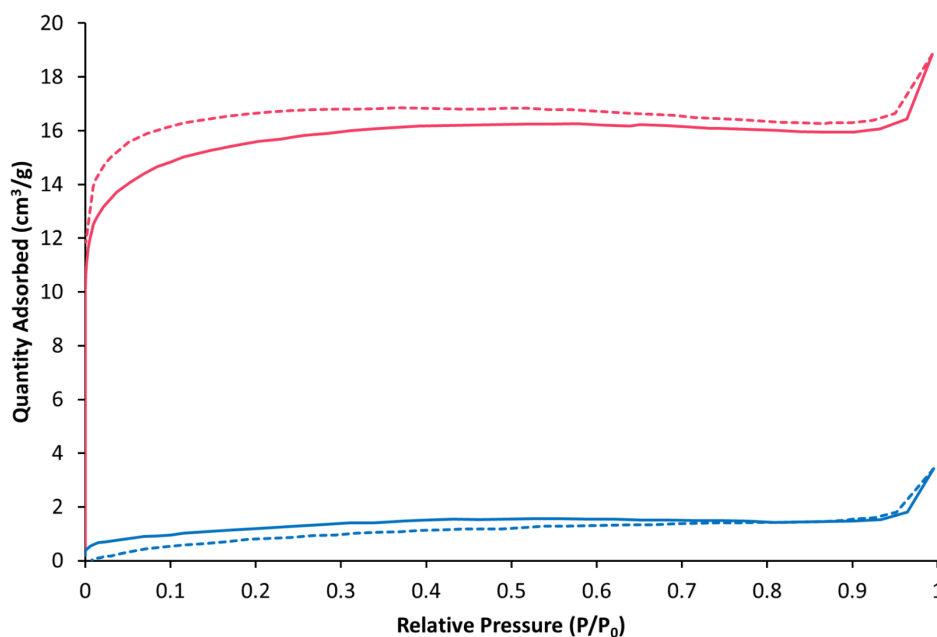


Figure 4.15. Nitrogen adsorption isotherms for STAM-17-OEt, where the pink line represents a sample which has been activated at 423 K prior to measurement and the blue line represents a sample that has been activated, though has not been heated. Solid lines represent adsorption and dashed lines represent desorption.

The low porosity in STAM-17-OEt is due to its switchable structure, where upon activation, the pores in STAM-17-OEt become constricted by the change in the coordination environment of the copper paddlewheels. This constriction consequently reduces the porosity in the material. The sample that was not heated prior to measurement was not as thoroughly degassed as the sample activated at 423 K, which consequently decreased the availability of the smallest pores in the material and lead to the very low surface area reported.

4.4.6 Water stability of STAM-17-OEt

Water stability is highly important area in metal-organic frameworks and is imperative in materials that shall be exposed to humid airstreams. Water stability in STAM-17-OEt was investigated using Dynamic Vapour Sorption (DVS) analysis and was analysed using infrared spectroscopy and powder X-ray diffraction.

4.4.6.1 Water adsorption of STAM-17-OEt

The water adsorption isotherm of activated STAM-17-OEt (Figure 4.16) shows the water uptake of the material with increasing levels of relative humidity (RH). The trace shows almost no hysteresis in the desorption branch, suggesting little to no capillary condensation. A gate opening effect is observed at low RH, which is due to structural flexibility caused by the initial transition from the activated to hydrated phase upon readsorption of water.

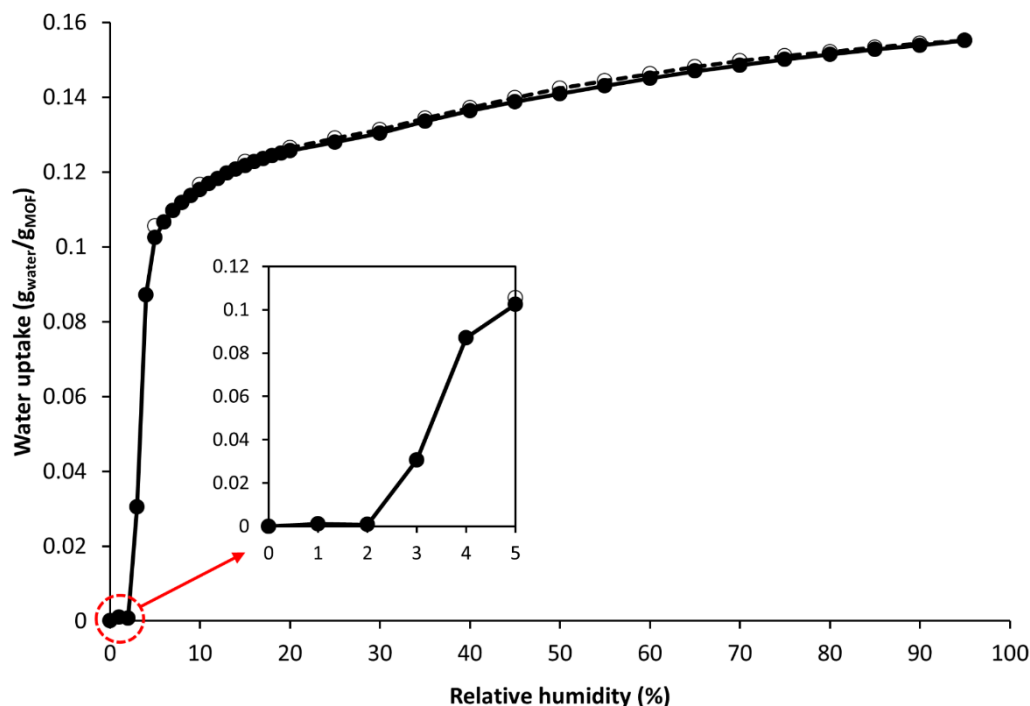


Figure 4.16. Water adsorption isotherm at 298 K for STAM-17-OEt, showing little to no hysteresis in the desorption branch. The solid line with closed circles represents the adsorption branch and the dashed line with open circles represents the desorption branch. A gate opening effect may be observed at low RH (inset).

The main question to be answered in this section is whether STAM-17-OEt actually shows improved stability to water when compared to HKUST-1.

The poor water stability of HKUST-1 is well known and the molecular mechanism behind the breakdown process has been recently elucidated.^{11,23} Upon exposure to moisture, the water molecules bind to the open metal sites in the framework and upon sustained exposure, water molecules accumulate in large quantities within the pores. The energy associated with these processes make hydrolysis of the Cu-O bond within the paddlewheel favourable, which leads to partial decomposition of the copper paddlewheels. Further water molecules then

bind to the Cu sites made available by hydrolysis and the process continues until the framework collapses.

Figure 4.17 shows the evolution of the mass of dehydrated HKUST-1 and STAM-17-OEt structures on exposure to a humid environment at 298 K. STAM-17-OEt shows an initial rapid increase in mass as the dehydrated material adsorbs water. There is then no further change over the remainder of the experiment (up to 5 days). HKUST-1 conversely shows a similar immediate mass gain as the water interacts with the open metal sites, but within the first hours the material begins to gain further mass as water molecules start to react with other Cu sites that have been made available through degradation. This process continues until a maximum mass is reached at just under 20 h.

To accommodate increased water uptake during this period, water interacts with the ‘extra’ Cu sites that were not available in the initial dehydrated material. As explained previously, these are produced as water interacts with the open metal sites, releasing energy, which is used to break metal-carboxylate oxygen bonds in the structure. This opens up new metal sites for further coordination to water,^{11,23} which leads to the extra mass gain. As more of the bonds are successively broken there comes a time when there are not enough such bonds to hold the MOF intact, and so HKUST-1 begins to collapse, releasing water during the process. Under the conditions of our experiment this leads to the loss of mass between 20 and 40 h, after which time the mass stabilises as the entire HKUST-1 structure has been lost. In contrast to HKUST-1, after the initial adsorption of water (with its associated mass gain), the mass of STAM-17-OEt remains unchanged throughout the remainder of the experiment.

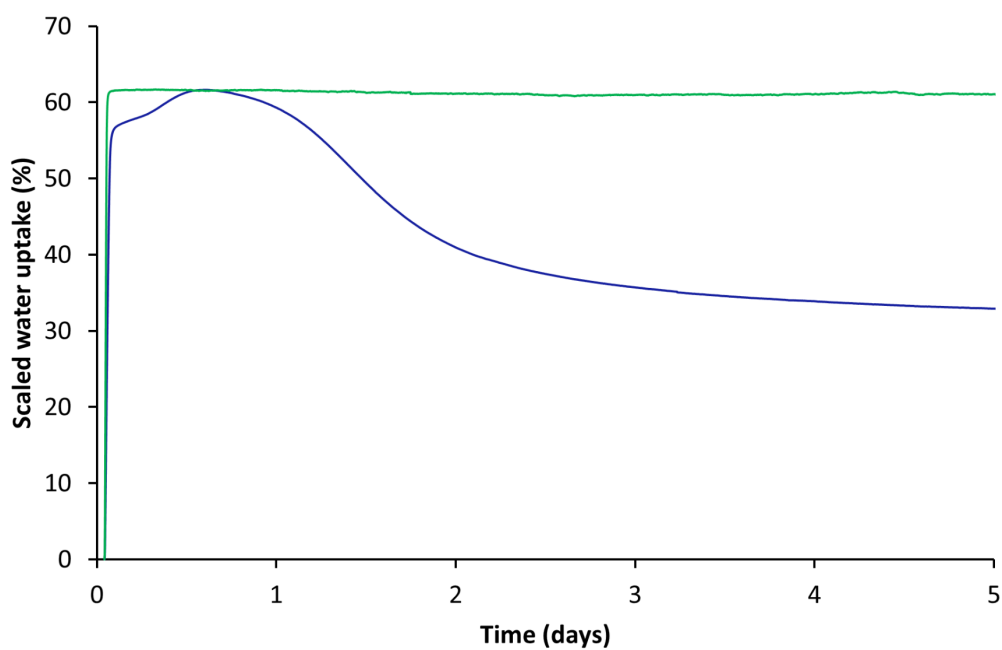


Figure 4.17. Overlaid traces of the evolution of the total mass of samples of activated STAM-17-OEt (green) and HKUST-1 (blue) on exposure to an atmosphere of 90% RH over a period of five days.

As demonstrated by the infrared spectra, HKUST-1 undergoes significant change on exposure to a humid atmosphere (Figure 4.18 (a)), while the spectrum of STAM-17-OEt (Figure 4.18 (b)) remains unchanged.

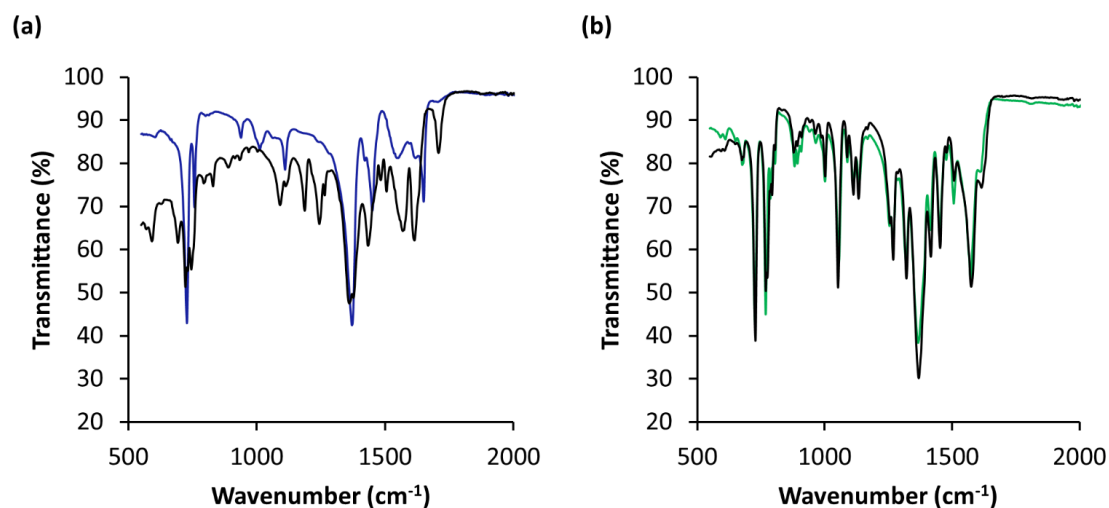


Figure 4.18. Infrared spectra for HKUST-1 (a) and STAM-17-OEt (b). In each panel, the coloured trace shows the original material and the black trace after exposure to 90% RH for five days. The spectrum for HKUST-1 changes significantly on exposure to water while that of STAM-17-OEt is unchanged.

4.4.6.2 Water cycling

Cycling of the relative humidity between 0 and 90% at 298 K (16 h for each cycle for a total of 120 h) further illustrates the significant improvement in stability of STAM-17-OEt compared to HKUST-1. The maximum water uptake capacity of HKUST-1 (Figure 4.19) decreases with every cycle, while that of the STAM-17-OEt sample remains constant throughout the experiment (Figure 4.20). Such testing simulates “real world” conditions experienced in extreme environments that a material must withstand to be viable in an industrial or military capacity.

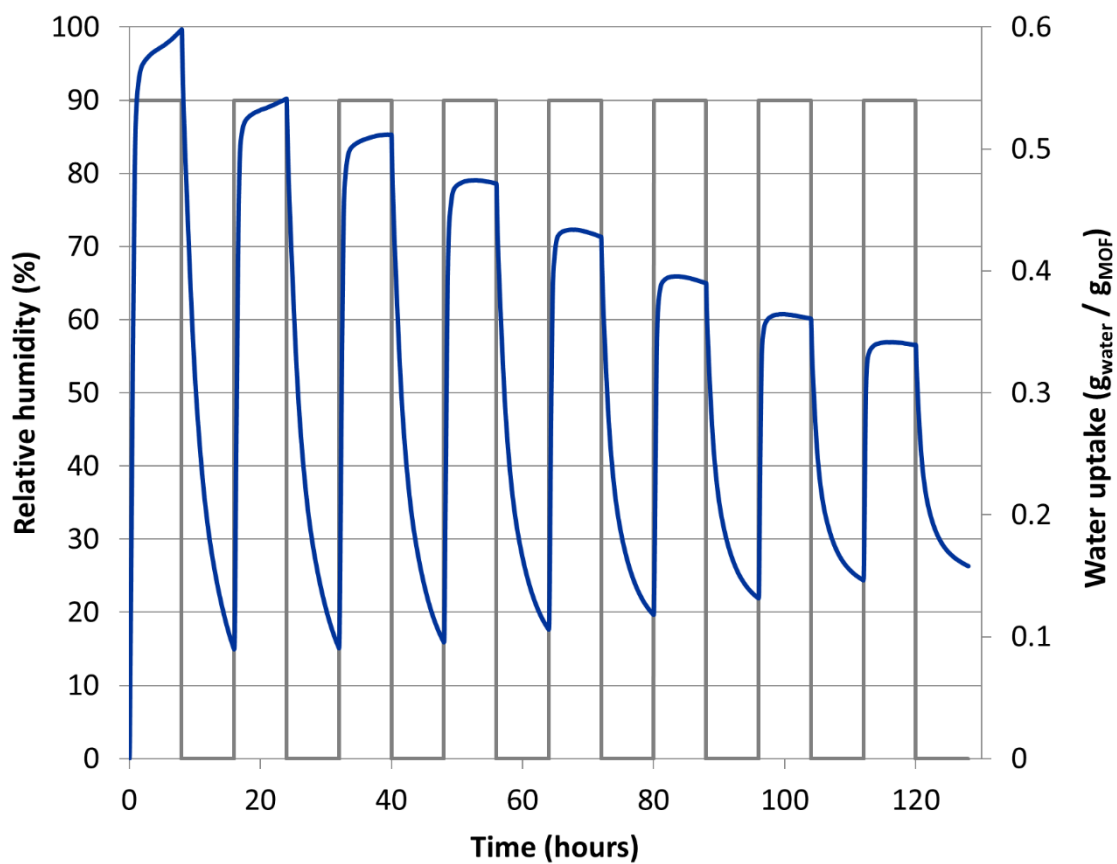


Figure 4.19. Vapour water stability at 298 K for HKUST-1, demonstrated by the change in the sample's water uptake through 8 water adsorption/desorption cycle measurements (blue trace) to 90% relative humidity (grey trace). The chart shows that after the initial water uptake, the sorption capacity in HKUST-1 decreases throughout the experiment, beginning with the first cycle.

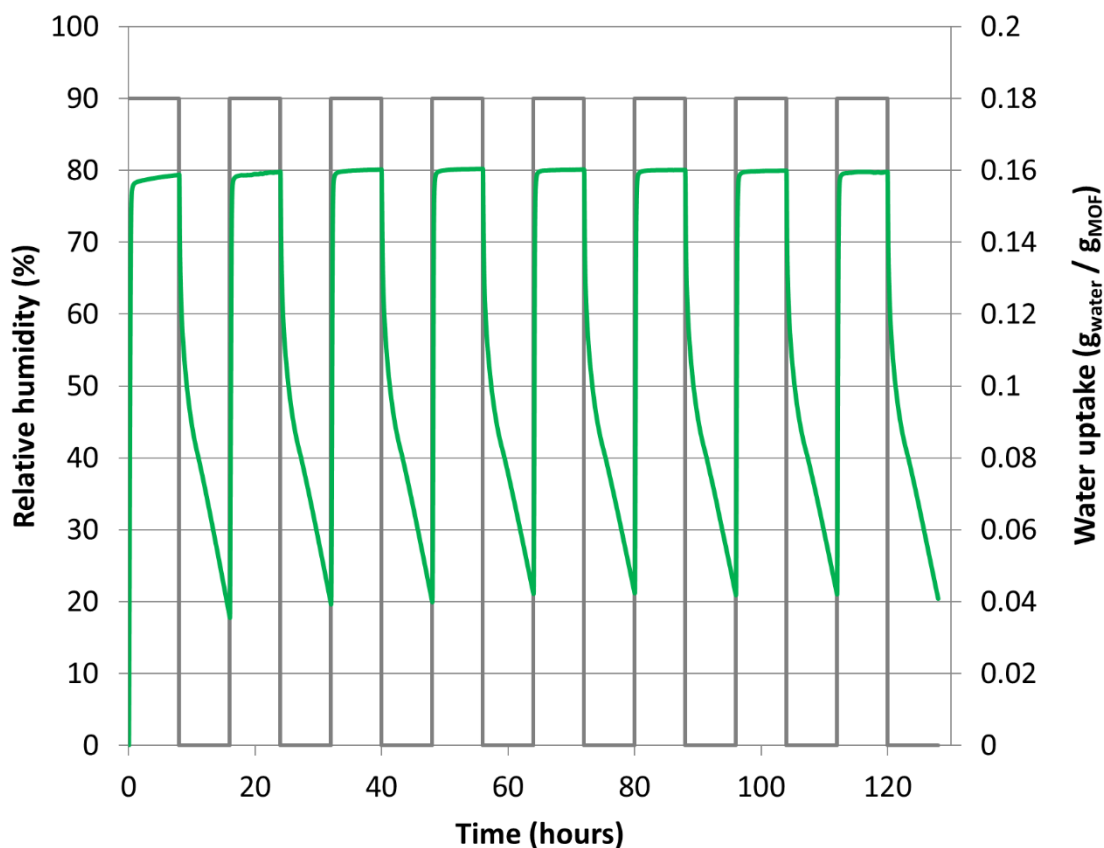


Figure 4.20. Vapour water stability at 298 K for STAM-17-OEt, demonstrated by the change in the sample's water uptake through 8 water adsorption/desorption cycle measurements (green trace) to 90% relative humidity (grey trace). The chart shows that after the initial water uptake, the sorption capacity in STAM-17-OEt remains constant throughout the experiment.

Powder X-ray diffraction analysis of the samples recovered from the experiments show that, once again, the structural integrity in HKUST-1 is lost, while STAM-17-OEt retains its structure and crystallinity (Figure 4.21).

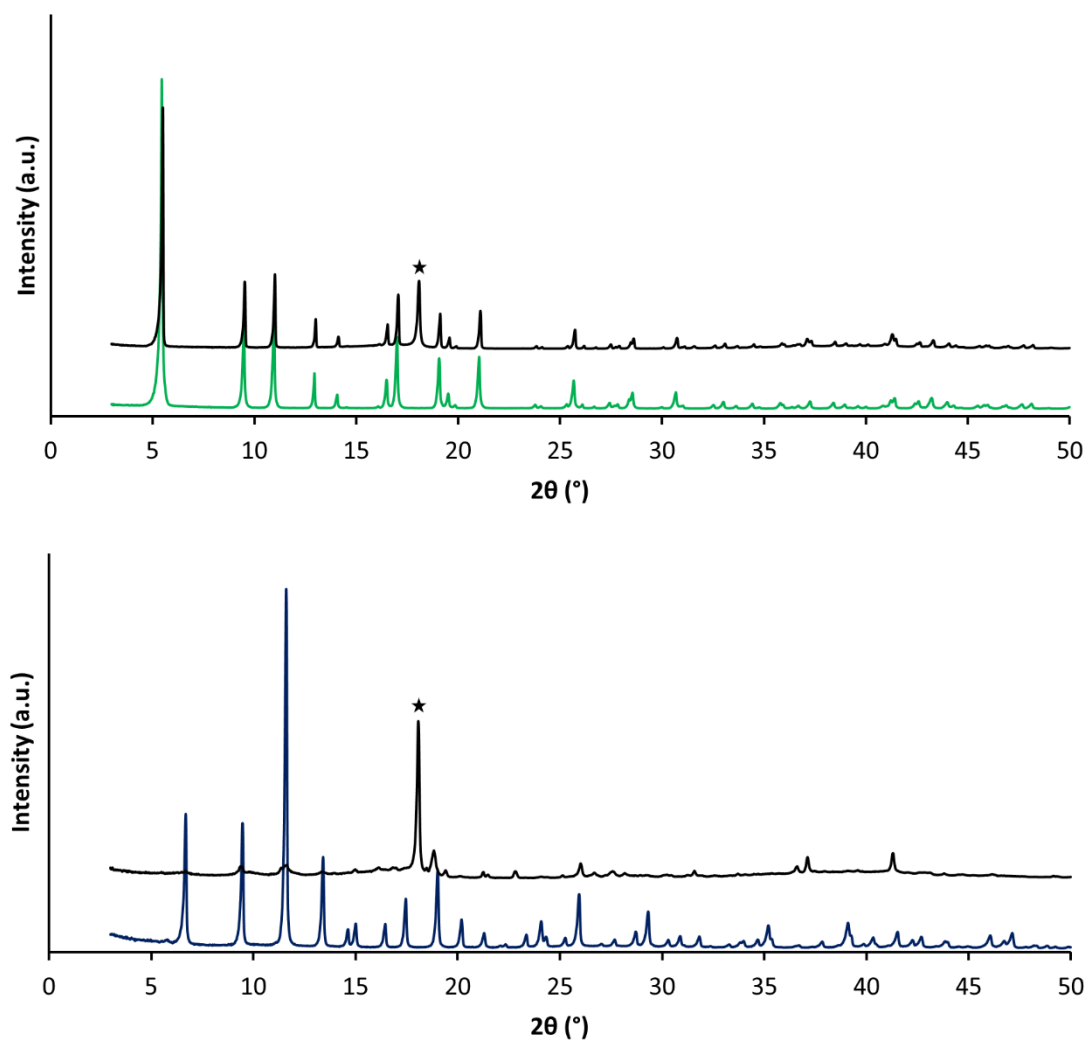


Figure 4.21. Powder X-ray diffraction patterns of as-made STAM-17-OEt (green line) and HKUST-1 (blue line), plus STAM-17-OEt and HKUST-1 after exposure to repeated cycling at 90% RH (black lines). The peak marked with a star in each case is a Teflon peak from the insert used during the diffraction experiment. The retention of structure and crystallinity in STAM-17-OEt may be observed, while HKUST-1 has decomposed.

A longer-term experiment where STAM-17-OEt was left in contact with water for one year at room temperature showed no degradation in the crystallinity of the material (Figure 4.22).

Given that HKUST-1 loses its crystallinity in less than two days under comparable conditions, it is clear that STAM-17-OEt has significantly enhanced hydrolytic stability compared to HKUST-1.

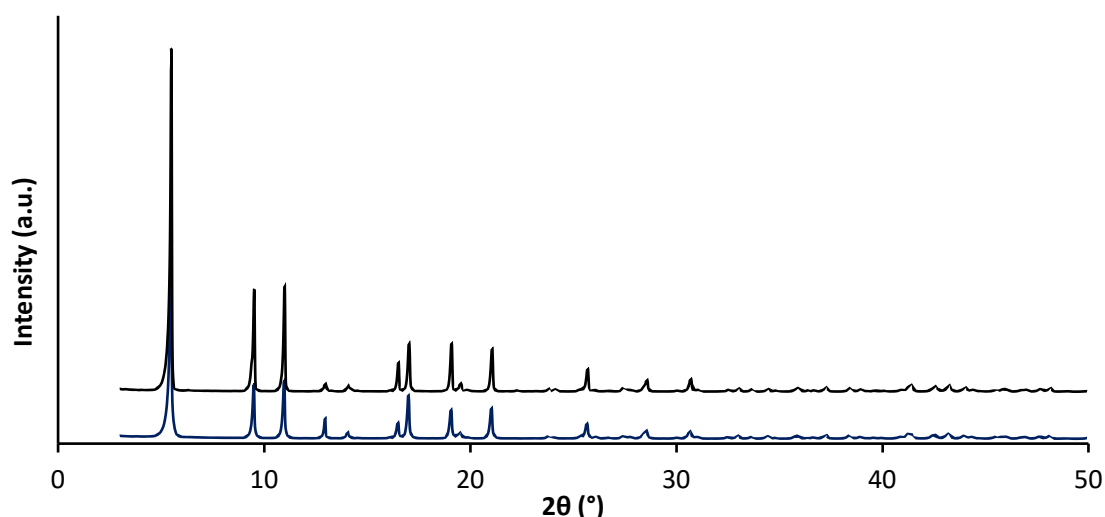


Figure 4.22. Powder X-ray diffraction pattern of as-made STAM-17-OEt (blue line) and STAM-17-OEt after submersion in water for 1 year (black line). The overall retention of structure and crystallinity in the sample may be seen, with very little change observed between the patterns after such prolonged water-exposure.

4.4.7 EPR spectroscopy

EPR measurements were performed on a Bruker EMX micro spectrometer, working at a frequency of approximately 9.5 GHz (X-band), with a magnetic-field modulation frequency set at 100 kHz. Samples were placed into a Clear Fused-Quartz EPR tube, which was closed with a stopper and a layer of Parafilm. The spectra were acquired by inserting the EPR tube containing the sample inside a Dewar flask. For measurements conducted at 77 K, the Dewar flask was filled with liquid nitrogen. For measurements conducted at 77 K, the Dewar flask

was filled with liquid nitrogen. Samples referred to as ‘dehydrated’ were pre-activated at 423 K prior to measurement and samples exposed to 100% relative humidity were kept in humidity chambers for the desired period prior to testing. As the tubes were not evacuated or flame sealed, there was always a column of air present in the EPR tube, though they were determined to be sufficiently protected from the external environment for testing purposes.

4.4.7.1 EPR spectroscopy of STAM-17-OEt

The EPR spectra of as-made and dehydrated STAM-17-OEt samples recorded at $T=300$ K and 77 K respectively may be observed in Figure 4.23.

In the spectra recorded at 300 K (Figure 4.23 (a)), the dehydrated sample (black line) shows a similar line shape with respect to that of activated HKUST-1 though is wider by approximately 30 mT.^{11,24,25} For the as-made sample (green line), three components are observed: one dominant signal centred at 320 mT, and two other less intense ‘shoulder’ signals at approximately 50 mT and 480 mT. The presence of the two smaller signals has been previously observed in the EPR spectrum of as-made STAM-1.²³ Differences in the intensity of the as-made and dehydrated sample are also observed, though this has been observed in previous studies involving HKUST-1, where activated samples were compared with those exposed to air for a short time.¹¹

In the spectra recorded at 77 K (Figure 4.23 (b)), the spectra of as-made and dehydrated samples show similar components. The signals at approximately 50 mT, 480 mT and 600 mT are due to a triplet centre arising from the exchange coupling between of two spins $S=1/2$ from Cu^{2+} ions within the same paddle-wheels.²⁵ Another small signal may be observed at approximately 330 mT, which can be assigned to Cu^{2+} monomers that are defects (copper ions uncoordinated with the network) formed during the material synthesis.^{11,24-26}

The EPR spectra in STAM-1²⁶ and HKUST-1 have similar lineshapes to STAM-17-

OEt,^{11,20,21} though STAM-17-OEt has lower amplitudes. The differences between the components of the triplet centres may be related to the different paddlewheel structures in the as-made and dehydrated samples. The interactions between neighbouring paddlewheels in the as-made sample are more ordered than in the dehydrated sample and this increase in structural order is responsible for the narrowing of the triplet centre resonances in the as-made sample with respect to the dehydrated one.

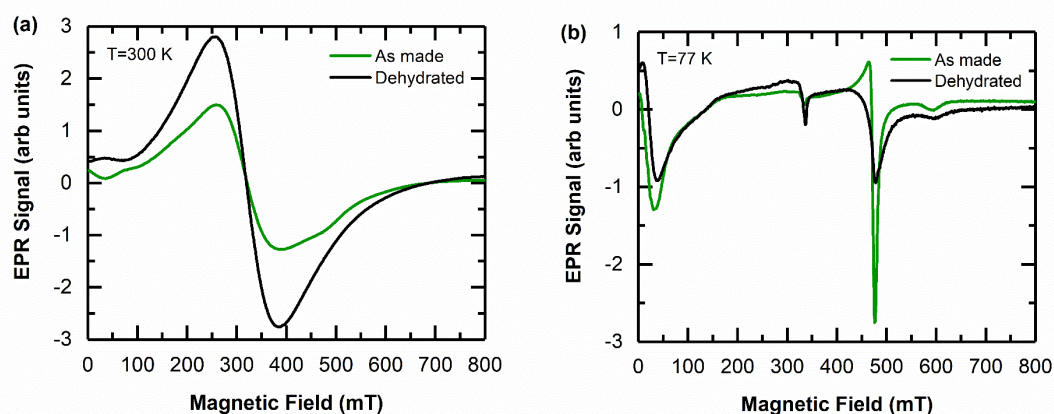


Figure 4.23. EPR spectra of as-made and dehydrated STAM-17-OEt recorded at (a) 300 K and (b) 77 K.

The EPR spectra of dehydrated STAM-17-OEt samples exposed to 100% RH for between 1.5 hours and 60 days and recorded at $T=300$ K and 77 K respectively may be observed in Figure 4.24.

In the spectra obtained at 300 K (Figure 4.24 (a)), the intensity of the signal decreases during the first 6 hours and the line shape of the spectrum is very similar to that of as made STAM-17-OEt. For exposure times longer than 6 hours, no other significant change is observed,

where the intensity and line shape of the resonance remain almost unchanged until the end of observation.

For the spectra acquired at 77 K (Figure 4.24 (b)), the signals observed at approximately 50 mT, 480 mT and 600 mT (related to triplet centres) are similar to those obtained for dehydrated STAM-17-OEt, while a more intense peak than those seen previous STAM-17-OEt samples may be observed at 350 mT. This result indicates a larger quantity of synthetic defects (monomeric copper uncoordinated with the network).

After a few hours of humidity exposure, the transition from activated to hydrated STAM-17-OEt has occurred, with a reduction in the peak width at 480 mT. The change in peak width may be attributed to the different paddlewheel structures in the dehydrated and as-made samples. For exposure times longer than 6 hours, a small reduction in the intensity of the signal of the triplet centres and some readjustments of the line shape related to copper-related defects within the material are observed. After two months of exposure to 100% RH, STAM-17-OEt shows no traces of hydrolysis, further highlighting the hydrolytic stability of the material.

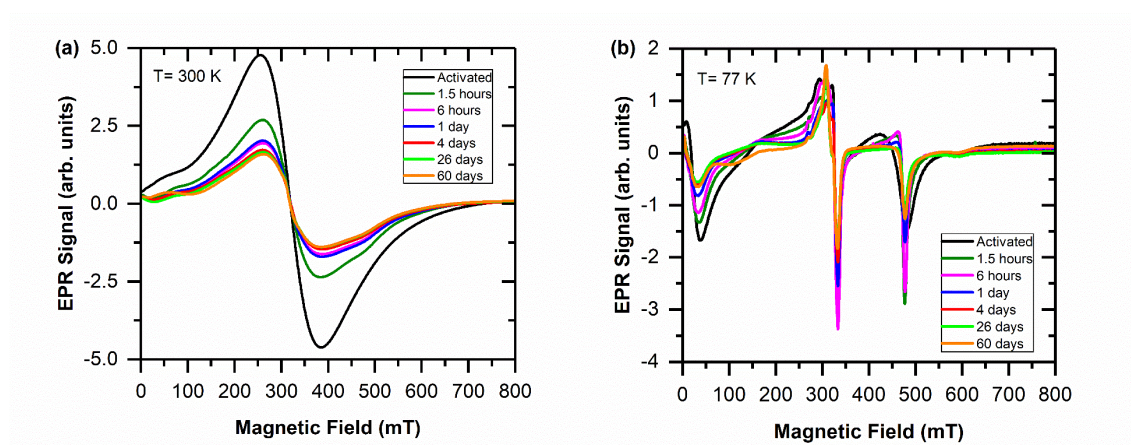


Figure 4.24. EPR spectra of activated STAM-17-OEt exposed to 100% RH for between 1.5 hours and 60 days, recorded at (a) 300 K and (b) 77 K.

4.4.8 Ammonia Adsorption

Ammonia micro-breakthrough testing was performed using a micro-breakthrough apparatus. The set-up allows testing of MOF materials against known concentrations of gases under either dry or humid (relative humidity = 80%) conditions. Samples of ca. 20 mg were packed between two cotton wool plugs in a glass tube with an internal diameter of 4 mm. Ammonia gas at a concentration of 500 ppm was passed through the sample at a flow rate of 30 ml min^{-1} and the challenge gas output concentration was monitored using a photoionization detector (Phocheck Tiger). All experiments were performed at 298 K.

4.4.8.1 Ammonia Adsorption in STAM-17-OEt

Pre-activated STAM-17-OEt and HKUST-1 samples were exposed to humid air for a certain period of time, before being exposed to ammonia gas. The ammonia micro-breakthrough curves for STAM-17-OEt and HKUST-1 samples may be seen in Figure 4.25.

STAM-17-OEt exposed to a stream of dry ammonia has a lower breakthrough time than HKUST-1 (Table 4.3), due mainly to the greater number of open metal sites available for ammonia binding in HKUST-1 and partially due to the inaccessibility of the hydrophilic pore in STAM-17-OEt in a dry airstream. When humidity is introduced to the samples for between 20 minutes and approximately 16 hours prior to ammonia exposure, the HKUST-1 again outperforms STAM-17-OEt, though this is due to the continual exposure of open metal sites as the framework begins to collapse. After long term exposure, HKUST-1 begins to lose structural integrity and the hydrophilic pore of STAM-17-OEt becomes less constrained and more accessible to ammonia, bringing STAM-17-OEt to a comparable level as HKUST-1.

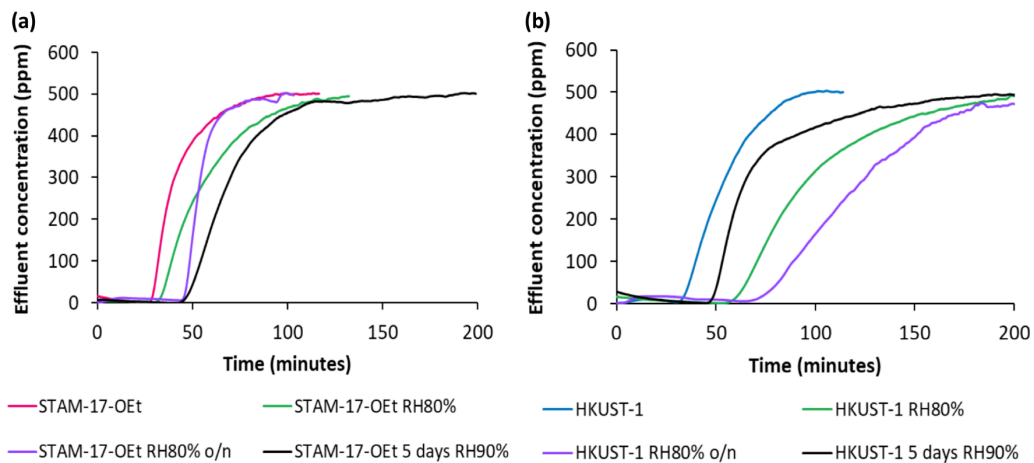


Figure 4.25. Ammonia micro-breakthrough curves for (a) STAM-17-OEt and (b) HKUST-1 in dry ammonia, an ammonia gas stream at 80% RH after pre-exposure for 20 minutes, an ammonia gas stream at 80% RH after pre-exposure overnight and an ammonia gas stream at 80% RH after pre-exposure to 90% RH for 5 days.

Table 4.3. Summary of ammonia breakthrough times recorded for STAM-17-OEt and HKUST-1.

Conditions:	STAM-17-OEt breakthrough time (minutes):	HKUST-1 breakthrough time (minutes):
Dry	27	31
80% RH 20 min	32	57
80% RH overnight	45	67
90% RH 5 days	46	46

This cooperative ammonia/water adsorption has been noticed previously,²⁷ and Figure 4.26 shows the breakthrough time to reach 10% of influent concentration (i.e. 50 ppm) for ammonia on STAM-17-OEt. This series of snapshots shows that on samples that have only

been treated for a short time with moisture, ammonia adsorption capacity on HKUST-1 increases in the same way as for the water experiments before eventually falling back to levels close to the original capacity of HKUST-1. The ammonia capacity of STAM-17-OEt also increases slightly over the course of the experiments but a maximum has not been reached even after five days exposure to 90% humidity, indicating improved performance with exposure to humidity.

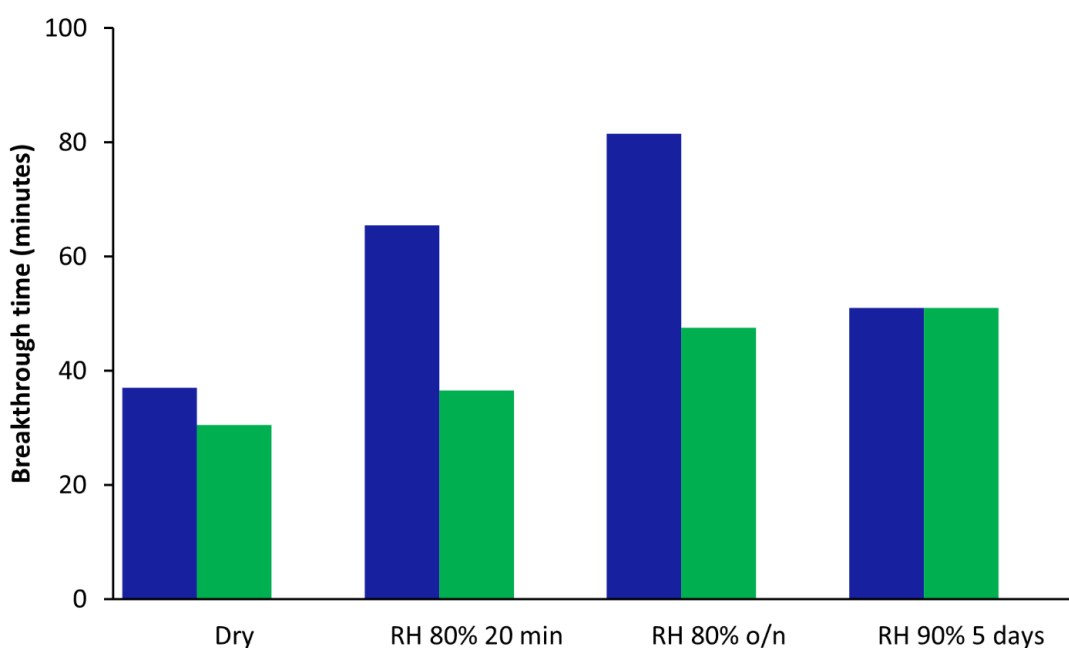


Figure 4.26. Breakthrough time to reach 10% of the influent concentration for ammonia on HKUST-1 (blue) and STAM-17-OEt (green). RH, relative humidity; o/n, overnight.

Infrared spectroscopy (Figure 4.27) again shows very little difference between as-synthesised STAM-17-OEt and material that has been in contact with ammonia. This is in contrast to HKUST-1, where a significant difference may be observed in the spectra before and after exposure to ammonia.

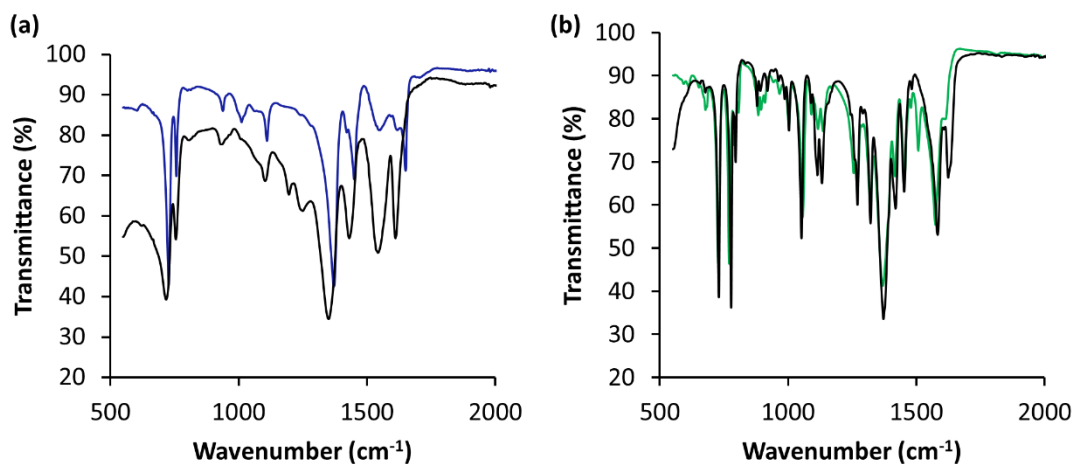


Figure 4.27. Infrared spectra for HKUST-1 (a) and STAM-17-OEt (b) after exposure to ammonia. In each spectrum, the coloured trace shows the original material and the black trace shows the material after exposure to ammonia.

A second set of micro-breakthrough measurements were recorded to further investigate the effect of long-term humidity exposure on the ammonia uptake in both STAM-17-OEt and HKUST-1 (Figure 4.28). In this case, the ammonia uptake of each material was recorded rather than the breakthrough time. Pre-activated samples were exposed to a stream of dry ammonia at 455 ppm, or were pre-exposed to 80% relative humidity for increasing time periods prior to ammonia testing. As in the previous tests, the gradual collapse of HKUST-1 with long term humidity exposure leads to lower quantities of ammonia being adsorbed, where after two weeks' pre-exposure, the uptake of HKUST-1 falls below the value observed in the initial dry test (Table 4.4). The quantity of ammonia adsorbed by STAM-17-OEt also exceeds that of HKUST-1 after 2 weeks' exposure, though this may be partially attributed to experimental errors, due to the small differences between values. The overall uptake of STAM-17-OEt however remains relatively constant throughout testing, again demonstrating the increased hydrolytic stability in the material.

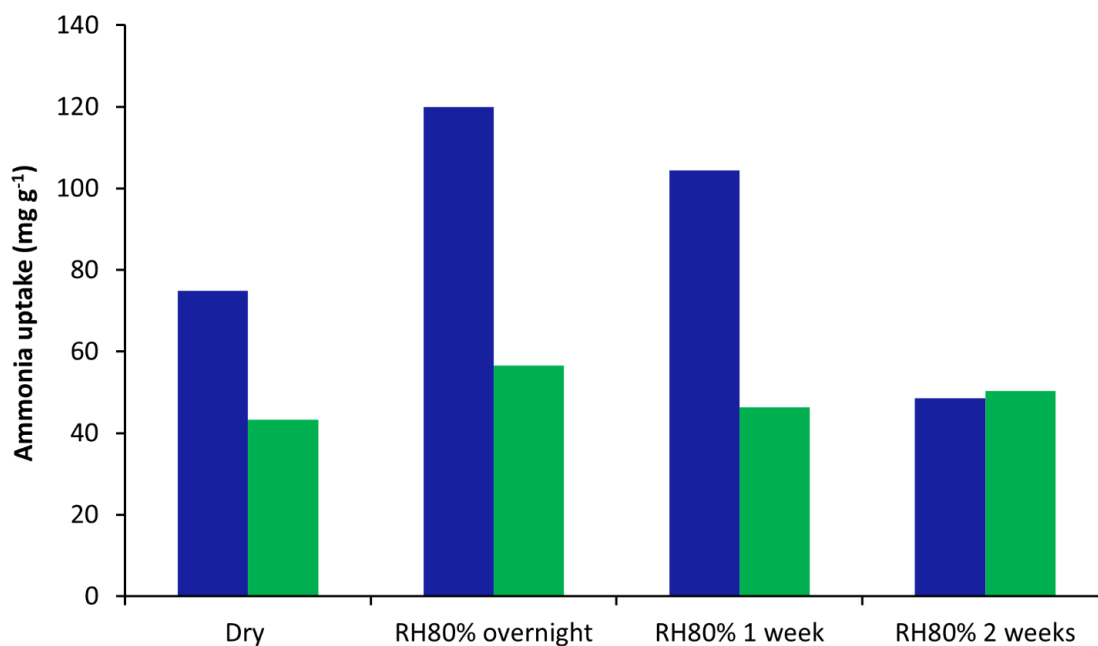


Figure 4.28. Ammonia uptake of HKUST-1 (blue) and STAM-17-OEt (green) after exposure to dry ammonia and pre-exposure to RH 80% for up to two weeks. RH, relative humidity.

Table 4.4. Summary of ammonia uptake values recorded for STAM-17-OEt and HKUST-1.

Conditions:	STAM-17-OEt Ammonia uptake (mg g ⁻¹):	HKUST-1 Ammonia uptake (mg g ⁻¹):
Dry	43.3	74.9
80% RH overnight	56.6	120.0
80% RH 1 week	46.3	104.4
90% RH 2 weeks	50.3	48.5

4.4.9 “Crumple-zone” mechanism

The key question overall is why the paddlewheel units in HKUST-1 are degraded upon prolonged exposure to humidity, but the same units in STAM-17-OEt are not?

The ‘crumple zone’ mechanism described in Figure 4.29 for water adsorption on STAM-17-OEt effectively directs the energy produced away from the critical bonding that makes up the paddlewheel unit (Figure 4.29 (a)), in exactly the same way that a crumple zone in a car directs energy from a collision away from the passengers in a road traffic accident. There is no such mechanism available in HKUST-1 (see section 4.4.6.1), and any energy released on adsorption of water on the open metal sites can be used to break a metal-oxygen bond in the paddlewheel, which then potentially opens up new metal sites for water adsorption (Figure 4.29 (b)). Initially, this can lead to an apparent increase in adsorption capacity, as previously seen in Figure 4.26. However, as this mechanism continues, the structural integrity of the paddlewheel is compromised and the structure will fall apart.

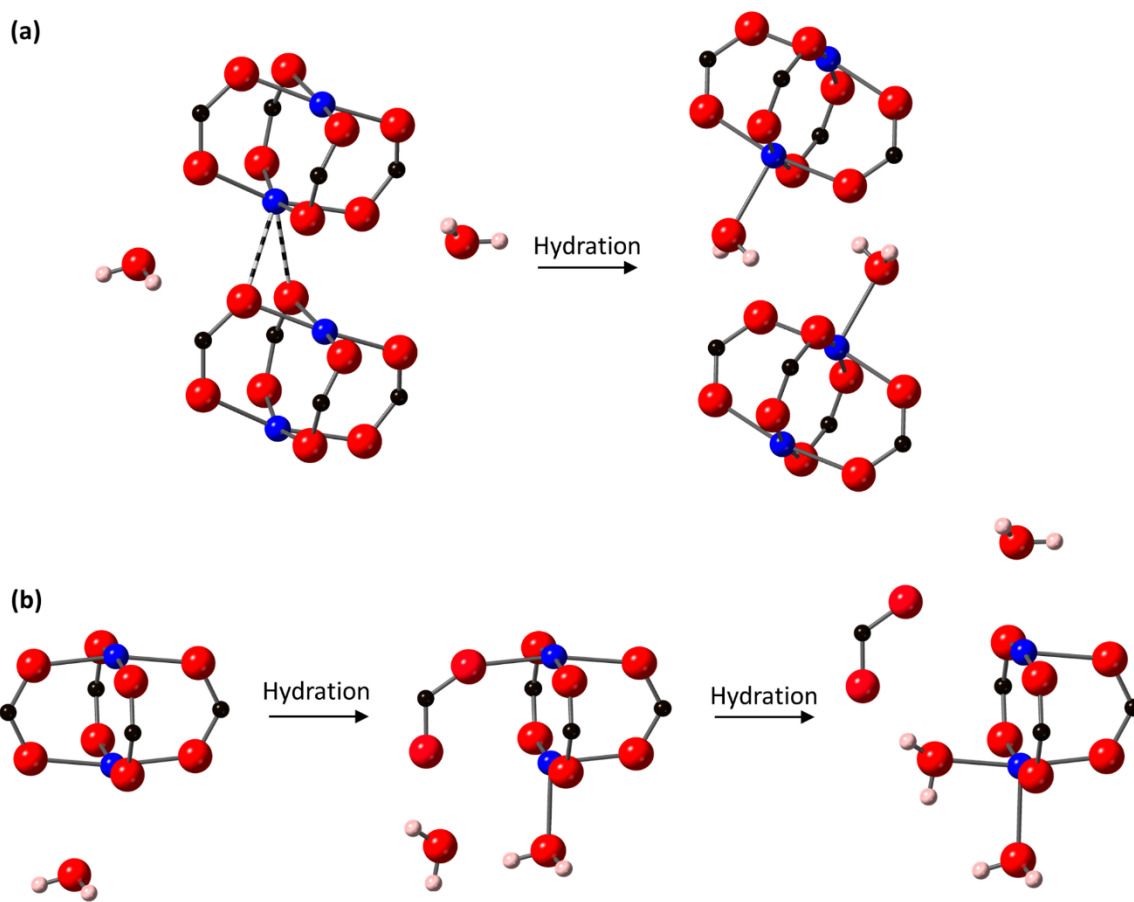


Figure 4.29. (a) Mechanism of water adsorption on dehydrated STAM-17-OEt. Energy released by water adsorption onto the one open metal site in the structure releases energy, which is then used to break the weak Cu...O interactions and move the paddlewheel units relative to each other. (b) Mechanism of paddlewheel breakdown in HKUST-1 where the adsorption of water onto the open metal sites in HKUST-1 can release energy that can then be used to break metal-carboxylate oxygen bonds in the paddlewheel, opening up further sites for more water adsorption, leading to the breaking of another metal-carboxylate oxygen bond and eventual breakdown of the HKUST-1 structure. Key: blue: Cu; red: O; black: C; pink: H.

4.4.10 Long-Term Humidity Study

A long-term water stability study was conducted on STAM-17-OEt,²⁸ involving exposing activated samples of STAM-17-OEt to ~100% relative humidity for increasing time periods and monitoring any changes in structure using powder X-ray diffraction, BET and solid-state NMR.

Samples (ca. 150 mg) were first activated at 150 °C for 16 hours, before placing inside pre-made humidity chambers containing a saturated potassium sulfate salt solution. The samples were left inside the chambers for either 1 day, 4 days or 60 days, before powder X-ray diffraction, BET and NMR measurements were recorded to investigate any changes in structure post-exposure. One sample exposed to humidity for 60 days was re-activated at 150 °C for 16 hours, before measurements were recorded.

4.4.10.1 Effect of Long-Term Humidity on STAM-17-OEt

Powder X-ray diffraction patterns (Figure 4.30) show no structure change or loss of crystallinity in the samples that have been activated and exposed to 100% relative humidity, even after exposure for 60 days. STAM-17-OEt remains stable throughout the duration of the experiment.

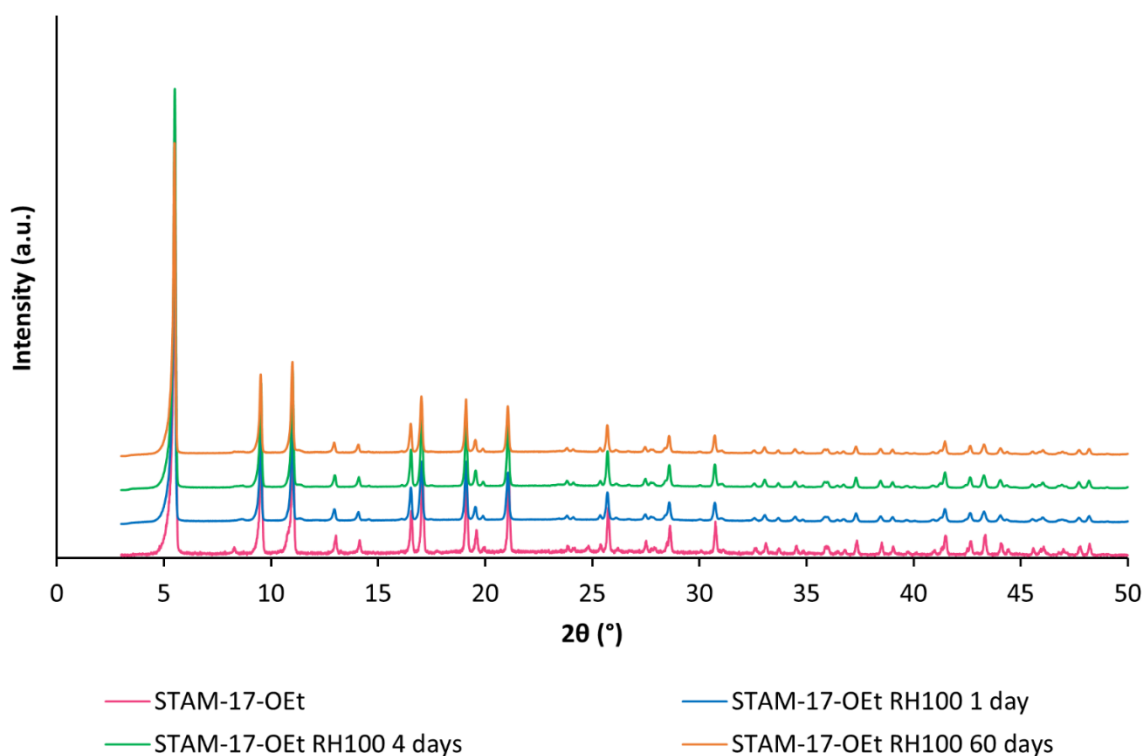


Figure 4.30. Powder X-ray diffraction patterns of pre-activated STAM-17-OEt samples exposed to 100% RH for between 1 and 60 days.

The powder X-ray diffraction patterns in Figure 4.31 show that there is also no change upon exposure to 60 days of 100% RH, followed by re-activation at 150 °C for 16 hours. Like in the humidity cycling experiments described in section 4.4.6.2, the process of water adsorption-desorption appears to be completely reversible.

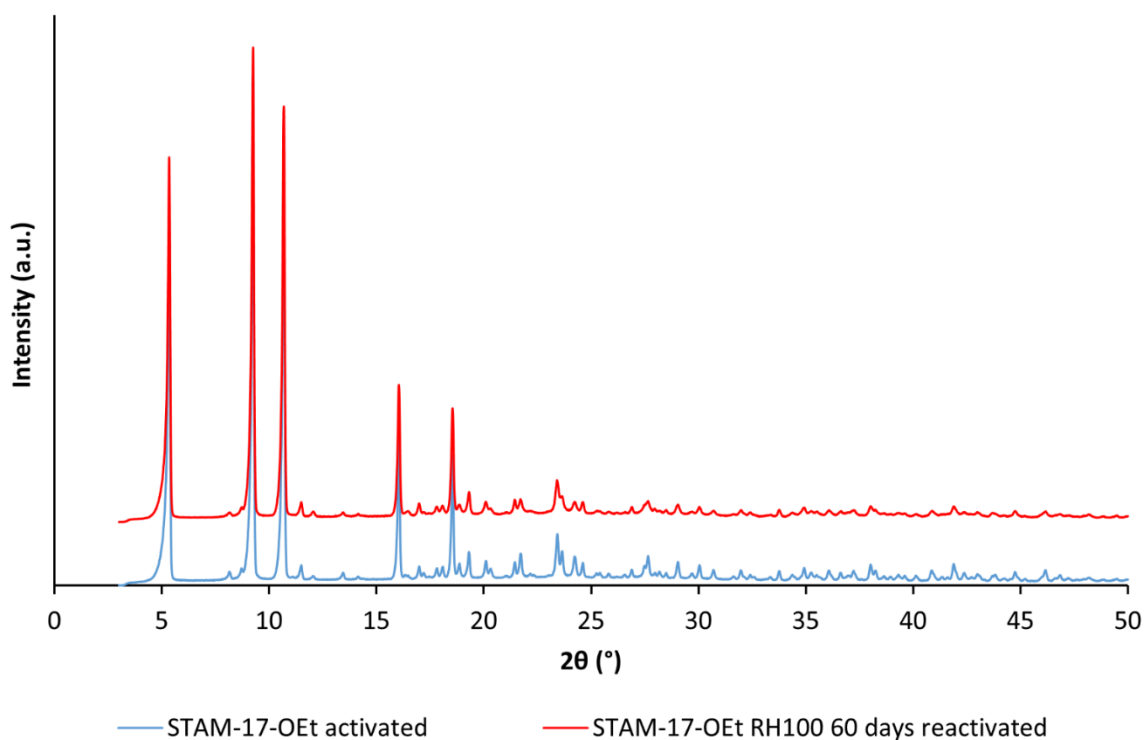


Figure 4.31. Powder X-ray diffraction patterns of activated STAM-17-OEt and STAM-17-OEt reactivated after exposure to 100% RH for 60 days.

The BET surface areas (Table 4.5) remain largely unchanged after exposure to high humidity. As the initial surface area for as-made STAM-17-OEt is so low, the inconsistent values may be partially attributed to experimental errors. This is also true for the higher surface area measured for as-made STAM-17-OEt than was reported in literature, where the value measured here is almost $20 \text{ m}^2/\text{g}$ higher than the reported literature value of $58.4 \pm 0.3 \text{ m}^2/\text{g}$.⁹ The trend remains clear though, where the porosity of the samples is only slightly impacted even after long term humidity exposure.

The experiments were repeated using HKUST-1 for comparison and in HKUST-1, a significant decrease in porosity may be observed, even after 1 day, where the surface area has

almost halved. The inconsistent value observed for HKUST-1 after 4 days' exposure may again be attributed to experimental error.

Table 4.5. Nitrogen BET surface areas of STAM-17-OEt and HKUST-1 samples before and after exposure to 100% RH.

Conditions:	STAM-17-OEt BET surface area (m²/g):	HKUST-1 BET surface area (m²/g):
As-made	77.0 ± 0.4	1662.4 ± 1.4
RH 100% 1 day	46.0 ± 0.1	859.8 ± 1.1
RH 100% 4 days	56.0 ± 0.2	25.9 ± 0.0
RH 100% 60 days	35.9 ± 0.2	62.0 ± 0.1
RH 100% 60 days reactivated	32.4 ± 0.2	62.3 ± 0.1

Figure 4.32 shows the ¹³C solid-state NMR spectra of as-made STAM-17-OEt, activated as-made STAM-17-OEt, STAM-17-OEt exposed to 100% RH for 1, 4 and 60 days, and STAM-17-OEt exposed to 100% RH for 60 days before being reactivated. No changes can be observed to the local structure of the hydrated MOFs over the course of the hydration study, and the spectra match that of the as-made MOF. The activated materials before and after exposure to 100% RH also yield identical spectra to each other, confirming the hydrothermal stability of the framework.

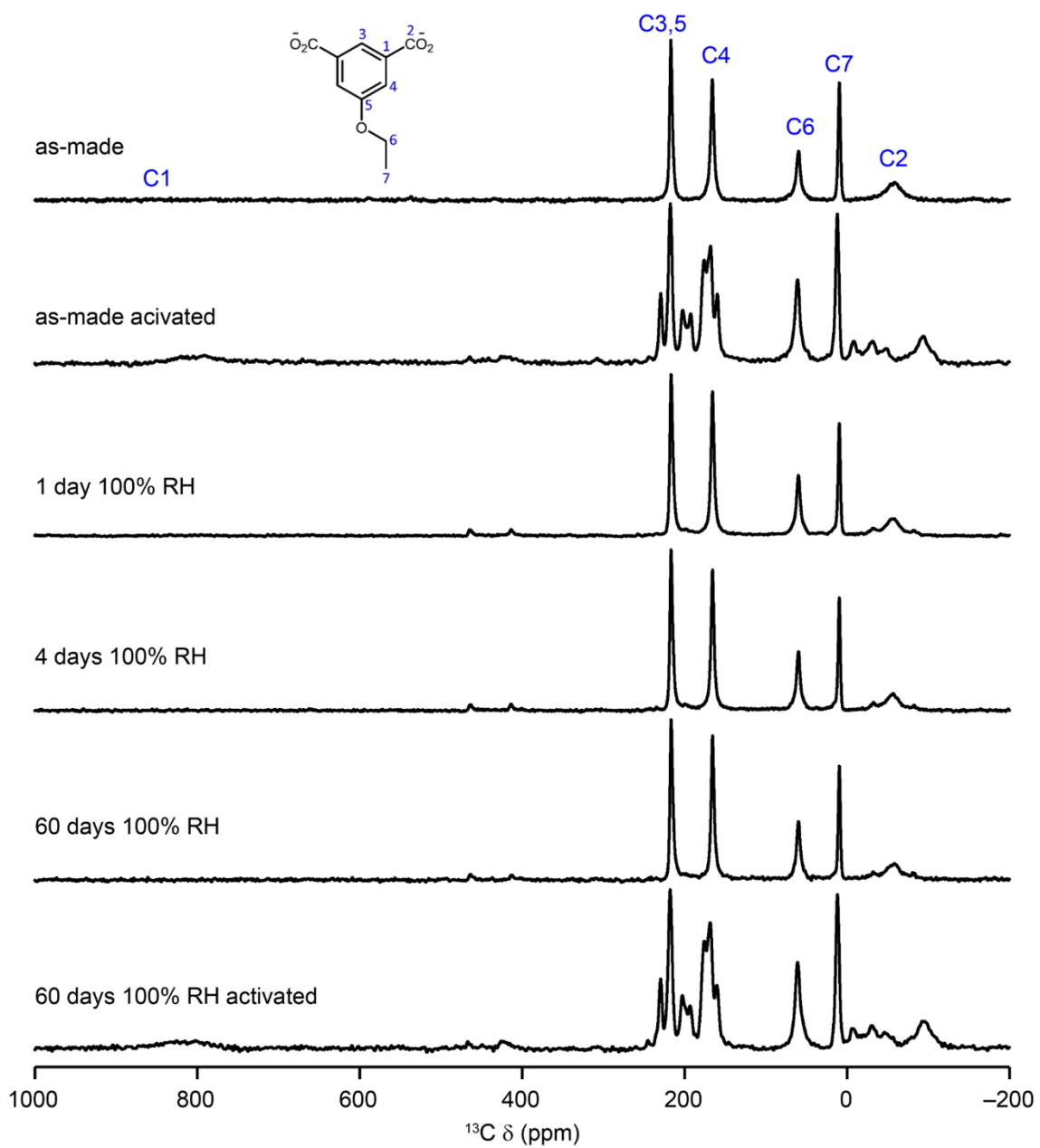


Figure 4.32. ^{13}C (14.1 T, 298 K, 37.5 kHz MAS) NMR spectra of a series of STAM-17-OEt samples treated as indicated.

4.5 Conclusion

STAM-17-OEt displays excellent water-stability and gas adsorption capabilities, especially so in humid environments. The new crumple zone mechanism displayed by STAM-17-OEt is one of the major reasons for the improved stability in the material, and that it offers new possibilities to reduce the long-standing issues regarding the stability of activated MOFs (especially when challenged with nucleophiles such as water) by understanding and then carefully controlling features such as flexibility arising from hemilability. Such an approach may reduce problems of stability to levels that allow applications in many other areas than are now possible.

4.6 References

- [1] H. Furukawa, K. E. Cordova, M. O'Keefe and O. M. Yaghi, *Science*, 2013, **341**, 1230444-1230456.
- [2] N C. Burtch, H. Jasuja and K. S. Walton, *Chem. Rev.*, 2014, **114**, 10575-10612.
- [3] J. L. C. Roswell and O. M. Yaghi, *Angew. Chem. Int. Ed.*, 2005, **44**, 4670-4679.
- [4] P. D. C. Dietzel, B. Panella, M. Hirscher, R. Blom and H. Fjellvåg, *Chem. Comm.*, 2006, **9**, 959-961.
- [5] A. G. Wong, A. J. Matzger and O. M. Yaghi, *J. Am. Chem. Soc.*, 2006, **128**, 3494-3495.
- [6] K. Uemura, R. Matsuda and S. Kitagawa, *J. Solid State Chem.*, 2005, **178**, 2420-2429.
- [7] S. Kitagawa and K. Uemura, *Chem. Soc. Rev.*, 2005, **34**, 109-119.
- [8] R. E. Morris and L. Brammer, *Chem. Soc. Rev.*, 2017, **46**, 5444-5462.
- [9] L. N. McHugh, M. J. McPherson, L. J. McCormick, S. A. Morris, P. S. Wheatley, S. J. Teat, D. McKay, D. M. Dawson, C. E. F. Sansome, S. E. Ashbrook, C. A. Stone, M. W. Smith and R. E. Morris, *Nat. Chem.*, 2018, **10**, 1096-1102.

- [10] S. S. Y., Chui, S. M. F. Lo, S, J. P. H. Charmant, A. G. Orpen, and I. D. Williams, *Science*, 1999, **283**, 1148-1150.
- [11] M. Todaro, G. Buscarino, L. Sciortino, A. Alessi, F. Messina, M. Taddei, M. Ranocchiari, M. Cannas and F. M. Gelardi, *J. Phys. Chem. C.*, 2016, **120**, 12879-12889.
- [12] Hoffmann-La Roche Inc., US Pat., US5521160A, 1996.
- [13] H. Abourahma, G. J. Bodwell, J. Lu, B. Moulton, I. R. Pottie, R. Bailey Walsh and M. J. Zaworotko, *Cryst. Growth. Des.*, 2003, **3**, 513-519.
- [14] H. W. Gibson, H. Wang, Z. Niu, C. Slebodnick, L. N. Zhakharov and A. L. Rheingold, *Macromolecules*, 2012, **45**, 1270-1280.
- [15] Bruker, *SADABS*, Bruker AXS Inc., 2001, Madison, Wisconsin, USA.
- [16] G. M. Sheldrick, *Acta Cryst.*, **A71**, 3-8.
- [17] G. M. Sheldrick, *Acta Cryst.*, **C71**, 3-8.
- [18] S. Brennan and P. L. Cowan, P. L., *Rev. Sci. Instrum.*, 1992, **63**, 850-853.
- [19] L. J. Farrugia, *J. Appl. Cryst.*, 2012, **45**, 849-854.
- [20] M. I. Mohideen, B. Xiao, P. S. Wheatley, A. C. McKinlay, Y. Li, A. M. Z. Slawin, D. W. Aldous, N. F. Cessford, T. Düren, X. Zhao, R. Gill, K. M. Thomas, J. M. Griffin, S. E. Ashbrook and R. E. Morris, *Nat. Chem.*, 2011, **3**, 304-310.
- [21] D. M. Dawson, L. E. Jamieson, M. I. H. Mohideen, A. C. McKinlay, I. A. Smellie, R. Cadou, N. S. Keddie, R. E. Morris and S. E. Ashbrook, *Phys. Chem. Chem. Phys.*, 2013, **15**, 919-929.
- [22] J. Rouquerol, D. Avnir, C. W. Fairbridge, D. H. Everett, J. M. Haynes, N. Pernicone, J. D. F. Ramsay, K. S. W. Sing, and K. K. Unger, *Pure Appl. Chem.*, 1994, **66**, 1739-1758.

- [23] N. Al-Janabi, A. Alfutimie, F. R. Siperstein and X. L. Fan, *Front. Chem. Sci. Eng.*, 2016, **10**, 103-107.
- [24] A. Pöpl, B. Jee, M. Icker, M. Hartmann and D. Himsl, *Chemie Ingenieur Technik*, 2010, **82**, 1025-1029.
- [25] A. Pöpl, S. Kunz, D. Himsl, M. Hartmann, *J. Phys. Chem. C.*, 2008, **112**, 2678-2684.
- [26] H. EL Mkami, M. I. H. Mohideen, C. Pal, A. McKinlay, O. Scheimann, R. E. Morris, *Chem. Phys. Lett.*, 2012, **544**, 17-21.
- [27] N. Nijem, K. Fursich, H. Bluhrn, S. R. Leone and M. K. Gilles, *J. Phys. Chem. C.*, 2015, **119**, 24781-24788.
- [28] A. Terracina, L. N. McHugh, M. Todaro, S. Agnello, P. S. Wheatley, F. M. Gelardi, R. E. Morris and G. Buscarino, 2019, manuscript under review.

Chapter 5: Toxic Gas Adsorption and Water Stability in the STAM Series of MOFs

5.1 Aim

Chapter 4 introduced a member of the STAM series of MOFs: STAM-17-OEt. In this chapter, the other members of the STAM series shall be introduced, their structural properties investigated and their ability to remove ammonia and hydrogen cyanide from contaminated airstreams will be investigated.

5.2 Introduction

The STAM series of MOFs was first introduced in 2011 with the parent compound: STAM-1,¹ and another member: STAM-17-OEt was reported in 2018.² STAM-17-OEt is a member of the STAM-17-n series, which have the same topology as STAM-1, though have either alkyl or alkoxy substituents at the 5-position of their linkers, rather than the methyl ester seen in STAM-1. Though the structural properties of STAM-1¹ and the NMR characterisation of the STAM series has been reported,³ many of the adsorptive properties such as water stability and gas adsorption have not been investigated. While chapter 4 focused heavily on STAM-17-OEt, this chapter will cover all members of the STAM series and will focus mainly on the adsorptive properties of the materials.

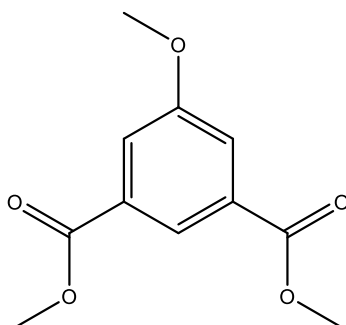
5.3 Experimental Procedure

All reagents were obtained from commercial sources and were used without further purification.

5.3.1 Ligand Syntheses

Syntheses of 1,3-dimethyl 5-hydroxybenzene-1,3-dicarboxylate, 1,3-dimethyl 5-ethoxybenzene-1,3-dicarboxylate and 5-ethoxybenzene-1,3-dicarboxylic acid are described in section 4.3.1.

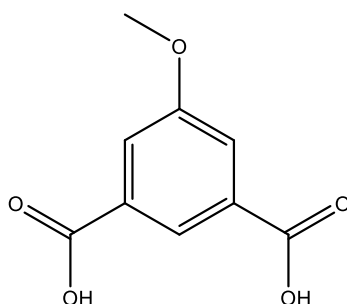
1,3-dimethyl 5-methoxybenzene-1,3-dicarboxylate⁴



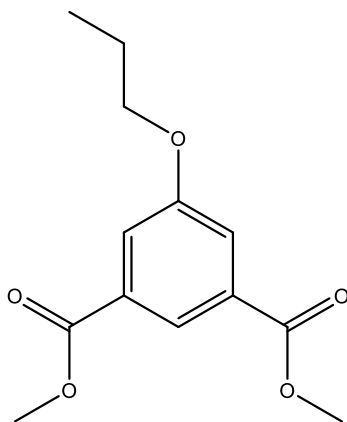
1,3-dimethyl 5-hydroxybenzene-1,3-dicarboxylate (3.93 g, 18.7 mmol) and potassium carbonate (5.53 g, 40.0 mmol) were dissolved in acetone (100 mL). Methyl iodide (2.68 mL, 43.0 mmol) was added to the solution and the mixture was allowed to stir at room temperature for 18 hours. The solvent was removed under reduced pressure and the residue taken up in DCM (100 mL) and distilled water (100 mL). The mixture was extracted with DCM (3 x 200 mL), before the divided organic layers were washed with brine (100 mL) and dried over anhydrous magnesium sulfate. The solution was filtered and the solvent removed

under reduced pressure to afford 1,3-dimethyl 5-methoxybenzene-1,3-dicarboxylate as a white crystalline solid (4.01 g, 19.1 mmol, 96% yield). ^1H (400 MHz, d_4 -MeOD) δ_{H} 8.21 (t, 1H, aromatic, $J = 2.80$ Hz), 7.76 (d, 2H, aromatic $J = 1.20$ Hz), 3.95 (s, 6H, $-\text{CH}_3$), 3.91 (s, 3H, $-\text{CH}_3$) ppm.

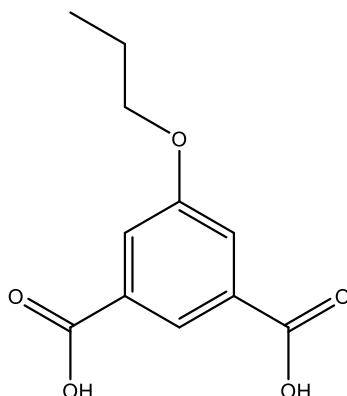
5-methoxybenzene-1,3-dicarboxylic acid⁵



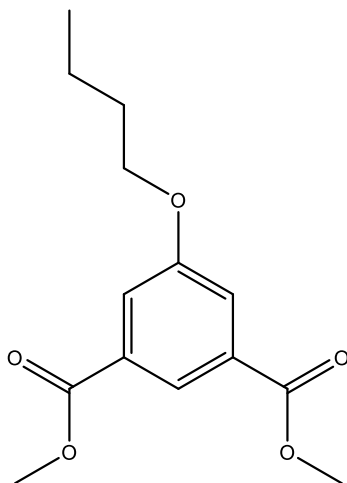
Potassium hydroxide (4.91 g, 87.6 mmol) and 1,3-dimethyl 5-methoxybenzene-1,3-dicarboxylate (3.93 g, 17.5 mmol) were dissolved in methanol (100 mL). The mixture was heated to reflux for 18 hours, before cooling to room temperature. 2M hydrochloric acid (250 mL) was added to the cooled solution and the resulting precipitated solid was collected by vacuum filtration. The white solid was washed copiously with water until the washings reached pH 6 and 5-methoxybenzene-1,3-dicarboxylic acid was then dried in air for several days (2.95 g, 15.0 mmol, 86% yield). ^1H (400 MHz, d_4 -MeOD) δ_{H} 8.26 (t, 1H, aromatic, $J = 3.20$ Hz), 7.77 (d, 2H, aromatic, $J = 1.60$ Hz), 3.91 (s, 3H, $-\text{CH}_3$) ppm.

1,3-dimethyl 5-*n*-propoxybenzene-1,3-dicarboxylate⁶

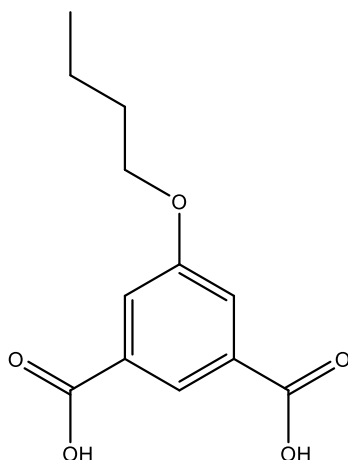
1,3-dimethyl 5-hydroxybenzene-1,3-dicarboxylate (10.05 g, 47.81 mmol) and potassium carbonate (12.73 g, 92.11 mmol) were dissolved in acetonitrile (160 mL). 1-iodopropane (5.60 mL, 57.4 mmol) was added to the solution and the reaction was heated to reflux for 48 hours. Upon cooling, the solvent was removed under reduced pressure and the residue taken up in DCM (200 mL) and distilled water (250 mL). The mixture was extracted with DCM (3 x 200 mL), before the divided organic layers were washed with brine (100 mL) and dried over anhydrous magnesium sulfate. The solvent was removed under reduced pressure to afford 1,3-dimethyl 5-*n*-propoxybenzene-1,3-dicarboxylate as a yellow oil, which set to provide an off-white solid (11.80 g, 46.78 mmol, 87% yield). ¹H (400 MHz, *d*₄-MeOD) δ_H 8.16 (t, 1H, aromatic, *J* = 2.80 Hz), 7.70 (d, 2H, aromatic, *J* = 1.60 Hz), 4.02 (t, 2H, -CH₂-, *J* = 13.2 Hz), 3.94 (s, 6H, -CH₃), 1.85 (dtd, 2H, -CH₂-, *J* = 35.2 Hz), 1.08 (t, 3H, -CH₃, *J* = 14.8 Hz) ppm.

5-*n*-propoxybenzene-1,3-dicarboxylic acid⁵

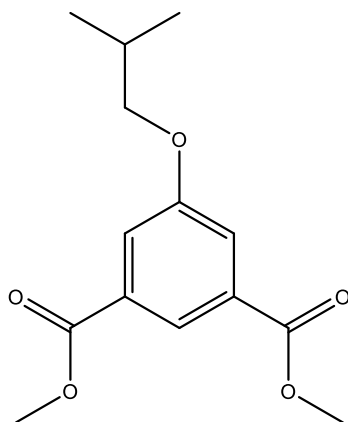
Potassium hydroxide (13.01 g, 231.9 mmol) and 1,3-dimethyl 5-*n*-propoxybenzene-1,3-dicarboxylate (11.70 g, 46.38 mmol) were dissolved in methanol (250 mL). The mixture was heated to reflux for 18 hours, before cooling to room temperature. 2M hydrochloric acid (250 mL) was added to the cooled solution and the resulting precipitated solid was collected by vacuum filtration. The white solid was washed copiously with water until the washings reached pH 6 and 5-*n*-propoxybenzene-1,3-dicarboxylic acid was then dried in air for several days (8.90 g, 39.7 mmol, 86% yield). ¹H (400 MHz, *d*₄-MeOD) δ_H 8.24 (t, 1H, aromatic, *J* = 3.20 Hz), 7.75 (d, 2H, aromatic, *J* = 1.20 Hz), 4.05 (t, 2H, -CH₂-, *J* = 12.8 Hz), 1.86 (dtd, 2H, -CH₂-, *J* = 35.2 Hz), 1.09 (t, 3H, -CH₃, *J* = 14.8 Hz) ppm.

1,3-dimethyl 5-*n*-butoxybenzene-1,3-dicarboxylate⁴

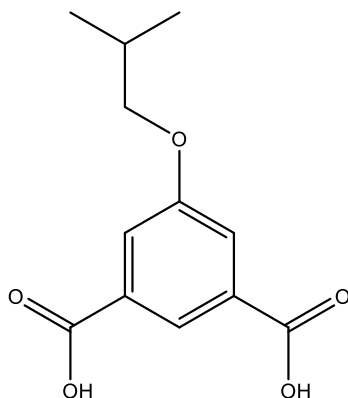
1,3-dimethyl 5-hydroxybenzene-1,3-dicarboxylate (10.04 g, 47.76 mmol) and potassium carbonate (13.38 g, 96.81 mmol) were dissolved in acetone (100 mL). 1-bromobutane (6.00 mL, 55.6 mmol) was added to the solution and the reaction was heated to reflux for 24 hours. Upon cooling, the solvent was removed under reduced pressure and the residue taken up in DCM (200 mL) and distilled water (200 mL). The mixture was extracted with DCM (3 x 200 mL), before the divided organic layers were washed with brine (100 mL) and dried over anhydrous magnesium sulfate. The solution was removed under reduced pressure to afford 1,3-dimethyl 5-*n*-butoxybenzene-1,3-dicarboxylate as a yellow oil (12.05 g, 45.25 mmol, 95% yield). ¹H (400 MHz, *d*₄-MeOD) δ_H 8.14 (t, 1H, aromatic, *J* = 2.80 Hz), 7.68 (d, 2H, aromatic, *J* = 1.60 Hz), 4.05 (t, 2H, -CH₂-, *J* = 12.8 Hz), 3.94 (s, 6H, -CH₃), 1.86-1.74 (m, 2H, -CH₂-), 1.54 (dtd, 2H, -CH₂-, *J* = 37.6 Hz), 1.02 (t, 3H, -CH₃, *J* = 14.8 Hz) ppm.

5-*n*-butoxybenzene-1,3-dicarboxylic acid⁵

Potassium hydroxide (12.69 g, 226.3 mmol) and 1,3-dimethyl 5-*n*-butoxybenzene-1,3-dicarboxylate (12.05 g, 45.25 mmol) were dissolved in methanol (250 mL). The mixture was heated to reflux for 24 hours, before cooling to room temperature. 2M hydrochloric acid (250 mL) was added to the cooled solution and the resulting precipitated solid was collected by vacuum filtration. The white solid was washed copiously with water until the washings reached pH 6 and 5-*n*-butoxybenzene-1,3-dicarboxylic acid was then dried in air for several days (9.52 g, 40.0 mmol, 88% yield). ¹H (400 MHz, *d*₄-MeOD) δ_H 8.24 (t, 1H, aromatic, *J* = 2.80 Hz), 7.74 (d, 2H, aromatic, *J* = 5.2 Hz), 4.09 (t, 2H, -CH₂-, *J* = 12.8 Hz), 1.88-1.76 (m, 2H, -CH₂-), 1.63-1.48 (m, 2H, -CH₂-), 1.03 (t, 3H, -CH₃, *J* = 14.8 Hz) ppm.

1,3-dimethyl 5-*i*-butoxybenzene-1,3-dicarboxylate⁴

1,3-dimethyl 5-hydroxybenzene-1,3-dicarboxylate (10.04 g, 47.76 mmol) and potassium carbonate (21.18 g, 153.3 mmol) were dissolved in acetone (160 mL). 1-bromo-2-methyl propane (13.00 mL, 119.55 mmol) was added to the solution and the reaction was heated to reflux for 72 hours. Upon cooling, the solvent was removed under reduced pressure and the residue taken up in DCM (300 mL) and distilled water (200 mL). The mixture was extracted with DCM (total volume - 1.5 L), before the divided organic layers were washed with brine (100 mL) and dried over anhydrous magnesium sulfate. The solvent was removed under reduced pressure to afford 1,3-dimethyl 5-*i*-butoxybenzene-1,3-dicarboxylate as a yellow oil, which set to provide an off-white solid (11.80 g, 46.78 mmol, 87% yield). ¹H (400 MHz, *d*-MeOD) δ_{H} 8.12 (t, 1H, aromatic, $J = 2.80$ Hz), 7.66 (d, 2H, aromatic, $J = 1.60$ Hz), 3.93 (s, 6H, -CH₃), 3.80 (d, 2H, -CH₂-, $J = 6.40$ Hz), 2.09 (hept, 1H, -CH-, $J = 40.0$ Hz), 1.07 (d, 6H, -CH₃, $J = 16.4$ Hz) ppm.

5-*i*-butoxybenzene-1,3-dicarboxylic acid⁵

Potassium hydroxide (7.33 g, 130 mmol) and 1,3-dimethyl 5-*i*-butoxybenzene-1,3-dicarboxylate (11.60 g, 43.56 mmol) were dissolved in methanol (150 mL). The mixture was heated to reflux for 24 hours, before cooling to room temperature. 2M hydrochloric acid (250 mL) was added to the cooled solution and the resulting precipitated solid was collected by vacuum filtration. The white solid was washed copiously with water until the washings reached pH 6 and 5-*i*-butoxybenzene-1,3-dicarboxylic acid was then dried in air for several days (8.60 g, 36.10 mmol, 75% yield). ¹H (400 MHz, *d*₄-MeOD) δ_H 8.24 (t, 1H, aromatic, *J* = 2.80 Hz), 7.74 (d, 2H, aromatic *J* = 1.20 Hz), 3.85 (d, 2H, -CH₂-, *J* = 6.40 Hz), 2.12 (hept, 1H, -CH-, *J* = 40.0 Hz), 1.08 (d, 6H, -CH₃, *J* = 6.80 Hz) ppm.

5.3.2 MOF Synthesis

STAM-17-Me³

5-methylbenzene-1,3-dicarboxylic acid (0.18 g, 1.00 mmol) was dissolved in methanol (10 mL) and copper acetate monohydrate (0.20 g, 1.00 mmol) was dissolved in distilled water (5 mL). The two solutions were stirred separately for 15 minutes at room temperature, after which, the solutions were combined and stirred at room temperature for a further 30 minutes. The combined solution was added to a Teflon-lined stainless-steel autoclave and the sealed autoclave was heated in an oven at 110 °C for 3 days. The resulting crystals were isolated via Buchner filtration, washed with distilled water and ethanol and dried in air. A typical yield was 0.20 g, 0.77 mmol, 76%.

STAM-17-OMe³

5-methoxybenzene-1,3-dicarboxylic acid (0.20 g, 1.00 mmol), copper acetate monohydrate (0.20 g, 1.00 mmol) and a 2:1 solution of methanol and distilled water (15 mL) were added to a Teflon-lined stainless-steel autoclave. The sealed autoclave was heated in an oven at 110 °C for 3 days and the resulting crystals were isolated via Buchner filtration, washed with distilled water and ethanol and dried in air. A typical yield was 0.25 g, 0.85 mmol, 84%.

STAM-17-OEt²

5-ethoxybenzene-1,3-dicarboxylic acid (0.21 g, 1.00 mmol), copper acetate monohydrate (0.20 g, 1.00 mmol) and distilled water (15 mL) were added to a Teflon-lined stainless-steel autoclave. The sealed autoclave was heated in an oven at 110 °C for 3 days and the resulting crystals were isolated via Buchner filtration, washed with distilled water and ethanol and dried in air. A typical yield was 0.24 g, 0.80 mmol, 80%.

STAM-17-O*n*Pr²

5-*n*-propoxybenzene-1,3-dicarboxylic acid (0.22 g, 1.00 mmol), copper acetate monohydrate (0.20 g, 1.00 mmol) and distilled water (15 mL) were added to a Teflon-lined stainless-steel autoclave. The sealed autoclave was heated in an oven at 110 °C for 3 days and the resulting crystals were isolated via Buchner filtration, washed with distilled water and ethanol and dried in air. A typical yield was 0.28 g, 0.86 mmol, 85%.

STAM-17-O*n*Bu²

5-*n*-butoxybenzene-1,3-dicarboxylic acid (0.24 g, 1.00 mmol), copper acetate monohydrate (0.20 g, 1.00 mmol) and distilled water (15 mL) were added to a Teflon-lined stainless-steel autoclave. The sealed autoclave was heated in an oven at 110 °C for 3 days and the resulting crystals were isolated via Buchner filtration, washed with distilled water and ethanol and dried in air. A typical yield was 0.27 g, 0.80 mmol, 82%.

STAM-17-O*i*Bu²

5-*i*-butoxybenzene-1,3-dicarboxylic acid (0.24 g, 1.00 mmol), copper acetate monohydrate (0.20 g, 1.00 mmol) and distilled water (15 mL) were added to a Teflon-lined stainless-steel autoclave. The sealed autoclave was heated in an oven at 110 °C for 3 days and the resulting crystals were isolated via Buchner filtration, washed with distilled water and ethanol and dried in air. A typical yield was 0.28 g, 0.84 mmol, 85%.

STAM-1¹

1,3,5-benzenetricarboxylic acid (0.42 g, 2.00 mmol) was dissolved in methanol (10 mL) and copper nitrate trihydrate (0.48 g, 2.00 mmol) was dissolved in distilled water (10 mL). The

two solutions were stirred separately for 15 minutes at room temperature, after which, the solutions were combined and stirred at room temperature for a further 30 minutes. The combined solution was added to a Teflon-lined stainless-steel autoclave and the sealed autoclave was heated in an oven at 110 °C for 7 days. The resulting crystals were isolated via Buchner filtration, washed with distilled water and acetone and dried in air. A typical yield was 0.57 g, 1.71 mmol, 85%.

5.4 Results and Discussion

5.4.1 Formation of the STAM Series

The STAM-17-n series of MOFs was synthesised in quantitative yields using the required 1,3-dicarboxylic acid linker and copper acetate, using either water or an aqueous methanol solution as a solvent (Figure 5.1). The “n” in the STAM-17-n series denotes the length of the alkyl side chain on the 1,3-dicarboxylic acid linker used, where STAM-17-OMe would indicate that the linker 5-methoxybenzene-1,3-dicarboxylic acid was used. All the materials are related to the parent literature compound STAM-1 and are members of the same series as the previously discussed STAM-17-OEt.

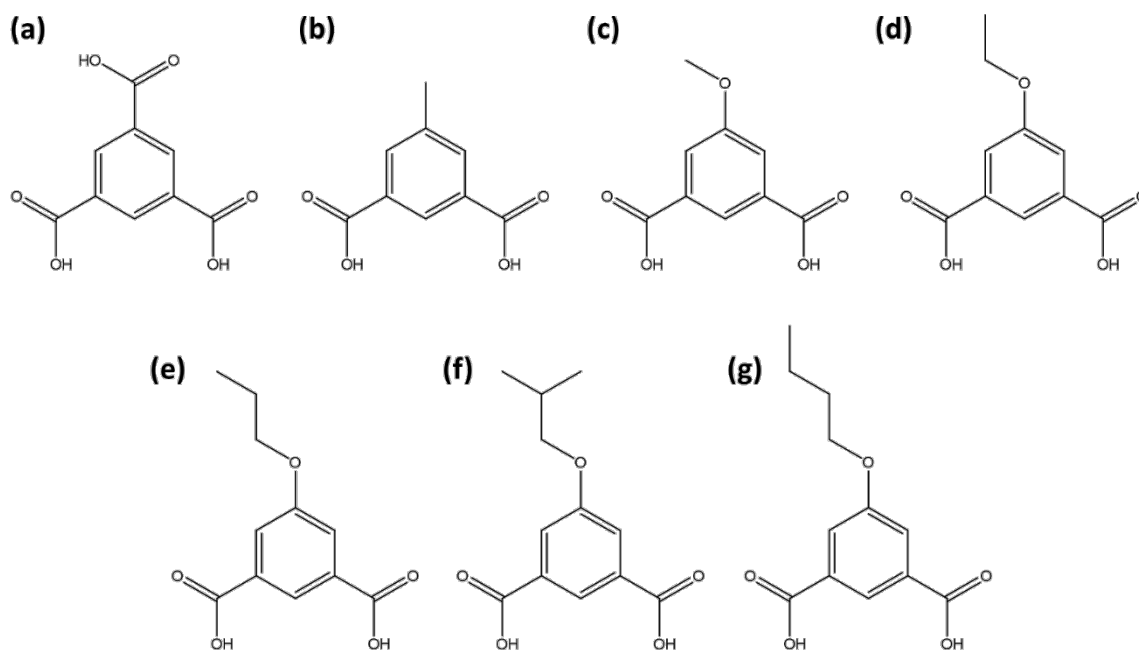


Figure 5.1. Images of the linkers used in the synthesis of members of the STAM series: (a) 1,3,5-benzenetricarboxylic acid; (b) 5-methylbenzene-1,3-dicarboxylic acid; (c) 5-methoxybenzene-1,3-dicarboxylic acid; (d) 5-ethoxybenzene-1,3-dicarboxylic acid; (e) 5-*n*-propoxybenzene-1,3-dicarboxylic acid; (f) 5-*i*-butoxybenzene-1,3-dicarboxylic acid; (g) 5-*n*-butoxybenzene-1,3-dicarboxylic acid.

The synthesised materials are formed as highly crystalline materials and powder X-ray diffraction of the samples highlights that members of the STAM-17-*n* series share the same STAM topology as the parent compound: STAM-1 (Figure 5.2).

There are some differences between the patterns in some cases, such as the intensity and peak positions, though these may be attributed to differences in the crystallinity of samples and differences in the sizes of the unit cells respectively. Overall, members of the STAM series form an isostructural series of MOFs.

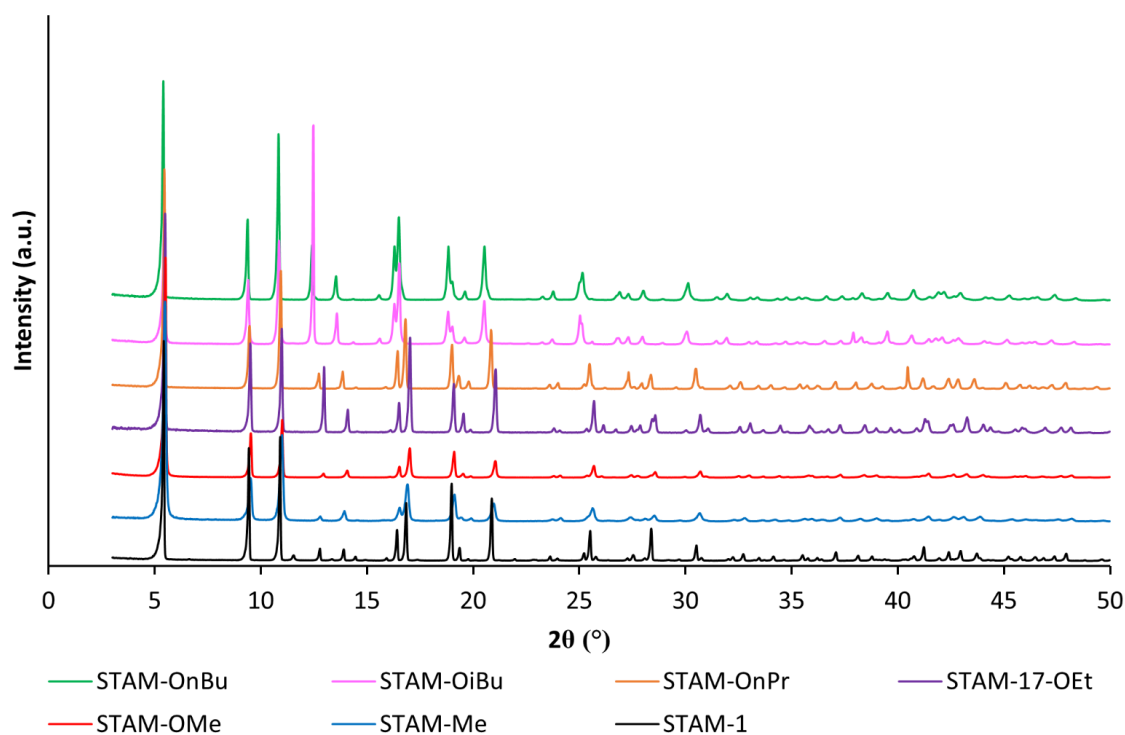


Figure 5.2. Powder X-ray diffraction patterns of the members of the STAM series of MOFs, highlighting the shared STAM topology within the series.

5.4.2. Crystal Structure Analysis

From single crystal X-ray diffraction, the materials display the typical STAM topology, with a Kagome lattice structure and two types of pore system present.

The overall crystal structure is similar for all studied members of the STAM series, with a methyl ester side chain protruding into the hydrophobic pore in the case of STAM-1 (Figure 5.3) and a methoxy or *n*-butoxy side chain protruding into the pore in the case of STAM-17-OMe and STAM-17-*O**n*Bu (Figure 5.4). The alkyl side chain protrudes into the hydrophobic pore to a lesser degree for shorter chain MOFs such as STAM-17-OMe and to a greater degree with longer chained MOFs such as STAM-17-*O**n*Bu.

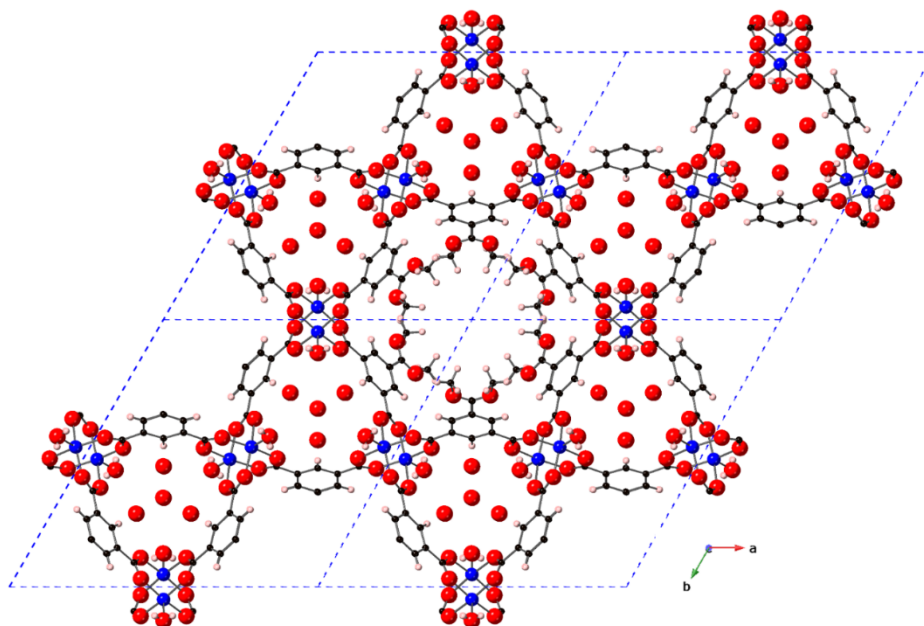


Figure 5.3. Crystal structure of STAM-1 viewed down the crystallographic c axis, highlighting the hydrophobic and hydrophilic pores within the structure. The methyl ester groups protrude into the hydrophobic pore and are disordered over two possible crystallographic sites, each of which is 50% occupied. Key: blue: Cu; red: O; black: C and pink: H.

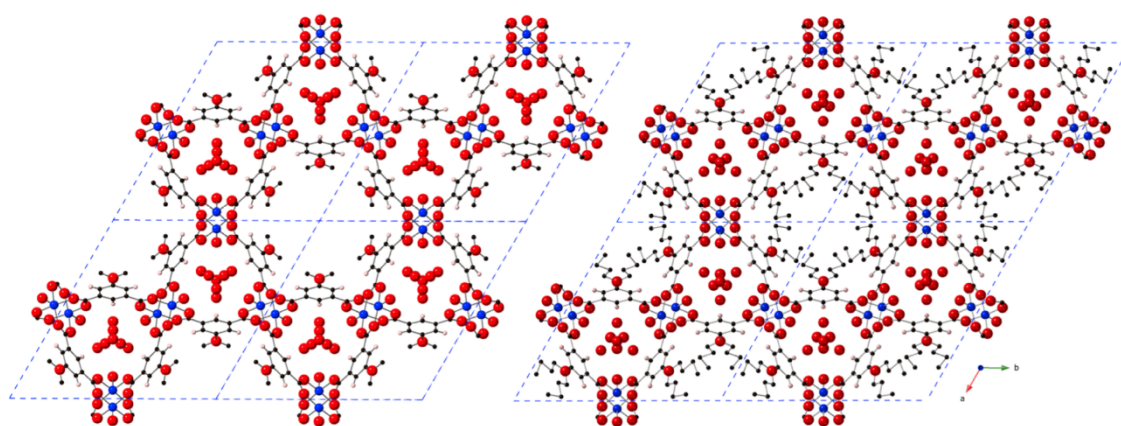


Figure 5.4. Crystal structures of STAM-17-OMe (left) and STAM-17-OnBu (right), viewed down their crystallographic c axes. The alkyl chains are disordered over two possible crystallographic sites, each of which is 50% occupied and the chains protrude into the hydrophobic pore. Key: blue: Cu; red: O; black: C and pink: H.

The single crystal structure for STAM-17-Me was not recorded, as the material formed as a microcrystalline solid, though from the powder diffraction pattern discussed previously, the material is known to be a member of the STAM series.

5.4.3 Porosity Measurements

Argon BET analysis was performed on all STAM samples at 87 K, on a Micromeritics ASAP 2020 Surface Area and Porosity Analyser. Samples were activated at 423 K overnight prior to measurement and the BET surface areas were calculated using the Rouquerol method.⁷

The surface area measurements may be observed in Table 5.1.

The length of the side chain in the STAM series has a significant impact upon the porosity of the material and there is a clear correlation between the length of the alkyl chain in the STAM-17-*n* series with the measured surface area. The material with the greatest surface area is the one with the smallest alkyl side chain: STAM-17-Me, which displays an argon BET surface area of $251.3 \pm 1.0 \text{ m}^2/\text{g}$, followed by STAM-17-OMe and STAM-17-OEt respectively. STAM-1 has increased steric bulk compared to STAM-17-OMe due to the presence of a methyl ester side chain and consequently displays a slightly lower surface area. As discussed in the previous chapter, the low porosity observed in the STAM series is due to the switchable structure of the materials. Upon activation, the pores become constricted by the change in the coordination environment of the copper paddlewheels, which impairs the porosity. The bulky alkyl chains in STAM-17-O n Pr, STAM-17-O n Bu and STAM-17-O n Bu significantly block access to the hydrophobic pores and the materials display such low surface areas that they are considered almost non-porous. The reduction of the BET surface area to almost zero suggests that the hydrophilic pore is completely closed upon activation in longer-chained materials, due to the reduced flexibility within the frameworks. STAM-17-O n Pr and STAM-17-O n Bu display the lowest surface area of all the materials, suggesting that

long and linear alkyl chains impact the porosity greater than the branched alkyl chain observed in STAM-17-*O**i*Bu. The slightly lower value of $1.9 \pm 0.3 \text{ m}^2/\text{g}$ observed for STAM-17-*O**n*Pr compared to $2.2 \pm 0.0 \text{ m}^2/\text{g}$ for STAM-17-*O**n*Bu may be attributed to experimental error, due to the very low surface areas reported.

Table 5.1. Argon BET surface areas measured for the STAM series.

Sample	BET surface area (m^2/g)
STAM-1	66.6 ± 0.2
STAM-17-Me	251.3 ± 1.0
STAM-17-OMe	98.5 ± 1.5
STAM-17-OEt	43.1 ± 0.2
STAM-17- <i>O</i> <i>n</i> Pr	1.9 ± 0.3
STAM-17- <i>O</i> <i>n</i> Bu	2.2 ± 0.0
STAM-17- <i>O</i> <i>i</i> Bu	9.7 ± 0.1

5.4.4 Water Adsorption and Stability in the STAM Series

Water adsorption within the STAM series was investigated using Dynamic Vapour Sorption (DVS) analysis and as in STAM-17-OEt, how the STAM materials were affected by exposure to humidity was one of the most important characteristics within this study. Selected members were exposed to increasing levels of relative humidity (RH) and their corresponding water adsorption isotherms were recorded, where the shape of the adsorption isotherm depends on the nature of the interactions between the guest molecules and the sorbent. Despite being members of the same series, certain members show significantly different shaped water isotherms. Water adsorption was first investigated in the parent compound STAM-1 and the material shows a water adsorption isotherm with hysteresis

observed in the desorption branch (Figure 5.5). There are also two small steps in the isotherm with associated water uptakes of ca. 0.16 g g^{-1} and 0.18 g g^{-1} respectively, suggesting staggered pore filling, where the hydrophobic pores become accessible to water molecules after the hydrophilic pores. The isotherm of STAM-1 reflects a favourable adsorption mechanism between its structure and adsorbing water molecules and as such, the material may be classified as a hydrophilic MOF.

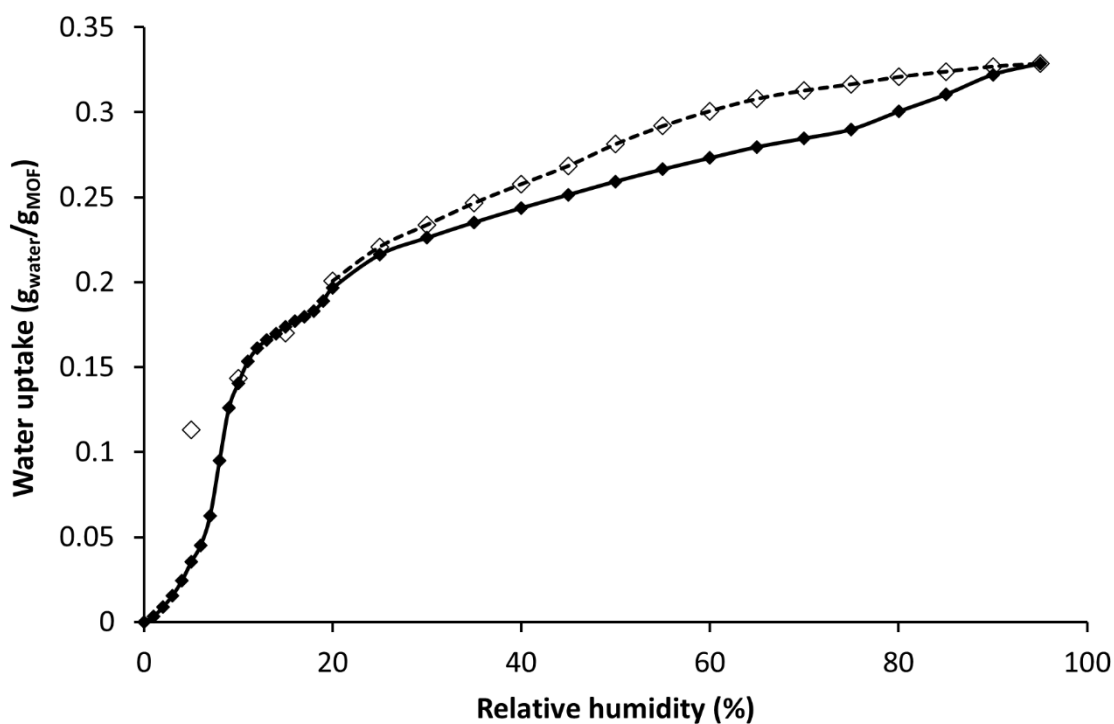


Figure 5.5. Water adsorption isotherm recorded at 298 K for STAM-1, showing small steps in the isotherm and a hysteresis loop. Solid line and filled diamonds: adsorption branch; dashed line and open diamonds: desorption branch.

STAM-17-*O*n**Pr displays a water isotherm that is similar to STAM-17-OEt, which is shown for comparison (Figure 5.6). The material exhibits a gate-opening effect similar to STAM-17-OEt at low levels of relative humidity, due to structural flexibility caused by the initial transition from the activated to hydrated phase upon readsorption of water. The pore filling appears to be more gradual in STAM-17-*O*n**Pr, which is due to the presence of a bulkier alkyl chain protruding into the hydrophobic pore and a less flexible framework. STAM-17-*O*n**Pr and STAM-17-OEt also do not show the steps observed in STAM-1, suggesting that greater energy is necessary to fill the hydrophobic pores than was required in STAM-1, which may again be attributed to the longer length of the alkyl chains in both STAM-17-*O*n**Pr and STAM-17-OEt restricting access to water molecules. Unlike STAM-17-OEt, the desorption path does not follow the adsorption path and the material displays significant hysteresis in the desorption branch at lower values of relative humidity. The material appears to require a lower level of relative humidity to drive the water out of the pores and switch the structure back to the activated phase than was initially required for the introduction of water.

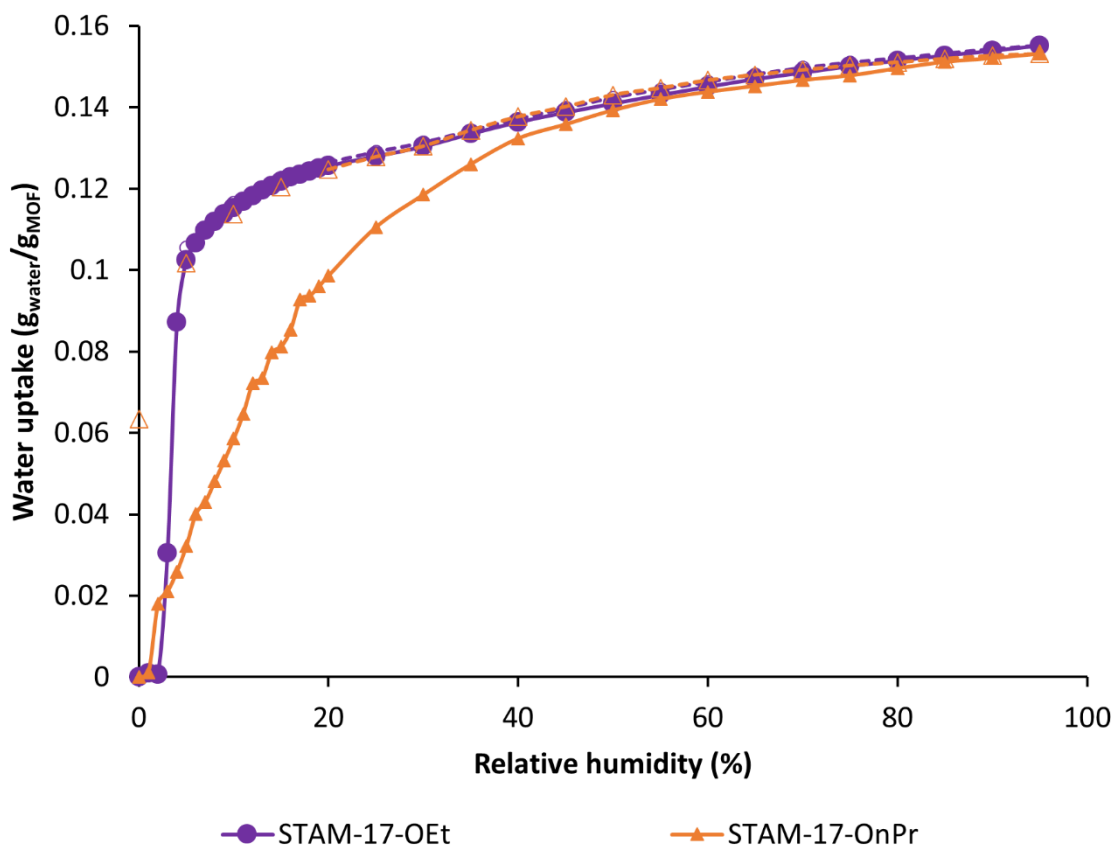


Figure 5.6. Water adsorption isotherms recorded at 298 K for STAM-17-OnPr and STAM-17-OEt, where both show a gate opening effect at low RH and STAM-17-OnPr displays hysteresis in the desorption branch. Solid line and filled markers: adsorption branch; dashed line and open markers: desorption branch.

STAM-17-OMe displays the most interesting adsorption isotherm of all, with a clear ‘stepped’ isotherm similar to that observed in the Al-fumarate MOF.⁸ The material does not show a typical hydrophilic or hydrophobic behaviour, but an isotherm shape in between these two extremes. The two-step water adsorption isotherm reveals a complex interaction mechanism between water molecules and the STAM-17-OMe framework and hysteretic behaviour is again observed in the desorption branch (Figure 5.7). The material first exhibits

a gate-opening effect at low levels of relative humidity arising from the initial transition from the activated to hydrated phase upon readsorption of water. The two clear steps in the STAM-17-OMe isotherm show differences in water uptake of ca. 0.14 g g^{-1} in the first step and ca. 0.11 g g^{-1} for the second step and are related to the two types of pores present in the STAM materials, where the hydrophilic pores are filled in the first step and the hydrophobic pores are filled in the second. A similar behaviour was observed in the water isotherm of STAM-1, though to a much lesser degree, suggesting that the smaller steric bulk from the methoxy alkyl chain in STAM-17-OMe reduces the energy required to open the hydrophobic pore to water and facilitates pore filling. This two-step adsorption mechanism is not unexpected in the STAM series due to their switchable nature and similar behaviour was observed regarding humid ammonia testing on STAM-17-OEt in chapter 4. In testing, ammonia is first taken up by the hydrophobic pores in a dry airstream and humidity exposure promotes relaxation of the hydrophilic pores to allow access to ammonia.

As in STAM-17-OPr, the material requires a lower level of relative humidity to remove water from the pores and switch the structure back to the activated phase than was initially required in the adsorption of water.

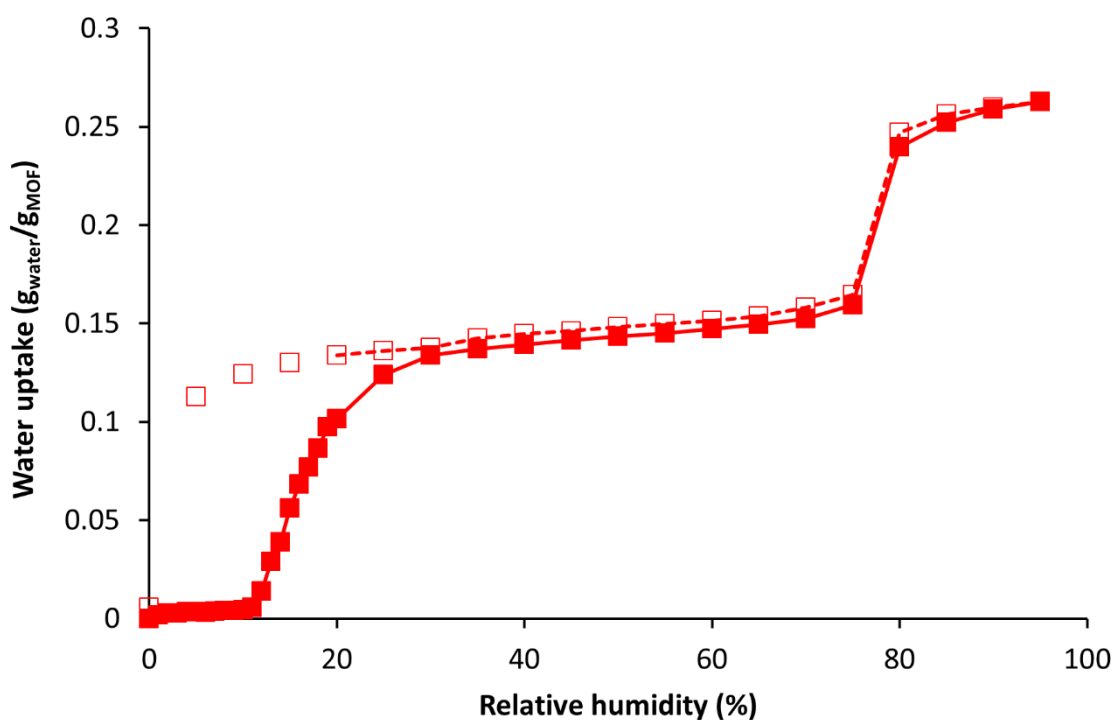


Figure 5.7. Water adsorption isotherm recorded at 298 K for STAM-17-OMe, showing a gate-opening effect at low RH, a clear two-step isotherm and hysteresis in the desorption branch. Solid line and filled squares: adsorption branch; dashed line and open squares: desorption branch.

The water isotherms for selected members of the STAM series show that despite the similarities between their structures, the adsorptive properties in each member may be very different. STAM-1 and STAM-17-OMe both show steps in their isotherms to varying degrees, while STAM-17-O*n*Pr and STAM-17-OEt do not show steps in their isotherms and STAM-1 is the only member of the tested materials that does not show a gate-opening effect at low values of relative humidity.

The results highlight the complicated relationship between the alkyl substituent, the switchable nature of the STAM framework and their subsequent effects on water adsorption.

Water stability was an important structural feature of STAM-17-OEt in the previous chapter and water stability experiments were repeated for selected members of the STAM series to ensure that the feature was observable across the series.

Figure 5.8 shows the evolution of the mass of dehydrated STAM-1 and STAM-17-*O_n*Pr samples on exposure to 90% relative humidity at 298 K. The results for STAM-17-OEt are shown for comparison and like STAM-17-OEt, both STAM-17-*O_n*Pr and STAM-1 show an initial rapid increase in mass as the dehydrated material adsorbs water. There is then no further change over the remainder of the experiment (up to 5 days). STAM-17-*O_n*Pr and STAM-17-OEt display almost identical water uptake values, while STAM-1 adsorbs a higher quantity. The trend across the series is clear though, where the size of the substituent at the 5-position has no significant effect on the long-term water stability of the material.

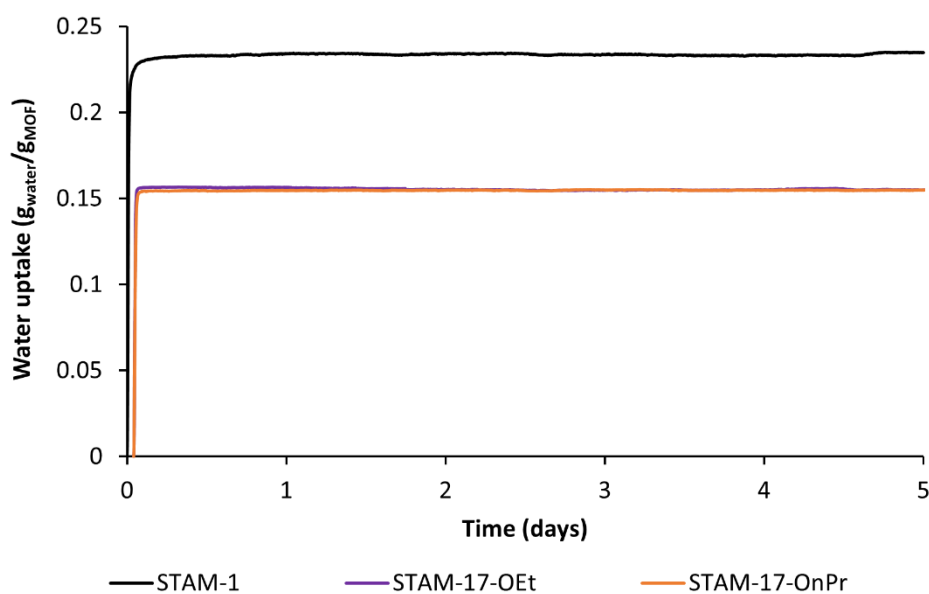


Figure 5.8. Evolution of the total mass of samples of activated STAM-1 and STAM-17-*O_n*Pr on exposure to an atmosphere of 90% RH over a period of five days. STAM-17-OEt shown for comparison.

Though the chemistry of the parent compound STAM-1 and the STAM-17-n series is very similar, they differ in their electronic structure, with an electron donating substituent, such as ethoxy (as in STAM-17-OEt), to the electron withdrawing methylcarboxy ($-\text{CO}_2\text{Me}$) or STAM-1.²

Much like the cycling experiments performed for STAM-17-OEt and HKUST-1 in the previous chapter, the experiment was undertaken on STAM-1 (Figure 5.9) to prove that the cyclability is true across the whole STAM series, irrespective of electronic properties.

STAM-1 behaves in a similar way to STAM-17-OEt, where exposure to water for long periods and repeated cycling of relative humidity between 0 and 90% at 298 K (8 h for each cycle for a total of 120 h) have no effect on the structure of the material.

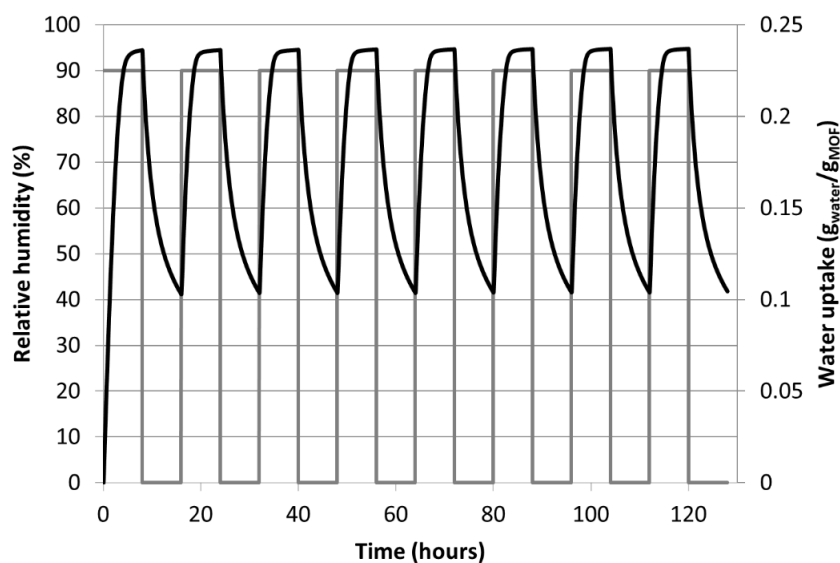


Figure 5.9. Vapour water stability at 298 K for STAM-1, demonstrated by the change in the sample's water uptake through 8 water adsorption/desorption cycle measurements (black trace) to 90% relative humidity (grey trace). The chart shows that after the initial water uptake, the sorption capacity in STAM-1 remains constant throughout the experiment, as observed in the isostructural STAM-17-OEt.

As with STAM-17-OEt and HKUST-1 in the previous chapter, activated STAM-1 samples were exposed to $\sim 100\%$ RH for up to 60 days and the effects on the structure were determined.⁹

Powder X-ray diffraction patterns (Figure 5.10) show no structure change or loss of crystallinity in the samples that have been activated and exposed to 100% relative humidity, even after exposure for 60 days. The material may also be reactivated at 150 °C after exposure to 100% humidity for 60 days. Like STAM-17-OEt, STAM-1 remains stable throughout the duration of the experiment.

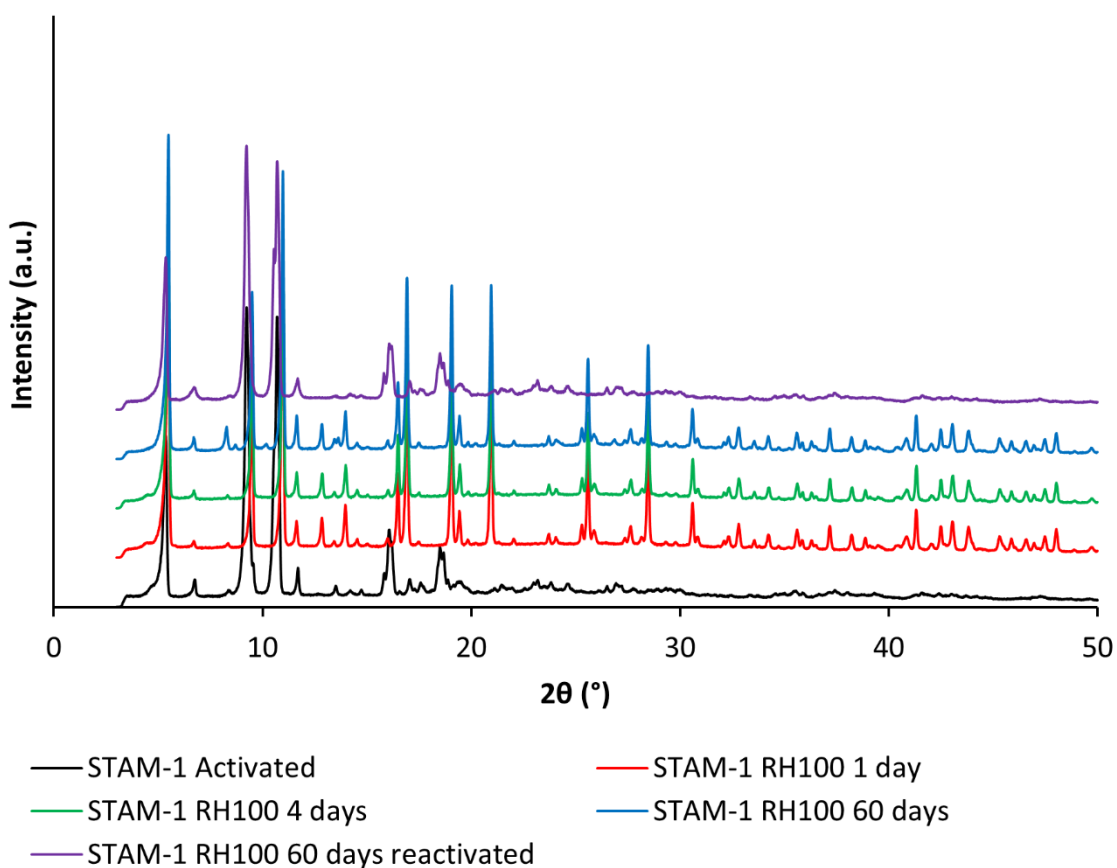


Figure 5.10. Powder X-ray diffraction patterns of STAM-1 samples exposed to 100% RH for up to 60 days.

Nitrogen surface area analysis was performed on STAM-1 samples at 77 K on a Micromeritics ASAP 2020 Surface Area and Porosity Analyser and the BET surface areas were calculated using the Rouquerol method.⁷

The nitrogen BET surface areas (Table 5.2) remain largely unchanged after exposure to high humidity. The initial nitrogen BET surface area for as-made STAM-1 is relatively low and the inconsistent values may consequently be partially attributed to experimental errors. The trend remains clear though, where the porosity of STAM-1 remains relatively constant even after long term humidity exposure.

Table 5.2. Nitrogen BET surface areas of STAM-1 samples before and after exposure to 100% RH.

Conditions:	STAM-1 BET surface area (m²/g):
As-made	81.4 ± 0.1
RH 100% 1 day	73.7 ± 0.2
RH 100% 4 days	93.5 ± 0.3
RH 100% 60 days	89.5 ± 0.3
RH 100% 60 days reactivated	94.4 ± 0.2

Solid-state NMR was conducted on samples using a Bruker Avance III solid-state spectrometer equipped with a wide-bore 14.1 T superconducting magnet. Samples were packed into 1.9 mm zirconia rotors and rotated at the magic angle at a rate of 37.5 kHz. Figure 5.11 shows the ¹³C solid-state NMR spectra of as-made STAM-1, activated as-made STAM-1, STAM-1 exposed to 100% RH for 1, 4 and 60 days, and STAM-1 exposed to 100% RH for 60 days before being reactivated. No changes can be observed to the local structure of the hydrated MOFs over the course of the hydration study, and the spectra match that of

the as-made MOF. The activated materials before and after exposure to 100% RH also yield identical spectra to each other, confirming the hydrothermal stability of the framework.

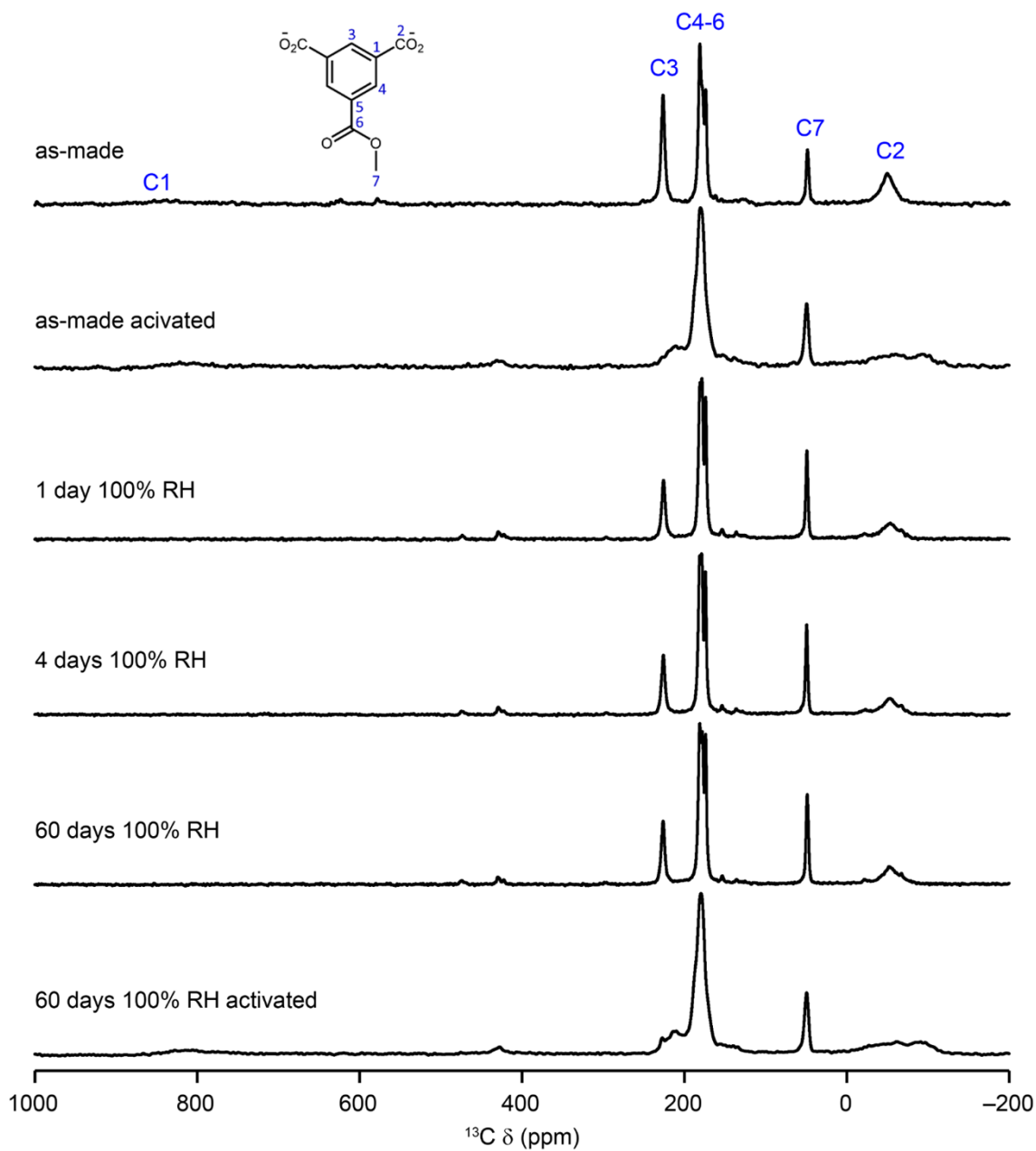


Figure 5.11. ^{13}C (14.1 T, 298 K, 37.5 kHz MAS) NMR spectra of a series of STAM-1 samples treated as indicated.

5.4.5 Ammonia Adsorption

Ammonia micro-breakthrough testing was performed using a micro-breakthrough apparatus. Samples of ca. 20 mg were packed between two cotton wool plugs in a glass tube with an internal diameter of 4 mm. Ammonia gas at a concentration of 500 ppm was passed through the sample at a flow rate of 30 ml min⁻¹ and the challenge gas output concentration was monitored using a photoionization detector (Phocheck Tiger). All experiments were performed at 298 K.

4.4.5.1 Ammonia Adsorption in the STAM Series

Samples of STAM materials were exposed to a stream of dry ammonia and the associated ammonia micro-breakthrough curves were recorded (Figure 5.12). The effluent concentration value initially recorded on the y-axis was recorded in “arbitrary units” and was adjusted at the point where the curve levelled off to provide normalised values of $C(\text{out})/C(\text{in})$.

The parent material: STAM-1 displayed an ammonia micro-breakthrough time of 62 minutes, while that STAM-17-n material with the shortest alkyl chain: STAM-17-Me recorded the highest micro-breakthrough time of 92 minutes (Table 5.3). This was followed by STAM-17-OMe and STAM-17-OEt with breakthrough times of 82 and 78 minutes respectively. STAM-17-O*n*Pr recorded a breakthrough time of 60 minutes and the materials with the bulkiest alkyl chains: STAM-17-O*n*Bu and STAM-17-O*t*Bu had the lowest breakthrough times of 40 minutes and 38 minutes respectively.

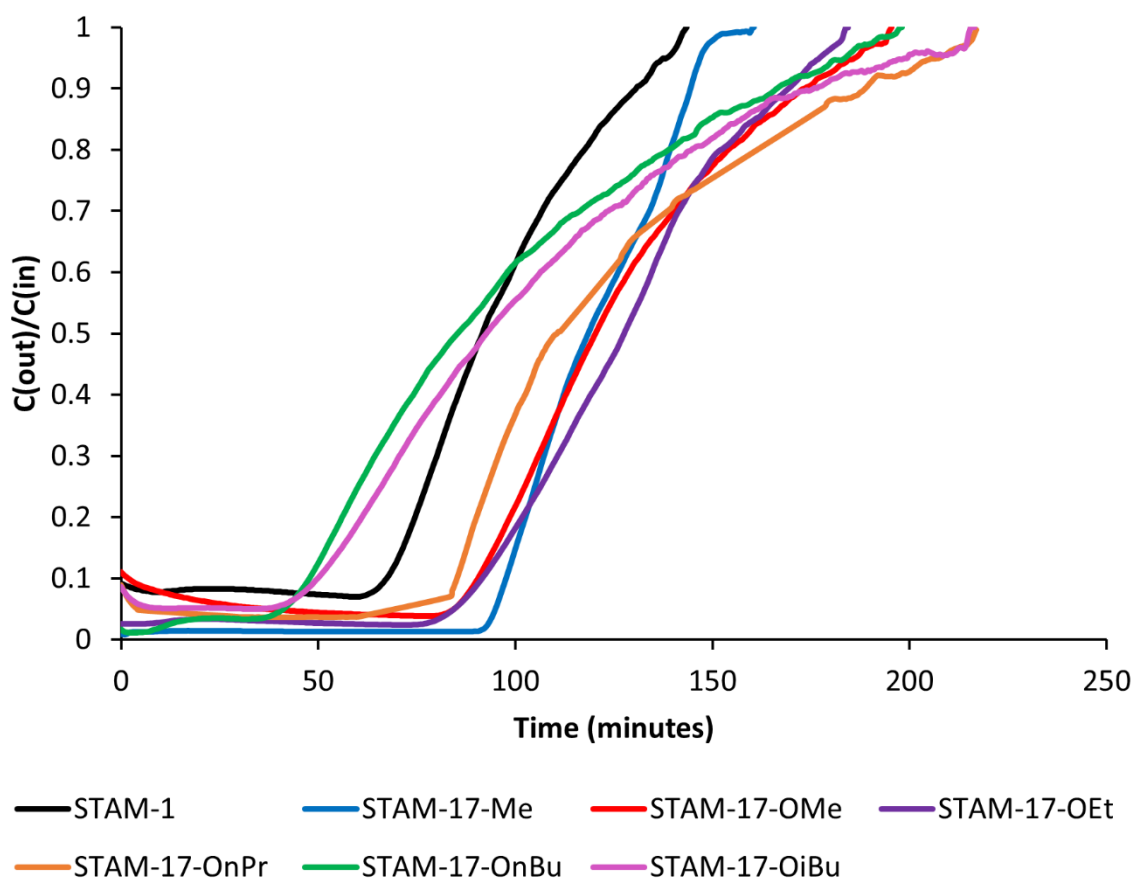


Figure 5.12. Normalised ammonia micro-breakthrough curves for the STAM series of MOFs.

Table 5.3. Ammonia breakthrough times for members of the STAM series.

Name:	Breakthrough time (minutes):
STAM-17-Me	92
STAM-17-OMe	82
STAM-17-OEt	78
STAM-1	62
STAM-17-OnPr	60
STAM-17-OnBu	40
STAM-17-OiBu	38

The time taken for ammonia to break through a plug of STAM-17-n sample appears to follow a linear trend, where the longer the alkyl substituent, the shorter the time taken to

break through the material (Figure 5.13). Such a trend may be correlated to the higher degree of pore-blocking in the hydrophobic pore with increasing alkyl chain length. In a dry ammonia airstream, the gas binds to the open metal sites of the MOF, though also enters the hydrophobic pore, so the greater the degree of pore blocking, the greater the impact on the breakthrough time. Another factor contributing to the trend may be the effect of chain length on the flexibility of the materials, which was shown to have an effect on argon and water adsorption. Longer chained members are less flexible and consequently allow the uptake of a lower quantity of ammonia. The parent material STAM-1 displayed a breakthrough time between that of STAM-17-OEt and STAM-17-OnPr, suggesting that steric bulk also has an effect on the ammonia breakthrough time and this was also seen in STAM-17-OnBu and STAM-17-OiBu, where the branched *i*-butoxy chain lead to a slight reduction in the time taken for ammonia to break through the material.

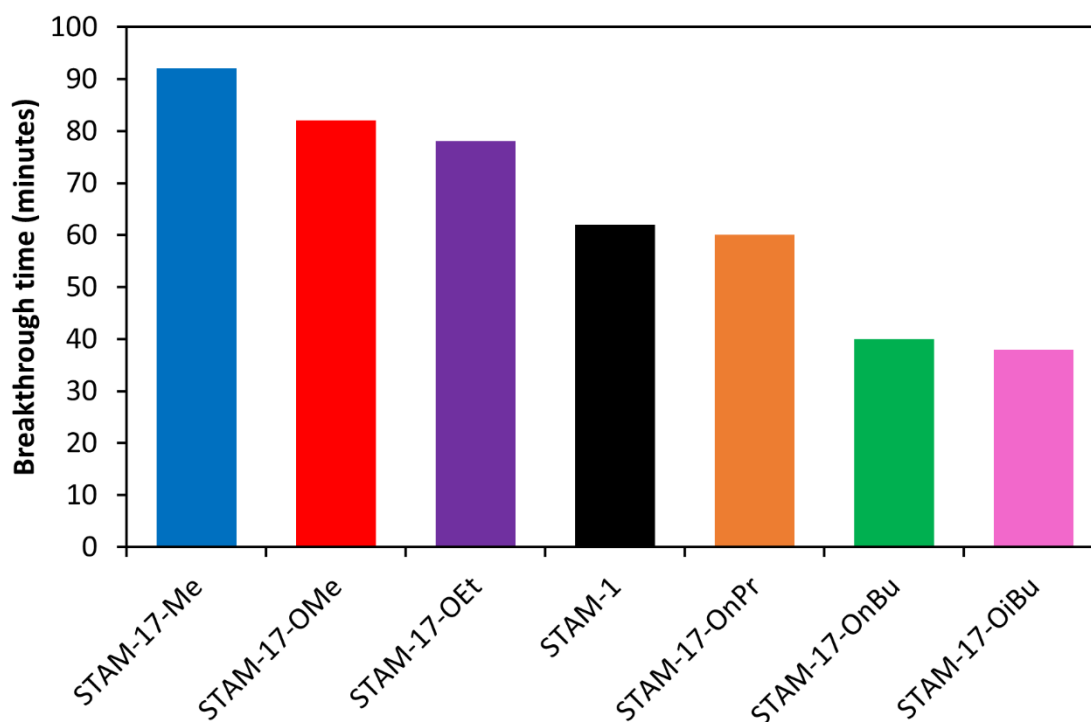


Figure 5.13. Trend of ammonia breakthrough times across the STAM series.

5.4.6 Hydrogen Cyanide Adsorption

Hydrogen cyanide micro-breakthrough testing was performed similarly to ammonia testing, using a micro-breakthrough apparatus. Samples of ca. 20 mg were packed between two cotton wool plugs in a glass tube with an internal diameter of 4 mm. Hydrogen cyanide gas at a concentration of 500 ppm was passed through the sample at a flow rate of 30 ml min⁻¹ and the challenge gas output concentration was monitored using either a photoionization detector (Phocheck Tiger) or a mass spectrometer. All experiments were performed at 298 K.

5.4.6.1 Hydrogen Cyanide Adsorption and Cyanogen Production in STAM-1 and HKUST-1

Tests against hydrogen cyanide were performed on STAM-1 and HKUST-1 for comparison. A sample tube was attached to the micro-breakthrough rig and dry air from a pre-filled gas-bag was flowed through the sample plug for 20 minutes, before changing the flow from dry air to 500 ppm hydrogen cyanide in nitrogen gas.

Upon adsorption of cyanide on a copper-containing compound in an oxygen-containing atmosphere, the toxic gas cyanogen (CN)₂ is produced from the reaction shown in Equation 1.1¹⁰



The quantity of cyanogen produced is tied to the quantity of hydrogen cyanide that is adsorbed and the concentration of cyanogen was monitored by mass spectrometry, where the greater the quantity of hydrogen cyanide removed from an airstream, the higher the quantity of cyanogen produced.

HKUST-1 removes significantly more cyanide than STAM-1 from an airstream and consequently produces much more cyanogen (Figure 5.14). While HKUST-1 decomposes in both water and hydrogen cyanide, the structural features that make STAM-1 stable to water and able to function in a humid environment also seem to prevent significant removal of cyanide from airstreams.

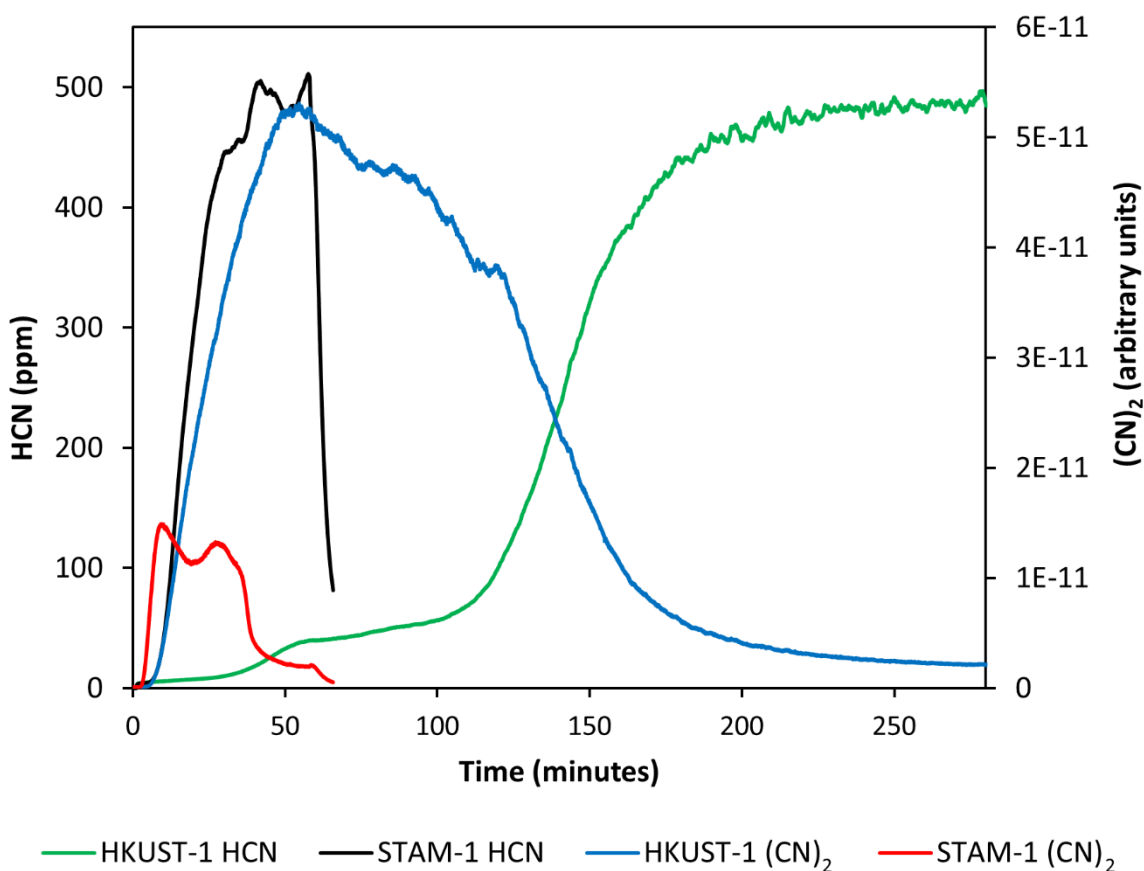


Figure 5.14. Hydrogen cyanide uptake and cyanogen production in STAM-1 and HKUST-1.

5.4.6.2 Hydrogen Cyanide Adsorption in the STAM Series

Samples of STAM materials were exposed to a stream of hydrogen cyanide in nitrogen and the associated cyanide micro-breakthrough curves were recorded (Figure 5.15). The effluent

concentration displayed on the y-axis was recorded using a mass spectrometer and is expressed in “arbitrary units”.

STAM-1 performs better than all of the STAM-17-n derivatives in dry cyanide testing, with a cyanide breakthrough time of 377 seconds (Table 5.4). STAM-17-*O**n*Pr, STAM-17-Me and STAM-17-OMe follow behind, with breakthrough times of 135, 110 and 104 s respectively. STAM-17-*O**i*Bu, STAM-17-OMe and STAM-17-*O**n*Bu show the lowest breakthrough times of 99, 86 and 79 s respectively.

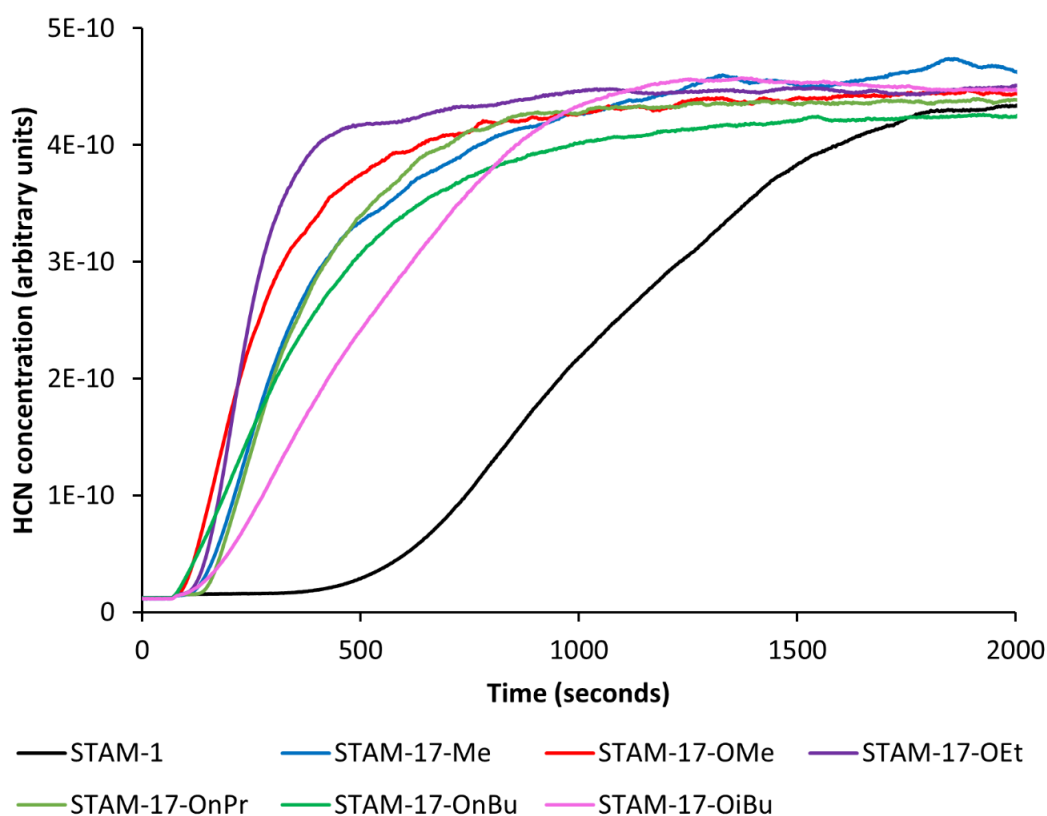


Figure 5.15. Hydrogen cyanide micro-breakthrough curves for the STAM series of MOFs.

Table 5.4. Hydrogen cyanide breakthrough times for STAM materials.

Material:	Breakthrough time (seconds):
STAM-1	377
STAM-17-Me	110
STAM-17-OMe	86
STAM-17-OEt	104
STAM-17-O <i>n</i> Pr	135
STAM-17-O <i>n</i> Bu	79
STAM-17-O <i>i</i> Bu	99

Testing against hydrogen cyanide in MOFs is not observed in literature and these initial tests were designed to investigate whether the STAM materials are viable candidates for the removal of hydrogen cyanide from airstreams. The results for hydrogen cyanide are not as clear as for ammonia and do not follow the same linear trend that was observed (Figure 5.16). This may be partially due to the rudimentary nature of the testing, where there will be a large degree of error associated with the very low micro-breakthrough times observed, though may truly be caused by complicated adsorption mechanisms that differ between frameworks. STAM-1 removes the greatest quantity of hydrogen cyanide, while the STAM-17-n series all remove significantly less, with no clear trend visible. The significantly greater cyanide adsorption displayed by STAM-1 further suggests a complicated adsorption mechanism involving both steric and electronic effects.

Despite the errors associated with measurements, the tests have shown that the STAM materials do remove hydrogen cyanide from airstreams and are therefore viable candidates in future testing, though further investigation is required to fully explain the mechanism behind adsorption.

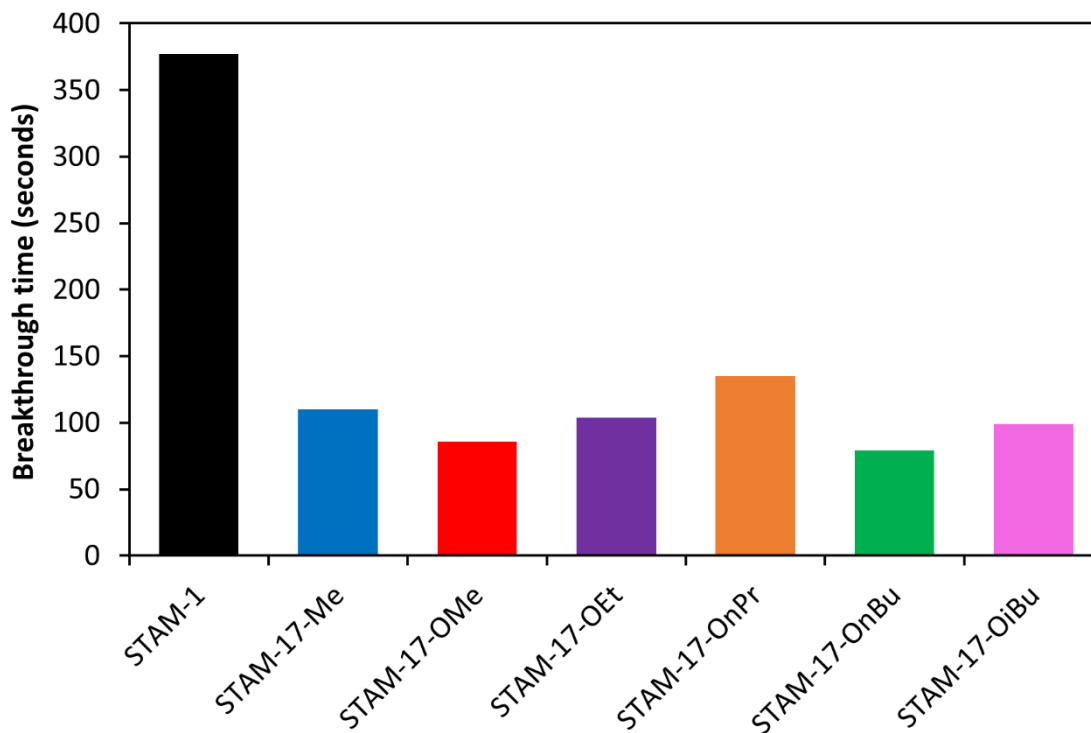


Figure 5.16. Trend of hydrogen cyanide breakthrough times across the STAM series.

5.5 Conclusion

In this chapter, other members of the STAM series of MOFs were introduced and their porosity, water uptake and gas adsorption capabilities were investigated.

Water stability measurements undertaken for selected materials show that the long-term hydrolytic stability described in chapter 4 for STAM-17-OEt is also seen in other members of the series and ammonia uptake follows a linear trend across the series, where members with shorter alkyl chains display greater micro breakthrough times than those with longer alkyl chains. Hydrogen cyanide testing was performed to investigate the viability of metal-organic frameworks for such an application and the cyanide uptake does not follow a linear trend across the STAM series. It does appear that the structural features that make STAM-1

and other STAM materials stable to water and able to function in humid environments seems to prevent significant removal of cyanide from airstreams.

5.6 References

- [1] M. I. Mohideen, B. Xiao, P. S. Wheatley, A. C. McKinlay, Y. Li, A. M. Z. Slawin, D. W. Aldous, N. F. Cessford, T. Düren, X. Zhao, R. Gill, K. M. Thomas, J. M. Griffin, S. E. Ashbrook and R. E. Morris, *Nat. Chem.*, 2011, **3**, 304-310.
- [2] L. N. McHugh, M. J. McPherson, L. J. McCormick, S. A. Morris, P. S. Wheatley, S. J. Teat, D. McKay, D. M. Dawson, C. E. F. Sansome, S. E. Ashbrook, C. A. Stone, M. W. Smith and R. E. Morris, *Nat. Chem.*, 2018, **10**, 1096-1102.
- [3] D. M. Dawson, C. E. F. Sansome, L. N. McHugh, M. J. McPherson, L. J. McCormick, M. J. McPherson, R. E. Morris and S. E. Ashbrook, *Solid State Nucl. Magn. Reson.*, 2019, **101**, 44-50.
- [4] H. Abourahma, G. J. Bodwell, J. Lu, B. Moulton, I. R. Pottie, R. Bailey Walsh and M. J. Zaworotko, *Cryst. Growth. Des.*, 2003, **3**, 513-519.
- [5] H. W. Gibson, H. Wang, Z. Niu, C. Slebodnick, L. N. Zhakharov and A. L. Rheingold, *Macromolecules*, 2012, **45**, 1270-1280.
- [6] A. Vidonne and D. Philp, *Tetrahedron*, 2008, **64**, 8464-8475.
- [7] J. Rouquerol, D. Avnir, C. W. Fairbridge, D. H. Everett, J. M. Haynes, N. Pernicone, J. D. F. Ramsay, K. S. W. Sing and K. K. Unger, *Pure Appl. Chem.*, 1994, **66**, 1739-1758.
- [8] B. Bozbiyik, T. Van Assche, J. Lannoeye, D. E. De Vos, G. V. Baron, and J. F. M. Denayer, *Adsorption*, 2016, **23**, 185-192.
- [9] A. Terracina, L. N. McHugh, M. Todaro, S. Agnello, P. S. Wheatley, F. M. Gelardi, R. E. Morris and G. Buscarino, 2019, manuscript under review.
- [10] L. Wang, X. Wang, X. Jing and P. Ning, *RSC Adv.*, 2016, **6**, 113834-113843.

Chapter 6: Metal-organic Framework-Activated Carbon Composite Materials for the Removal of Ammonia from Contaminated Airstreams

6.1 Aim

The aim of this chapter is to describe the synthesis of materials where a MOF may be combined with activated carbon to provide MOF-activated carbon composite materials and to then investigate their gas adsorption capacity and water stability. The composites allow powdered MOF samples to be manufactured into a more useable, granular form that may potentially be used inside a filter in air purification systems.

6.2 Introduction

MOFs have shown potential as adsorbent materials in the removal of toxic industrial chemicals such as ammonia from airstreams,^{1,2} and research is currently underway into the possibility of incorporating the material into personal protective equipment, such as respirator canisters.³

One of the main issues regarding the potential use of MOFs in personal protective equipment is the physical form of MOFs in that they typically form fine powders, which a wearer cannot breathe through. This may be addressed by adopting form-altering techniques such as pelletization,⁴ though this leads to increased synthetic and engineering costs compared to cheaper, currently used adsorbent materials such as activated carbon. One compromise may be to combine a MOF and activated carbon into a composite material that exhibits positive characteristics from both materials. The growth of MOFs within activated

carbons in order to improve the mechanostability of MOFs was reported by Casco,⁵ and was further developed by Aurbach to impart electrical conductivity into an otherwise non-conducting MOF.⁶ MOFs are chemically good choices for the adsorption of smaller molecules such as ammonia and hydrogen sulfide, due to the strong and selective interactions formed between the framework and the target chemicals. Activated carbons conversely excel in the physisorption of larger molecules such as nerve agents due to their greater porosity and larger pore diameters.^{7,8} By tuning the weight proportion of MOF incorporated into the materials, it is reasonable to suggest that the composites may be tailored to remove specific gases or a broader range of contaminants.

In chapter 4, the structure of STAM-17-OEt was reported and its exceptional hydrolytic stability and ability to remove ammonia from both dry and humid airstreams were highlighted. In chapter 5, STAM-17-O*n*Pr was highlighted as another promising material in gas adsorption. In this chapter, the synthesis of novel MOF-carbon composite materials containing STAM-17-OEt or STAM-17-O*n*Pr and BPL activated carbon are reported. BPL is an unimpregnated coal-based carbon, which is representative of activated carbons that have been used to prepare impregnated carbons such as those often used in respiratory protection.

This chapter will mainly focus on the STAM-17-OEt@BPL materials,⁹ though some analysis of the STAM-17-O*n*Pr@BPL materials shall be discussed, along with other attempts at STAM@AC composite synthesis.

6.3 Experimental Procedures

All reagents, unless stated, were obtained from commercial sources and were used without further purification.

The BPL activated carbon used in this research was supplied by Chemviron Carbon Ltd, unnamed carbon foam was provided by Dstl and general purpose adsorbent matrix activated coconut charcoal, 20-40 mesh was supplied by Sigma Aldrich.

6.3.1 Synthesis of STAM-17-OEt@BPL composites⁹

STAM-17-OEt@BPL₁ was prepared by suspending BPL activated carbon (0.24 g, 20.3 mmol) and 5-ethoxybenzene-1,3-dicarboxylic acid (0.13 g, 0.60 mmol) in distilled water (10 mL), before stirring at 45 °C for 2 hours. Copper acetate monohydrate (0.12 g, 0.60 mmol) was added and stirring was continued at 45 °C for a further 2 hours. The temperature was increased to 95 °C and the mixture stirred for a further 3 days. The suspension was centrifuged at 6000 rpm for 10 minutes, and the solid was washed with distilled water (15 mL). The centrifuging and washing cycle was repeated a further 3 times, before drying the solid in air to provide a material with 77% STAM-17-OEt by weight. STAM-17-OEt@BPL₂ and STAM-17-OEt@BPL₃ were synthesised using the same procedure and quantity of BPL carbon, and appropriate quantities of STAM-17-OEt precursors: 5-ethoxybenzene-1,3-dicarboxylic acid (0.08 g and 0.06 g respectively) and 1 equivalent of copper acetate monohydrate (0.08 g and 0.06 g respectively), resulting in composites with 51% and 39% STAM-17-OEt by weight.

6.3.2 Synthesis of STAM-17-*O_n*Pr@BPL Composites

STAM-17-*O_n*Pr@BPL_1 was prepared by suspending BPL activated carbon (0.24 g, 20.3 mmol) and 5-*n*-propoxybenzene-1,3-dicarboxylic acid (0.13 g, 0.57 mmol) in distilled water (10 mL), before stirring at 45 °C for 2 hours. Copper acetate monohydrate (0.11 g, 0.57 mmol) was added and stirring was continued at 45 °C for a further 2 hours. The temperature was increased to 95 °C and the mixture stirred for a further 3 days. The suspension was centrifuged at 6000 rpm for 10 minutes, and the solid was washed with distilled water (15 mL). The centrifuging and washing cycle was repeated a further 3 times, before drying the solid in air to provide a material with 77% STAM-17-*O_n*Pr by weight. STAM-17-*O_n*Pr@BPL_2 and STAM-17-*O_n*Pr@BPL_3 were synthesised using the same procedure and quantity of BPL carbon, and appropriate quantities of STAM-17-*O_n*Pr precursors: 5-*n*-propoxybenzene-1,3-dicarboxylic acid (0.09 g and 0.06 g respectively) and 1 equivalent of copper acetate monohydrate (0.08 g and 0.06 g respectively), resulting in composites with 51% and 39% STAM-17-*O_n*Pr by weight.

6.3.3 Attempted Synthesis of STAM-17-OEt@Coconut Shell Carbon Composites

STAM-17-OEt@coconut shell materials were prepared using the same procedure and quantities used in the synthesis of the STAM-17-OEt@BPL composite materials as discussed in section 6.3.1.

6.3.4 Attempted Synthesis of STAM-17-OEt@Carbon Foam Composites

STAM-17-OEt@carbon foam was prepared by suspending carbon foam (0.24 g, 20.3 mmol) and 5-ethoxybenzene-1,3-dicarboxylic acid (0.13 g, 0.60 mmol) in distilled water (10 mL), before stirring at 45 °C for 2 hours. Copper acetate monohydrate (0.12 g, 0.60 mmol) was added and stirring was continued at 45 °C for a further 2 hours. The temperature was increased to 95 °C and the mixture stirred for a further 3 days. The suspension was centrifuged at 6000 rpm for 10 minutes, and the solid was washed with distilled water (15 mL). The centrifuging and washing cycle was repeated a further 3 times, before drying the solid in air.

6.4 Results and Discussion

6.4.1 Formation of STAM@BPL Composites

The STAM@BPL materials were synthesised by combining the required linker: either 5-ethoxybenzene-1,3-dicarboxylic acid or 5-*n*-propoxybenzene-1,3-dicarboxylic acid with copper acetate monohydrate and BPL activated carbon in an aqueous solution at reflux over the course of three days (Figure 6.1).

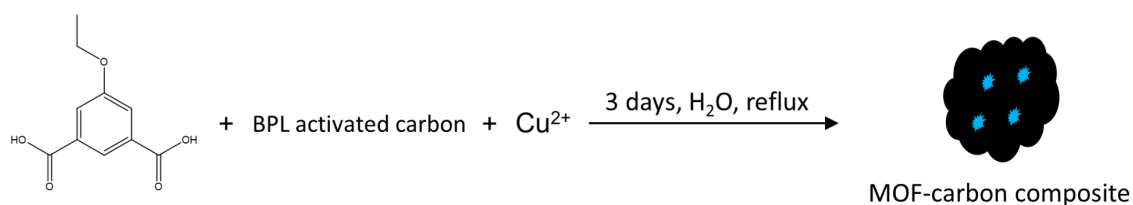


Figure 6.1. Schematic of MOF-activated carbon composite synthesis, showing 5-ethoxybenzene-1,3-dicarboxylic acid as an example.

As shown schematically in Figure 6.2, the synthesis of MOF-activated carbon composite materials involves two steps: (1) *In situ* synthesis of the STAM MOF inside BPL activated carbon particles and (2) Centrifugation and washing of the resulting suspension to afford the STAM@BPL composite materials.

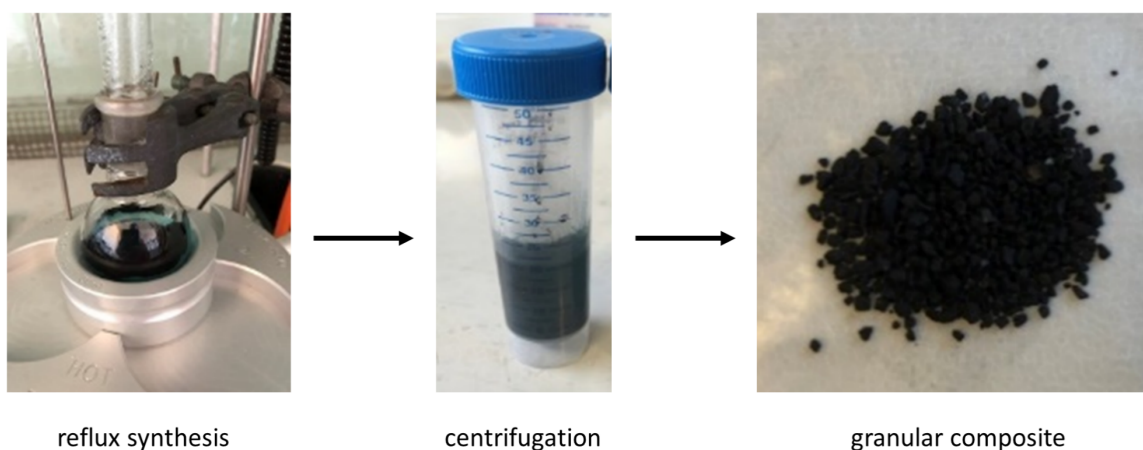


Figure 6.2. Three-step synthesis of MOF-activated carbon composite materials. The resulting granular material has no obvious ‘free’ MOF particles.

The procedure leads to black granular materials that appear to the naked eye similar to unimpregnated carbon samples. Importantly, no ‘free’ STAM-17-OEt or STAM-17-OnPr crystals were observed optically, suggesting that the MOF is confined within the carbon. The granular form of the STAM@BPL composites addresses a key issue in the preparation of functional filtration materials, where typically unusable powdered MOF samples have been manufactured into a more useable form by incorporation into a granular activated carbon.

Three weight percentages of STAM-17-OEt@BPL are presented here, with 77%, 51% and 39% w/w MOF loading and are henceforth named STAM-17-OEt@BPL_1, STAM-17-

OEt@BPL_2 and STAM-17-OEt@BPL_3 respectively. Three STAM-17-OnPr@BPL composite are also presented, also with 77%, 51% and 39% w/w MOF loading and are henceforth named STAM-17-OnPr@BPL_1, STAM-17-OnPr@BPL_2 and STAM-17-OnPr@BPL_3 respectively. The loadings are expressed in weight percentage of MOF, based on an assumed 100% yield of STAM MOF, for example, where 77% loading signifies that each gram of carbon has 0.77 g of MOF added.

6.4.2 Powder X-ray Diffraction of STAM@BPL Composites

Powder X-ray diffraction patterns were collected in flat plate discs, using a PANalytical Empyrean with Cu X-ray tube and primary beam monochromator (Cu $K\alpha_1$). Measurements were performed at 298 K and samples did not require activation prior to recording. Samples were not ground prior to measurement, in order to maintain the physical structure of the composite materials.

6.4.2.1 Powder X-ray Diffraction Analysis

Powder X-ray diffraction confirms the presence of the parent MOFs: STAM-17-OEt (Figure 6.3) and STAM-17-OnPr (Figure 6.4) in the composite materials, since some of the crystallinity associated with the MOFs may be observed along with amorphous character arising from the carbon.

The characteristic peaks associated with STAM-17-OEt and STAM-17-OnPr are present in the composite samples and the relative peak positions are unchanged. MOF may be observed at all three loadings, where the samples containing the highest weight percentage of MOF, i.e. STAM-17-OEt@BPL_1 and STAM-17-OnPr@BPL_1, display the greatest level of

crystallinity. STAM-17@OEt_BPL_3 and STAM-17-O n Pr@BPL_3 show considerably less intensity due to the significantly lower quantity of MOF incorporation.

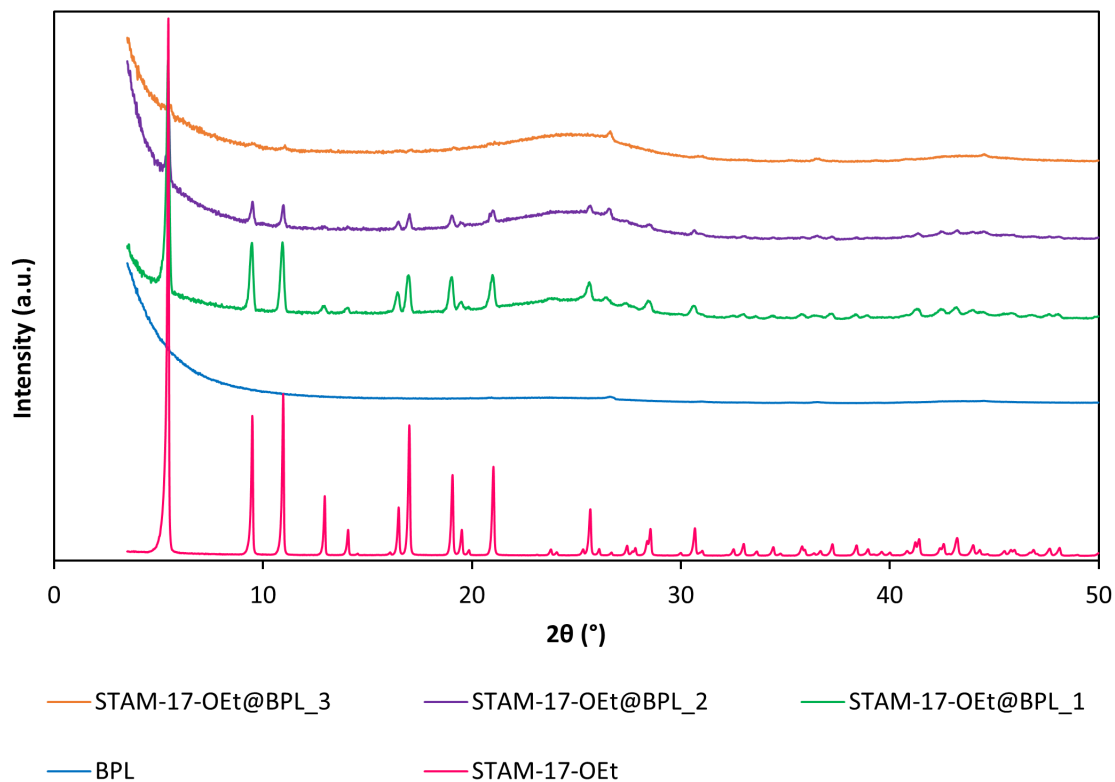


Figure 6.3. Powder X-ray diffraction patterns of the STAM-17-OEt@BPL composite materials showing the decreasing crystallinity in the samples with lower quantities of MOF incorporation.

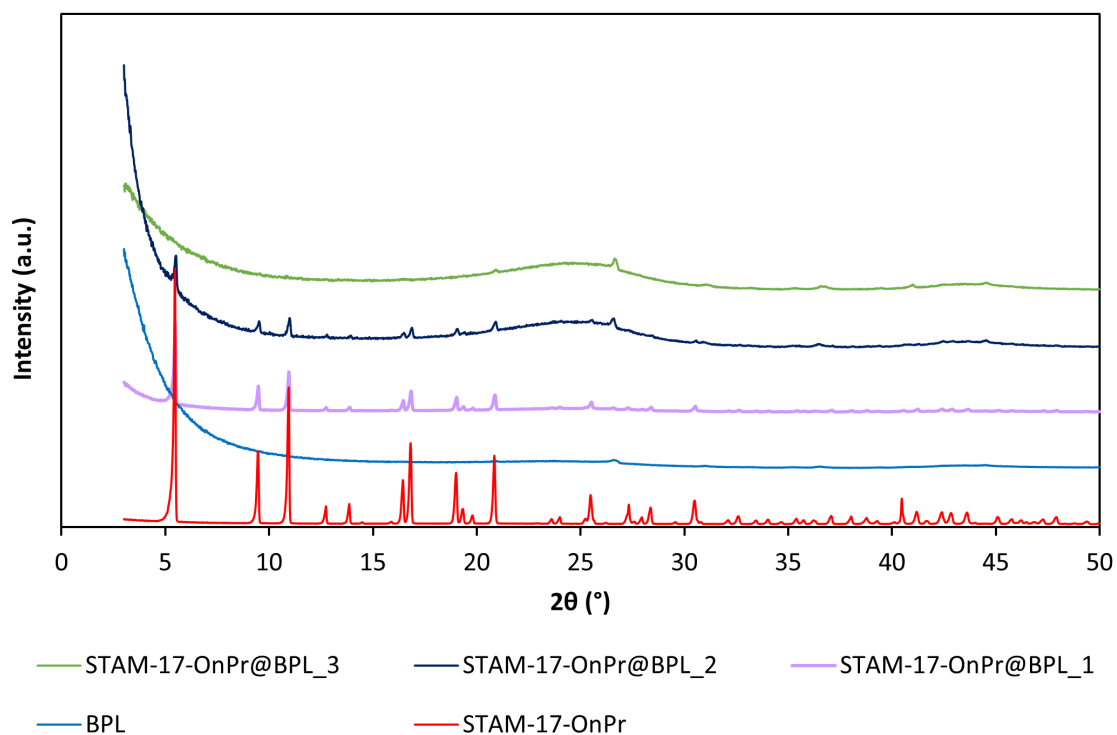


Figure 6.4. Powder X-ray diffraction patterns of the STAM-17-OnPr@BPL composite materials, again showing the decreasing crystallinity in the samples with lower quantities of MOF incorporation.

6.4.3 Scanning Electron Microscopy

Scanning electron microscopy (SEM) images were recorded using a Jeol JSM 5600 scanning electron microscope at 25 kV and energy dispersive X-ray spectroscopy (EDX) copper elemental mapping was performed using an Oxford Inca Energy system.

6.4.3.1 Scanning Electron Microscopy Analysis of STAM-17-OEt@BPL Composites

Powder X-ray diffraction proves the presence of MOF crystals in the composite samples, though it does not indicate whether the MOF is incorporated within the carbon granules or exists separately. SEM images (Figure 6.5) display the overall morphology of the unimpregnated BPL carbon and STAM-17-OEt respectively.

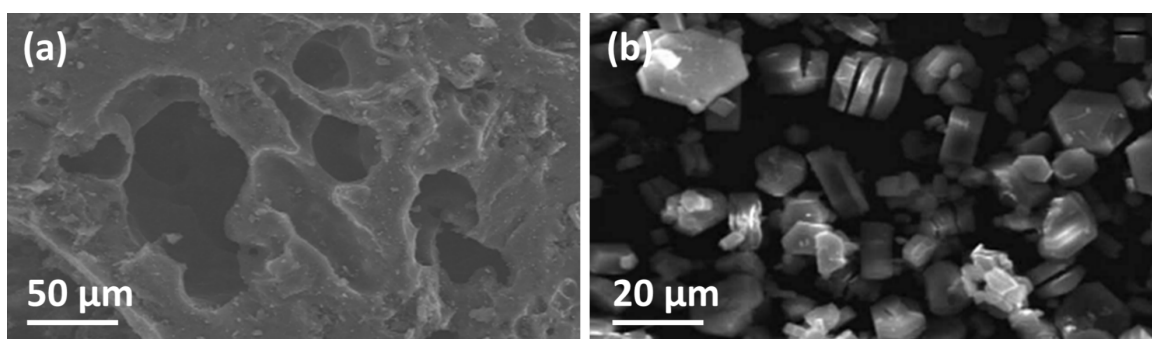


Figure 6.5. SEM images of (a) BPL activated carbon and (b) STAM-17-OEt.

The large voids of $\sim 50 \mu\text{m}$ in BPL carbon are clearly visible and allow entry of the MOF components into the granules and therefore the synthesis of smaller MOF crystals within the carbon. STAM-17-OEt crystals have hexagonal morphology and are usually observed as stacked hexagons with typically $\sim 20 \mu\text{m}$ diameter.¹⁰ SEM images and associated EDX copper elemental mapping images of STAM-17-OEt@BPL₁ (Figure 6.6 (a), (b)), STAM-17-OEt@BPL₂ (Figure 6.6 (c), (d)) and STAM-17-OEt@BPL₃ (Figure 6.6 (e), (f)) verify the fairly even distribution of copper and therefore STAM-17-OEt throughout the carbon. Some areas of more concentrated copper are visible on the surface of the materials, and this is especially true of the samples with higher MOF loading, which suggests that a small amount

of STAM-17-OEt has crystallised on the outside of the carbon particles. No discrete MOF particles were observed however, further signifying that STAM-17-OEt is largely confined inside the carbon particles.

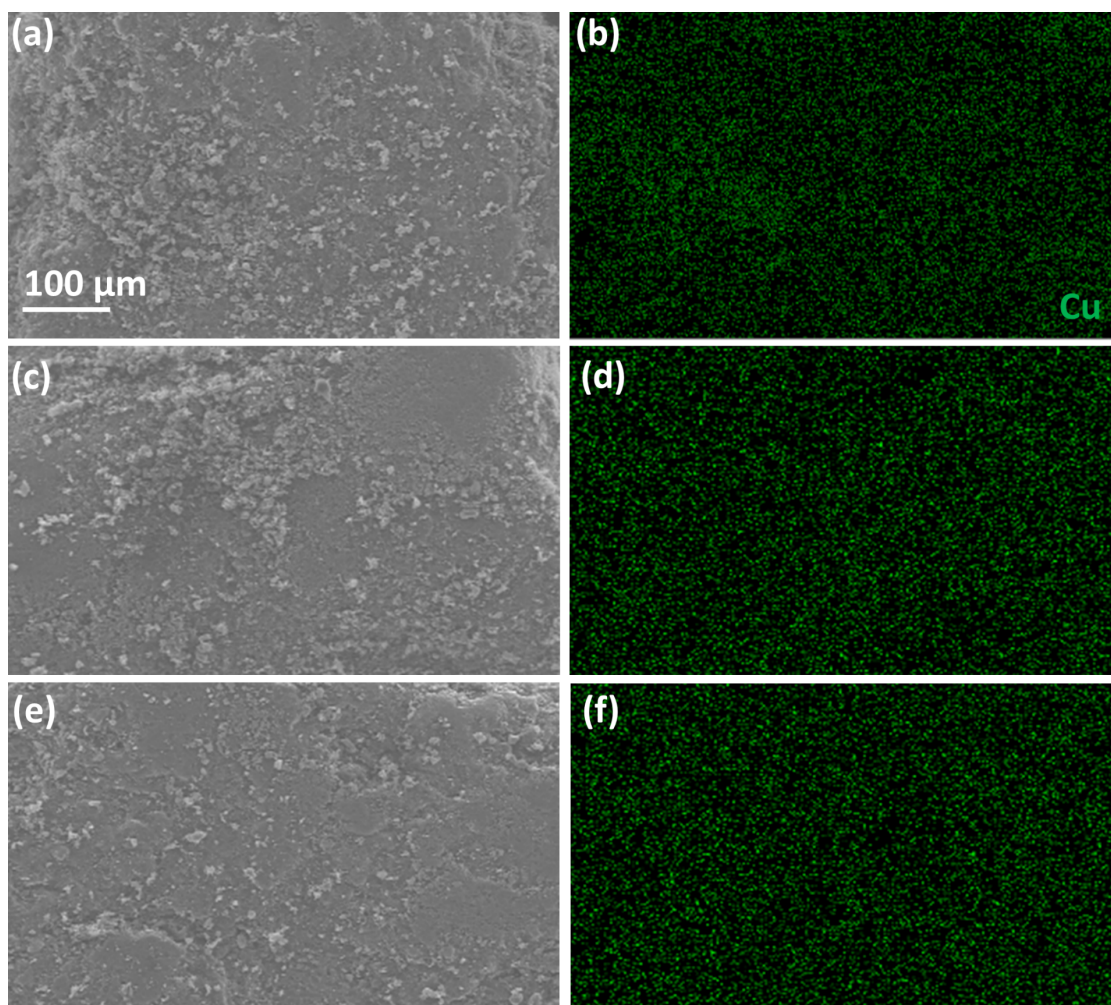


Figure 6.6. SEM images and their corresponding EDX copper electron mapping images of: (a) STAM-17-OEt@BPL_1; (b) STAM-17-OEt@BPL_2 and (c) STAM-17-OEt@BPL_3.

6.4.3.2 Scanning Electron Microscopy Analysis of Other Selected Attempted Composites

While BPL activated carbon was ultimately successful in terms of MOF incorporation, the material is a somewhat unrefined carbon source. Consequently, many other carbons that contained fewer impurities were used in the attempted syntheses of composite materials, though in most cases, the MOF was not incorporated into the carbon due to the large degree of microporosity in the materials and the relative lack of larger porosity, which did not provide enough space for the MOF crystals to grow. In other cases, it was attempted to grow the MOF around a carbon support, such as a carbon-based “foam”, where individual carbon beads are fused into a porous network structure. The MOF ‘clings’ to the outside of the carbon beads, due to the inherent microporosity in the material. The lack of large pores or voids leads the MOF to form on the outside of the carbon foam (Figure 6.7).

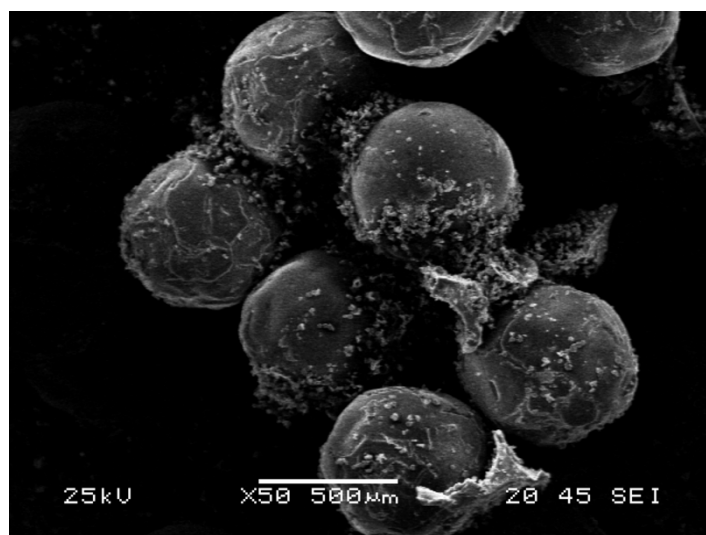


Figure 6.7. SEM image of carbon ‘foam’, with STAM-17-OEt adhered to the outside of the carbon ‘beads’.

While this was ultimately successful, it was unclear how resistant to handling the foam composite would be, so further investigation was not undertaken and it was decided to continue with only granular carbons.

An alternative to coal-based activated carbons are those derived from coconut shells.¹¹ Due to the granular nature of the activated carbon, it was hoped that the carbon would provide similar composites to those obtained using BPL activated carbon. General purpose adsorbent matrix activated coconut charcoal, 20-40 mesh was purchased and it was attempted to synthesise three composites with equal MOF loadings to those used in the synthesis of the STAM@BPL composites. Evidence of free MOF crystals was observed with the naked eye after synthesis and SEM images further indicate that STAM-17-OEt exists only on the surface of the carbon (Figure 6.8). The material lacks the large ‘voids’ observed in BPL carbon that appear to be required in order to allow the MOF inside the carbon.

It was therefore decided to focus on BPL as a carbon support in subsequent studies.

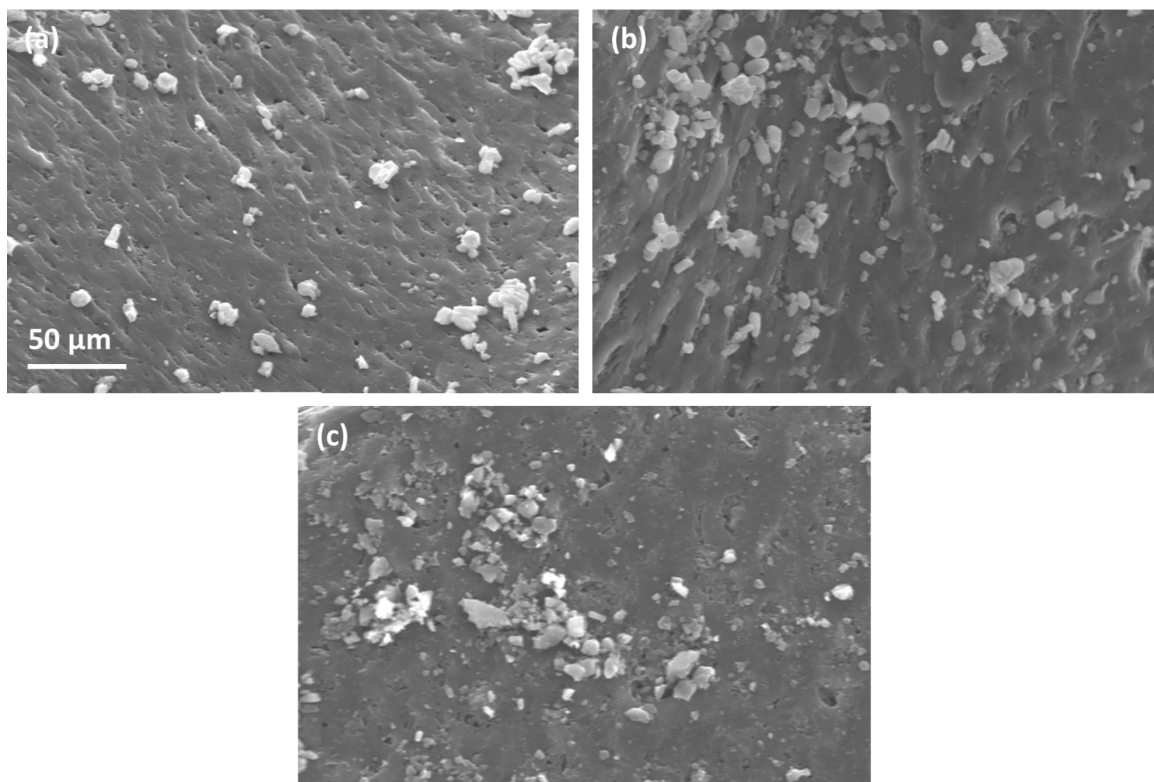


Figure 6.8. SEM images of: (a) STAM-17-OEt@coconut shell_1; (b) STAM-17-OEt@coconut shell_2 and (c) STAM-17-OEt@coconut shell_3, where the MOF may be seen coating the surface of the carbon. The MOF appears to only exist on the surface of the carbon.

6.4.4 Surface Area Analysis

Nitrogen BET analysis was performed on STAM-17-OEt@BPL samples at 77 K on a Micromeritics ASAP 2020 Surface Area and Porosity Analyser and the BET surface areas were calculated using the Rouquerol method.¹² Samples (ca. 120 mg) were activated at 423 K overnight prior to measurement.

6.4.4.1 Surface Area Analysis of STAM-17@BPL Composites

In order to investigate the effect of MOF incorporation on carbon porosity, nitrogen BET adsorption measurements were performed. BPL activated carbon has a wide pore size distribution, consisting of both micro and mesopores and has a measured surface area of $1209.2 \pm 7.1 \text{ m}^2/\text{g}$, which is comparable to the literature value of $1200 \text{ m}^2/\text{g}$.¹³ STAM-17-OEt, like other MOFs, is a microporous material, though has a surprisingly low surface area of $58.4 \pm 0.3 \text{ m}^2/\text{g}$.¹⁰ As described in chapter 4, the low porosity in STAM-17-OEt is due to the switchable structure of the material, where upon activation, the pores in STAM-17-OEt become constricted by the change in the coordination environment of the copper paddlewheels. The constriction of the pores consequently impacts the porosity, though the low surface area observed for STAM-17-OEt is not representative of the material's overall gas adsorption capability. A significant drop in the porosity of the carbon upon incorporation of the MOF would provide further evidence that STAM-17-OEt is inside the carbon, due to partial pore-blocking by STAM-17-OEt crystals. The surface areas of the composites do fall in-between those of the MOF and carbon alone, where the higher the MOF content, the lower the surface area (Figure 6.9 and Table 6.1). The greatest loss of porosity is observed in the highest loading sample: STAM-17-OEt@BPL_1, with a percentage decrease of 90% compared to unimpregnated BPL activated carbon.

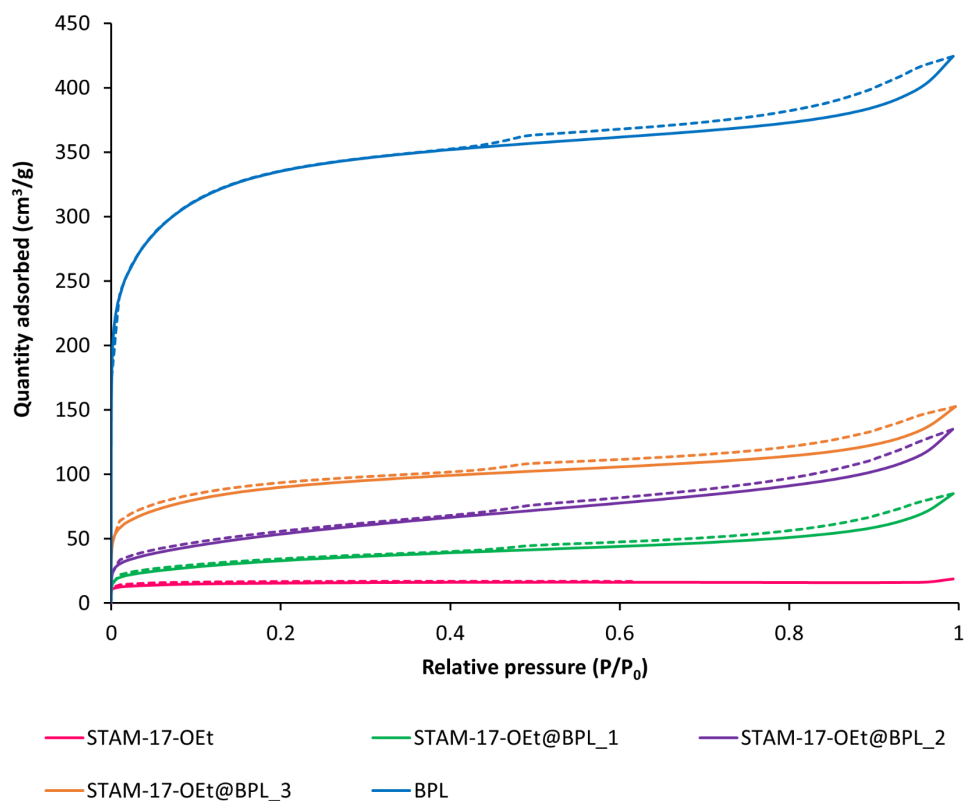


Figure 6.9. Nitrogen isotherms recorded at 77 K of STAM-17-OEt, STAM-17-OEt@BPL₁, STAM-17-OEt@BPL₂, STAM-17-OEt@BPL₃ and BPL activated carbon. Solid lines represent adsorption and dashed lines represent desorption.

Table 6.1. Nitrogen BET surface areas of STAM-17-OEt, BPL activated carbon and the three STAM-17-OEt@BPL composites.

Material	BET Surface Area (m ² /g)
STAM-17-OEt	58.4 ± 0.3
STAM-17-OEt@BPL ₁	115.8 ± 0.8
STAM-17-OEt@BPL ₂	188.2 ± 1.6
STAM-17-OEt@BPL ₃	323.3 ± 2.1
BPL activated carbon	1209.2 ± 7.1

6.4.5 Adsorption Isotherms of STAM-17-OEt@BPL Materials

SEM and BET analyses both suggest that STAM-17-OEt is largely confined to the pores of BPL activated carbon, but to prove whether the MOF is actually inside the carbon, dynamic vapour sorption (DVS) studies using either cyclohexane or water vapours were performed using a DVS instrument. Cyclohexane is known to adsorb on the carbon but not the MOF (due to its relatively small pore size); whilst water vapour adsorbs on both, the resulting isotherms are very different in shape. In either case, pre-activated samples were exposed to increasing levels of relative pressure and the associated uptake was measured at each point. Comparison of the adsorption branches in the water isotherms (Figure 6.10) shows that BPL, STAM-17-OEt and a physical mixture of the two components equivalent to the highest composite carbon:MOF ratio of 1.00:0.77 weighted average all show a similar mass uptake (ca. 15% w/w) at approximately 55% relative humidity. A lower water uptake of ~12% for STAM-17-OEt@BPL₁ is observed at the same level of RH, suggesting that the MOF is ‘inside’ the composite and therefore the pores, rather than outside as seen in the physical mixture. The shape of the STAM-17-OEt@BPL₁ isotherm is closer to BPL than STAM-17-OEt, though the total water uptake after exposure to 95% RH is closer to that of STAM-17-OEt, showing that the composites show adsorption characteristics arising from both materials.

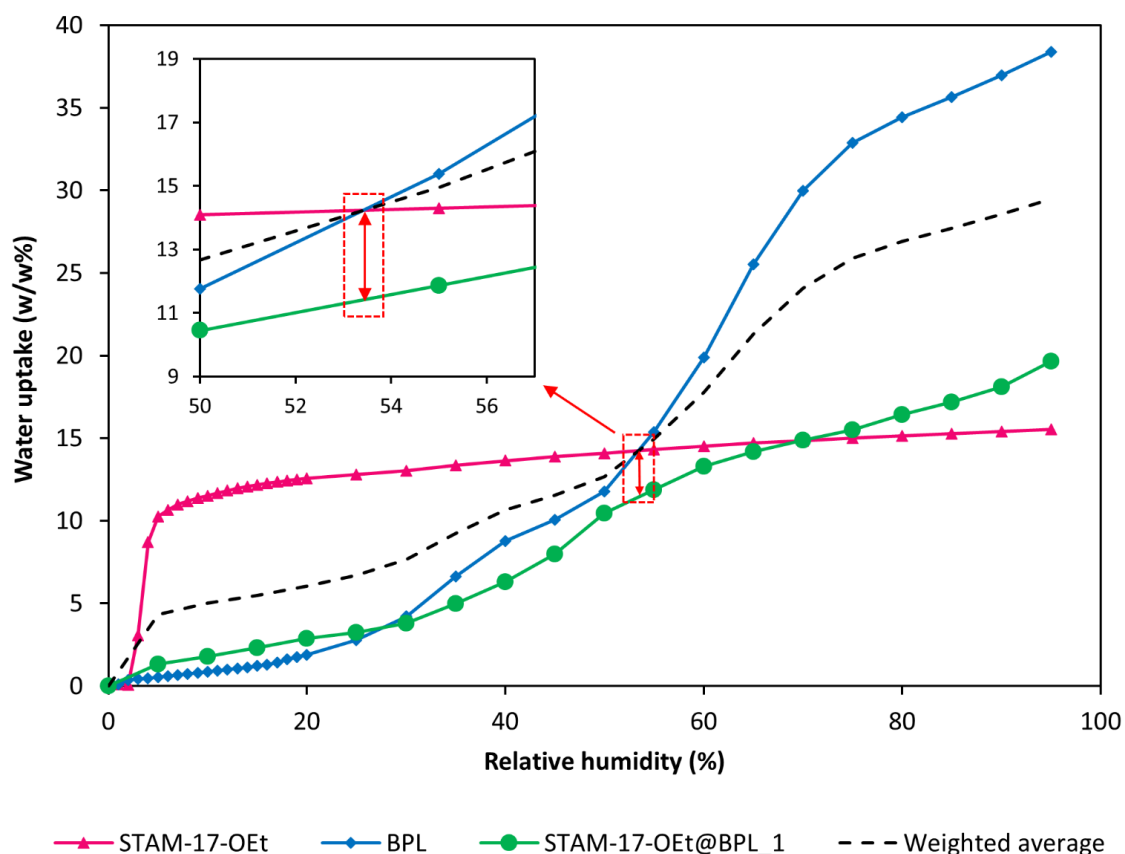


Figure 6.10. Adsorption branches of water isotherms displaying the shape difference and decrease in water uptake in the isotherm of STAM-17-OEt@BPL_1. An expansion of the region from 50–57% RH highlighting the difference in water uptake values may be observed in the figure inset.

Adsorption isotherms of cyclohexane are shown in Figure 6.11. This molecule has been used as a model physisorbed chemical which is often used to assess the performance of respirator canisters.¹⁴ It has an atomic radius of 5.8 \AA ,¹⁵ and the microporous nature of STAM-17-OEt prevents significant uptake of cyclohexane. The abundance of larger micro- and mesopores found in BPL activated carbon however,¹³ leads to a much greater uptake than in the MOF. The isotherms show that in the composite materials some of the carbon is still accessible to

cyclohexane, even at the highest MOF loading in STAM-17-OEt@BPL_1, showing that the transport pores are not simply being ‘plugged’ with MOF.

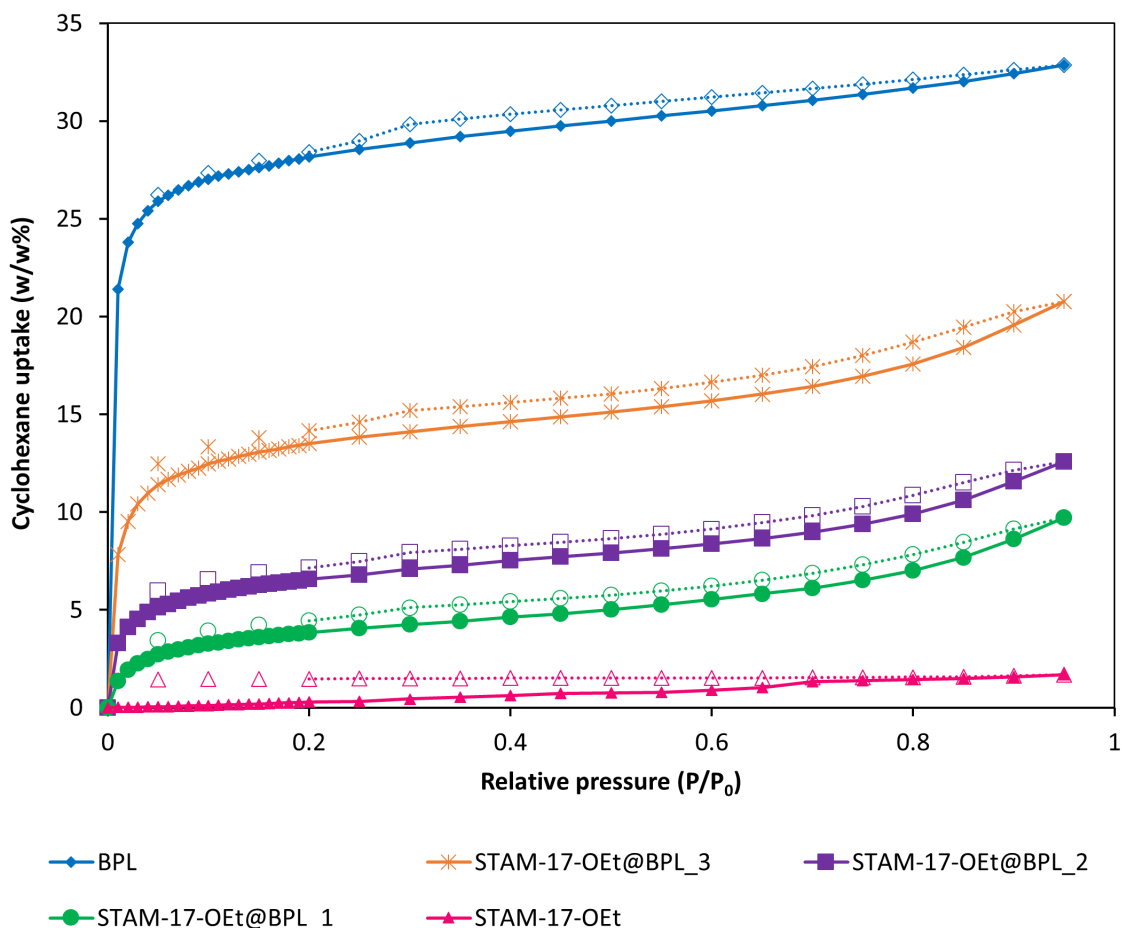


Figure 6.11. Cyclohexane isotherms of BPL activated carbon and the STAM-17-OEt@BPL composites showing the decrease in cyclohexane uptake with increasing MOF loading.

Both STAM-17-OEt and BPL activated carbon are stable to moisture and it was anticipated that the MOF-carbon composite materials would maintain this water stability. A water adsorption-desorption cycling experiment was employed to investigate this, where a pre-activated sample was exposed to 90% RH in a series of 8 hour cycles.¹⁶ The maximum water uptake (Figure 6.12) remains consistent throughout the cycling experiments, suggesting that

the composite is stable even in very harsh conditions. Such hydrolytic stability is undoubtedly imperative in this context due to the moisture always present in breathable air.

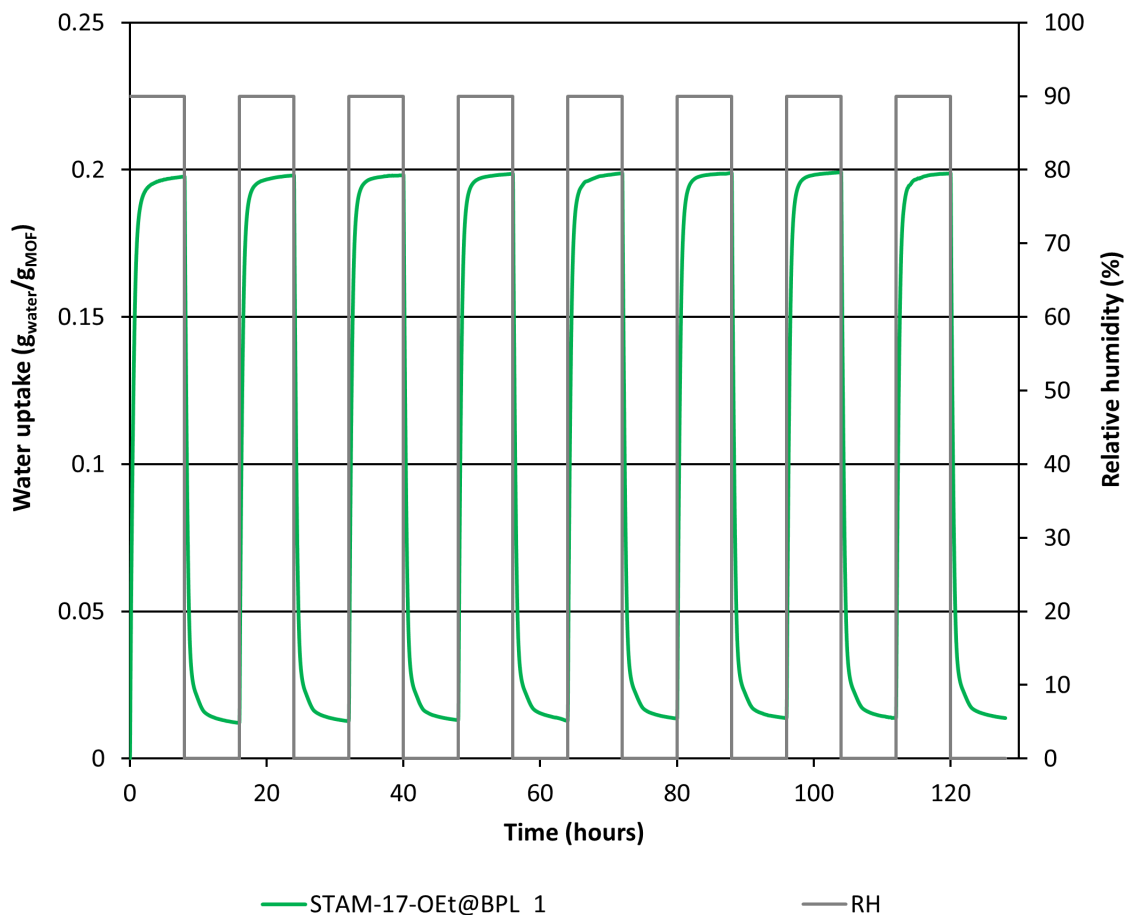


Figure 6.12. Vapour water stability at 298 K for STAM-17-OEt@BPL_1, demonstrated by the change in the sample's water uptake through 8 water adsorption/desorption cycle measurements (green trace) to 90% relative humidity (grey trace). The chart shows that after the initial water uptake, the sorption capacity remains constant throughout the experiment.

6.4.6 Ammonia Uptake

Ammonia micro-breakthrough testing was performed using a micro-breakthrough apparatus. The set-up allowed the testing of porous materials against known concentrations

of challenge gases. Pre-activated samples (ca. 20 mg) were placed on frit inside a metal sample holder and the sample was placed inside a chamber, where ammonia gas at a concentration of 450 ppm was passed through the sample at a flow rate of 55 mL min⁻¹. The effluent concentration was monitored using a photoionization detector (Phocheck Tiger) and all experiments were performed at 298 K.

6.4.6.1 Micro-breakthrough

In order to investigate the TIC gas adsorption capacity of the materials, micro-breakthrough experiments were undertaken, using ammonia as the challenge gas. The resulting micro-breakthrough curves (Figure 6.13) show that BPL carbon alone is fairly ineffective in the removal of ammonia - with an ammonia uptake of 4.3 mg g⁻¹. STAM-17-OEt performs significantly better, adsorbing 43.3 mg g⁻¹. The highest loading MOF-carbon sample STAM-17-OEt@BPL_1 adsorbs 17.8 mg g⁻¹, which is almost halfway between the values for unimpregnated BPL carbon and STAM-17-OEt. The ammonia uptake values for all loadings are shown in Table 6.2.

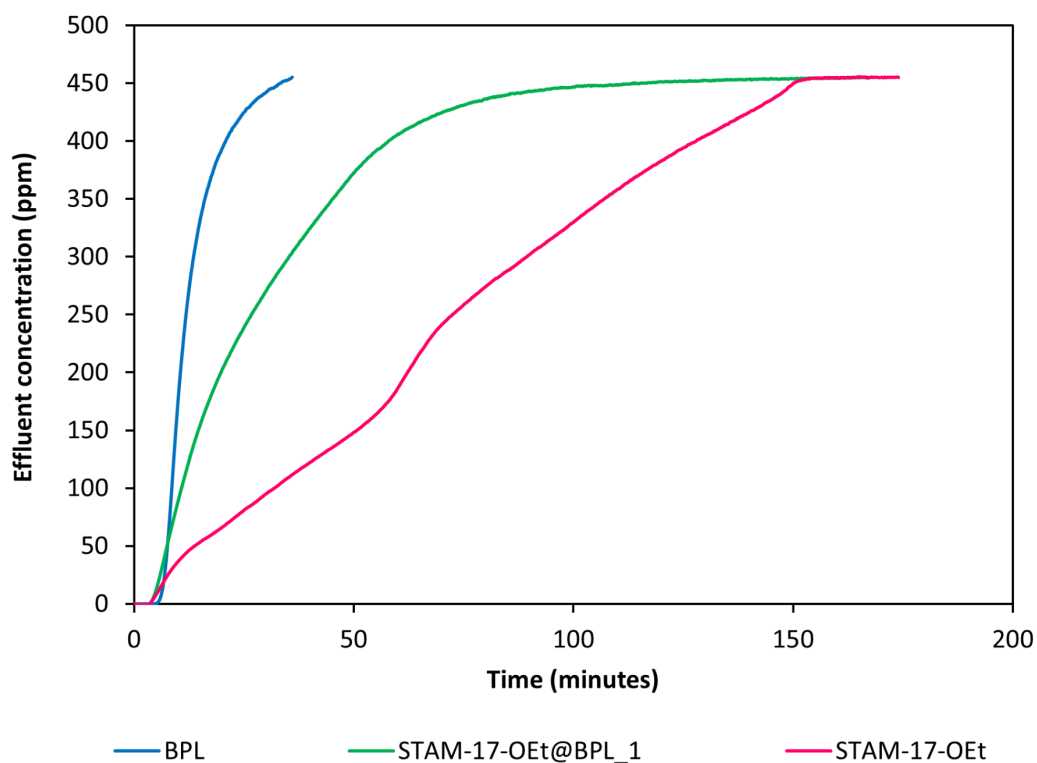


Figure 6.13. Ammonia micro-breakthrough curves of BPL activated carbon, STAM-17-OEt and STAM-17-OEt@BPL₁.

Table 6.2. Quantity of ammonia removed from airstream based on weight of sample for BPL activated carbon, the three STAM-17-OEt@BPL composites and STAM-17-OEt.

Material	Ammonia uptake (mg g ⁻¹)
STAM-17-OEt	43.3
STAM-17-OEt@BPL ₁	17.8
STAM-17-OEt@BPL ₂	14.2
STAM-17-OEt@BPL ₃	13.3
BPL activated carbon	4.3

The trend across the series may be observed in Figure 6.14, where increasing MOF loading in the composites leads to an overall increase in the uptake of ammonia. Comparison of the ammonia uptakes with the loadings of MOF on the composites suggest that ca. 80-90% of the MOF is available for ammonia removal and therefore most of the MOF is accessible to ammonia.

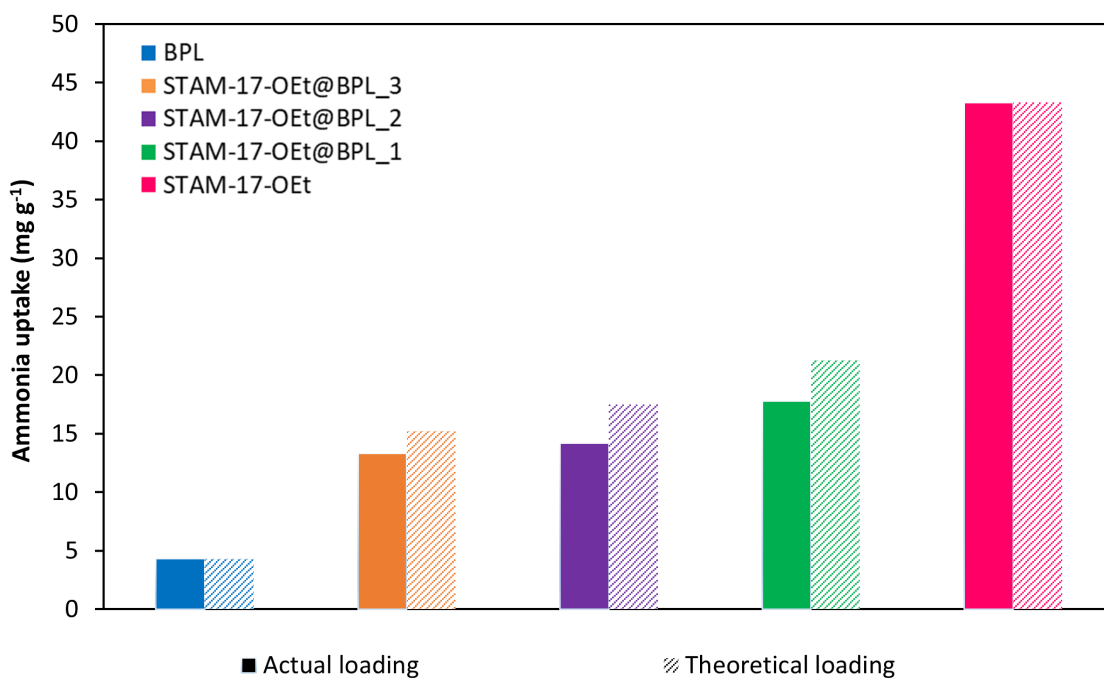


Figure 6.14. Ammonia uptake across the STAM-17-OEt@BPL series showing that the higher the quantity of MOF within the composite, the greater the quantity of ammonia removed from an airstream. The solid bars represent the actual ammonia uptakes and the shaded bars represent the theoretical uptake based on the loading of MOF.

Activated carbon is known to have low effectiveness in removing smaller molecules such as ammonia from airstreams, as it lacks the strong and selective interactions formed between the metals in MOFs and the gases themselves. STAM-17-OEt forms strong and favourable interactions and this makes it much better for the adsorption of gases such as ammonia. This

is in contrast to what was observed in cyclohexane adsorption, where higher MOF loading leads to a decrease in cyclohexane uptake. This relationship leads to the postulation that by controlling the amount of MOF in the pores, we can tailor the performance of the composites accordingly.

Comparable micro-breakthrough experiments were also undertaken using STAM-17-*OnPr* and two members of the STAM-17-*OnPr*@BPL series of composites. Micro-breakthrough curves (Figure 6.15) again show that STAM-17-*OnPr* performs significantly better than BPL activated carbon, adsorbing 37.2 mg g⁻¹. The highest loading MOF-carbon sample STAM-17-*OnPr*@BPL_1 adsorbs 16.5 mg g⁻¹, which is again almost halfway between the values for unimpregnated BPL carbon and STAM-17-*OnPr*. The ammonia uptake values for all loadings are shown in Table 6.3.

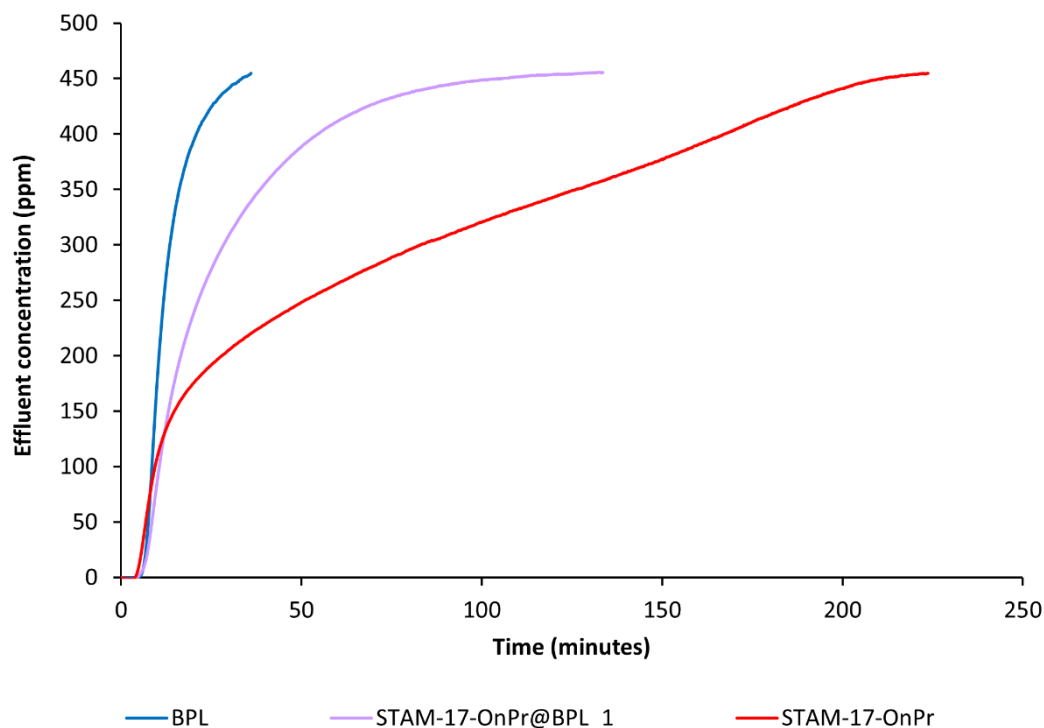


Figure 6.15. Ammonia micro-breakthrough curves of BPL activated carbon, STAM-17-*OnPr* and STAM-17-*OnPr*@BPL_1.

Table 6.3. Quantity of ammonia removed from airstream based on weight of sample for BPL activated carbon, the two tested STAM-17-*O_n*Pr@BPL composites and STAM-17-*O_n*Pr.

Material	Ammonia uptake (mg g ⁻¹)
STAM-17- <i>O_n</i> Pr	37.2
STAM- 17- <i>O_n</i> Pr@BPL_1	16.5
STAM- 17- <i>O_n</i> Pr@BPL_3	10.4
BPL activated carbon	4.3

The trend across the series may be observed in Figure 6.16, where increasing MOF loading in the composites again leads to an overall increase in the uptake of ammonia. Comparison of the ammonia uptakes with the loadings of MOF on the composites suggest that ca. 75-90% of the MOF is available for ammonia removal. The results from the STAM-17-*O_n*Pr@BPL series assist in reinforcing the conclusion that most of, if not all of the MOF within the composite is accessible.

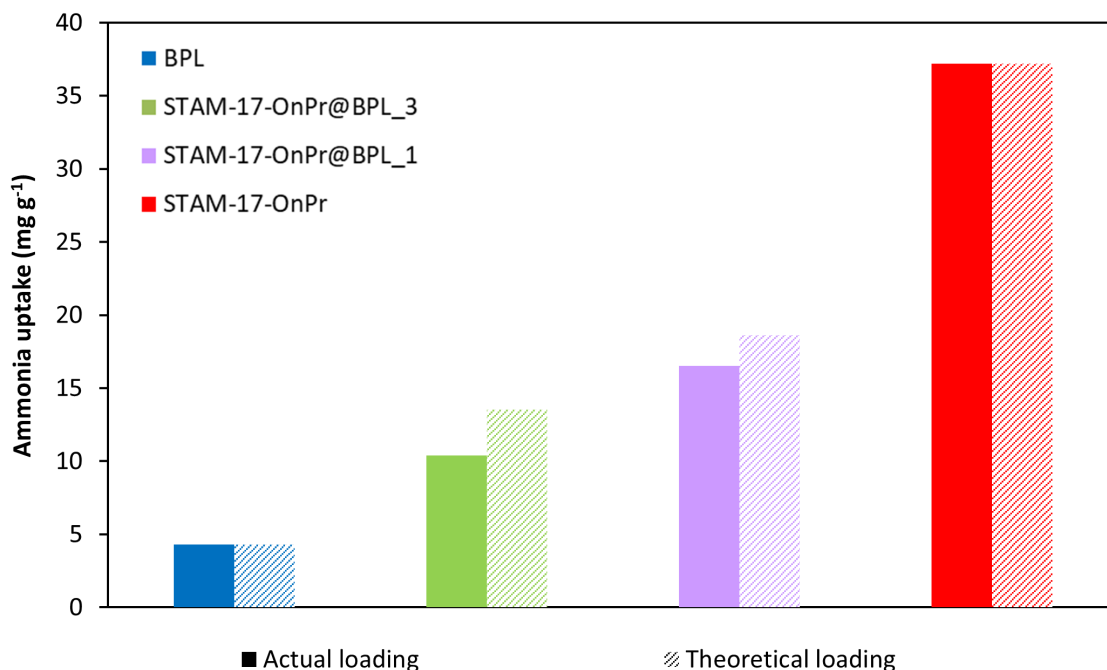


Figure 6.16. Ammonia uptake in the STAM-17-OnPr@BPL series. The solid bars represent the actual ammonia uptakes and the shaded bars represent the theoretical uptake based on the loading of MOF.

6.4.7 EPR Spectroscopy

EPR measurements were performed using a Bruker EMX micro spectrometer, working at a frequency of approximately 9.5 GHz (X-band), with a magnetic-field modulation frequency set at 100 kHz. Samples were placed into a Clear Fused-Quartz EPR tube, which was closed with a stopper and a layer of Parafilm. The spectra were acquired by inserting the EPR tube containing the sample inside a Dewar flask. For measurements conducted at 77 K, the Dewar flask was filled with liquid nitrogen. For measurements conducted at 77 K, the Dewar flask was filled with liquid nitrogen. Samples were pre-activated at 423 K prior to measurement. As the tubes were not evacuated or flame sealed, there was always a column of air present in

the EPR tube, though they were determined to be sufficiently protected from the external environment for testing purposes.

6.4.7.1 EPR Spectroscopy of STAM-17-OEt@BPL Materials

EPR spectra of activated STAM-17-OEt and the STAM-17-OEt@BPL materials were acquired at $T = 77$ K and 300 K. The spectra were normalized by all instrumental parameters and the estimated mass of STAM-17-OEt present in each sample (Figure 6.17) and normalized by the amplitude of the main peak (Figure 6.18). The EPR spectra of activated STAM-17-OEt (see section 4.4.7.1) at 77 K (Figure 6.17 (a) and Figure 6.18 (a)), show signals at 25 mT, 480 mT and 600 mT due to a triplet centre arising from the exchange coupling between the two spins ($S=1/2$) from Cu^{2+} ions within the paddlewheel structure. The signal at 330 mT is from Cu^{2+} monomers, which are defects formed during synthesis of the material and the large and unresolved signal observed at 300 K (Figure 6.17 (b) and Figure 6.18 (b)) apply to the triplet centres. The appearance of a single symmetric line for such $S=1$ centres, instead of the expected multi peak resonance, is due to the exchange interaction between the near magnetic paddle-wheels. The strength of this interaction intensifies upon increasing the temperature as a consequence of the population of the $S=1$ (triplet) state and it is significant at room temperature.¹⁷ The EPR spectra of STAM-17-OEt@BPL samples are, however, very different. The peaks corresponding to the triplet centres in STAM-17-OEt are no longer present and only a single resonance at both temperatures with similar features is observed. This narrower resonance, centred at ~ 340 mT, shows a fine structure comprising a multiplet of four lines, originating from the hyperfine interaction between the electron spin $S = 1/2$ of the Cu^{2+} ion and its nuclear spin $I_{\text{Cu}} = 3/2$. This multiplet was also present in pristine STAM-17-OEt, but was much less evident.

Significant changes were also observed in the EPR spectra of a similar MOF in another hybrid system, where HKUST-1 was confined within mesostructured silica.¹⁸ The changes in the spectra were attributed to the significantly reduced number of neighbouring paramagnetic centres caused by the widely spaced pores in BPL activated carbon.

The almost total disappearance of the resonances concerning the triplet centres at 77 K suggests a stronger change in the electronic environment of the paddlewheels with respect to the cited case and it appears that the signal observed at both 77 and 300 K in the STAM-17-OEt@BPL spectra arise from decoupled copper ions. A similar change in the magnetic properties of MOFs upon incorporation into an activated carbon matrix was observed for HKUST-1.⁶ The reasons of this apparent decoupling are still unclear, but it appears to be closely linked to the nature of MOF growth inside a porous carbon matrix.

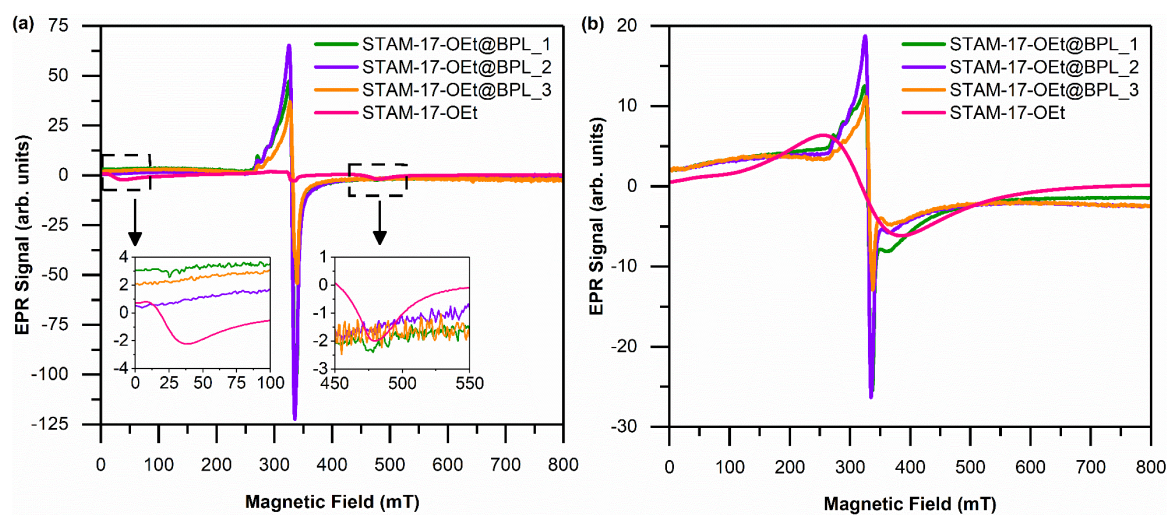


Figure 6.17. EPR spectra normalized by the estimated mass of STAM-17-OEt present in each sample at: (a) 77 K and (b) 300 K.

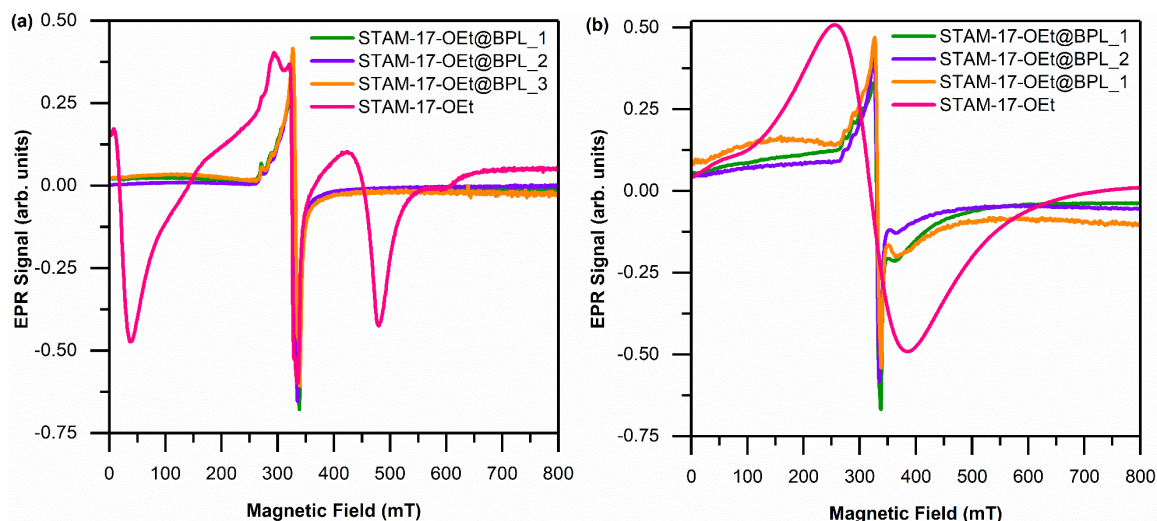


Figure 6.18. EPR spectra normalized by the peak-to-peak amplitude of the central resonance line at: (a) 77 K and (b) 300 K.

6.5 Conclusion

In conclusion, this chapter describes the synthesis of MOF-carbon composite materials, where STAM-17-OEt and STAM-17-O μ Pr have been incorporated into the commercially available BPL activated carbon at a series of loadings. SEM, water adsorption, cyclohexane uptake and EPR suggest that the MOF is formed within the pores of BPL carbon and water adsorption-desorption cycling highlights the hydrolytic stability of the composites. Micro-breakthrough experiments show that the MOF-carbon composite materials increase the quantities of ammonia removed from contaminated airstreams compared with the carbon, and cyclohexane uptake shows that the composites can adsorb significantly more cyclohexane than the MOF alone. Many different activated carbons were used in the attempted synthesis of composites, though they did not have the same degree of mesoporosity observed in BPL activated carbon that ultimately allowed synthesis of STAM MOFs within the carbon. The granular form of the STAM@BPL composites also overcomes

a major hurdle in the engineering of materials used in personal protective equipment, whereby a powdered MOF has been manufactured into a form that can potentially be used inside a filter. These findings suggest that MOF-carbon composites are exciting materials for use in air purification and by altering the loading of MOF within the composites, the materials may be tailored to remove a broader range of contaminants than the individual components alone.

6.6 References

- [1] G. W. Peterson, G. W. Wagner, A. Balboa, J. Mahle, T. Sewell and C. J. Karwacki, *J. Phys. Chem. C.*, 2009, **113**, 13906-13917.
- [2] E. Barea, C. Montoro and J. A. R. Navarro, *Chem. Soc. Rev.*, 2014, **43**, 5419-5430.
- [3] M. Jacoby, *Chem. Eng. News.*, 2014, **92**, 34-38.
- [4] S. Hindocha and S. Poulston, *Faraday Discuss.*, 2017, **201**, 113-125.
- [5] M. E. Casco, J. Fernández-Catalá, M. Martínez-Escandell, F. Rodríguez-Reinoso, E. V. Ramos-Fernández and J. Silvestre-Albero, *Chem. Comm.*, 2015, **51**, 14191-14194.
- [6] O. Fleker, A. Borenstein, R. Lavi, L. Benisvy, S. Ruthstein and D. Aurbach, *Langmuir*, 2016, **32**, 4935-4944.
- [7] R. Osovsky, D. Kaplan, I. Nir, H. Rotter, S. Elisha and I. Columbus, *Environ. Sci. Technol.*, 2014, **48**, 10912-10918.
- [8] D. Kaplan, L. Shmueli, I. Nir, D. Waysbort and I. Columbus, *Clean*, 2007, **35**, 172-177.
- [9] L. N. McHugh, A. Terracina, P. S. Wheatley, G. Buscarino, M. W. Smith and R. E. Morris, *Angew. Chem. Int. Ed.*, 2019, **58**, 11747-11751.

- [10] L. N. McHugh, M. J. McPherson, L. J. McCormick, S. A. Morris, P. S. Wheatley, S. J. Teat, D. McKay, D. M. Dawson, C. E. F. Sansome, S. E. Ashbrook, C. A. Stone, M. W. Smith and R. E. Morris, *Nat. Chem.*, 2018, **10**, 1096-1102.
- [11] L. Li, S. Liu and J. Liu, *Journal of Hazardous Materials*, 2011, **192**, 683-690.
- [12] J. Rouquerol, D. Avnir, C. W. Fairbridge, D. H. Everett, J. M. Haynes, N. Pernicone, J. D. F. Ramsay, K. S. W. Sing, and K. K. Unger, *Pure Appl. Chem.*, 1994, **66**, 1739-1758.
- [13] B. P. Russell and M. D. Levan, *Carbon*, 1994, **32**, 845-855.
- [14] CEN European Normalization Committee, European Norm EN 14387, Respiratory Protective device - gas filters and combined filters - Requirements, testing, marking (BSI British standards, London 2004).
- [15] F. D. Magalhães, R. L. Laurence and W. C. Conner, *J. Phys. Chem. B.*, 1998, **102**, 2317-2324.
- [16] J. R. Álvarez, E. Sánchez-González, E. Pérez, E. Schneider-Revueltas, A. Martínez, A. Tejada-Cruz, A. Islas-Jácome, E. González-Zamora and I. A. Ibarra, *Dalton Trans.*, 2017, **46**, 9192-9200.
- [17] M. Todaro, G. Buscarino, L. Sciortino, A. Alessi, F. Messina, M. Taddei, M. Ranocchiari, M. Cannas and F. M. Gelardi, *J. Phys. Chem. C.*, 2016, **120**, 12879-12889.
- [18] M. Mazaj, T. Čendak, G. Buscarino, M. Todaro and N. Zabukovec Logar, *J. Mat. Chem. A.*, 2017, **5**, 22305-22315.

Chapter 7: Synthetic and Crystallographic Investigation of Two Novel Copper Frameworks

7.1 Aim

The aim of this chapter is to investigate the synthesis, structure and properties of two novel copper frameworks synthesised using an amine ligand: 5-dimethylaminobenzene-1,3-dicarboxylic acid and an extended version of the 5-ethoxybenzene-1,3-dicarboxylic acid linker: 1,3-bis(4-carboxyphenyl)-5-ethoxybenzene.

7.2 Introduction

The STAM series of MOFs are formed from a series of carboxylate linkers with side chains containing an oxygen atom. In the STAM-17-n series, the oxygen-containing side chain protrudes into the hydrophobic pore and in this chapter, the synthesis and structure of an alkyl amino variant named STAM-NMe₂¹ is discussed, in which the material contains a nitrogen atom in the methyl amino side chain. The structure is comparable to that of the alkoxy-based equivalent material: STAM-17-OMe.²

Metal-organic frameworks show enormous potential for gas adsorption, though many, including the STAM series, are unsuitable for the uptake of larger molecules due to their relatively small pores. One way to overcome this is by increasing the size of the linker to generate larger pores, while maintaining the main structural features of the initial linker in order to retain the favourable chemistry observed in the STAM series. In this chapter, an extended variant of the 5-ethoxybenzene-1,3-dicarboxylic acid linker used in the synthesis of STAM-17-OEt³ is synthesised and the corresponding MOF produced. In this case though,

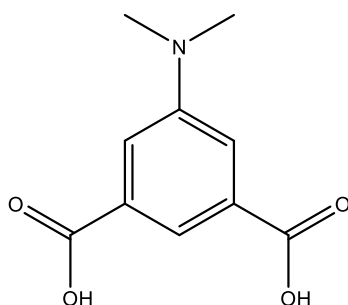
the linker and metal coordinate in a different way than in the STAM materials to produce a layered structure with orthorhombic symmetry.

7.3 Experimental Procedure

All reagents were obtained from commercial sources and were used without further purification.

7.3.1 Preparation of STAM-NMe₂

7.3.1.1 Synthesis of 5-dimethylaminobenzene-1,3-dicarboxylic acid⁴



Formaldehyde solution (37 wt% in water, 6 mL, 10 eq.) was added to a solution of 5-aminobenzene-1,3-dicarboxylic acid (1.38 g, 7.62 mmol) in DMF (10 mL) and the solution was stirred at ambient temperature for 20 minutes. The solution was cooled to 0 °C and sodium cyanoborohydride (1.42 g, 22.6 mmol) was slowly added. The solution was then stirred for 5 hours at ambient temperature. After evaporation of the solvent, the residue was dissolved in water and precipitated by addition of 2 M hydrochloric acid. The white precipitate was filtrated and washed with water until the pH value of the filtrate was neutral, to yield 5-dimethylaminobenzene-1,3-dicarboxylic acid (5.28 g, 25.2 mmol, 83 %) as a pale

yellow solid. ^1H NMR (400 MHz, d_6 -DMSO) δ_{H} 7.79 (1 H, t, $J = 2.8$ Hz), 7.44 (2 H, d, $J = 1.2$ Hz), 2.99 (6 H, s) ppm.

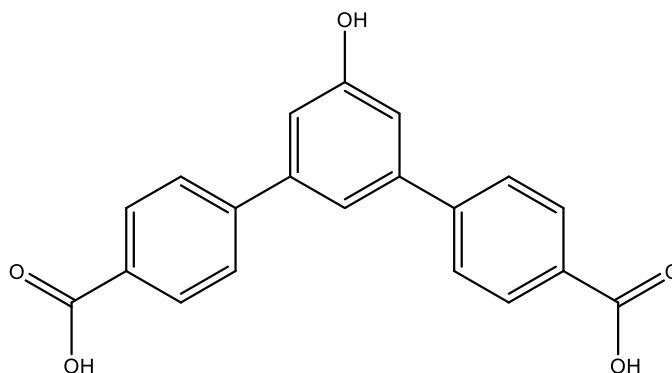
7.3.1.2 Synthesis of STAM-NMe₂¹

5-dimethylaminobenzene-1,3-dicarboxylic acid (0.11 g, 0.53 mmol) and copper acetate monohydrate (0.10 g, 0.50 mmol) were suspended in distilled water (7.5 mL) inside the Teflon liner of a stainless-steel autoclave. The sealed autoclave was placed in an oven at 110 °C for 4 days. Upon cooling, the contents were filtered and washed with distilled water and ethanol before drying in air to provide a green, crystalline solid (0.10 g, 0.35 mmol, 70% yield).

7.3.2 Preparation of Copper-1,3-bis(4-carboxyphenyl)-5-ethoxybenzene

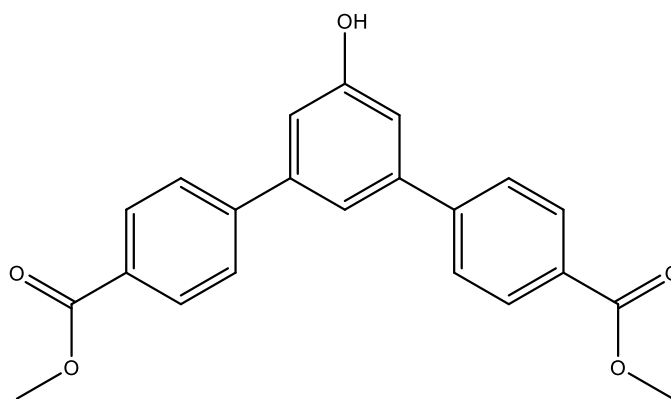
7.3.2.1 Synthesis of 1,3-bis(4-carboxyphenyl)-5-ethoxybenzene

1,3-bis(4-carboxyphenyl)-5-hydroxybenzene⁵



A mixture of acetonitrile (60 mL) and distilled water (60 mL) were degassed in a Schlenk flask at room temperature for 1 hour under argon, before 3,5-dibromophenol (1.89 g, 7.50 mmol), 4-carboxyphenylboronic acid (2.74 g, 16.5 mmol) and dried potassium carbonate (8.23 g, 59.6 mmol) were added. The flask was evacuated and back filled with argon 3 times before bis(triphenylphosphine) palladium (II) dichloride (0.50 g, 0.71 mmol) was added and the flask was evacuated and back filled with argon a further 3 times. The flask was heated at 100 °C under argon for 72 hours. Upon cooling to room temperature, the resulting suspension was filtered and then diluted to 200 mL volume with distilled water. The solution was washed once with hexane: ethyl acetate (1:1) (50 mL) and acidified with 2M hydrochloric acid to produce an off-white precipitate, which was dried in air (3.44 g, 10.3 mmol, 69% yield). ^1H (400 MHz, d_6 -DMSO) δ_{H} 8.03 (4H, m), 7.84 (4H, m), 7.46 (1H, t, $J=3.6$ Hz), 7.16 (2H, d, $J=1.2$ Hz).

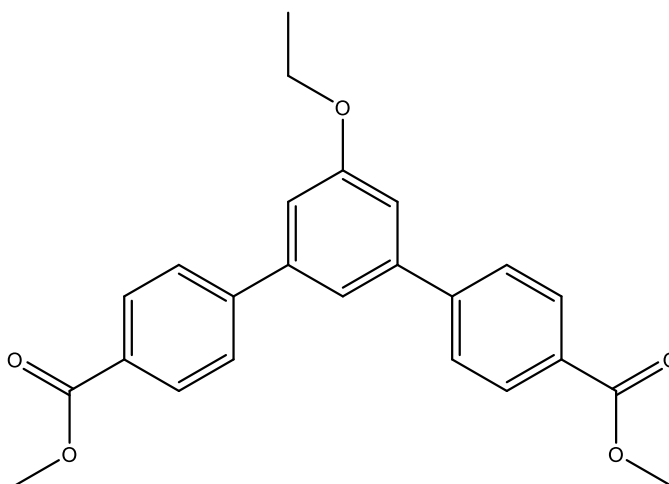
1,3-bis(4-methoxycarbonylphenyl)-5-hydroxybenzene⁵



1,3-bis(4-carboxyphenyl)-5-hydroxybenzene (3.44 g, 10.3 mmol) was suspended in methanol (225 mL), before concentrated sulfuric acid (5.69 mL, 106 mmol) was added at room temperature. The suspension was heated at 80 °C for 48 hours, before being cooled to room

temperature. The solution was diluted to 900 mL volume with distilled water, to produce an off-white precipitate that was filtered and washed copiously with distilled water, before being dried in air (2.37 g, 6.54 mmol, 63% yield). ^1H (400 MHz, d_6 -DMSO) δ_{H} 9.96 (1H, s), 8.05 (4H, m), 7.88 (4H, m), 7.49 (1H, t, $J= 3.2$ Hz), 7.16 (2H, d, $J= 1.6$ Hz), 3.89 (s, 6H).

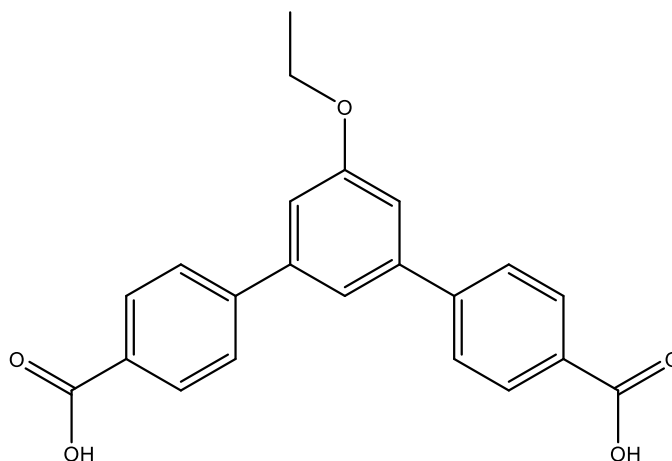
1,3-bis(4-methoxycarbonylphenyl)-5-ethoxybenzene⁶



1,3-bis(4-methoxycarbonylphenyl)-5-hydroxybenzene (2.37 g, 6.54 mmol) and dried potassium carbonate (1.72 g, 12.4 mmol) were suspended in acetone (100 mL) and heated under reflux for 2 hours, before iodoethane (0.60 mL, 7.50 mmol) was added and the suspension was stirred under reflux for a further 3 days. Upon cooling to room temperature, the acetone was removed under reduced pressure, before the resulting solid was suspended in dichloromethane (60 mL) and distilled water (60 mL). The solution was extracted with dichloromethane (3 x 60 mL) and the combined organic fractions were washed with brine (60 mL), before being dried over anhydrous magnesium sulfate. The dichloromethane was removed under reduced pressure and the beige solid was dried in air (2.38 g, 6.10 mmol, 93%

yield). ^1H (400 MHz, d_6 -DMSO) δ_{H} 8.05 (4H, m), 7.95 (4H, m), 7.62 (1H, t, $J=3.2$ Hz), 7.31 (2H, d, $J=1.6$ Hz), 4.22 (2H, q, $J=20.8$ Hz), 3.89 (6H, s), 1.39 (3H, t, $J=14.0$ Hz).

1,3-bis(4-carboxyphenyl)-5-ethoxybenzene⁶



Potassium hydroxide (1.71 g, 30.50 mmol) was dissolved in methanol (120 mL) and 1,3-bis(4-methoxycarbonylphenyl)-5-ethoxybenzene (2.38 g, 6.10 mmol) was suspended in the solution. The suspension was heated at 80 °C for 18 hours. The resulting solution was cooled to room temperature and 2M hydrochloric acid (120 mL) was added to produce a white precipitate. The precipitate was washed copiously with water until the washings reached pH~6, before being dried in air (1.94 g, 5.35 mmol, 88% yield). ^1H (400 MHz, d_6 -DMSO) δ_{H} 8.03 (4H, m), 7.93 (4H, m), 7.62 (1H, t, $J=3.2$ Hz), 7.31 (2H, d, $J=1.6$ Hz), 4.23 (2H, q, $J=20.8$ Hz), 1.40 (3H, t, $J=14.0$ Hz).

7.3.2.2 Synthesis of Copper-1,3-bis(4-carboxyphenyl)-5-ethoxybenzene⁶

1,3-bis(4-carboxyphenyl)-5-ethoxybenzene (0.27 g, 0.75 mmol) was stirred in ethanol (3.51 mL, 60.0 mmol) and DMF (0.75 mL, 9.69 mmol) for 10 minutes at ambient temperature. A

separate solution of copper acetate monohydrate (0.15 g, 0.75 mmol) in distilled water (2.37 mL, 131 mmol) was then added and the solution was stirred for a further 10 minutes at ambient temperature. The solution was sealed in a Teflon-lined stainless-steel autoclave and was heated at 110 °C for 5 days. The solution was filtered upon cooling and the resulting blue crystalline solid was washed with distilled water and ethanol, before being dried in air (0.22 g, 0.25 mmol, 33% yield).

Soxhlet extraction was performed on the solid to remove residual DMF in the sample. The sample was placed inside a Soxhlet extraction apparatus for 5 days, using ethanol as the exchange solvent. After recovery, the solid was dried in an oven overnight.

7.4 Results and Discussion

7.4.1 Formation of an Amine Member of the STAM Series

The STAM series of MOFs are based on alkoxy-based linkers, though the alkoxy group does not play a large part in the overall structure direction of MOF formation. It was therefore decided to change the oxygen atom with a nitrogen atom. The direct replacement for an alkoxy linker is the corresponding di-alkyl linker (Figure 7.1) and the dimethyl variant was chosen due to the wide availability of aqueous formaldehyde solution which was used in the linker synthesis. The formed material was named: STAM-NMe₂.

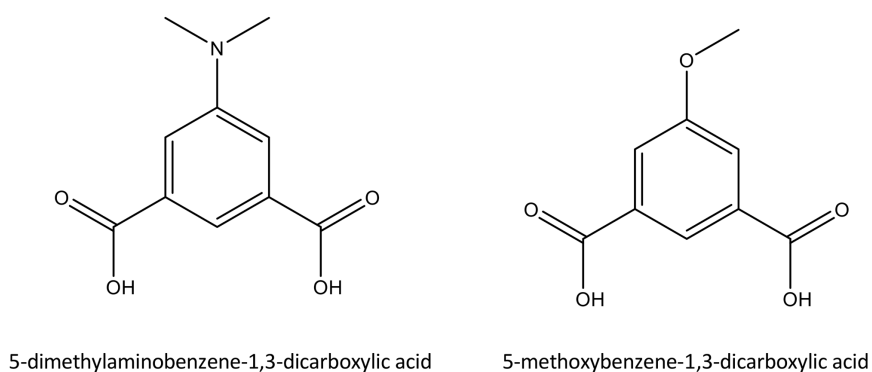


Figure 7.1. Structure of 5-dimethylaminobenzene-1,3-dicarboxylic acid and its direct alkoxy comparison: 5-methoxybenzene-1,3-dicarboxylic acid.

7.4.2 Crystal Structure Determination of STAM-NMe₂

Single crystals of sufficient size for “in-house” diffraction were collected at 173 K on a Rigaku FR-X Ultra-high brilliance diffractometer with Mo K α radiation source ($\lambda = 0.71073$ Å) and a RigakuXtaLAB P200 detector. Absorption corrections were applied using multi-scan methods in CrysAlisPro 1.171.38.46.⁷ The structure solution was obtained using SHELXT⁸ and refined by full matrix on F^2 using SHELXL⁹ within the Olex2¹⁰ suite. All full occupancy non-hydrogen atoms were refined with anisotropic thermal displacement parameters. Aromatic hydrogen atoms and hydrogen atoms belonging to coordinated water molecules were included at their geometrically estimated positions and disordered solvent molecules present in the hydrophilic pores were masked during the refinement.

7.4.2.1 Crystal Structure Analysis of STAM-NMe₂

STAM-NMe₂ was prepared hydrothermally and yielded green block crystals in good yield (70%). The crystals from the bulk batch were of sufficient size and quality for “in-house”

single crystal analysis and PXRD measurements show that the pattern of the as-made material perfectly matches the simulated powder pattern obtained crystallographically from the cif file (Figure 7.2).

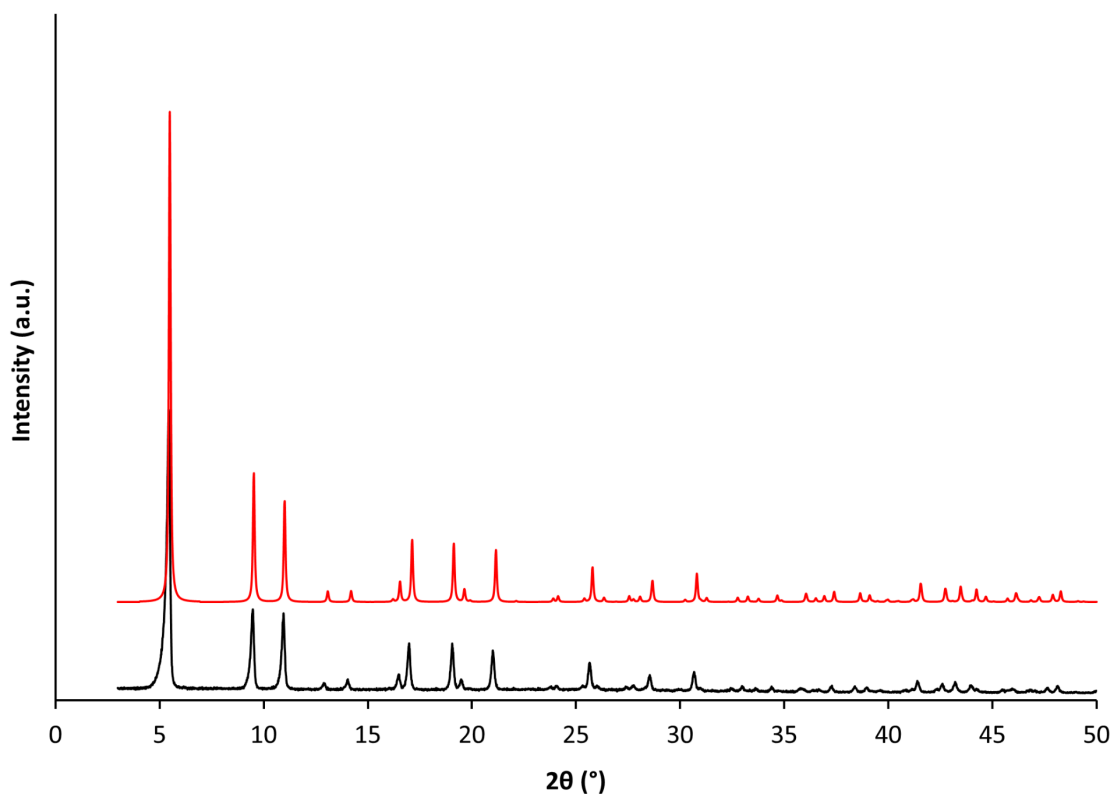


Figure 7.2. A comparison of the experimental (black trace) and simulated (red trace) powder X-ray diffraction patterns for STAM-NMe₂. The calculated pattern is based upon the single crystal X-ray diffraction data obtained.

Crystals of STAM-NMe₂ have a Kagome lattice structure, with the Trigonal space group $P\bar{3}m1$ and unit cell dimensions of $a = 18.5382(5)$ Å and $c = 6.7599(2)$ Å and the final crystallographic parameters may be observed in Table 7.1.

Table 7.1. Crystallographic data from the structure determination of STAM-NMe₂ (associated bond lengths and angles may be found in appendix tables 9.5 and 9.6 respectively).

Identification code	STAM-NMe₂
Empirical formula	C ₁₀ H ₁₁ CuNO ₅
Formula weight	288.74 g mol ⁻¹
Temperature	173 K
Wavelength	0.71073 Å
Crystal system, space group	Trigonal, $P\bar{3}m1$
Unit cell dimensions	$a = 18.5382(5)$ Å
	$b = 18.5382(5)$ Å
	$c = 6.7599(2)$ Å
Volume	2011.90(12) Å ³
Z	6
Calculated density	1.430 g cm ⁻³
Absorption coefficient	1.635 mm ⁻¹
$F(000)$	882.0
GooF on F^2	1.124
Crystal size	0.04 x 0.04 x 0.02 mm ³
Theta range for data collection	4.394 to 57.87°
Reflections collected/unique	26670/1842 [R(int) = 0.0713]
Final R indices ($I > 2\sigma(I)$)	R ₁ = 0.0367 wR ₂ = 0.0941
Final R indices (all data)	R ₁ = 0.0565 wR ₂ = 0.0992

The structure consists of copper paddlewheel units connected in two dimensions via carboxylate bridging ligands to provide a porous network. All copper centres and ligands are crystallographically equivalent and the material contains both hydrophilic and hydrophobic channels, as observed in the oxygen-containing STAM members. Coordinated water molecules protrude into the hydrophilic pores and the hydrophobic pores are lined with dimethylamino side chains (Figure 7.3).

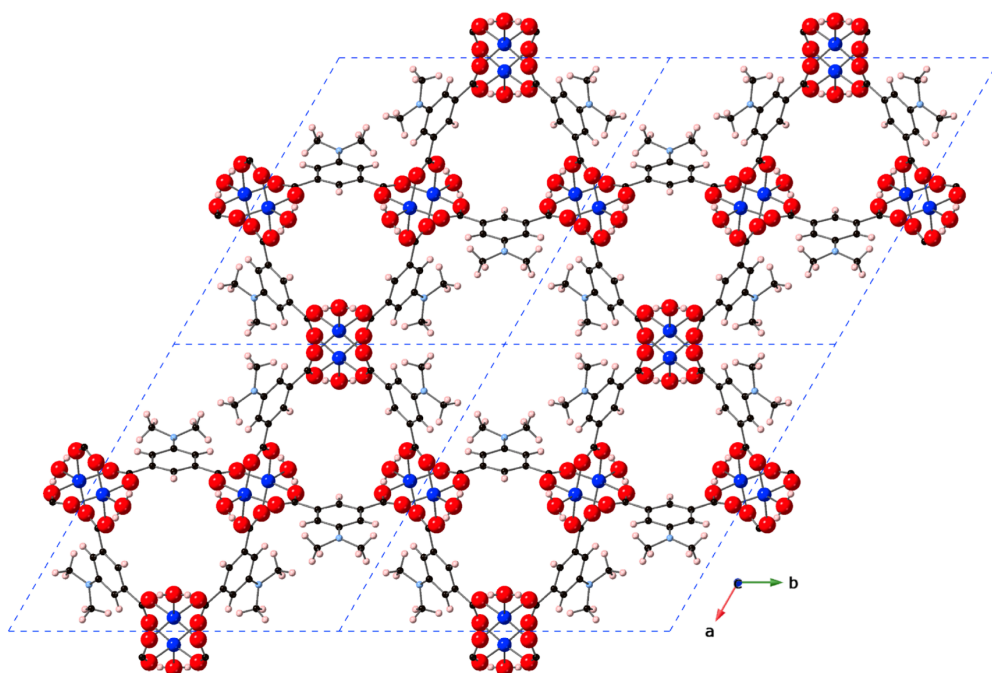


Figure 7.3. Structure of STAM-NMe₂ viewed down the crystallographic *c* axis, displaying the dual pore structure seen in the STAM series and a Kagome lattice structure. Key: dark blue: Cu; red: O; black: C; light blue: N; pink: H.

The dimethylamino side chains protrude into the hydrophobic pore, but unlike in the STAM-17-n series, the dimethylamino group is not disordered over two sites. The nitrogen atom within the dimethylamino group is bound to three carbon atoms and the increased steric bulk from the presence of two methyl groups leads to a more ordered structure (Figure 7.4).

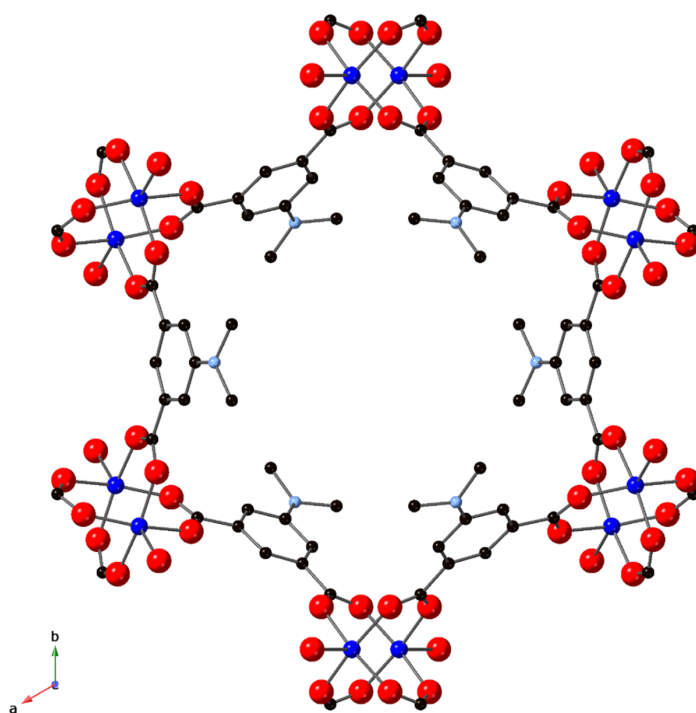


Figure 7.4. The hydrophobic pore in STAM-NMe₂ viewed down the crystallographic *c* axis, showing the ordered dimethyl amino chains protruding into the pore. Key: dark blue: Cu; red: O; black: C; light blue: N. H atoms have been omitted for clarity.

The structure is comprised of parallel sheets, where the axial coordinated water molecules on the copper paddlewheel units participate in hydrogen bonding interactions ($\text{O}\cdots\text{O}$, 3.071 Å) with adjacent carboxylate oxygen atoms, creating a cross-linked structure (Figure 7.5).

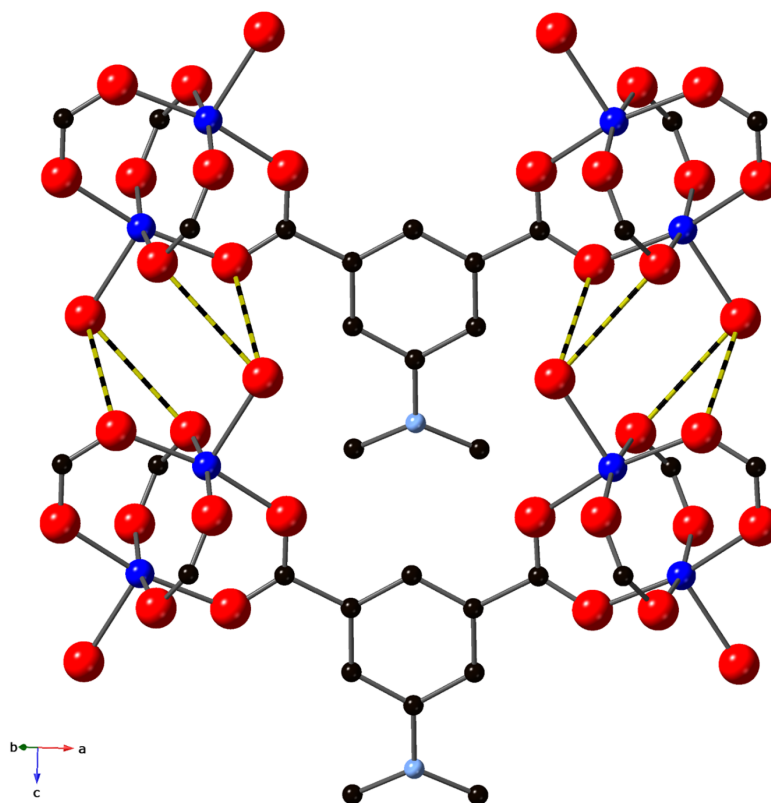


Figure 7.5. Hydrogen bonding between adjacent copper acetate units. Key: dark blue: Cu; red: O; black: C; light blue: N. H atoms have been omitted for clarity. Hydrated hydrogen bonds are represented by black and yellow dashed bonds.

7.4.3 Characterisation of STAM-NMe₂

TGA was collected under air using a Stanton Redcroft STA-780 series thermal analyser from ambient temperature to 700 °C, with a 10 °C per minute heating rate. The trace shows a series of mass loss steps, where non-coordinated solvent molecules are first lost from the structure up to 125 °C, followed by coordinated water molecules up to approximately 200 °C (Figure 7.6). This is followed by a large mass loss up to 300 °C, where the dimethylamino groups are lost from the structure. Framework stability is completely lost from approximately 350 °C, where the material decomposes into residual copper oxide.

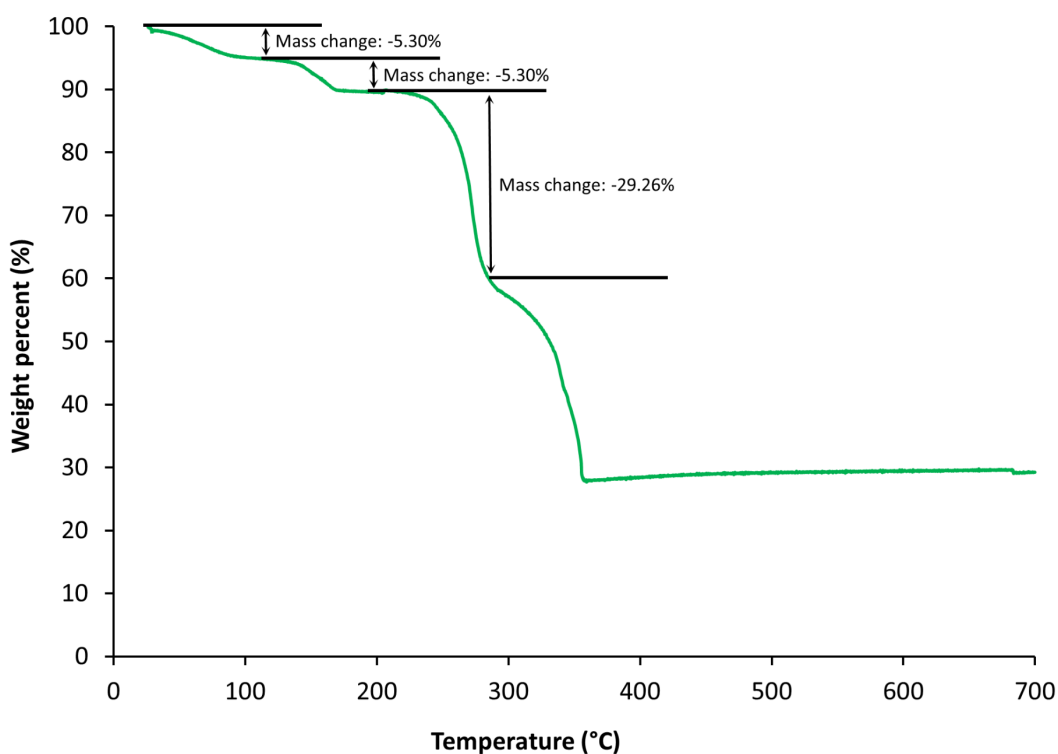


Figure 7.6. TGA trace of STAM-NMe₂ measured in air, showing the loss of solvent molecules up to 200 °C, amine groups up to 300 °C and the collapse of the framework from 350 °C.

Variable temperature powder X-ray diffraction was collected under vacuum on a PANalytical Empyrean X'celerator RTMS detector diffractometer using Mo K $\alpha_{1,2}$ radiation in an alumina sample holder. The technique was used to investigate the effect of dehydration on the structure of STAM-NMe₂ and was collected using Mo K $\alpha_{1,2}$ radiation under vacuum (Figure 7.7). Half of the first peak is not visible due to its occurrence at approximately 1° 2 θ , which could not be measured on the instrument. A pattern was first collected at 25 °C in air to serve as a comparison to further collections under vacuum.

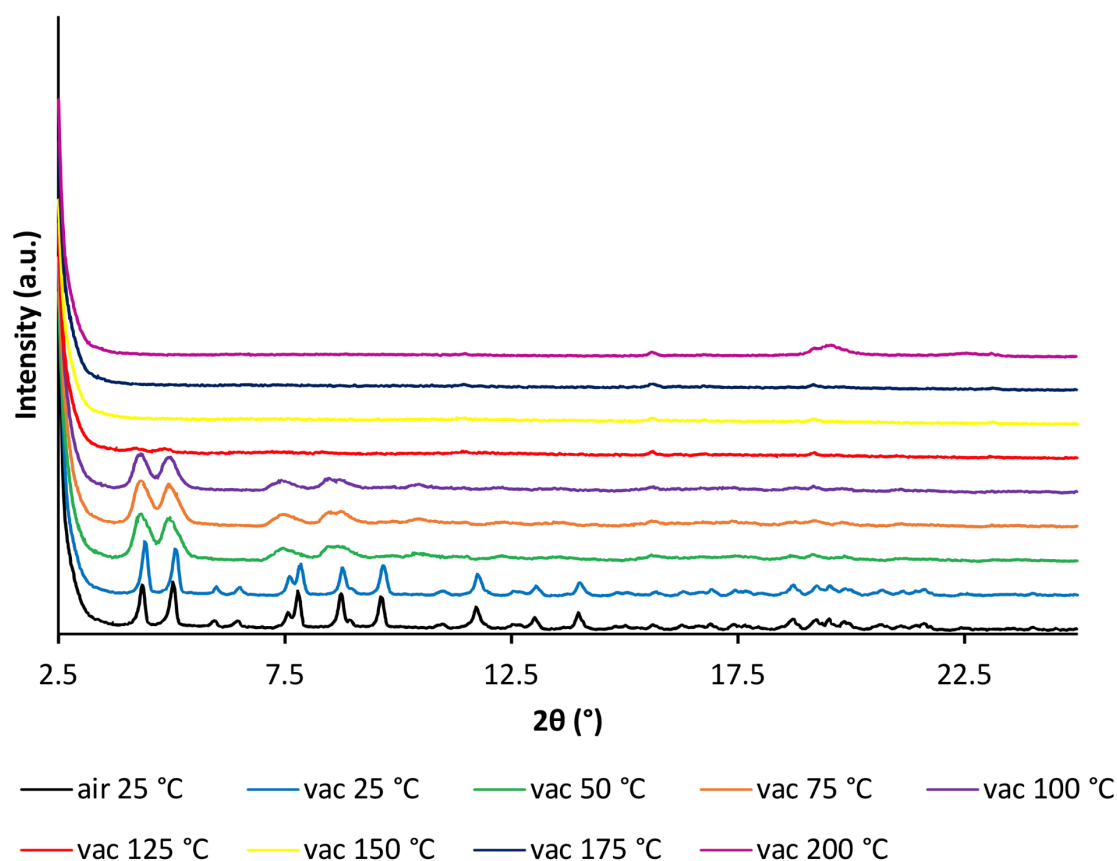


Figure 7.7. Variable temperature powder X-ray diffraction patterns of STAM-NMe₂ collected first in air at 25 °C, followed by vacuum up to 200 °C.

The structure is stable under vacuum at 25 °C, though begins to lose crystallinity at 50 °C when the non-coordinated water molecules within the hydrophilic pores are lost. Near total loss of crystallinity is observed at 125 °C, when water molecules coordinated to the copper acetate units are removed.

This low thermal stability is in contrast to STAM-17-OEt, where crystallinity is retained throughout the measurement and after rehydration. The loss of crystallinity even at low temperatures when under vacuum may be attributed to the lower stability of amines in

relation to alkoxy substituents and it appears that the inclusion of an amine in the structure causes the framework to collapse upon heating under vacuum.

Nitrogen BET surface area analysis was performed on a Micromeritics ASAP 2020 surface area and porosity analyser and the BET surface areas were calculated using the Rouquerol method.¹¹ Due to the difficulty in observing a dehydrated phase in the material, it was consequently decided to obtain nitrogen surface area measurements after activation at 100 °C, where some crystallinity still remained in variable temperature powder X-ray diffraction and with no thermal activation at all (Figure 7.8). The associated BET surface areas were $44.9 \pm 0.2 \text{ m}^2/\text{g}$ and $44.2 \pm 0.2 \text{ m}^2/\text{g}$ respectively, where pre-activation prior to nitrogen adsorption appears to have no effect on the porosity of the material. Such low surface areas are typical in STAM materials, with the related material: STAM-17-OEt displaying a BET surface area of $58.4 \pm 0.3 \text{ m}^2/\text{g}$. The low porosity is due to the limited access to nitrogen afforded at the experimental temperature of 77 K caused by a constriction of the pores.

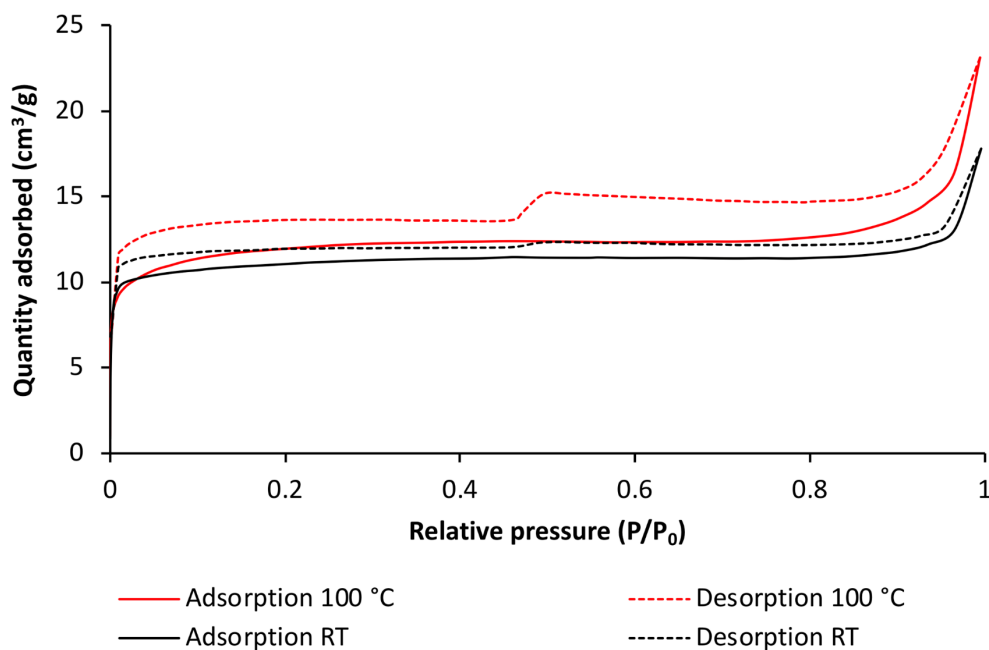


Figure 7.8. Nitrogen adsorption isotherms for STAM-NMe₂ samples pre-activated under vacuum at 100 °C and at room temperature. Both measurements were recorded at 77 K.

7.4.4 Formation of Copper-1,3-bis(4-carboxyphenyl)-5-ethoxybenzene

The STAM-17-n series of MOFs use 1,3-dicarboxylic acid linkers that are substituted at the 5-position, though these linkers are not large enough to produce pores large enough to allow entry of larger molecules. It was consequently decided to extend the length of the linker by adding two more aromatic rings. The linker 5-ethoxybenzene-1,3-dicarboxylic acid, which is used to synthesise the highly stable MOF STAM-17-OEt was chosen as the basis for the new, extended linker, which has been named 1,3-bis(4-carboxyphenyl)-5-ethoxybenzene (Figure 7.9).

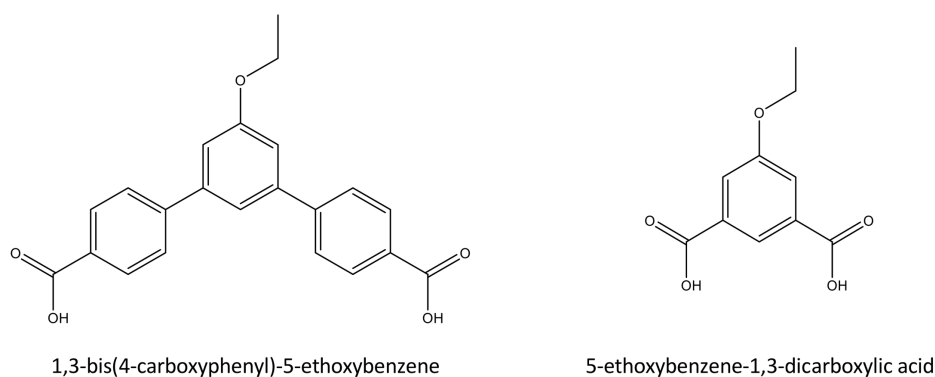


Figure 7.9. Structures of 1,3-bis(4-carboxyphenyl)-5-ethoxybenzene and 5-ethoxybenzene-1,3-dicarboxylic acid.

Efforts to synthesise a MOF using water alone as a solvent were unsuccessful, almost certainly due to the size of the linker and its poor solubility and no further success was achieved using aqueous methanol or ethanol, so DMF was used during synthesis along with an aqueous ethanol solution to increase the potential of crystallisation.

Crystals were then repeatedly washed with hot ethanol using a Soxhlet extraction experiment to remove residual DMF from the framework, though the crystal quality was affected, leading to poor quality single crystal data.

7.4.5 Crystal Structure Determination of Copper-1,3-bis(4-carboxyphenyl)-5-ethoxybenzene

Single crystals of copper-1,3-bis(4-carboxyphenyl)-5-ethoxybenzene(DMF) were initially collected using “in-house” diffraction at 173 K on an Rigaku MM-007HF diffractometer with Cu K α radiation source ($\lambda = 1.54184 \text{ \AA}$) and a RigakuXtaLAB P100K detector. Absorption corrections were applied using multi-scan methods in CrysAlisPro 1.171.38.46.⁷

The structure solution was obtained using SHELXT⁸ and refined by full matrix on F^2 using SHELXL⁹ within the Olex2¹⁰ suite.

Ethyl chains were disordered over two crystallographic sites, each of which was 50% occupied. All full occupancy non-hydrogen atoms were refined with anisotropic thermal displacement parameters. Aromatic hydrogen atoms were included at their geometrically estimated positions and hydrogen atoms belonging to coordinated water molecules were not modelled. One DMF molecule bound to the copper paddlewheel unit was modelled and other residual disordered solvent molecules were masked during the refinement.

After Soxhlet extraction, single crystals of copper-1,3-bis(4-carboxyphenyl)-5-ethoxybenzene were collected using “in-house” diffraction at 125 K on a Rigaku MM-007HF diffractometer with Cu K α radiation source ($\lambda = 1.54184 \text{ \AA}$) and a RigakuXtaLAB P200K detector. The molecule was refined as before, where all full occupancy non-hydrogen atoms were refined with anisotropic thermal displacement parameters and aromatic hydrogen atoms were included at their geometrically estimated positions. Hydrogen atoms belonging to coordinated water molecules were again not modelled and residual disordered solvent molecules were masked during the refinement.

7.4.5.1 Crystal Structure Analysis and Characterisation of Copper-1,3-bis(4-carboxyphenyl)-5-ethoxybenzene

Copper-1,3-bis(4-carboxyphenyl)-5-ethoxybenzene(DMF) was prepared solvothermally as blue single crystals and residual DMF was removed by Soxhlet extraction to afford copper-1,3-bis(4-carboxyphenyl)-5-ethoxybenzene. PXRD measurements show that the measured pattern of copper-1,3-bis(4-carboxyphenyl)-5-ethoxybenzene matches the simulated powder pattern obtained from the experimentally refined structure model (Fig. 7.10).

A copper oxide (Cu_2O) impurity may be observed in the pattern of copper-1,3-bis(4-carboxyphenyl)-5-ethoxybenzene, though this impurity was present in all batches made.

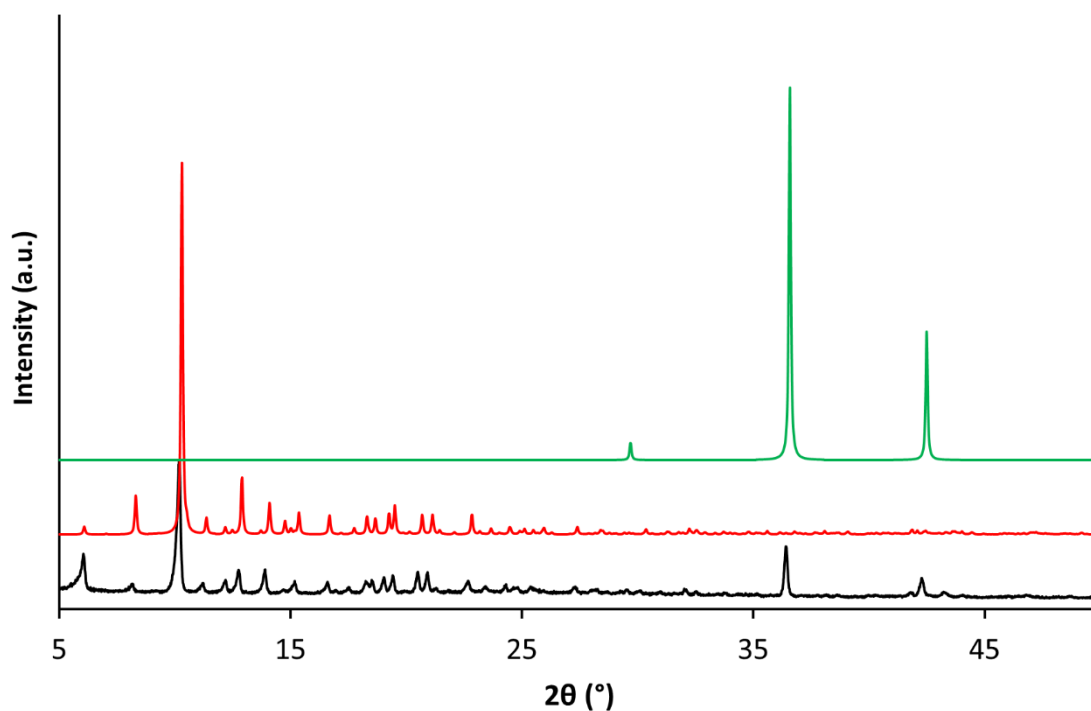


Figure 7.10. A comparison of the experimental (black trace) and simulated (red trace) powder X-ray diffraction patterns for copper-1,3-bis(4-carboxyphenyl)-5-ethoxybenzene. The Cu_2O impurity (green trace) may be seen at 37 and 42° 2θ . The calculated pattern is based upon the single crystal X-ray diffraction data obtained.

The crystal structure of the as-made material was initially recorded, though residual DMF was found in the structure solution. The solvent was removed accordingly and another dataset was recorded. The final crystallographic parameters for both copper-1,3-bis(4-carboxyphenyl)-5-ethoxybenzene(DMF) and copper-1,3-bis(4-carboxyphenyl)-5-ethoxybenzene may be observed in Table 7.2.

Table 7.2. Crystallographic data from the structure determination of copper-1,3-bis(4-carboxyphenyl)-5-ethoxybenzene(DMF) and copper-1,3-bis(4-carboxyphenyl)-5-ethoxybenzene (associated bond lengths and angles may be found in appendix tables 9.7-9.10).

Identification code	Copper-1,3-bis(4-carboxyphenyl)-5-ethoxybenzene(DMF)	Copper-1,3-bis(4-carboxyphenyl)-5-ethoxybenzene
Empirical formula	C _{45.5} H _{35.5} Cu ₂ N _{0.5} O ₁₂	C ₄₄ H ₃₂ Cu ₂ O ₁₂
Formula weight	908.32 g mol ⁻¹	879.77 g mol ⁻¹
Temperature	173 K	125 K
Wavelength	1.54184 Å	1.54184 Å
Crystal system, space group	Orthorhombic, <i>Ibam</i>	Orthorhombic, <i>Ibam</i>
Unit cell dimensions	<i>a</i> = 15.7246(5) Å	<i>a</i> = 15.5652(7) Å
	<i>b</i> = 20.1588(8) Å	<i>b</i> = 21.2718(15) Å
	<i>c</i> = 28.9989(9) Å	<i>c</i> = 29.0545(9) Å
Volume	9192.3(5) Å ³	9619.9(9) Å ³
Z	8	8
Calculated density	1.313 g cm ⁻³	1.215 g cm ⁻³
Absorption coefficient	1.635 mm ⁻¹	1.544 mm ⁻¹
<i>F</i> (000)	3728.0	3600.0
GooF on <i>F</i> ²	1.049	1.000
Crystal size	0.03 x 0.03 x 0.02 mm ³	0.04 x 0.04 x 0.02 mm ³
Theta range for data collection	6.096 to 136.684°	6.084 to 151.536°
Reflections collected/unique	47728/4302 [R(int) = 0.1094]	54930/5051 [R(int) = 0.2107]
Final R indices (<i>I</i> >2σ(<i>I</i>))	R ₁ = 0.0510 wR ₂ = 0.1477	R ₁ = 0.0953 wR ₂ = 0.2672
Final R indices (all data)	R ₁ = 0.0717 wR ₂ = 0.1609	R ₁ = 0.1428 wR ₂ = 0.3092

In copper-1,3-bis(4-carboxyphenyl)-5-ethoxybenzene(DMF), DMF was shown to bind to half of the Cu^{2+} metal sites. In the structure refinement, only one coordinated DMF molecule was fully resolved, though it appeared that the molecule was disordered over several sites around the Cu^{2+} binding site. Efforts were taken to resolve the disordered DMF molecules onto multiple sites, though were ultimately unsuccessful. An oxygen atom was also bound to the other Cu^{2+} binding site and though this was most likely to be a part of a coordinated water molecule, hydrogen atoms were not modelled due to difficulties during refinement and concerns regarding the presence of other solvents. Diffuse electron density within the structure was SQUEEZED out using the mask command in Olex2. The structure with bound DMF may be observed in Figures 7.11 and 7.12.

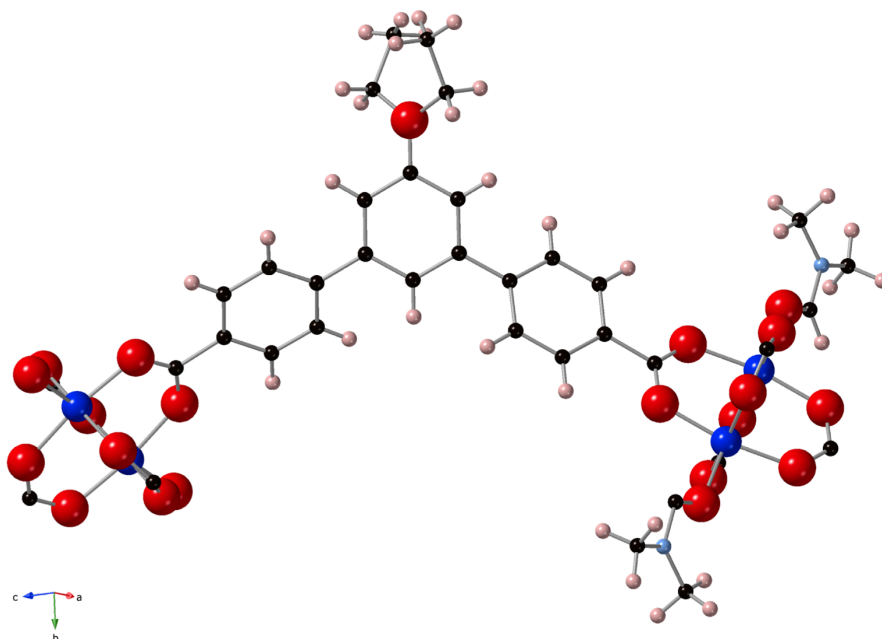


Figure 7.11. The structural unit of copper-1,3-bis(4-carboxyphenyl)-5-ethoxybenzene(DMF) highlighting both the 1,3-bis(4-carboxyphenyl)-5-ethoxybenzene linker and the DMF molecules bound to the Cu^{2+} metal sites on half of the copper paddlewheel units. Key: dark blue: Cu; red: O; black: C; light blue: N; pink: H.

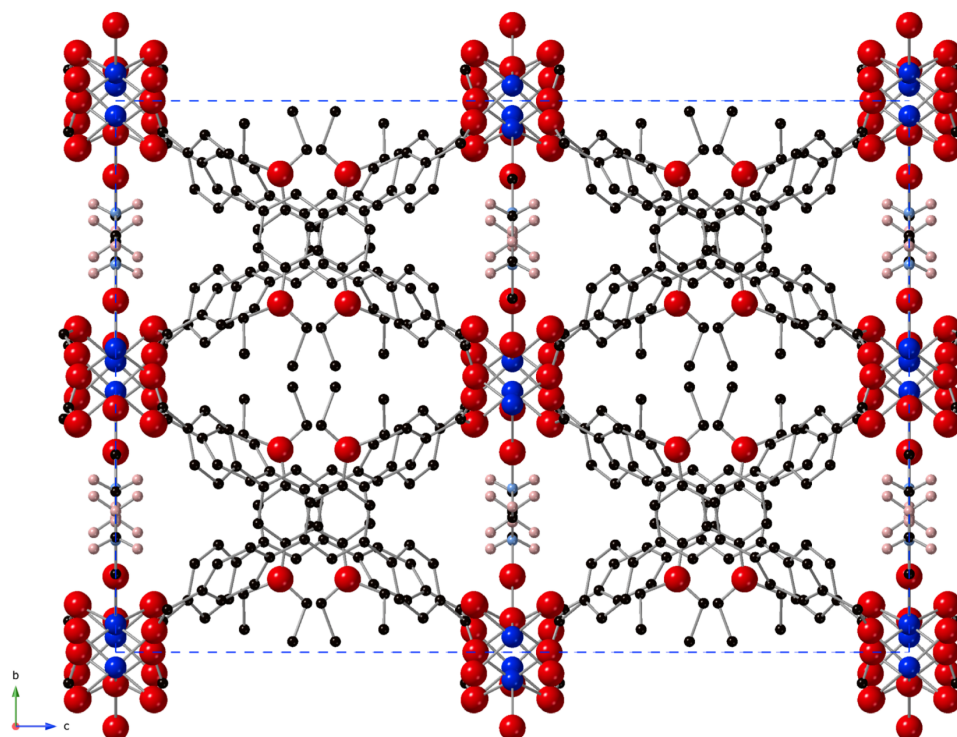


Figure 7.12. Structure of copper-1,3-bis(4-carboxyphenyl)-5-ethoxybenzene(DMF) viewed down the crystallographic a axis showing DMF molecules protruding into to the channels within the structure. Key: dark blue: Cu; red: O; black: C; light blue: N; pink: H. H atoms on the aromatic carbons and ethyl chains have been omitted for clarity.

TGA was collected under air using a Stanton Redcroft STA-780 series thermal analyser from ambient temperature to 750 °C, with a 10 °C per minute heating rate. Figure 7.13 shows the TGA trace of copper-1,3-bis(4-carboxyphenyl)-5-ethoxybenzene(DMF), where the initial mass loss of ca. 4% suggests the loss of water molecules from the material upon activation. No obvious loss of DMF is observed from TGA, suggesting strong solvent binding.

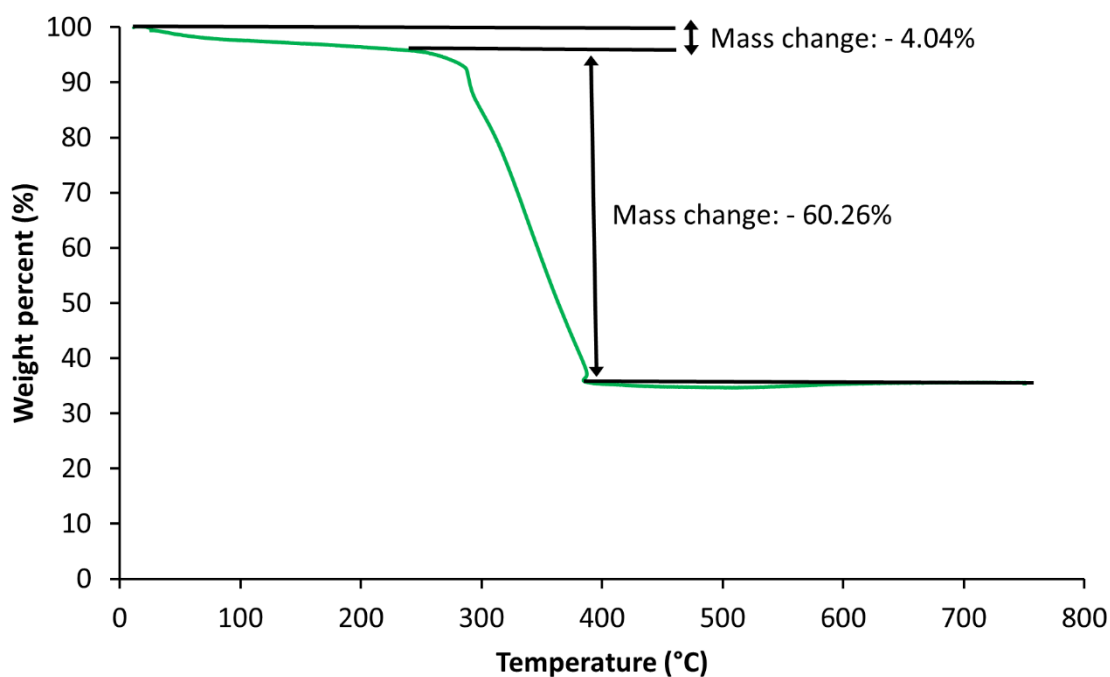


Figure 7.13. TGA trace of copper-1,3-bis(4-carboxyphenyl)-5-ethoxybenzene(DMF) measured in air.

Soxhlet extraction was undertaken with ethanol as an exchange solvent and infrared spectroscopy was used to determine whether the DMF was removed. Figure 7.14 shows the infrared spectra of copper-1,3-bis(4-carboxyphenyl)-5-ethoxybenzene before and after solvent exchange with ethanol. The peak at 1670 cm^{-1} that corresponds to the amide C=O stretch in DMF is not present in the sample after exchange, verifying the loss of DMF from the structure.

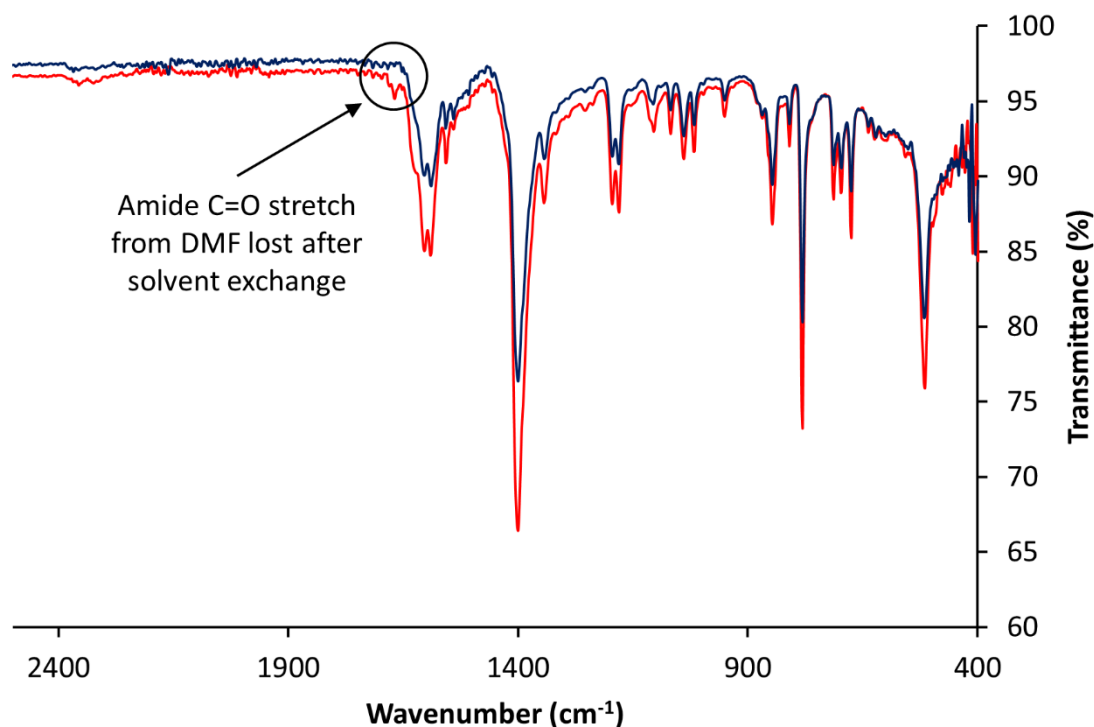


Figure 7.14. Infrared spectra of copper-1,3-bis(4-carboxyphenyl)-5-ethoxybenzene before (red trace) and after (blue trace) solvent exchange with ethanol. The characteristic IR stretch corresponding to the C=O amide stretch in the DMF is no longer present in the sample after solvent exchange, showing successful removal of solvent.

Upon removal of DMF from the structure, the crystal quality was impacted and thus resulted in poor quality data, with the R_{int} value almost doubling from 10.94 to 21.07%. This was attributed to partial degradation of the crystals caused by exposure to hot ethanol during Soxhlet extraction. Room temperature solvent exchange using aqueous chloroform was attempted on a previous sample, though this proved unsuccessful and while more volatile solvents may generally be removed by heating under vacuum, the high boiling point of DMF requires harsh heating and can damage the sample, so this was not attempted. As previously, hydrogen atoms were not modelled on the oxygen atom bound to the other Cu²⁺ binding site and diffuse electron density within the structure was masked.

Crystals of copper-1,3-bis(4-carboxyphenyl)-5-ethoxybenzene formed in the orthorhombic space group *Ibam* and rather than forming a traditional porous MOF structure like the STAM materials, the size and orientation of the ligand caused the material to form as a layered structure or a 'layered coordination framework'. The discrete layers are separated by the disordered ethyl groups, which form a 'backbone' through the structure (Figure 7.15).

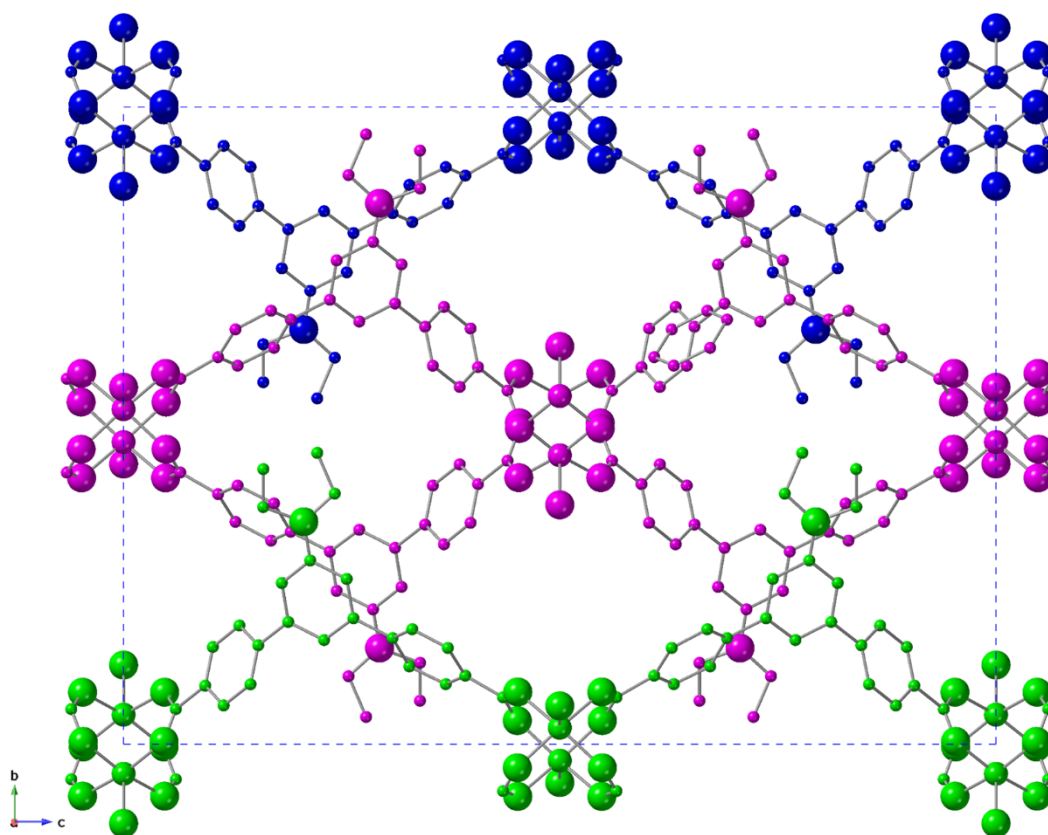


Figure 7.15. Structure of copper-1,3-bis(4-carboxyphenyl)-5-ethoxybenzene viewed down the crystallographic *a* axis showing the individual layers in the material (blue, pink and green). The layers are not connected and are separated by the disordered ethyl chains, which form a 'backbone' through the structure.

The material does have a degree of porosity, though the channels within the structure are discrete and not connected into a traditional porous network. The voids in the framework may be seen in Figure 7.16.

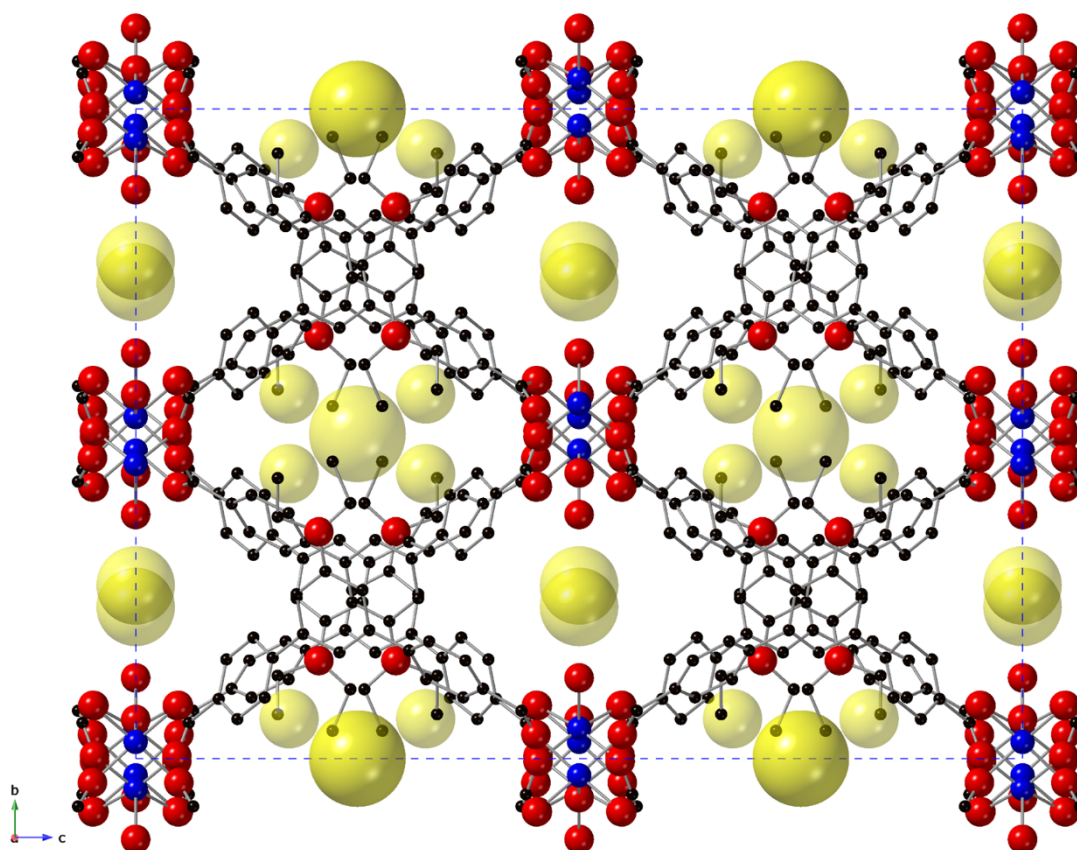


Figure 7.16. Structure of copper-1,3-bis(4-carboxyphenyl)-5-ethoxybenzene viewed down the crystallographic a axis, highlighting the void space in the framework. Key: dark blue: Cu; red: O; black: C; yellow spheres: void space. H atoms have been omitted for clarity.

7.5 Conclusions

A new member of the STAM series of copper MOFs: STAM-NMe₂ was synthesised hydrothermally and analysed by single crystal diffraction, variable temperature powder X-ray diffraction and nitrogen BET surface area analysis. Crystals large enough for in-house single crystal X-ray diffraction were collected, where it was shown that STAM-NMe₂ has a Kagome lattice topology, with a dual pore system consisting of both hydrophilic and hydrophobic pores. Variable temperature powder X-ray diffraction showed that crystallinity in the material is lost upon activation under vacuum, which is contrary to what has been observed for others in the STAM series. While the material has STAM topology, it appears that the inclusion of a dimethylamino group within the structure impairs the thermal stability of STAM-NMe₂.

The novel layered coordination framework copper-1,3-bis(4-carboxyphenyl)-5-ethoxybenzene was synthesised solvothermally and characterised by single crystal X-ray diffraction. The material formed as a layered structure, with disordered DMF molecules bound to one half of the copper paddlewheel units. Upon removal of DMF via Soxhlet extraction with ethanol, the crystal structure was again analysed and though DMF was removed from the structure, crystal quality was impaired as a result.

This chapter shows that new members of the STAM series of MOFs may be synthesised by functionalisation at the 5-position of a 1,3-dicarboxylic acid and that although they may have STAM topology, their structural properties may be affected by the chemistry of the functionalised group. The conformation of the linker is also highly important in synthesising materials with STAM topology, where the coordinating carboxylic acid groups must be

situated in the correct conformation, or a different topology such as that of copper-1,3-bis(4-carboxyphenyl)-5-ethoxybenzene will be observed.

Future work may include the synthesis of an isorecticular series of frameworks, where the conformation of the linker remains the same, though larger pores are produced, thus increasing the porosity.

7.6 References

- [1] L. N. McHugh, L. J. Olivera Perez, P. S. Wheatley, D. B. Cordes, A. M. Z. Slawin and R. E. Morris, *CrystEngComm*, 2019, **21**, 5387-5391.
- [2] D. M. Dawson, C. E. F. Sansome, L. N. McHugh, M. J. McPherson, L. J. McCormick McPherson, R. E. Morris and S. E. Ashbrook, *Solid State Nucl. Magn. Reson.*, 2019, **101**, 44-50.
- [3] L. N. McHugh, M. J. McPherson, L. J. McCormick, S. A. Morris, P. S. Wheatley, S. J. Teat, D. McKay, D. M. Dawson, C. E. F. Sansome, S. E. Ashbrook, C. A. Stone, M. W. Smith and R. E. Morris, *Nat. Chem.*, 2018, **10**, 1096-1102.
- [4] D. Lagnoux, E. Delort, C Douat-Casassus, A. Esposito and J-L. Reymond, *Chem. Eur. J.*, 2004, **10**, 1215-1226.
- [5] Z. Chen, Ł. J. Weseliński, K. Adil, Y. Belmabkhout, A. Shkurenko, H. Jiang, P. M. Bhatt, V. Guillerm, E. Dauton, D.-X. Xue, M. O’Keeffe and M. Eddaoudi, *J. Am. Chem. Soc.*, 2017, **139**, 3265-3274.
- [6] L. N. McHugh, D. B. Cordes, P. S. Wheatley, A. M. Z. Slawin and R. E. Morris, 2019, manuscript submitted.
- [7] CrysAlisPRO, Oxford Diffraction /Agilent Technologies UK Ltd, Yarnton, England.
- [8] G. M. Sheldrick, *Acta Crystallogr A*, 2015, **71**, 3-8.
- [9] G. M. Sheldrick, *Acta Crystallogr C*, 2015, **71**, 3-8.

[10] O. V. Dolomanov, L. J. Bourhis, R. J. Gildea, J. A. K. Howard and H. Puschmann, *J. Appl. Crystallogr.*, 2009, **42**, 339-341.

[11] J. Rouquerol, D. Avnir, C. W. Fairbridge, D. H. Everett, J. M. Haynes, N. Pernicone, J. D. F. Ramsay, K. S. W. Sing, and K. K. Unger, *Pure Appl. Chem.*, 1994, **66**, 1739-1758.

Chapter 8: Conclusions and Future Work

8.1 Conclusions

The key conclusions are included at the end of each chapter, though a comprehensive series of conclusions covering chapters 4, 5, 6 and 7 is included here.

The main aim of this thesis was to investigate the water stability and removal of selected toxic industrial chemicals from contaminated airstreams using a series of copper MOFs. The main application considered within this thesis was the potential use of MOFs inside a filter in future air purification systems.

The series of MOFs used within this study was the STAM series of MOFs, which are copper-based frameworks containing two types of accessible pores.

Chapter 4 highlighted the structural features behind the excellent hydrolytic stability and ammonia adsorption properties of STAM-17-OEt, which was chosen as the main member of the STAM series. An in-depth investigation into the structure of the material was performed using single crystal X-ray diffraction, which showed a change in the coordination environments of copper atoms (the hemilability) upon dehydration, resulting in the formation of long and weak interactions between adjacent copper paddlewheel sub-units. The material was found to be stable upon rehydration, which was an exciting finding considering the proposed application, where the material would have to first be dehydrated to provide open metal sites for the binding of contaminants, though also stable to the moisture always present in breathable air. The hemilability in the material is responsible for the exceptional long-term hydrolytic stability observed in STAM-17-OEt and was described mechanistically by the new “crumple-zone” mechanism, where upon rehydration, the long

and weak interactions present in the dehydrated material are preferentially broken, which protects the critical copper-oxygen bonds within the copper paddlewheel units. Such weak interactions are not present within other copper MOFs such as HKUST-1, which leads to degradation of the material upon prolonged contact with moisture and hence the structural properties of HKUST-1 were used as a comparison for STAM-17-OEt throughout the chapter.

The inherent hydrolytic stability shown by STAM-17-OEt also allowed significant uptake of ammonia from contaminated airstreams and the micro-breakthrough times were increased upon exposure to moisture, while remaining relatively constant even after exposure to high levels of humidity for long periods. HKUST-1 by comparison initially outperformed STAM-17-OEt, though performed poorly after sustained exposure to moisture.

STAM-17-OEt is a member of the STAM series of MOFs, which consist of the parent compound: STAM-1 and other STAM-17-*n* members, where *n* represents the length of the alkyl chain on the associated 1,3-dicarboxylic acid linker. Chapter 5 focused mainly on other members of the STAM series and investigated their porosity, water stability and gas-adsorption capabilities. The long-term water stability first seen in STAM-17-OEt was shown to be present for other members of the series and ammonia micro-breakthrough testing showed a clear linear adsorption trend visible across the series, where members with shorter alkyl chains displayed greater micro-breakthrough times. The materials were tested against hydrogen cyanide using an experimental set-up comparable to that used in ammonia testing. The materials all removed hydrogen cyanide from an airstream, though testing did not show a clear trend across the series and it appeared that the structural features that make STAM-1 and other STAM materials stable to water and able to function in humid environments, prevents significant removal of cyanide from airstreams.

Chapter 6 presented a series of MOF-activated carbon composite materials named the STAM@BPL composites, where STAM-17-OEt and STAM-17-ONPr were grown inside the commercially available BPL activated carbon at a series of loadings. The MOFs were shown to form mainly inside the pores of the activated carbon and water adsorption isotherms showed that the composites displayed adsorption characteristics arising from the MOF and the carbon. As with the STAM materials, the composites were shown to be water stable and adsorbed both cyclohexane and ammonia to varying degrees. The abundance of larger micro- and mesopores present in BPL activated carbon allowed composites with lower MOF loading to adsorb greater quantities of cyclohexane than those with higher MOF incorporation, while the strong and selective interactions formed between the MOF and ammonia lead to greater adsorption in composites with higher MOF loading. The results showed that by altering the loading of MOF within the composites, the materials may be tailored to remove a broader range of contaminants than the individual components alone. The granular form of the STAM@BPL composites also overcame one of the main problems in the engineering of materials used in personal protective equipment, whereby powdered MOF samples may be manufactured into a form that can potentially be used inside a filter.

Chapter 7 discussed the synthesis and characterisation of two novel copper-based frameworks that were not tested for their gas adsorption properties.

STAM-NMe₂ displayed STAM topology, though differed from others in the STAM series due to the presence of a nitrogen-containing dimethylamino side chain, rather than the oxygen-containing side chains present in those previously reported in this thesis.

Variable temperature powder X-ray diffraction showed that crystallinity in the material was lost upon activation under vacuum, which was unexpected when compared to previous observations for others in the STAM series. Though the material had STAM topology, it

appeared that the inclusion of a dimethylamino group in the material impaired the thermal stability of STAM-NMe₂.

Copper-1,3-bis(4-carboxyphenyl)-5-ethoxybenzene was synthesised using an extended version of the 5-ethoxybenzene-1,3-dicarboxylic acid used in the synthesis of STAM-17-OEt, though was found to bond in a different way to the STAM materials and formed an orthorhombic, layered material or a 'layered coordination framework'. The material required DMF to form and initially contained coordinated DMF molecules before their removal through solvent exchange with ethanol by Soxhlet extraction. Upon removal of DMF, the crystal quality was consequently impacted and the single crystal X-ray diffraction solution was of fairly low quality.

With regards to the proposed application, this thesis has shown that MOFs are viable candidates for the removal of toxic industrial chemicals for airstreams. The materials have shown stability to moisture and promising results in the uptake of both ammonia and hydrogen cyanide and MOFs may also be incorporated into activated carbons to provide them in a more useable form. While many further steps must be taken before MOFs may be used in air purification systems, this thesis has shown a series of MOFs and MOF-activated carbon materials that could be prime candidates for use in the removal of contaminants from airstreams.

8.2 Future Work

This thesis has highlighted the potential of MOFs for air purification, though further work is required to fully assess their potential. Some potential future experiments are proposed here:

1. Test the STAM series against other toxic industrial chemicals such as hydrogen sulfide, sulfur dioxide and chlorine. Testing against a range of chemicals is currently being undertaken on STAM-17-OEt, STAM-17-O*n*Pr and STAM-1 by collaborators at the Australian DST Group laboratories, though details of experiments are currently unknown.
2. Test the whole STAM series against humid ammonia, as was performed for STAM-17-OEt.
3. Repeat hydrogen cyanide testing across the STAM series under more controlled conditions.
4. Further investigate the STAM@BPL composites for their adsorption properties, with possible testing against nerve agent simulants.
5. Investigate effect of pelletization on STAM-17-OEt and subsequent testing against ammonia and other chemicals.
6. Synthesis of an isorecticular series of STAM frameworks with increased porosity.

Chapter 9: Appendix

Table 9.1 Bond Lengths for STAM_17_OEt_hydrated_300K

Atom	Atom	Length/Å	Atom	Atom	Length/Å
Cu1	O2 ¹	1.9548(16)	O3	C6 ⁴	1.320(6)
Cu1	O2	1.9548(16)	O3	C5	1.357(4)
Cu1	O1 ²	1.9695(16)	C1	C2	1.495(3)
Cu1	O1 ³	1.9695(16)	C2	C3	1.391(3)
Cu1	O1W	2.150(2)	C2	C4	1.395(3)
Cu1	Cu1 ²	2.6062(7)	C3	C2 ⁴	1.391(3)
O1	C1	1.250(3)	C4	C5	1.396(3)
O1	Cu1 ²	1.9696(16)	C5	C4 ⁴	1.396(3)
O2	C1	1.249(3)	C6	C7	1.488(9)
O3	C6	1.320(6)	O2W	O4W	1.28(2)

¹1-Y,1-X,+Z; ²1-X,1-Y,1-Z; ³+Y,+X,1-Z; ⁴1+Y-X,+Y,+Z

Table 9.2 Bond Angles for STAM_17_OEt_hydrated_300K

Atom	Atom	Atom	Angle/°	Atom	Atom	Atom	Angle/°
O2 ¹	Cu1	O2	89.73(12)	C1	O2	Cu1	123.86(14)
O2 ¹	Cu1	O1 ²	89.84(9)	C6	O3	C6 ⁴	109.7(6)
O2	Cu1	O1 ²	168.62(7)	C6	O3	C5	124.7(3)
O2 ¹	Cu1	O1 ³	168.62(7)	C6 ⁴	O3	C5	124.7(3)
O2	Cu1	O1 ³	89.84(9)	O2	C1	O1	125.14(19)
O1 ²	Cu1	O1 ³	88.35(13)	O2	C1	C2	117.26(18)
O2 ¹	Cu1	O1W	95.91(7)	O1	C1	C2	117.59(19)
O2	Cu1	O1W	95.91(7)	C3	C2	C4	120.6(2)
O1 ²	Cu1	O1W	95.45(7)	C3	C2	C1	119.4(2)
O1 ³	Cu1	O1W	95.45(7)	C4	C2	C1	120.07(19)
O2 ¹	Cu1	Cu1 ²	83.99(5)	C2 ⁴	C3	C2	119.3(3)
O2	Cu1	Cu1 ²	83.99(5)	C2	C4	C5	120.0(2)
O1 ²	Cu1	Cu1 ²	84.65(5)	O3	C5	C4 ⁴	120.24(15)
O1 ³	Cu1	Cu1 ²	84.65(5)	O3	C5	C4	120.24(15)
O1W	Cu1	Cu1 ²	179.85(8)	C4 ⁴	C5	C4	119.5(3)
C1	O1	Cu1 ²	122.31(15)	O3	C6	C7	110.5(6)

¹1-Y,1-X,+Z; ²1-X,1-Y,1-Z; ³+Y,+X,1-Z; ⁴1+Y-X,+Y,+Z

Table 9.3 Bond Lengths for STAM_17_OEt_dehydrated_vac_300K

Atom	Atom	Length/Å	Atom	Atom	Length/Å
C1	O2	1.21(4)	C25	Cu3	2.52(4)
C1	O1	1.35(4)	C26	C31	1.40(2)
C1	C2	1.50(3)	C26	C27	1.40(2)
C2	C3	1.38(3)	C27	C28	1.39(2)
C2	C4	1.40(3)	C27	C32	1.51(3)
C3	C2 ¹	1.38(3)	C28	C29	1.38(3)
C4	C5	1.37(3)	C29	C30	1.39(3)
C5	O3	1.21(7)	C29	O16	1.41(8)
C5	C4 ¹	1.37(3)	C30	C31	1.39(2)
C6	O3	1.43(4)	C32	O14	1.24(3)
C6	C7	1.53(6)	C32	O15	1.24(3)
C8	O5	1.23(5)	C33	O16	1.43(4)
C8	O4	1.27(5)	C33	C34	1.54(5)
C8	C9	1.50(3)	O1	Cu1	1.97(3)
C9	C10	1.37(2)	O2	Cu2	1.93(3)
C9	C11	1.38(3)	O4	Cu1	2.05(2)
C10	C9 ²	1.37(3)	O4	Cu2 ⁵	2.24(2)
C11	C12	1.37(3)	O5	Cu2	1.95(3)
C12	O6	1.30(6)	O7	Cu1	1.95(3)
C12	C11 ²	1.37(3)	O8	Cu2	2.02(3)
C13	O6	1.43(4)	O8	Cu1 ⁶	2.19(3)
C13	C14	1.54(5)	O9	Cu4	2.00(4)
C15	O7	1.20(4)	O10	Cu3	2.04(5)
C15	O8	1.34(5)	O12	Cu4	1.98(4)
C15	C21	1.49(3)	O13	Cu3	1.87(3)
C16	C21	1.39(2)	O14	Cu1	1.92(3)
C16	C17	1.39(2)	O15	Cu2	1.99(3)
C17	C18	1.38(2)	Cu1	O8 ⁵	2.19(3)
C17	C22 ³	1.51(4)	Cu1	Cu2	2.600(8)
C18	C19	1.38(3)	Cu2	O4 ⁶	2.24(2)
C19	O11	1.31(6)	Cu2	O12 ⁷	9.65(4)
C19	C20	1.37(3)	Cu3	O13 ²	1.87(3)
C20	C21	1.38(2)	Cu3	O10 ²	2.04(5)
C22	O10	1.10(6)	Cu3	C25 ²	2.52(4)
C22	O9	1.30(7)	Cu3	Cu4	2.566(10)
C22	C17 ⁴	1.51(4)	Cu3	O12 ⁶	2.87(3)
C23	O11	1.43(4)	Cu4	O12 ²	1.98(4)
C23	C24	1.54(5)	Cu4	O9 ²	2.00(4)
C25	O13	1.23(3)	Cu4	O10 ⁸	2.98(4)
C25	O12	1.25(3)	Cu4	O10 ⁵	2.98(4)
C25	C31	1.55(3)			

¹+Y,+X,+Z; ²1-Y+X,2-Y,+Z; ³1-X,-X+Y,+Z; ⁴1-X,1-X+Y,+Z; ⁵+X,+Y,-1+Z; ⁶+X,+Y,1+Z; ⁷1-Y+X,2-Y,1+Z; ⁸1-Y+X,2-Y,-1+Z

Table 9.4 Bond Angles for STAM_17_OEt_dehydrated_vac_300K

Atom	Atom	Atom	Angle/°	Atom	Atom	Atom	Angle/°
O2	C1	O1	120(3)	O14	Cu1	O7	89.5(12)
O2	C1	C2	119(3)	O14	Cu1	O1	169.9(13)
O1	C1	C2	119(3)	O7	Cu1	O1	91.3(12)
C3	C2	C4	120(3)	O14	Cu1	O4	87.3(11)
C3	C2	C1	121(2)	O7	Cu1	O4	167.4(11)
C4	C2	C1	118(3)	O1	Cu1	O4	89.8(11)
C2 ¹	C3	C2	116(4)	O14	Cu1	O8 ⁵	83.7(11)
C5	C4	C2	127(4)	O7	Cu1	O8 ⁵	112.0(11)
O3	C5	C4 ¹	125(3)	O1	Cu1	O8 ⁵	105.3(12)
O3	C5	C4	125(3)	O4	Cu1	O8 ⁵	79.8(9)
C4 ¹	C5	C4	110(5)	O14	Cu1	Cu2	77.1(8)
O3	C6	C7	114(9)	O7	Cu1	Cu2	83.1(8)
O5	C8	O4	126(3)	O1	Cu1	Cu2	93.0(9)
O5	C8	C9	115(3)	O4	Cu1	Cu2	84.2(7)
O4	C8	C9	119(3)	O8 ⁵	Cu1	Cu2	155.5(8)
C10	C9	C11	121(3)	O2	Cu2	O5	88.8(12)
C10	C9	C8	119(3)	O2	Cu2	O15	165.7(11)
C11	C9	C8	121(3)	O5	Cu2	O15	85.1(12)
C9 ²	C10	C9	117(4)	O2	Cu2	O8	92.8(11)
C12	C11	C9	124(4)	O5	Cu2	O8	170.0(12)
O6	C12	C11 ²	123(3)	O15	Cu2	O8	91.1(12)
O6	C12	C11	123(2)	O2	Cu2	O4 ⁶	88.2(10)
C11 ²	C12	C11	113(5)	O5	Cu2	O4 ⁶	110.8(10)
O6	C13	C14	109(9)	O15	Cu2	O4 ⁶	106.0(10)
O7	C15	O8	123(3)	O8	Cu2	O4 ⁶	79.1(9)
O7	C15	C21	119(3)	O2	Cu2	Cu1	75.0(8)
O8	C15	C21	117(3)	O5	Cu2	Cu1	84.8(9)
C21	C16	C17	110(5)	O15	Cu2	Cu1	91.6(8)
C18	C17	C16	127(4)	O8	Cu2	Cu1	86.0(9)
C18	C17	C22 ³	105(4)	O4 ⁶	Cu2	Cu1	157.0(6)
C16	C17	C22 ³	125(4)	O2	Cu2	O12 ⁷	151.2(8)
C17	C18	C19	118(4)	O5	Cu2	O12 ⁷	79.8(9)
O11	C19	C20	120(4)	O15	Cu2	O12 ⁷	39.5(8)
O11	C19	C18	119(4)	O8	Cu2	O12 ⁷	103.0(9)
C20	C19	C18	120(5)	O4 ⁶	Cu2	O12 ⁷	71.7(6)
C19	C20	C21	117(4)	Cu1	Cu2	O12 ⁷	129.4(3)
C20	C21	C16	128(4)	O13	Cu3	O13 ²	89(2)
C20	C21	C15	119(3)	O13	Cu3	O10 ²	90.0(16)

C16	C21	C15	113(3)	O13 ²	Cu3	O10 ²	175.4(16)
O10	C22	O9	119(5)	O13	Cu3	O10	175.4(16)
O10	C22	C17 ⁴	132(6)	O13 ²	Cu3	O10	90.0(16)
O9	C22	C17 ⁴	98(4)	O10 ²	Cu3	O10	90(2)
O11	C23	C24	109(5)	O13	Cu3	C25 ²	88.7(14)
O13	C25	O12	138(4)	O13 ²	Cu3	C25 ²	28.0(9)
O13	C25	C31	128(4)	O10 ²	Cu3	C25 ²	147.5(15)
O12	C25	C31	94(3)	O10	Cu3	C25 ²	88.5(13)
O13	C25	Cu3	45(2)	O13	Cu3	C25	28.0(9)
O12	C25	Cu3	93(3)	O13 ²	Cu3	C25	88.7(13)
C31	C25	Cu3	173(3)	O10 ²	Cu3	C25	88.5(13)
C31	C26	C27	131(5)	O10	Cu3	C25	147.5(15)
C28	C27	C26	109(4)	C25 ²	Cu3	C25	75.5(12)
C28	C27	C32	123(4)	O13	Cu3	Cu4	95.7(10)
C26	C27	C32	127(4)	O13 ²	Cu3	Cu4	95.7(10)
C29	C28	C27	129(5)	O10 ²	Cu3	Cu4	79.9(13)
C28	C29	C30	113(6)	O10	Cu3	Cu4	79.9(13)
C28	C29	O16	117(5)	C25 ²	Cu3	Cu4	67.9(8)
C30	C29	O16	129(5)	C25	Cu3	Cu4	68.0(8)
C29	C30	C31	128(5)	O13	Cu3	O12 ⁶	83.2(12)
C30	C31	C26	109(4)	O13 ²	Cu3	O12 ⁶	117.1(12)
C30	C31	C25	132(4)	O10 ²	Cu3	O12 ⁶	67.3(15)
C26	C31	C25	117(4)	O10	Cu3	O12 ⁶	101.2(15)
O14	C32	O15	128(4)	C25 ²	Cu3	O12 ⁶	144.5(13)
O14	C32	C27	114(3)	C25	Cu3	O12 ⁶	108.3(11)
O15	C32	C27	118(3)	Cu4	Cu3	O12 ⁶	147.1(8)
O16	C33	C34	103(6)	O12	Cu4	O12 ²	72(2)
C1	O1	Cu1	111(2)	O12	Cu4	O9 ²	96.7(16)
C1	O2	Cu2	136(2)	O12 ²	Cu4	O9 ²	161.4(16)
C5	O3	C6	121(4)	O12	Cu4	O9	161.4(16)
C8	O4	Cu1	120(2)	O12 ²	Cu4	O9	96.7(16)
C8	O4	Cu2 ⁵	138(2)	O9 ²	Cu4	O9	90(2)
Cu1	O4	Cu2 ⁵	99.4(10)	O12	Cu4	Cu3	77.0(10)
C8	O5	Cu2	124(2)	O12 ²	Cu4	Cu3	77.0(10)
C12	O6	C13	120(3)	O9 ²	Cu4	Cu3	86.0(12)
C15	O7	Cu1	129(2)	O9	Cu4	Cu3	86.0(12)
C15	O8	Cu2	119(2)	O12	Cu4	O10 ⁸	65.3(13)
C15	O8	Cu1 ⁶	136(2)	O12 ²	Cu4	O10 ⁸	98.9(14)
Cu2	O8	Cu1 ⁶	101.7(12)	O9 ²	Cu4	O10 ⁸	89.5(15)
C22	O9	Cu4	120(3)	O9	Cu4	O10 ⁸	132.5(15)
C22	O10	Cu3	130(4)	Cu3	Cu4	O10 ⁸	141.2(9)
C19	O11	C23	125(4)	O12	Cu4	O10 ⁵	98.9(14)
C25	O12	Cu4	121(3)	O12 ²	Cu4	O10 ⁵	65.3(13)
C25	O13	Cu3	107(3)	O9 ²	Cu4	O10 ⁵	132.5(15)

C32	O14	Cu1	131(3)	O9	Cu4	O10 ⁵	89.5(15)
C32	O15	Cu2	111(2)	Cu3	Cu4	O10 ⁵	141.2(9)
C29	O16	C33	111(5)	O10 ⁸	Cu4	O10 ⁵	58.1(17)

¹+Y,+X,+Z; ²1-Y+X,2-Y,+Z; ³1-X,-X+Y,+Z; ⁴1-X,1-X+Y,+Z; ⁵+X,+Y,-1+Z; ⁶+X,+Y,1+Z; ⁷1-Y+X,2-Y,1+Z; ⁸1-Y+X,2-Y,-1+Z

Table 9.5 Bond Lengths for STAM-NMe₂

Atom	Atom	Length/Å	Atom	Atom	Length/Å
Cu1	Cu1 ¹	2.6032(7)	N1	C5	1.386(4)
Cu1	O1W	2.146(2)	N1	C6	1.443(3)
Cu1	O2 ¹	1.9649(16)	N1	C6 ⁴	1.443(3)
Cu1	O2 ²	1.9649(16)	C1	C2	1.491(3)
Cu1	O1	1.9524(18)	C2	C4	1.392(3)
Cu1	O1 ³	1.9523(18)	C2	C3	1.392(3)
O2	C1	1.253(3)	C5	C4	1.411(3)
O1	C1	1.256(3)	C5	C4 ⁴	1.411(3)

¹1-X,1-Y,1-Z; ²+Y,+X,1-Z; ³1-Y,1-X,+Z; ⁴+X,1+X-Y,+Z

Table 9.6 Bond Angles for STAM-NMe₂

Atom	Atom	Atom	Angle/°	Atom	Atom	Atom	Angle/°
O1W	Cu1	Cu1 ¹	179.02(7)	C1	O1	Cu1	124.42(16)
O2 ¹	Cu1	Cu1 ¹	84.86(5)	C5	N1	C6 ⁴	119.29(16)
O2 ²	Cu1	Cu1 ¹	84.86(5)	C5	N1	C6	119.29(16)
O2 ¹	Cu1	O1W	95.83(7)	C6 ⁴	N1	C6	116.9(3)
O2 ²	Cu1	O1W	95.83(7)	O2	C1	O1	124.2(2)
O2 ¹	Cu1	O2 ²	88.58(12)	O2	C1	C2	118.4(2)
O1	Cu1	Cu1 ¹	83.82(5)	O1	C1	C2	117.4(2)
O1 ³	Cu1	Cu1 ¹	83.82(5)	C4	C2	C1	119.9(2)
O1	Cu1	O1W	95.50(7)	C3	C2	C1	119.2(2)
O1 ³	Cu1	O1W	95.50(7)	C3	C2	C4	120.8(2)
O1 ³	Cu1	O2 ²	168.65(7)	N1	C5	C4	121.47(15)
O1 ³	Cu1	O2 ¹	89.66(9)	N1	C5	C4 ⁴	121.47(15)
O1	Cu1	O2 ¹	168.65(7)	C4	C5	C4 ⁴	117.0(3)
O1	Cu1	O2 ²	89.66(9)	C2	C4	C5	121.3(2)
O1 ³	Cu1	O1	89.86(13)	C2 ⁴	C3	C2	118.9(3)
C1	O2	Cu1 ¹	122.66(15)				

¹1-X,1-Y,1-Z; ²+Y,+X,1-Z; ³1-Y,1-X,+Z; ⁴+X,1+X-Y,+Z

Table 9.7 Bond Lengths for Copper-1,3-bis(4-carboxyphenyl)-5-ethoxybenzene(DMF)

Atom	Atom	Length/Å	Atom	Atom	Length/Å
Cu01	Cu01 ¹	2.6188(13)	C7	C6	1.401(5)
Cu01	O2 ²	1.969(2)	C2	C3	1.389(5)
Cu01	O2 ¹	1.969(2)	C2	C1	1.494(5)
Cu01	O1 ³	1.962(2)	C2	C4	1.393(5)
Cu01	O1	1.962(2)	C14	C12	1.484(5)
Cu01	O1W	2.191(4)	C14	C15	1.392(5)
Cu02	Cu02 ⁴	2.6384(14)	C14	C16	1.389(5)
Cu02	O3	1.953(3)	C10	C12	1.387(5)
Cu02	O3 ⁵	1.953(3)	C3	C5	1.383(5)
Cu02	O4 ⁴	1.956(3)	C9	C11	1.385(5)
Cu02	O4 ⁶	1.956(3)	C12	C13	1.397(5)
Cu02	O5	2.165(5)	C11	C13	1.394(5)
O2	C1	1.265(4)	C20	C19	1.498(5)
O1	C1	1.253(4)	C19	C17	1.379(6)
O3	C20	1.257(5)	C19	C18	1.394(5)
O4	C20	1.255(5)	C15	C17	1.386(5)
O6	C11	1.361(5)	C6	C4	1.381(5)
O6	C23	1.482(11)	C16	C18	1.385(5)
O6	C21	1.320(10)	C23	C24	1.516(17)
O5	C25	1.227(18)	C21	C22	1.512(16)
C8	C7	1.480(5)	N1	C25	1.38(2)
C8	C10	1.391(5)	N1	C27	1.25(3)
C8	C9	1.395(5)	N1	C26	1.45(3)
C7	C5	1.388(5)			

¹1-X,1-Y,2-Z; ²1-X,1-Y,+Z; ³+X,+Y,2-Z; ⁴2-X,1-Y,1-Z; ⁵+X,+Y,1-Z; ⁶2-X,1-Y,+Z

Table 9.8 Bond Angles for Copper-1,3-bis(4-carboxyphenyl)-5-ethoxybenzene(DMF)

Atom	Atom	Atom	Angle/°	Atom	Atom	Atom	Angle/°
O2 ¹	Cu01	Cu01 ²	81.72(8)	C5	C7	C6	117.4(3)
O2 ²	Cu01	Cu01 ²	81.72(8)	C6	C7	C8	120.5(3)
O2 ²	Cu01	O2 ¹	91.65(16)	C3	C2	C1	121.9(3)
O2 ²	Cu01	O1W	91.90(12)	C3	C2	C4	117.8(3)
O2 ¹	Cu01	O1W	91.90(12)	C4	C2	C1	120.2(3)
O1 ³	Cu01	Cu01 ²	87.16(7)	C15	C14	C12	119.6(3)
O1	Cu01	Cu01 ²	87.16(7)	C16	C14	C12	122.2(3)
O1	Cu01	O2 ¹	87.27(11)	C16	C14	C15	118.1(3)
O1	Cu01	O2 ²	168.87(11)	C12	C10	C8	121.5(3)
O1 ³	Cu01	O2 ²	87.27(11)	C5	C3	C2	120.8(3)

O1 ³	Cu01	O2 ¹	168.87(11)	C11	C9	C8	120.3(3)
O1	Cu01	O1 ³	91.66(16)	C10	C12	C14	120.4(3)
O1	Cu01	O1W	99.20(11)	C10	C12	C13	119.4(3)
O1 ³	Cu01	O1W	99.20(11)	C13	C12	C14	120.0(3)
O1W	Cu01	Cu01 ²	170.81(13)	O6	C11	C9	120.1(3)
O3 ⁴	Cu02	Cu02 ⁵	82.81(9)	O6	C11	C13	119.2(3)
O3	Cu02	Cu02 ⁵	82.81(9)	C9	C11	C13	120.7(4)
O3	Cu02	O3 ⁴	88.23(19)	C3	C5	C7	121.7(3)
O3	Cu02	O4 ⁵	168.20(13)	O3	C20	C19	116.7(3)
O3 ⁴	Cu02	O4 ⁵	91.29(14)	O4	C20	O3	126.0(3)
O3	Cu02	O4 ⁶	91.29(14)	O4	C20	C19	117.2(3)
O3 ⁴	Cu02	O4 ⁶	168.20(13)	C17	C19	C20	120.9(3)
O3 ⁴	Cu02	O5	94.85(13)	C17	C19	C18	119.2(3)
O3	Cu02	O5	94.85(13)	C18	C19	C20	119.9(4)
O4 ⁶	Cu02	Cu02 ⁵	85.43(9)	C11	C13	C12	119.3(3)
O4 ⁵	Cu02	Cu02 ⁵	85.43(9)	C17	C15	C14	121.3(4)
O4 ⁶	Cu02	O4 ⁵	86.8(2)	C4	C6	C7	120.8(3)
O4 ⁵	Cu02	O5	96.94(14)	O2	C1	C2	116.3(3)
O4 ⁶	Cu02	O5	96.94(14)	O1	C1	O2	125.5(3)
O5	Cu02	Cu02 ⁵	176.72(15)	O1	C1	C2	118.2(3)
C1	O2	Cu01 ²	125.2(2)	C6	C4	C2	121.3(3)
C1	O1	Cu01	119.4(2)	C19	C17	C15	120.1(4)
C20	O3	Cu02	124.4(2)	C18	C16	C14	120.8(3)
C20	O4	Cu02 ⁵	121.2(2)	C16	C18	C19	120.4(4)
C11	O6	C23	121.4(5)	O6	C23	C24	113.7(10)
C21	O6	C11	125.0(5)	O6	C21	C22	110.0(8)
C25	O5	Cu02	130.5(11)	C25	N1	C26	110(2)
C10	C8	C7	120.9(3)	C27	N1	C25	123(2)
C10	C8	C9	118.7(3)	C27	N1	C26	127(2)
C9	C8	C7	120.4(3)	O5	C25	N1	122(2)
C5	C7	C8	122.1(3)				

¹1-X,1-Y,+Z; ²1-X,1-Y,2-Z; ³+X,+Y,2-Z; ⁴+X,+Y,1-Z; ⁵2-X,1-Y,1-Z; ⁶2-X,1-Y,+Z

Table 9.9 Bond Lengths for Copper-1,3-bis(4-carboxyphenyl)-5-ethoxybenzene

Atom	Atom	Length/Å	Atom	Atom	Length/Å
Cu01	Cu01 ¹	2.635(2)	C1	C2	1.514(9)
Cu01	O3	1.963(4)	C2	C3	1.337(11)
Cu01	O3 ²	1.963(4)	C2	C4	1.401(10)
Cu01	O4 ³	1.972(5)	C12	C13	1.369(10)
Cu01	O4 ¹	1.972(5)	C12	C10	1.399(9)
Cu01	O2W	2.176(6)	C12	C14	1.498(8)

Cu02	Cu02 ⁴	2.626(3)	C13	C11	1.412(9)
Cu02	O1 ⁵	1.949(5)	C17	C15	1.380(9)
Cu02	O1 ⁴	1.949(5)	C11	C9	1.379(10)
Cu02	O2 ⁶	1.952(6)	C10	C8	1.395(9)
Cu02	O2	1.952(6)	C7	C8	1.497(9)
Cu02	O1W	2.147(10)	C7	C6	1.349(10)
O3	C20	1.285(8)	C7	C5	1.402(9)
O4	C20	1.250(8)	C8	C9	1.367(10)
O1	C1	1.268(8)	C14	C15	1.394(9)
O5	C11	1.349(9)	C14	C16	1.373(10)
O5	C21	1.464(13)	C6	C4	1.396(10)
O5	C23	1.415(16)	C3	C5	1.403(9)
O2	C1	1.217(9)	C18	C16	1.378(10)
C19	C17	1.388(10)	C21	C22	1.39(2)
C19	C20	1.489(9)	C24	C23	1.48(2)
C19	C18	1.407(9)			

¹1-X,1-Y,1-Z; ²+X,+Y,1-Z; ³1-X,1-Y,+Z; ⁴2-X,1-Y,-Z; ⁵2-X,1-Y,+Z; ⁶+X,+Y,-Z

Table 9.10 Bond Angles for Copper-1,3-bis(4-carboxyphenyl)-5-ethoxybenzene

Atom	Atom	Atom	Angle/°	Atom	Atom	Atom	Angle/°
O3	Cu01	Cu01 ¹	86.44(14)	C18	C19	C20	119.3(6)
O3 ²	Cu01	Cu01 ¹	86.44(14)	O1	C1	C2	115.8(7)
O3 ²	Cu01	O3	91.0(3)	O2	C1	O1	125.3(6)
O3 ²	Cu01	O4 ³	168.62(19)	O2	C1	C2	118.9(6)
O3	Cu01	O4 ¹	168.62(19)	C3	C2	C1	121.7(6)
O3 ²	Cu01	O4 ¹	87.5(2)	C3	C2	C4	120.2(6)
O3	Cu01	O4 ³	87.5(2)	C4	C2	C1	118.1(7)
O3	Cu01	O2W	97.1(2)	C13	C12	C10	119.6(6)
O3 ²	Cu01	O2W	97.1(2)	C13	C12	C14	121.0(6)
O4 ³	Cu01	Cu01 ¹	82.21(14)	C10	C12	C14	119.4(7)
O4 ¹	Cu01	Cu01 ¹	82.21(14)	C12	C13	C11	119.9(6)
O4 ¹	Cu01	O4 ³	91.7(3)	C15	C17	C19	121.1(6)
O4 ³	Cu01	O2W	94.3(2)	O5	C11	C13	119.5(6)
O4 ¹	Cu01	O2W	94.3(2)	O5	C11	C9	121.5(6)
O2W	Cu01	Cu01 ¹	175.0(2)	C9	C11	C13	119.0(8)
O1 ⁴	Cu02	Cu02 ⁵	83.85(17)	C8	C10	C12	121.0(7)
O1 ⁵	Cu02	Cu02 ⁵	83.85(17)	C6	C7	C8	122.8(6)
O1 ⁴	Cu02	O1 ⁵	89.0(4)	C6	C7	C5	119.6(6)
O1 ⁴	Cu02	O2 ⁶	167.6(3)	C5	C7	C8	117.5(7)
O1 ⁴	Cu02	O2	90.6(3)	C10	C8	C7	120.0(7)
O1 ⁵	Cu02	O2 ⁶	90.6(3)	C9	C8	C10	118.3(6)
O1 ⁵	Cu02	O2	167.6(3)	C9	C8	C7	121.8(6)

O1 ⁵	Cu02	O1W	94.9(3)	C15	C14	C12	120.8(6)
O1 ⁴	Cu02	O1W	94.9(3)	C16	C14	C12	121.4(6)
O2	Cu02	Cu02 ⁵	83.82(19)	C16	C14	C15	117.8(6)
O2 ⁶	Cu02	Cu02 ⁵	83.82(19)	C7	C6	C4	121.1(6)
O2	Cu02	O2 ⁶	87.2(4)	C2	C3	C5	120.9(7)
O2 ⁶	Cu02	O1W	97.5(3)	C7	C5	C3	119.2(7)
O2	Cu02	O1W	97.5(3)	O3	C20	C19	117.3(6)
O1W	Cu02	Cu02 ⁵	178.2(3)	O4	C20	O3	124.7(6)
C20	O3	Cu01	120.2(4)	O4	C20	C19	117.8(6)
C20	O4	Cu01 ¹	125.6(4)	C17	C15	C14	120.9(6)
C1	O1	Cu02 ⁵	122.9(5)	C8	C9	C11	122.2(6)
C11	O5	C21	121.0(8)	C16	C18	C19	119.7(7)
C11	O5	C23	124.0(8)	C6	C4	C2	119.1(7)
C1	O2	Cu02	124.1(5)	C14	C16	C18	122.3(6)
C17	C19	C20	122.7(6)	C22	C21	O5	112.4(12)
C17	C19	C18	118.0(6)	O5	C23	C24	108.3(12)

¹1-X,1-Y,1-Z; ²+X,+Y,1-Z; ³1-X,1-Y,+Z; ⁴2-X,1-Y,+Z; ⁵2-X,1-Y,-Z; ⁶+X,+Y,-Z